Simulation of Viscoelastic Fluids using Brownian Configuration Fields

Simulation von viskoelastischen Flüssigkeiten mit
brownschen Konfigurationsfeldern

Der Naturwissenschaftlichen Fakultät
der Friedrich-Alexander-Universität
Erlangen-Nürnberg

Dissertation

zur Erlangung des Doktorgrades

Dr. rer. nat.

vorgelegt von

Andreas Meier

Als Dissertation genehmigt
von der Naturwissenschaftlichen Fakultät
der Friedrich-Alexander-Universität Erlangen-Nürnberg

Tag der mündlichen Prüfung:	22.10.2024
Gutachter:	Prof. Dr. Eberhard Bänsch
	Prof. Dr. Carsten Gräser

Contents

Acknowledgement

I would like to thank my supervisor Prof. Dr. Eberhard Bänsch for proposing this fascinating topic and my second supervisor Prof. Dr. Günther Grün for giving me the liberty to perform my own research. Special thanks for the financial support goes to the Research Training Group 2339 Interfaces, Complex Structures, and Singular Limits. Many thanks to Dr. Florian Frank for the good advices over the years and our collaboration in the simulation project "Simulicious". I would also like to extend my gratitude to my colleague Prof. Dr. Carsten Gräser for many interesting discussions concerning implementations. Further, I would like to extend my sincere thanks to my office mate Dr. Martin Doß for the companionship through this journey and for always having an open ear for discussions concerning my research. I must also thank my coauthors Dr. Stephan Gärttner and Prof. Dr. Nadja Ray. Finally, I would like to thank all of my friends and family for their ongoing support.

Zusammenfassung

Simulation von viskoelastischen Flüssigkeiten mit brownschen Konfigurationsfeldern

Nicht-Newtonsche viskoelastische Flüssigkeiten sind in verschiedenen industriellen und medizinischen Anwendungen weit verbreitet. So können beispielsweise Lösungen, die DNA-Moleküle enthalten, oder Blut als viskoelastische Flüssigkeiten eingestuft werden. Eine noch umfangreicherer Klasse von viskoelastischen Flüssigkeiten sind die Polymerfluide. Schon die geringe Hinzugabe von Makromolekülen (Polymerketten) in Flüssigkeiten führt zu erheblichen quantitativen und rheologischen Unterschieden im Vergleich zu newtonschen Flüssigkeiten. Zu den bemerkenswertesten Fließphänomenen von Polymerfluiden gehört zum Beispiel der Weissenberg-Effekt, der das Hinaufklettern einer Flüssigkeit an einem rotierenden Stab beschreibt, und die Reduktion des Strömungswiderstandes (*drag reduction*) durch Polymere [11].

Zur Modellierung viskoelastischer Flüssigkeiten gibt es mehrere Ansätze. So gehört beispielsweise das bekannte Oldroyd-B-Modell zur Klasse der konstitutiven Modelle [62]. Alternativ dazu stellen Mehrskalenansätze genauere Modelle bereit, die die Dynamik der Polymere auf der Mikroskala mit Werkzeugen aus der kinetischen Theorie beschreiben [12, 17]. Zu diesen Modellen gehören die *bead-spring-rod*-Modelle, in denen Polymerketten mit Hilfe von kleinen Kügelchen dargestellt werden, die durch frei bewegliche Federn oder Stäbchen miteinander verbunden sind [63]. Im *bead-rod*-Kettenmodell bleibt die gesamte Kettenlänge in Bezug auf mögliche Verformungen konstant, während die Kettenlänge im *bead-spring*-Modell durch die Ausdehnung und Stauchung der Federn variieren kann. Im Hinblick auf die konstante Länge einer Polymerkette kann das *bead-rod*-Kettenmodell als genaueres Modell für die Beschreibung von Polymerketten eingestuft werden.

Simulationen von *bead-spring-rod*-Modellen mit homogenen Hintergrundströmungen wurden bereits mehrfach durchgeführt [50, 75]. Diese Art von Strömungen werden durch einen räumlich konstanten Geschwindigkeitsgradienten charakterisiert. Beispiele hierfür sind Scherströmung (*shear flow*) oder die Dehnungsströmung (*extensional flow*). Die Vorgabe einer homogenen Hintergrundströmung ist jedoch eine starke Vereinfachung und verhindert die Simulation von instationären Strömungen. Durch die Kopplung der Mikroskalenmodelle (*bead-spring* oder *bead-rod*) mit den Navier–Stokes-Gleichungen wird die Betrachtung realistischer Strömungsszenarien möglich. Die Polymerketten sind dadurch in der Lage, das zugrunde liegende Strömungsfeld zeitlich und räumlich zu beeinflussen. Die numerische Simulation solcher gekoppelten Modelle in komplex strukturierten Gebieten ist sehr herausfordernd, da zum Beispiel hohe Spannungsgefälle in kleinen Bereichen feine Diskretisierungsgitter benötigen, um diese räumlich aufzulösen. Derartige Simulation wurden nur für niedrigdimensionale *bead-spring*-Modelle oder konsti-

tutive Modelle durchgeführt [40, 70, 83]. Die Kopplung des höherdimensionalen *bead-rod*-Kettenmodells mit den Navier–Stokes-Gleichungen ist darüber hinaus sogar noch rechenintensiver, da *bead-spring*-Modelle niedrigdimensionale Approximationen von *bead-rod*-Kettenmodellen sind. Soweit uns bekannt ist, wurden bisher keine derartigen Simulationen in der Literatur veröffentlicht.

In dieser Arbeit simulieren wir Strömungen nicht-newtonscher Polymerfluide, die durch das mikroskopische *bead-spring*-Modell oder *bead-rod*-Kettenmodell beschrieben werden, welches zusätzlich mit den Navier–Stokes-Gleichungen gekoppelt wurde. Dadurch schließen wir die oben genannte Forschungslücke. Es werden fortgeschrittene Strömungsszenarien betrachtet, die die zugrunde liegende Geometrie berücksichtigen, wie z.B. die Strömung um einen Zylinder und die Strömung durch eine flache Kontraktion. In diesen Szenarien analysieren wir in mehreren Untersuchungen, wie sich die Länge der *bead-rod*-Ketten auf die makroskopische Geschwindigkeit der Strömung und den resultierenden Strömungswiderstand auswirkt. Zusätzlich werden quantitative Vergleiche mit Simulationen des gekoppelten *bead-spring*-Modells gemacht.

Im Prinzip gibt es zwei Möglichkeiten für die Simulation von Mehrskalenmodellen. Der Monte–Carlo-Ansatz, bei dem viele Realisierungen einer stochastischen Differentialgleichung auf der Mikroskala berechnet werden oder alternativ das Lösen einer dazu assoziierten Fokker–Planck-Gleichung [5, 9, 32]. Für *bead-rod*-Ketten, wie sie in dieser Arbeit betrachtet werden, ist der Monte–Carlo-Ansatz der einzig praktikable, da die Dimension der Fokker–Planck-Gleichung mit der Anzahl an Kügelchen skaliert (*curse of dimensionality*).

Für die Diskretisierung wird eine Kombination aus Finite-Element-Methode (FEM) und brownscher Konfigurationsfeld-Methode [40] verwendet. Aufgrund der zusätzlichen Nebenbedingungen an die Stäbchenlänge, die im *bead-rod*-Kettenmodell auftreten, müssen zusätzliche Aspekte in der Diskretisierung berücksichtigt werden. Diese Art von expliziten Nebenbedingungen sind bei *bead-spring*-Modellen nicht vorhanden. Mit der heutigen zur Verfügung stehenden Rechenleistung ist es nun möglich, erste Simulationen von Strömungen gekoppelter *bead-rod*-Kettenmodelle durchzuführen.

Die Arbeit ist folgendermaßen aufgebaut: In Abschnitt 1 wird eine kurze Einführung zu Polymerfluiden gegeben, die Navier-Stokes-Gleichungen hergeleitet, verschiedene Randbedingungen präsentiert und bekannte konstitutive Gleichungen für Polymerfluide diskutiert. Abschnitt 2 leitet die stochastischen Differentialgleichungen für das *bead-spring*-Modell und *bead-rod*-Kettenmodell mit den entsprechenden Ausdrücken für die Spannungstensoren her, die für die Kopplung mit den Navier-Stokes-Gleichungen benötigt werden. Danach werden in Abschnitt 3 alle Aspekte, die für Diskretisierung und Lösung der gekoppelten Modelle benötigt werden, besprochen. Abschnitt 4 diskutiert die wichtigen Parallelisierungsansätze der Implementierung und untersucht die daraus resultierende parallele Skalierbarkeit des Codes. Abschnitt 5 präsentiert und diskutiert die aus den Simulationen der oben genannten Strömungsszenarien gewonnenen Erkenntnisse.

Abstract

Non-Newtonian viscoelastic fluids are widely present in various industrial and medical applications. For instance, solutions containing DNA molecules [41] or blood can be classified as viscoelastic fluids. An even larger field are polymeric fluids, where the presence of macro molecules (polymer chains) leads to significant quantitative rheological distinctions when compared to Newtonian fluids. Notable flow phenomena of polymeric fluids include the rod climbing effect, drag reduction, and extrudate swell [11]. The drag reduction effect is widely exploited in industry, e.g., transport of oil through pipelines or to increase the effectiveness of fire fighting equipment [53, 68].

There are multiple approaches to model viscoelastic fluids. For instance, the well-known Oldroyd-B model [62] belongs to the class of constitutive models. Alternatively, multiscale models, using kinetic theory to describe the dynamics on the micro scale, provide more accurate models [12, 17]. These models include bead-spring-rod models, which represent polymer chains as beads interconnected by springs or rods [63]. In the pure bead-rod case, the chain length remains constant w.r.t. possible deformations, whereas the chain length in the bead-spring case is allowed to vary. Concerning the constant length of a polymer chain, the bead-rod chain model can be viewed as more accurate model for approximating polymer chains.

Brownian dynamic simulations of bead-rod-spring models w.r.t. simple homogeneous flows (shear flow, extensional flow) were already analyzed multiple times [50, 75]. However, assuming a prescribed constant flow field is a strong simplification and prevents the simulation of instationary flows. The coupling of the bead-rod-spring micro-scale models to the Navier–Stokes equations enables the consideration of more realistic scenarios in which polymer chains can actually affect the underlying flow field. The numerical simulation of such fluids in complex domains is very challenging since high-stress profiles near the boundary require fine discretization meshes. Simulation of coupled models is computationally expensive and was done for low dimensional bead-spring chain models [40, 70, 83] or constitutive models. Coupling the higher-dimensional bead-rod chain model to Navier–Stokes is even more computationally expensive since bead-spring models are simplified coarse-grained versions of bead-rod models. To the best of our knowledge, no such simulations have been published to date in the literature.

In this thesis, we simulate non-Newtonian polymeric fluids described by the microscopic bead-spring dumbbell and bead-rod chain model [12], also known as Kramers chain [13], coupled with the Navier–Stokes equations and close the above-mentioned research gap. We consider advanced scenarios with flows fully resolving the underlying geometry such as the start-up shear flow, flow around a cylinder and flow through a planar contraction. In these scenarios, we analyze how the bead-rod chain length affects the macroscopic velocity and drag coefficient in multiple studies by varying the number of beads and thus the chain lengths. Additionally, quantitative comparison to bead-spring dumbbell simulations are made.

In principle, there are two options for the simulations of multiscale models: Monte–Carlo methods that compute many realizations of a small problem on the micro scale or alternatively solving a corresponding Fokker–Planck equation, see for instance [5, 9, 32]. For Kramers chains like treated in this thesis, a Monte–Carlo method seems to be the only feasible approach, since otherwise one had to solve a prohibitively high-dimensional Fokker–Planck equation, where the dimension scales with the number of beads (*curse of dimensionality*).

We combine finite elements with the Brownian configuration field (BCF) approach, a method that was first introduced by [40]. Due to the constant rod length constraints appearing in the bead-rod chain model, additional numerical challenges need to be carefully treated. This type of explicit constant length constraint does not arise in bead-spring type models either. As computational resources are now readily available, we are able to begin with the study of bead-rod models coupled to Navier–Stokes equations.

The structure of the thesis is as follows. In Section 1, we give a brief introduction into polymeric fluids, derive the Navier–Stokes equations with various boundary conditions and discuss well-known constitutive equations. Section 2 derives the governing equations for the bead-spring dumbbell and bead-rod chain model with its corresponding polymeric stress tensors, which are used for the coupling to the Navier–Stokes equations. Section 3 covers all aspects, which are needed for the discretization of the coupled models. In Section 4, we discuss the crucial parallelization approaches of our implementation and its resulting parallel performance. In Section 5, we present and discuss the insights obtained from simulations of the above mentioned flow scenarios.

1 Introduction to dilute polymeric fluids

In order to get a sufficient understanding about polymers for the scope of this thesis, we start by giving a brief introduction to polymers and polymeric fluids in the next sections. At first, we give some background information on the structure and characterization of polymeric fluids in Section 1.1. In Section 1.2, we demonstrate some quantitative differences between common Newtonian fluids and polymeric fluids. Crucial conservation equations that form the basis of fluid dynamics are derived in Section 1.3. Section 1.4 discusses a selection of commonly used constitutive equations. Relevant boundary conditions are introduced in Section 1.5. Section 1.6 non-dimensionalizes the Navier–Stokes equations in the context of polymeric fluids. Lastly, Section 1.7 gives a proof for the unique existence of weak solutions for the stationary Stokes problem with periodic boundary conditions and a constant flowrate condition.

1.1 Polymer background information

This section is based on [11, Ch. 2]. A polymer or macromolecule is a chain-like concatenation of many simple chemical structural units of the same type. In the case of a linear polymer, a structural unit is connected to two other units. Otherwise, it is called branched. Depending on the number of different structural units, one can differentiate between biological and synthetic polymers. Synthetic polymers are typically constructed with a single type of structural unit. In a chemical reaction called polymerization, monomers that resemble the structural units are connected to form polymers. In Figure 1.1, the simplified polymerization of polyethylene is visualized. By contrast, biological polymers, like polypeptide chains that are used for building proteins, are build with around 20 different structural units [11, p. 56]. Due to their sheer size, polymers have a large molecular weight. Synthetic polymer molecules are in the range of $10^4 - 10^6$g/mol and the (biological) Tobacco mosaic virus shows an even larger weight of $4 \cdot 10^7$g/mol [11, p. 57]. Flexible polymers have many admissible configurations in space due to rotations around chemical bonds, i.e., they can be strechted or contracted. There are also stiff polymers like the aforementioned tobacco mosaic virus, which can only rotate as a whole.

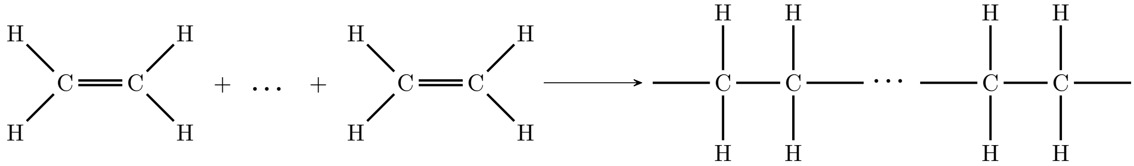

Figure 1.1. Simplified visualization of polyethylene polymerization. Ethylene monomers are joined together to form polyethylene. See [11, p. 57], for a detailed description of the individual chemical reaction steps.

In order to obtain polymeric fluids, a bulk of polymers is dissolved into a solvent to form a solution. These polymeric fluids show significant quantitative rheological differences compared to Newtonian fluids. Polymeric fluids are a special type of viscoelastic fluid, as they show properties from both, viscous and elastic materials, depending on the observed time scale. The molecular weight of dissolved polymers plays a significant role, as fluids with small molecules behave differently compared to macromolecular fluids. An overview of different viscoelastic effects is presented in Section 1.2. A solution is called dilute if individual polymers are far enough apart, such that they have negligible influence on each other and polymer-solvent interactions dominate [11, p. 77]. The dilutness of a solution highly depends on its concentration and the molecular weight of the dissolved polymers. In [11, p. 77], a dilute solution is defined as one in which its viscosity increases linearly with concentration. For concentrated solutions, polymer-polymer interactions cannot be neglected anymore and the viscosity no longer depends linearly on the concentration.

1.2 Viscoelastic flow effects

The goal of this section is to highlight quantitative rheological differences for Newtonian and polymeric fluids, when it comes to flow behavior. In [11, Ch. 3], several flow phenomena are discussed and we present three of them. This should underline that not every fluid behavior can be captured by a Newtonian fluid.

Weissenberg effect The rod-climbing or Weissenberg effect is an impressive demonstration of a counterintuitive viscoelastic flow phenomena. In this experiment, a rotating rod is inserted into a beaker containing a Newtonian fluid, like glycerin, and into a second beaker, which contains a polymeric fluid. One possible polymeric fluid could be polyacrylamide dissolved in glycerin. In Figure 1.2, the beakers are visualized with the corresponding fluid surfaces. In the case of the Newtonian fluid, the fluid moves away from the rod in radial direction due to centrifugal forces. This results in a higher fluid distribution near the beaker wall and a lower one in the center (cf. Figure 1.2a). Repeating the same procedure in the polymeric fluid beaker, leads to a completely different result. Now, instead of pushed away from the rod, the fluid unintuitively climbs up the rotating rod (cf. Figure 1.2b) due to a positive normal force, which is a result of the polymer entanglement near the rod.

Barus effect The Barus effect or extrudate swell effect occurs, when a polymeric fluid is pushed out of a tube through a narrow circular exit. In the case of a Newtonian fluid, the diameter of the resulting jet will be the same as the exits diameter or even smaller (cf. Figure 1.3a). By contrast, the jet diameter of a polymeric fluid can go up to three or four times of the tube diameter [11, p. 101]. This effect is visualized in Figure 1.3b.

A first explanation for this phenomenon could be the fading memory effect of polymeric fluids, i.e., polymeric fluids try to reverse deformations on short time scales. However, as experiments demonstrate, this effects still occurs if the length of the narrow exit is increased [11, p. 102]. See [11, p. 103], for a more detailed explanation attempt. Note that the Barus effect is still an active area of research.

(a) Newtonian fluid (b) Polymeric fluid

Figure 1.2. Visualization of the rod-climbing or Weissenberg effect. A rotating rod is inserted into beakers, containing different types of fluid.

(a) Newtonian fluid (b) Polymeric fluid

Figure 1.3. Visualization of the extrudate swell or Barus effect. Fluids of different type are pushed through a tube with a contracted exit.

Turbulent drag reduction The turbulent drag reduction phenomenon is widely exploited in the industry, where large amounts of fluids need to be efficiently transported. Adding small amounts of long chain polymers into solvents, leads to remarkable pressure drops at high flow rates. Common applications are the transport of gasoline or oil through pipelines [53] or increasing the effectiveness of fire fighting equipment [68]. In [18], the polymer poly-α-olefin is used as drag reducer in crude oil to increase the transport effectiveness in pipelines.

1.3 Conservation equations for general fluids

In the following, we consider isothermal fluids with constant density, i.e., the fluid's temperature and density is constant in space and time. At first, we briefly derive the equations for conservation of mass and momentum for a general isothermal fluid with constant density. These equations form the starting point in fluid dynamics for the derivation of governing equations for more specific fluids, e.g., Newtonian or viscoelastic fluids. For the derivation of the conservation equations, we follow [11, Ch. 1.1], where an arbitrary but fixed control volume V is considered, cf. Figure 1.4.

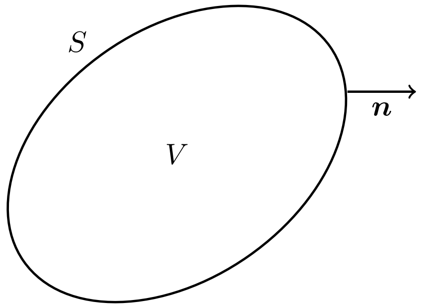

Figure 1.4. Control volume V with surface S and normal vector $\boldsymbol{n}$ in a fluid.

Conservation of mass Let $\boldsymbol{u}$ denote the fluid velocity and ρ its density. The total mass $\int_V \rho \, \mathrm{d}V$ in volume V can only change in time through mass fluxes across surface S. The corresponding equation is then given by

$$\frac{\mathrm{d}}{\mathrm{d}t} \int_V \rho \, \mathrm{d}V = - \int_S \rho \boldsymbol{u} \cdot \boldsymbol{n} \, \mathrm{d}S. \tag{1.1}$$

Applying Gauss's divergence theorem on the right hand side of (1.1) and using that V is fixed, yields after rearrangement

$$\int_V \left(\partial_t \rho + \boldsymbol{\nabla} \cdot (\rho \boldsymbol{u}) \right) \mathrm{d}V = 0. \tag{1.2}$$

Since the volume V was arbitrary, one can deduce from (1.2) the continuity equation

$$\partial_t \rho = -\boldsymbol{\nabla} \cdot (\rho \boldsymbol{u}) = -\boldsymbol{u} \cdot \boldsymbol{\nabla} \rho - \rho \boldsymbol{\nabla} \cdot \boldsymbol{u}, \tag{1.3}$$

which describes the conservation of mass. In our case, density $\rho > 0$ is just a constant. With this additional information, (1.3) simplifies to the well known incompressibility condition

$$\boldsymbol{\nabla} \cdot \boldsymbol{u} = 0. \tag{1.4}$$

Conservation of momentum There are multiple effects that influence the total momentum $\int_V \rho \boldsymbol{u} \, \mathrm{d}V$ in V over time. The first effect is due to momentum transfer over S through the moving fluid itself and is given by the rate $- \int_S \rho \boldsymbol{u} (\boldsymbol{u} \cdot \boldsymbol{n}) \, \mathrm{d}S$. The second momentum transfer rate over S is motivated by internal molecular motion and interaction within the fluid, which is expressed via $\int_S \boldsymbol{\sigma} \cdot \boldsymbol{n} \, \mathrm{d}S$, where the stress tensor $\boldsymbol{\sigma}$ is assumed to be a symmetric matrix. The equations for conservation of momentum are then given by

$$\frac{\mathrm{d}}{\mathrm{d}t}\int_V \rho\boldsymbol{u}\,\mathrm{d}V = -\int_S \rho\boldsymbol{u}(\boldsymbol{u}\cdot\boldsymbol{n})\,\mathrm{d}S + \int_S \boldsymbol{\sigma}\cdot\boldsymbol{n}\,\mathrm{d}S. \tag{1.5}$$

Applying the same argumentation as above, (1.5) can be further transformed to

$$\int_V (\partial_t(\rho\boldsymbol{u}) + \boldsymbol{\nabla}\cdot(\rho\boldsymbol{u}\otimes\boldsymbol{u}) - \boldsymbol{\nabla}\cdot\boldsymbol{\sigma}) = \boldsymbol{0}, \tag{1.6}$$

from which the equation for momentum conservation

$$\rho\,(\partial_t\boldsymbol{u} + \boldsymbol{u}\cdot\boldsymbol{\nabla}\boldsymbol{u}) - \boldsymbol{\nabla}\cdot\boldsymbol{\sigma} = \boldsymbol{0} \tag{1.7}$$

is obtained by utilizing the constant density assumption and the consequential incompressibility condition (1.4). In (1.6), $(\boldsymbol{u}\otimes\boldsymbol{u})_{ij} := u_i u_j$ denotes the outer product. Note that external forces on the fluid, such as gravitational force, were neglected here. The gravitational force can be included by adding the term $\rho\boldsymbol{g}$ to the right hand side of (1.7), where $\boldsymbol{g}$ denotes the gravitational force vector. The stress tensor $\boldsymbol{\sigma}$ is typically expressed as

$$\boldsymbol{\sigma} := \boldsymbol{\tau} - p\boldsymbol{I}, \tag{1.8}$$

where $\boldsymbol{\tau}$ is the non-isotropic *deviatoric* stress tensor that vanishes for fluids at rest and $-p\boldsymbol{I}$ is the isotropic part with p denoting the *pressure* [10, p. 142]. Specific choices for $\boldsymbol{\tau}$ depend on the underlying fluid model. Entry σ_{ji} can be interpreted as the force per unit area, which acts in negative j-direction on a surface that is perpendicular to i-direction.

For incompressible Newtonian fluids, we have the linear relation

$$\boldsymbol{\tau} = 2\mu\boldsymbol{D}(\boldsymbol{u}) \tag{1.9}$$

with μ being a scalar constant called *viscosity* [10, p. 146]. Thus, for incompressible Newtonian fluids, we have

$$\boldsymbol{\sigma} = 2\mu\boldsymbol{D}(\boldsymbol{u}) - p\boldsymbol{I}, \tag{1.10}$$

where $\boldsymbol{D}(\boldsymbol{u}) := \frac{1}{2}\left[\boldsymbol{\nabla}\boldsymbol{u} + (\boldsymbol{\nabla}\boldsymbol{u})^{\mathrm{T}}\right]$ denotes the *rate of strain* tensor. Substituting (1.10) into (1.7) gives

$$\rho\,(\partial_t\boldsymbol{u} + \boldsymbol{u}\cdot\boldsymbol{\nabla}\boldsymbol{u}) - 2\mu\boldsymbol{\nabla}\cdot\boldsymbol{D}(\boldsymbol{u}) + \boldsymbol{\nabla}p = \boldsymbol{0}. \tag{1.11}$$

Equation (1.11) together with the incompressibility condition (1.4) are the Navier–Stokes equations for incompressible Newtonian fluids.

A constitutive equation is an equation that assigns a value to the deviatoric stress tensor $\boldsymbol{\tau}$. Equation (1.9) is a first example of a constitutive equation. For polymeric fluids, we assume

$$\boldsymbol{\tau} = \boldsymbol{\tau}_{\mathrm{s}} + \boldsymbol{\tau}_{\mathrm{p}}, \tag{1.12}$$

where $\boldsymbol{\tau}_\mathrm{s}$ is the Newtonian solvent contribution and $\boldsymbol{\tau}_\mathrm{p}$ is the polymeric contribution to the stress tensor. Stress tensor $\boldsymbol{\tau}_\mathrm{s}$ is given by

$$\boldsymbol{\tau}_\mathrm{s} := 2\eta_\mathrm{s}\boldsymbol{D}(\boldsymbol{u}) \tag{1.13}$$

with η_s being the solvent viscosity. The final system, which is the starting point for further modeling, is then given by

$$\rho\left(\partial_t \boldsymbol{u} + \boldsymbol{u}\cdot\nabla\boldsymbol{u}\right) - 2\eta_\mathrm{s}\nabla\cdot\boldsymbol{D}(\boldsymbol{u}) - \nabla\cdot\boldsymbol{\tau}_\mathrm{p} + \nabla p = \boldsymbol{0}, \tag{1.14a}$$

$$\nabla\cdot\boldsymbol{u} = 0. \tag{1.14b}$$

In the next section, we take a closer look at well established polymeric fluid models that deliver constitutive equations for the polymeric stress tensor $\boldsymbol{\tau}_\mathrm{p}$.

1.4 Constitutive polymeric fluid models

In this section, we present three historical polymeric fluid models of increasing complexity and take a closer look at their properties. In Section 2, another class of polymeric fluid models is considered, where kinetic theory is used for derivation.

1.4.1 Maxwell model

In the following section, we consider the Maxwell (spring-dashpot) material for introducing viscoelastic materials. It is one of the simplest viscoelastic models, which already shows complex non Newtonian characteristics such as the stress relaxation (fading memory) property. Viscoelastic fluids are of non Newtonian type, i.e., there is no linear relation between the deviatoric stress tensor $\boldsymbol{\tau}$ and the rate of strain tensor $\boldsymbol{D}(\boldsymbol{u})$. These fluids show both, viscous and elastic material characteristics, depending on the time-scale of applied stresses/strains.

The equation for deviatoric stress tensor $\boldsymbol{\tau}$ is given by

$$\boldsymbol{\tau} + \frac{\mu}{G}\partial_t\boldsymbol{\tau} = 2\mu\boldsymbol{D}(\boldsymbol{u}), \tag{1.15}$$

where μ is a viscosity and G a modulus [11, p. 276]. One major drawback of this simple model is the lack of material frame-indifference due to the term $\partial_t\boldsymbol{\tau}$. The property of material frame-indifference states that the behavior of a material should be independent of the frame of reference. Consider the transformation

$$\bar{\boldsymbol{x}}(t) = \boldsymbol{Q}(t)\left(\boldsymbol{x}(t) - \boldsymbol{b}(t)\right), \tag{1.16a}$$

$$\boldsymbol{x}(t) = \boldsymbol{Q}(t)^\mathrm{T}\bar{\boldsymbol{x}}(t) + \boldsymbol{b}(t), \tag{1.16b}$$

where $\bar{\boldsymbol{x}}(t) \in \mathbb{R}^d$ and $\boldsymbol{x}(t) \in \mathbb{R}^d$ are coordinate vectors that describe the identical position in space w.r.t. different frames of reference with origins $\bar{\boldsymbol{O}}(t) \in \mathbb{R}^d$ and $\boldsymbol{O} \in \mathbb{R}^d$, which are related by $\bar{\boldsymbol{O}}(t) = \boldsymbol{O} + \boldsymbol{b}(t)$. The basis vectors $\bar{\boldsymbol{e}}_i(t)$, $i =$

$1, \dots, d$, w.r.t. the $\bar{\boldsymbol{O}}$-frame can be expressed with the basis vectors $\boldsymbol{e}_i$, $i = 1, \dots, d$, w.r.t. the $\boldsymbol{O}$-frame via

$$\bar{\boldsymbol{e}}_i(t) = \sum_{j=1}^{d} Q_{ij}(t)\boldsymbol{e}_j, \tag{1.17}$$

where $Q_{ij}(t)$ are the entries of the orthogonal matrix $\boldsymbol{Q}(t) \in \mathbb{R}^{d\times d}$ from (1.16). A tensor valued quantity $\boldsymbol{\pi}(\boldsymbol{x}, t)$ is called *frame-indifferent* if and only if $\bar{\boldsymbol{\pi}}(\bar{\boldsymbol{x}}, t) = \boldsymbol{Q}(t)\boldsymbol{\pi}(\boldsymbol{x}, t)\boldsymbol{Q}(t)^{\mathrm{T}}$ holds true, which is not the case for the partial time derivative $\partial_t \boldsymbol{\pi}$, since

$$\begin{aligned} \partial_t \bar{\pi}_{ij}(\bar{x}, t) =& \partial_t \left[Q_{im}(t)\pi_{mn}(\boldsymbol{x}, t)Q_{jn}(t)\right] \\ =& \dot{Q}_{im}(t)\pi_{mn}(\boldsymbol{x}, t)Q_{jn}(t) + Q_{im}(t)\pi_{mn}(\boldsymbol{x}, t)\dot{Q}_{jn}(t) \\ &+ Q_{im}(t)\partial_t\left(\pi_{mn}(\boldsymbol{x}, t)\right)Q_{jn}(t) \\ \neq& Q_{im}(t)\partial_t\left(\pi_{mn}(\boldsymbol{x}, t)\right)Q_{jn}(t). \end{aligned}$$

Above, we used the Einstein summation convention and the time derivatives of Q_{ij} are denoted by $\dot{Q}_{ij}$.

The model is sometimes called spring-dashpot model, as (1.15) is of the same form as the force F vs. rate of deformation $\dot{\epsilon}$ relation in a mechanical spring-dashpot model, which is derived in the following.

For this we followed [67]. The relation between force F and deformation ϵ is derived by considering a Newtonian dashpot and a Hookean spring that are connected in series (cf. Figure 1.5). We denote by F_{s} and F_{d} the force of the spring and dashpot, respectively. Analogously, the corresponding deformations are denoted by ϵ_{s}, ϵ_{d}. The relation between forces and deformations are given by

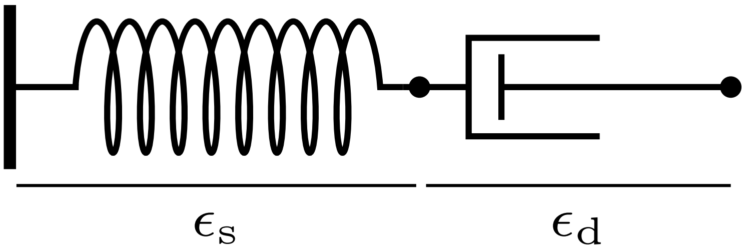

Figure 1.5. Visualization of the spring-dashpot model. A spring is connected in series with a dashpot.

$$F_{\mathrm{s}} = -G\epsilon_{\mathrm{s}}, \tag{1.18}$$
$$F_{\mathrm{d}} = -\mu\dot{\epsilon}_{\mathrm{d}}, \tag{1.19}$$

where G denotes the spring constant, μ viscosity, and $\dot{\epsilon}_{\mathrm{d}}$ the rate of deformation. Due to the connection in series of spring and dashpot, it holds for the total force F and total deformation ϵ,

$$F = F_{\mathrm{s}} = F_{\mathrm{d}}, \tag{1.20a}$$

]

$$\epsilon = \epsilon_{\mathrm{s}} + \epsilon_{\mathrm{d}}. \tag{1.20b}$$

From System (1.20), one can derive

$$F + \lambda \dot{F} = -\mu \dot{\epsilon}, \tag{1.21}$$

where $\lambda = \frac{\mu}{G}$ is a time constant. Note that (1.21) and (1.15) are of the same form with a flipped sign on the right hand side due to the sign convention of stress tensor in this thesis. Stress and strain are exchanged with force and deformation. With (1.15) and the analog mechanical spring-dashpot model in mind, it is now possible to discuss the characteristic behaviors of the viscoelastic Maxwell material from a mechanical point of view.

Stress relaxation over time Consider an initially relaxed material ($\epsilon = 0$) that is suddenly deformed and kept fixed to $\epsilon_0 > 0$ at $t_0 = 0$. The initial force is then given by $F_0 = -G\epsilon_0$. From (1.21) follows that the force (stress) decay over time is given by

$$F(t) = F_0 \exp\left(-\frac{t}{\lambda}\right) = -G\epsilon_0 \exp\left(-\frac{t}{\lambda}\right) \tag{1.22}$$

for fixed ϵ_0. Internally, the spring pulls on the dashpot, which is the reason for the force decay. From $\dot{\epsilon}(t) = 0$ follows

$$\epsilon_{\mathrm{d}}(t) = \epsilon_0 \left[1 - \exp\left(-\frac{t}{\lambda}\right)\right], \quad \text{and} \quad \epsilon_{\mathrm{s}}(t) = \epsilon_0 \exp\left(-\frac{t}{\lambda}\right). \tag{1.23}$$

Releasing the material after Δt results in a partial return to the original shape. In this scenario, the dashpot is irreversible and only the spring can reverse its deformation. The remaining force in the system at $t_1 = t_0 + \Delta t = \Delta t$, before the material is released, is

$$F(t_1) = -G\epsilon_0 \exp\left(-\frac{\Delta t}{\lambda}\right), \tag{1.24}$$

which jumps back to zero after release due to the spring. The reversible spring deformation and irreversible dashpot deformation at t_1 is

$$\epsilon_{\mathrm{s}}(t_1) = \epsilon_0 \exp\left(-\frac{t_1}{\lambda}\right) < \epsilon_0, \tag{1.25}$$

$$\epsilon_{\mathrm{d}}(t_1) = \epsilon_0 \left[1 - \exp\left(-\frac{t_1}{\lambda}\right)\right] > 0, \tag{1.26}$$

i.e., the system cannot restore to its initial shape, which demonstrates the fading memory property. A fully elastic material would restore to its initial shape. This process is visualized in Figure 1.6.

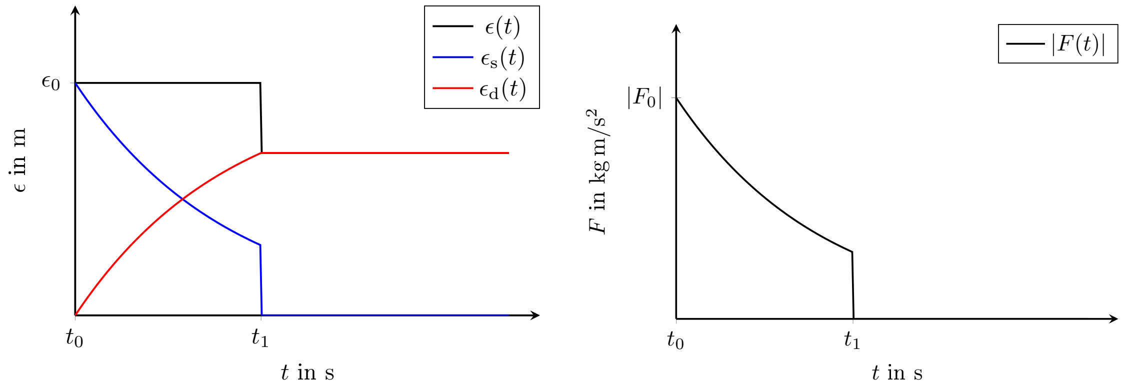

(a) Spring-dashpot deformations over time.

(b) Spring-dashpot force over time.

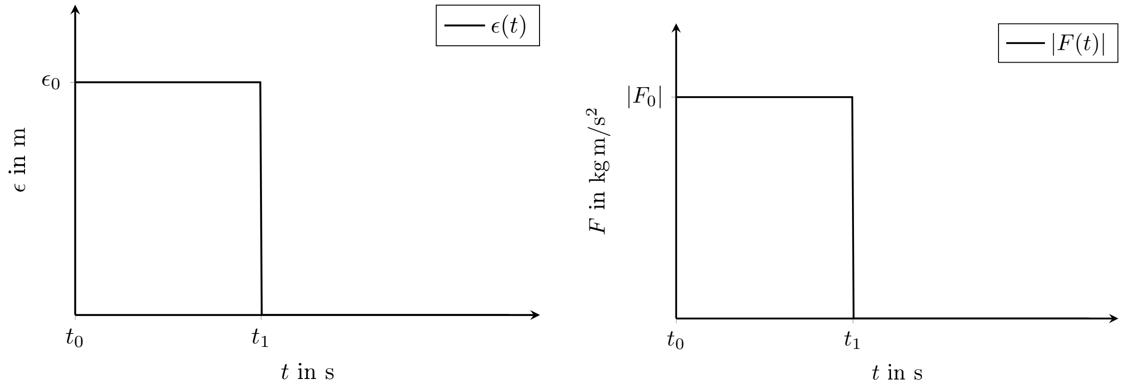

(c) Hookean spring deformation over time.

(d) Hookean spring force over time.

Figure 1.6. Qualitative comparison of the deformations for a mechanical spring-dashpot model and a Hookean spring under a sudden deformation. The qualitative behavior of strains and stresses for a Maxwell material and Hookean material is the same.

Constant strain-rate over time Applying a constant deformation-rate (strain-rate) $\dot{\epsilon} > 0$ to an initially relaxed spring-dashpot system, yields the expression

$$F(t) = -\mu\dot{\epsilon}\left[1 - \exp\left(-\frac{t}{\lambda}\right)\right] \tag{1.27}$$

for the force (stress). Note that $\lim_{t\to\infty} F(t) = -\mu\dot{\epsilon}$, i.e., in the limit, the Newtonian dashpot force behavior is recovered. The identical behavior is obtained in the Maxwell material case. In the case of a single dashpot model, the force would stay constant over time. For a single Hookean spring model, the force would linearly increase over time. This qualitative behavior is visualized in Figure 1.7.

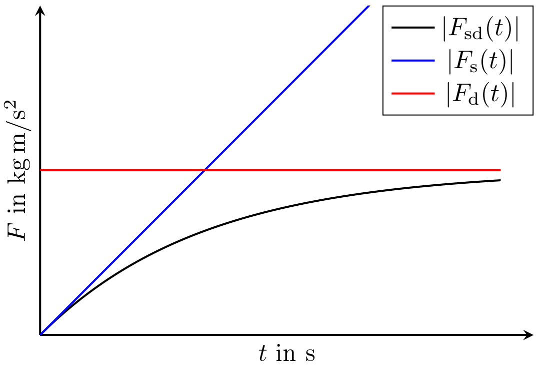

Figure 1.7. Qualitative comparison of the forces $F_{\mathrm{sd}}(t)$, $F_{\mathrm{s}}(t)$, and $F_{\mathrm{d}}(t)$ for a spring-dashpot, spring, and a dashpot model over time under a constant deformation-rate. The qualitative behavior of stress over time for a Maxwell material is identical to F_{sd} under constant strain-rate. Newtonian fluid stress would correspond to F_{d} and F_{s} to a Hookean material.

1.4.2 Upper convected Maxwell model

The upper convected Maxwell model is a generalization of the previous Maxwell material. It is obtained by substituting the time derivative $\partial_t \boldsymbol{\tau}$ in (1.15) with the upper-convected time derivative

$$\overset{\triangledown}{\boldsymbol{\tau}} := \partial_t \boldsymbol{\tau} + \boldsymbol{u} \cdot \nabla \boldsymbol{\tau} - (\nabla \boldsymbol{u})^{\mathrm{T}} \boldsymbol{\tau} - \boldsymbol{\tau} \nabla \boldsymbol{u}. \tag{1.28}$$

This leads to the upper-convected Maxwell model (cf. [66, Ch. 5.3.2])

$$\boldsymbol{\tau} + \lambda \overset{\triangledown}{\boldsymbol{\tau}} = 2\mu \boldsymbol{D}(\boldsymbol{u}), \tag{1.29}$$

where λ is a relaxation time constant, which is a measure for how fast the "memory" of the fluid fades.

In contrast to the Maxwell model, which is not frame-indifferent due to $\partial_t \boldsymbol{\tau}$, the upper convected Maxwell model is frame-indifferent as $\partial_t \boldsymbol{\tau}$ is replaced with the frame-indifferent upper-convected time derivative (1.28). See [11, Ch. 7.2] for details concerning frame-indifference.

1.4.3 Oldroyd-B model

Analog to the Maxwell model and upper-convected Maxwell model, the Oldroyd-B model is a frame-indifferent version of the Jeffreys model. Jeffreys model is given by

$$\boldsymbol{\tau} + \lambda_1 \partial_t \boldsymbol{\tau} = 2\eta_0 \left(\boldsymbol{D}(\boldsymbol{u}) + \lambda_2 \partial_t \boldsymbol{D}(\boldsymbol{u}) \right), \tag{1.30}$$

where λ_1, λ_2 are time constants and η_0 is the fluid viscosity (cf. (6.1-7) in [11]). The mechanical analog to (1.30) is visualized in Figure 1.8. For the total force F and deformation ϵ, it holds

$$F = F_1 = F_2, \tag{1.31a}$$

$$F_1 = \mu \dot{\epsilon}_1, \tag{1.31b}$$
$$F_2 = -G\epsilon_2 - \eta \dot{\epsilon}_2, \tag{1.31c}$$
$$\epsilon = \epsilon_1 + \epsilon_2, \tag{1.31d}$$

where F_1 is the force of the left dashpot, F_2 the force of the in parallel connected dashpot and spring, G the spring constant, μ, η viscosities of the dashpots, and ϵ_1, ϵ_2 are the deformations of first and second element in Figure 1.8. From System (1.31), one can derive

$$F + \frac{\mu}{G}\left(1 + \frac{\eta}{\mu}\right)\dot{F} = -\mu\left(\dot{\epsilon} + \frac{\eta}{G}\ddot{\epsilon}\right), \tag{1.32}$$

which is the mechanical analog to (1.30) with a flipped sign on the right hand side due to the sign convention of the stress tensor in this thesis. Substituting the partial time derivatives in (1.30) with upper-convected time derivatives (1.28) yields the Oldroyd-B model [62]

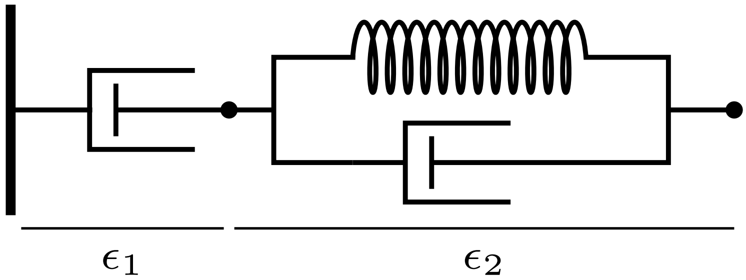

Figure 1.8. Visualization of the spring-dashpot model analog to Jeffreys model.

$$\boldsymbol{\tau} + \lambda_1 \overset{\triangledown}{\boldsymbol{\tau}} = 2\eta_0 \left(\boldsymbol{D}(\boldsymbol{u}) + \lambda_2 \overset{\triangledown}{\boldsymbol{D}}(\boldsymbol{u})\right). \tag{1.33}$$

Equation (1.33) can be transformed to

$$\boldsymbol{\tau}_\mathrm{p} + \lambda_1 \overset{\triangledown}{\boldsymbol{\tau}}_\mathrm{p} = 2\eta_\mathrm{p} \boldsymbol{D}(\boldsymbol{u}), \tag{1.34}$$

where we used (1.12), (1.13), $\eta_0 := \eta_\mathrm{p} + \eta_\mathrm{s}$ with η_s denoting the solvent viscosity and η_p the polymeric viscosity, $\eta_\mathrm{s} := (\lambda_2/\lambda_1)\eta_0$, and $\eta_\mathrm{p} := (1 - \lambda_2/\lambda_1)\eta_0$. The model is only meaningful for $\lambda_2 \leq \lambda_1$.

As in the overview paper [65] described, the Oldroyd-B model has some limitations. It considers only a single relaxation time λ_1 for the modeling of polymeric fluids. Additionally, it neglects the interaction between polymer molecules and treats the molecules as linearly elastic. The Oldroyd-B model can be applied to model Boger fluids [16], which are viscoelastic fluids with constant viscosity, i.e., no shear thinning/thickening effects.

Concerning the existence of solutions for the coupled initial value problem (1.14) together with (1.34), there are many results with different assumptions/simplifications. In [35], global existence of strong solutions for small data is proven with some restrictions on the retardation time λ_2 in 2D and 3D. In the 2D case, [39] proved global existence of weak solutions under some smallness and boundedness assumptions for the initial velocity and additional assumption on the initial deformation gradient. See Section 3 in [65] for more references.

1.5 Boundary conditions

In order to describe experimental meaningful flow scenarios, we need to close System (1.14) by prescribing boundary and initial conditions. In this thesis, the standard initial condition for the fluid velocity $\boldsymbol{u}(\boldsymbol{x}, t)$ is given by

$$\boldsymbol{u}(\boldsymbol{x}, 0) = \mathbf{0}. \tag{1.35}$$

Equation (1.35) states that the fluid is initially at rest.

Concerning boundary conditions (BC), we use the flow around a cylinder scenario to discuss the various BC choices. Figure 1.9 visualizes the flow domain Ω in two variants with possible boundary partitions. The first variant considers the whole flow domain Ω and the second variant exploits the symmetry of Ω and uses only the upper half of it. The BC should be chosen in such a way that a flow from left to right around the cylinder is created.

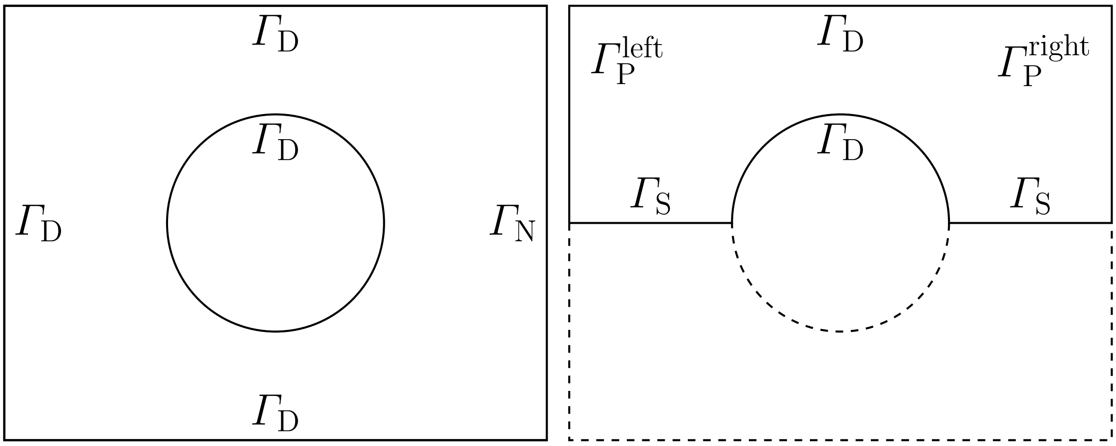

(a) Full domain. (b) Upper symmetric half.

Figure 1.9. Rectangular domain Ω with excluded cylinder in the middle.

Dirichlet boundary condition Walls and inflow parts of the boundary $\partial\Omega$ of Ω are usually assigned a Dirichlet BC

$$\boldsymbol{u} = \boldsymbol{g}_\mathrm{D} \quad \text{on } \Gamma_\mathrm{D}, \tag{1.36}$$

where the fluid velocity is prescribed by $\boldsymbol{g}_\mathrm{D} : \Gamma_\mathrm{D} \to \mathbb{R}^d$. At walls, the fluid velocity $\boldsymbol{u}$ should be zero, which leads to the choice $\boldsymbol{g}_\mathrm{D} = \mathbf{0}$ (homogeneous Dirichlet BC). On the inflow part of the boundary $\partial\Omega$ (left side of Figure 1.9a), a fully developed flow profile is the common choice.

Neumann boundary condition In order to model outlets (right side of Figure 1.9a), where the fluid leaves the domain and an exact velocity profile is a priori unknown, one applies Neumann BC

$$\boldsymbol{\sigma n} = (\boldsymbol{\tau}_s + \boldsymbol{\tau}_p - p\boldsymbol{I})\boldsymbol{n} = \boldsymbol{g}_\mathrm{N} \quad \text{on } \varGamma_\mathrm{N}, \tag{1.37}$$

where the full stress tensor $\boldsymbol{\sigma}$ is prescribed in normal direction $\boldsymbol{n}$ on $\varGamma_\mathrm{N}$ by $\boldsymbol{g}_\mathrm{N} : \varGamma_\mathrm{N} \to \mathbb{R}^d$. For an outlet, one sets $\boldsymbol{g}_\mathrm{N} = \boldsymbol{0}$.

Symmetry boundary condition If the flow problem exhibits a symmetry, it is possible to reduce the domain $\varOmega$ by considering only one symmetric part of it. In the case of the flow around a cylinder scenario, this would correspond to going from Figure 1.9a to Figure 1.9b. This requires a symmetry BC on the symmetric boundary $\varGamma_\mathrm{S}$, which is given by

$$\boldsymbol{u} \cdot \boldsymbol{n} = 0 \quad \text{on } \varGamma_\mathrm{S}, \tag{1.38a}$$

$$\boldsymbol{t} \cdot (\boldsymbol{\sigma n}) = 0 \quad \text{on } \varGamma_\mathrm{S}, \tag{1.38b}$$

where $\boldsymbol{n}$ is the outer unit normal vector and $\boldsymbol{t}$ are the tangential vectors, i.e., $\boldsymbol{n} \cdot \boldsymbol{t} = 0$.

Periodic boundary condition To prevent the prescription of inflow and outflow BC, one can choose periodic BC as visualized in Figure 1.9b. The flow is assumed to be periodic between $\varGamma_\mathrm{P}^\mathrm{left}$ and $\varGamma_\mathrm{P}^\mathrm{right}$, which gives the conditions

$$\boldsymbol{u}|_{\varGamma_\mathrm{P}^\mathrm{left}} = \boldsymbol{u}|_{\varGamma_\mathrm{P}^\mathrm{right}}, \tag{1.39a}$$

$$\partial_x \boldsymbol{u}|_{\varGamma_\mathrm{P}^\mathrm{left}} = \partial_x \boldsymbol{u}|_{\varGamma_\mathrm{P}^\mathrm{right}} \tag{1.39b}$$

for the fluid velocity $\boldsymbol{u}$.

In order to enforce a flow across the periodic boundary, there are multiple possibilities. The first would be a prescription of an additional pressure gradient. Here, we assume that the main flow is in x-direction. The additional pressure gradient is then achieved by substituting pressure p in (1.14a) with $p = p_p - \alpha x$, where $\alpha > 0$ is a constant and p_p is the new periodic pressure unknown. The substitution leads to an additional right hand side $\alpha \boldsymbol{e}_1$ in (1.14a), which enforces a flow in x-direction (controlled by parameter α).

The second possibility is the prescription of a constant flowrate $Q \in \mathbb{R}$ over the periodic boundary $\varGamma_\mathrm{P}^\mathrm{right}$. The corresponding condition is given by

$$\int_{\varGamma_\mathrm{P}^\mathrm{right}} \boldsymbol{u} \cdot \boldsymbol{n} = Q. \tag{1.40}$$

This can be achieved by introducing a new spatially constant scalar unknown $\bar{p} \in \mathbb{R}$ (Lagrangian multiplier) that may vary over time. Again, one substitutes the pressure p in (1.14a) with $p := p_p - \bar{p}x$, where p_p is the new pressure unknown. The Lagrangian multiplier $\bar{p}$ enables now control over the flowrate condition (1.40). Sections 1.7 and 3.2 discuss in detail, how (1.40) is included into the weak formulation of the stationary Stokes problem and System (1.14).

1.6 Units and non-dimensionalization

In this section, the Navier–Stokes System (1.14) is non-dimensionalized. Table 1.1 lists the units and names of the quantities that are used in the following. Generic unknown ζ is expressed via the relation $\zeta = \zeta_c \zeta^*$, where ζ_c is the corresponding characteristic unit and ζ^* the dimensionless unknown. The characteristic time is given by $T_c := L_c/U_c$ with L_c and U_c being the characteristic length and velocity, respectively. The characteristic pressure is set to be $p_c := \rho U_c^2$. For the characteristic stress, we choose $\tau_c^p := U_c(\eta_p + \eta_s)/L_c$, where η_p and η_s are the polymeric and solvent viscosity. The Reynolds number is given by

Symbol	**Unit**	**Name**
$\boldsymbol{u}$	m/s	Velocity
p	$\mathrm{kg/(m\,s^2)}$	Pressure
$\boldsymbol{\tau}_p$	$\mathrm{kg/(m\,s^2)}$	Polymeric stress
ρ	$\mathrm{kg/m^3}$	Fluid density
η_s	kg/(m s)	Solvent viscosity
η_p	kg/(m s)	Polymeric viscosity
L_c	m	Char. length
U_c	m/s	Char. velocity
T_c	s	Char. time
p_c	$\mathrm{kg/(m\,s^2)}$	Char. pressure
τ_c^p	$\mathrm{kg/(m\,s^2)}$	Char. polymeric stress
Re	1	Reynolds number
ϵ	1	Polymeric viscosity ratio

Table 1.1. Collection of symbols, units, and names

$$\mathrm{Re} := \rho U_c L_c/(\eta_s + \eta_p) \tag{1.41}$$

and the polymeric viscosity ratio is defined by

$$\epsilon := \eta_p/(\eta_p + \eta_s). \tag{1.42}$$

Using above quantities for the non-dimensionalization of (1.14a) yields

$$\begin{aligned}
&\rho\left(\partial_t \boldsymbol{u} + \boldsymbol{u}\cdot\nabla\boldsymbol{u}\right) - 2\eta_s \nabla\cdot\boldsymbol{D}(\boldsymbol{u}) - \nabla\cdot\boldsymbol{\tau}_p + \nabla p = 0\\
\Leftrightarrow\quad &\rho\left(\frac{U_c^2}{L_c}\partial_{t^*}\boldsymbol{u}^* + \frac{U_c^2}{L_c}\boldsymbol{u}^*\cdot\nabla^*\boldsymbol{u}^*\right) - 2\eta_s\frac{U_c}{L_c^2}\nabla^*\cdot\boldsymbol{D}^*(\boldsymbol{u}^*) - \frac{\tau_c^p}{L_c}\nabla^*\cdot\boldsymbol{\tau}_p^* + \frac{p_c}{L_c}\nabla^* p^* = 0\\
\Leftrightarrow\quad &\partial_{t^*}\boldsymbol{u}^* + \boldsymbol{u}^*\cdot\nabla^*\boldsymbol{u}^* - 2\frac{\eta_s}{\rho U_c L_c}\nabla^*\cdot\boldsymbol{D}^*(\boldsymbol{u}^*) - \frac{\tau_c^p}{\rho U_c^2}\nabla^*\cdot\boldsymbol{\tau}_p^* + \frac{p_c}{\rho U_c^2}\nabla^* p^* = 0\\
\Leftrightarrow\quad &\partial_{t^*}\boldsymbol{u}^* + \boldsymbol{u}^*\cdot\nabla^*\boldsymbol{u}^* - 2\frac{1-\epsilon}{\mathrm{Re}}\nabla^*\cdot\boldsymbol{D}^*(\boldsymbol{u}^*) - \frac{1}{\mathrm{Re}}\nabla^*\cdot\boldsymbol{\tau}_p^* + \nabla^* p^* = 0.
\end{aligned}$$

The gradient and divergence w.r.t. the non-dimensional spatial variable $\boldsymbol{x}^*$ are denoted by ∇^* and $\nabla^*\cdot$. The non-dimensional version of System (1.14) is then given by

$$\partial_{t^*}\boldsymbol{u}^* + \boldsymbol{u}^* \cdot \nabla^*\boldsymbol{u}^* - 2\frac{1-\epsilon}{\mathrm{Re}}\nabla^* \cdot \boldsymbol{D}^*(\boldsymbol{u}^*) - \frac{1}{\mathrm{Re}}\nabla^* \cdot \boldsymbol{\tau}_{\mathrm{p}}^* + \nabla^* p^* = 0, \tag{1.43a}$$

$$\nabla^* \cdot \boldsymbol{u}^* = 0. \tag{1.43b}$$

1.7 Well-posedness of the stationary Stokes problem with periodic BC and constant flowrate condition

As the periodic boundary condition (1.39) with the constant flowrate condition (1.40) is quiet special, it is a priori not clear that the (Navier–)Stokes problem is well-posed. In this subsection, we give a proof for the unique existence of weak solutions for the stationary Stokes problem with periodic BC, constant flowrate condition, and homogeneous BC (1.36).

The stationary Stokes problem

$$-2\nabla \cdot \boldsymbol{D}(\boldsymbol{u}) + \nabla p = 0, \tag{1.44a}$$

$$\nabla \cdot \boldsymbol{u} = 0, \tag{1.44b}$$

is obtained by dropping the first two terms in (1.14a) together with the polymeric stress tensor $\boldsymbol{\tau}_{\mathrm{p}}^*$ contribution. For simplicity, the physical constants are set to 1. We consider a rectangular domain $\Omega := (-L/2, L/2) \times (0,1) \subset \mathbb{R}^2$ with height 1 and length $L > 0$ (cf. Figure 1.10). In order to incorporate a constant flowrate condition

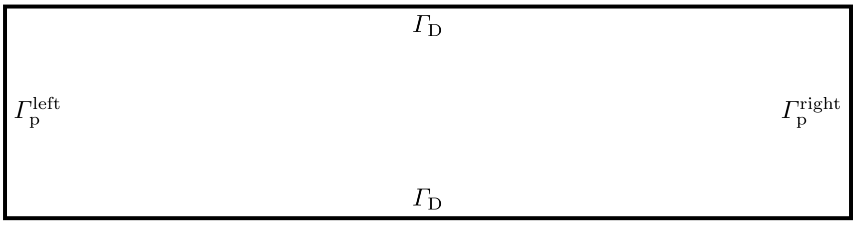

Figure 1.10. Visualization of the boundary conditions on the channel boundary $\partial\Omega$.

$$\int_{\Gamma_{\mathrm{P}}^{\mathrm{right}}} \boldsymbol{u} \cdot \boldsymbol{n} = Q \tag{1.45}$$

into the Stokes problem, one has to modify the pressure in (1.44a) to $\tilde{p} := p - \bar{p}x$, with $p \in P$ and $\bar{p} \in \mathbb{R}$ playing the role of an additional Lagrangian multiplier. The weak formulation of the Stokes problem with a constant flowrate condition is then given by:

For given $Q \in \mathbb{R}$ and $\boldsymbol{f} \in L^2(\Omega)^2$, find $(\boldsymbol{u}, p, \bar{p}) \in U \times P \times \mathbb{R}$ such that

$$\begin{cases} a(\boldsymbol{u}, \boldsymbol{v}) + b((p, \bar{p}), \boldsymbol{v}) = \int_\Omega \boldsymbol{f} \cdot \boldsymbol{v}, & \forall \boldsymbol{v} \in U, \\ b((q, \bar{q}), \boldsymbol{u}) = -QL\bar{q}, & \forall (q, \bar{q}) \in P \times \mathbb{R}, \end{cases} \tag{1.46}$$

where

$$U := \{\boldsymbol{v} \in H^1(\Omega)^2 \mid \boldsymbol{v}_{|\Gamma_\mathrm{D}} = \boldsymbol{0},\ \boldsymbol{v}_{|\Gamma_\mathrm{P}^\mathrm{left}} = \boldsymbol{v}_{|\Gamma_\mathrm{P}^\mathrm{right}}\}, \tag{1.47a}$$

$$P := L_0^2(\Omega) := \{p \in L^2(\Omega) \mid \textstyle\int_\Omega p = 0\}. \tag{1.47b}$$

The bilinear forms $a : U \times U \to \mathbb{R}$ and $b : (P \times \mathbb{R}) \times U \to \mathbb{R}$ are given by

$$a(\boldsymbol{u}, \boldsymbol{v}) := \int_\Omega \boldsymbol{D}(\boldsymbol{u}) : \boldsymbol{D}(\boldsymbol{v}), \tag{1.48a}$$

$$b((q, \bar{q}), \boldsymbol{u}) := -\int_\Omega q \nabla \cdot \boldsymbol{u} - \bar{q} \int_\Omega \boldsymbol{e}_1 \cdot \boldsymbol{u}. \tag{1.48b}$$

The constant flowrate condition can be unveiled from (1.46) in the following way: Testing the second equation of System (1.46) with $(q, 0)$ and $(0, \bar{q})$ yields the two equations

$$-\int_\Omega q \nabla \cdot \boldsymbol{u} = 0 \quad \forall q \in P, \tag{1.49a}$$

$$\bar{q} \int_\Omega \boldsymbol{e}_1 \cdot \boldsymbol{u} = LQ\bar{q} \quad \forall \bar{q} \in \mathbb{R}. \tag{1.49b}$$

Equation (1.49b) can be rewritten to

$$\bar{q} \int_\Omega \boldsymbol{e}_1 \cdot \boldsymbol{u} = \bar{q} \left(-\int_\Omega x \nabla \cdot \boldsymbol{u} + L \int_{\Gamma_\mathrm{P}^\mathrm{right}} \boldsymbol{u} \cdot \boldsymbol{n} \right) = \bar{q} L \int_{\Gamma_\mathrm{P}^\mathrm{right}} \boldsymbol{u} \cdot \boldsymbol{n} = LQ\bar{q}. \tag{1.50}$$

Since $x \in P = L_0^2(\Omega)$ and due to (1.49a), the integral $\int_\Omega x \nabla \cdot \boldsymbol{u}$ in (1.50) can be omitted.

In order to prove well-posedness of System (1.46), we need to check the conditions of the following theorem. See [24, Theorem 2.34], for a more detailed version with additional stability estimates.

Theorem 1.1. *System* (1.46) *is well-posed if and only if the following three conditions are satisfied:*

$$\exists \alpha > 0, \quad \inf_{\boldsymbol{u} \in \ker B} \sup_{\boldsymbol{v} \in \ker B} \frac{a(\boldsymbol{u}, \boldsymbol{v})}{\|\boldsymbol{u}\|_U \|\boldsymbol{v}\|_U} \geq \alpha, \tag{i}$$

$$\forall \boldsymbol{v} \in \ker B,\ (\forall \boldsymbol{u} \in \ker B, a(\boldsymbol{u}, \boldsymbol{v}) = 0) \implies (\boldsymbol{v} = \boldsymbol{0}), \tag{ii}$$

$$\exists \gamma > 0, \quad \inf_{(q,\bar{q}) \in P \times \mathbb{R}} \sup_{\boldsymbol{u} \in U} \frac{b((q, \bar{q}), \boldsymbol{u})}{\|(q, \bar{q})\|_{P \times \mathbb{R}} \|\boldsymbol{u}\|_U} \geq \gamma, \tag{iii}$$

where the space $\ker B$ *is given by*

$$\ker B := \{\boldsymbol{u} \in U \mid b((q, \bar{q}), \boldsymbol{u}) = 0\ \forall (q, \bar{q}) \in P \times \mathbb{R}\} \subset U. \tag{1.51}$$

Note that in Theorem 1.1 and for the rest of this section, we implicitly assume that division by zero is excluded, when the infimum or supremum is taken over a space.

First, we show that the bilinear form a is coercive on U with the help of the following two lemmas. Lemma 1.2 is taken from [24, Lemma A.38]. The coercivity property is used to prove the first two conditions of Theorem 1.1 later on.

Lemma 1.2 (Petree–Tartar). *Let X, Y, Z, be three Banach spaces. Let $A \in \mathcal{L}(X, Y)$ be an injective operator and let $T \in \mathcal{L}(X, Z)$ be a compact operator. If there is $c > 0$ such that $c\|x\|_X \leq \|Ax\|_Y + \|Tx\|_Z$, then there is $\alpha > 0$ such that*

$$\alpha\|x\|_X \leq \|Ax\|_Y. \tag{1.52}$$

Lemma 1.3 (Coercivity of a on U). *There is a constant $C > 0$ such that for all $\boldsymbol{u} \in U$, the estimate*

$$a(\boldsymbol{u}, \boldsymbol{u}) \geq C\|\boldsymbol{u}\|_U^2 \tag{1.53}$$

holds true.

Proof. We combine Korn's second inequality with Lemma 1.2. For $\boldsymbol{u} \in U$, Korn's second inequality (cf. [24, p. 156]) is

$$c\|\boldsymbol{u}\|_{H^1(\Omega)^2} \leq \|\boldsymbol{D}(\boldsymbol{u})\|_{L^2(\Omega)^{2\times2}} + \|\boldsymbol{u}\|_{L^2(\Omega)^2}. \tag{1.54}$$

In Lemma 1.2, we set $X := U$, $Y := L^2(\Omega)^{2\times2}$, and $Z := L^2(\Omega)^2$. The operators are $A : X \to Y$ with $A\boldsymbol{u} := \boldsymbol{D}(\boldsymbol{u})$, and $T : X \to Z$ is just the compact injection. Let $\boldsymbol{u} \in U$ with $\|A\boldsymbol{u}\|_Y = \|\boldsymbol{D}(\boldsymbol{u})\|_Y = 0$, i.e., $\boldsymbol{D}(\boldsymbol{u}) = \boldsymbol{0}$. This implies that $\boldsymbol{u}$ can be represented via

$$\boldsymbol{u}(\boldsymbol{x}) = \boldsymbol{v} + c\begin{bmatrix} 0 & -1 \\ 1 & 0 \end{bmatrix}\boldsymbol{x} \tag{1.55}$$

with $\boldsymbol{v} \in \mathbb{R}^2$ and $c \in \mathbb{R}$ (rigid displacement). For the second derivatives of the velocity components u_i, $i = 1, 2$, holds the identity

$$\begin{aligned}
\partial_j\partial_k u_i &= \frac{1}{2}\partial_j\partial_k u_i + \frac{1}{2}\partial_k\partial_j u_i && \text{(1.56a)}\\
&= \frac{1}{2}\partial_j\partial_k u_i + \frac{1}{2}\partial_k\partial_j u_i + \frac{1}{2}\partial_k\partial_i u_j - \frac{1}{2}\partial_i\partial_k u_j + \frac{1}{2}\partial_j\partial_i u_k - \frac{1}{2}\partial_i\partial_j u_k && \text{(1.56b)}\\
&= \frac{1}{2}\partial_k\left(\partial_j u_i + \partial_i u_j\right) + \frac{1}{2}\partial_j\left(\partial_k u_i + \partial_i u_k\right) - \frac{1}{2}\partial_i\left(\partial_k u_j + \partial_j u_k\right) && \text{(1.56c)}\\
&= \partial_k\boldsymbol{D}(\boldsymbol{u})_{ij} + \partial_j\boldsymbol{D}(\boldsymbol{u})_{ki} - \partial_i\boldsymbol{D}(\boldsymbol{u})_{kj} \overset{\boldsymbol{D}(\boldsymbol{u})=\boldsymbol{0}}{=} 0, && \text{(1.56d)}
\end{aligned}$$

which implies the representation $\boldsymbol{u}(\boldsymbol{x}) = \boldsymbol{v} + \boldsymbol{H}\boldsymbol{x}$ with $\boldsymbol{v} \in \mathbb{R}^2$ and $\boldsymbol{H} \in \mathbb{R}^{2\times2}$. From $\boldsymbol{D}(\boldsymbol{u}) = \boldsymbol{0}$, we can further deduce $\boldsymbol{H} + \boldsymbol{H}^{\mathrm{T}} = \boldsymbol{0}$, i.e., $\boldsymbol{H}$ is skew-symmetric, which yields (1.55) in 2D. As $\boldsymbol{u}_{|\Gamma_{\mathrm{D}}} = \boldsymbol{0}$, we deduce from (1.55), $\boldsymbol{v} = \boldsymbol{0}$ and $c = 0$, i.e., $\boldsymbol{u} = \boldsymbol{0}$ in Ω. Thus, the operator A is injective. Now, we can apply Lemma 1.2, which gives us $\alpha\|\boldsymbol{u}\|_U \leq \|\boldsymbol{D}(\boldsymbol{u})\|_Y$. This directly delivers the coerivity estimate

$$a(\boldsymbol{u}, \boldsymbol{u}) = \|\boldsymbol{D}(\boldsymbol{u})\|^2_{L^2(\Omega)^{2\times2}} \geq \alpha^2\|\boldsymbol{u}\|_U^2. \tag{1.57}$$

□

In the next two lemmas, we prove the third condition of Theorem 1.1.

Lemma 1.4. *For all* $(q, \bar{q}) \in P \times \mathbb{R}$*, there exists an* $\boldsymbol{u}_{(q,\bar{q})} \in U$*, such that*

$$\nabla \cdot \boldsymbol{u}_{(q,\bar{q})} = q \quad \text{and} \quad \int_\Omega \boldsymbol{e}_1 \cdot \boldsymbol{u}_{(q,\bar{q})} = \bar{q}.$$

Additionally, the estimate

$$\|\boldsymbol{u}_{(q,\bar{q})}\|_U \leq C\|(q, \bar{q})\|_{P\times\mathbb{R}}$$

holds true with a constant $C > 0$ *independent of* $\boldsymbol{u}, q, \bar{q}$*.*

Proof. First, we show that for all $\boldsymbol{u} \in U$, it holds $\nabla \cdot \boldsymbol{u} \in P = L^2_0(\Omega)$. Applying Gauss's divergence theorem on

$$\int_\Omega \nabla \cdot \boldsymbol{u} = \int_{\partial\Omega} \boldsymbol{u} \cdot \boldsymbol{n} = \int_{\Gamma_\mathrm{P}^\mathrm{left}} \boldsymbol{u} \cdot \boldsymbol{n} + \int_{\Gamma_\mathrm{P}^\mathrm{right}} \boldsymbol{u} \cdot \boldsymbol{n} = 0,$$

tells us $\nabla \cdot \boldsymbol{u} \in L^2_0$. Since the mapping $\nabla \cdot : H^1_0(\Omega)^2 \to L^2_0(\Omega)$ is surjective [24, Lemma B.69] and $H^1_0(\Omega)^2 \subset U$, the mapping $\nabla \cdot : U \to L^2_0(\Omega)$ is also surjective. Thus, for given $q \in L^2_0(\Omega)$, we find $\boldsymbol{u}_q \in U$, more precisely $\boldsymbol{u}_q \in H^1_0(\Omega)^2 \subset U$, such that $\nabla \cdot \boldsymbol{u}_q = q$. Applying Lemma A.39 + A.42 from [24], gives us the estimate $\alpha\|\boldsymbol{u}_q\|_U \leq \|q\|_P$ for some $\alpha > 0$ independent of q and $\boldsymbol{u}_q$.

In the next step, we take a look at the function $\hat{\boldsymbol{u}} : \mathbb{R}^2 \to \mathbb{R}^2$ with $\hat{\boldsymbol{u}}(x, y) = (y(1-y), 0)^\mathrm{T} \in U$. One can easily verify that $\hat{\boldsymbol{u}}$ satisfies the two properties $\nabla \cdot \hat{\boldsymbol{u}} = 0$ and $\int_\Omega \boldsymbol{e}_1 \cdot \hat{\boldsymbol{u}} = \frac{L}{6} \neq 0$. We exploit these properties to construct the final $\boldsymbol{u}_{(q,\bar{q})} \in U$ satisfying $\nabla \cdot \boldsymbol{u}_{(q,\bar{q})} = q$ and $\int_\Omega \boldsymbol{e}_1 \cdot \boldsymbol{u}_{(q,\bar{q})} = \bar{q}$, which is given by

$$\boldsymbol{u}_{(q,\hat{q})} := \boldsymbol{u}_q + c(q, \bar{q})\hat{\boldsymbol{u}} \quad \text{with} \quad c(q, \bar{q}) = \frac{6}{L}\left(\bar{q} - \int_\Omega \boldsymbol{e}_1 \cdot \boldsymbol{u}_q\right). \tag{1.58}$$

Note, that $\|\hat{\boldsymbol{u}}\|_U = \sqrt{\frac{L}{3}}$ and $|c(q, \bar{q})| \leq \frac{6}{L}\left(|\bar{q}| + \frac{1}{\alpha}\|q\|_P\right)$, from which follows

$$\begin{aligned} \|\boldsymbol{u}_{(q,\bar{q})}\|_U &\leq \|\boldsymbol{u}_q\|_U + |c(q, \bar{q})|\|\hat{\boldsymbol{u}}\|_U && (1.59\text{a}) \\ &\leq C(\alpha, L)\left(\|q\|_P + |\bar{q}|\right) && (1.59\text{b}) \\ &\leq C(a, L)\|(q, \bar{q})\|_{P\times\mathbb{R}}. && (1.59\text{c}) \end{aligned}$$

In the last step from (1.59b) to (1.59c), we used that the norm $\|q\|_P + |\bar{q}|$ is equivalent to the norm $\|(q, \bar{q})\|_{P\times\mathbb{R}} := \sqrt{\|q\|^2_P + |\bar{q}|^2}$. The corresponding equivalence constant is included in $C(\alpha, L)$. For given $(q, \bar{q}) \in P \times \mathbb{R}$, we have constructed an $\boldsymbol{u}_{(q,\bar{q})} \in U$ that satisfies the above mentioned properties and stability estimate, which concludes our proof. ☐

Lemma 1.5 (Inf-sup condition)**.** *For* $b : (P \times \mathbb{R}) \times U \to \mathbb{R}$ *with*

$$b\left((q, \bar{q}), \boldsymbol{u}\right) := -\int_\Omega q\nabla \cdot \boldsymbol{u} - \bar{q}\int_\Omega \boldsymbol{e}_1 \cdot \boldsymbol{u}, \tag{1.60}$$

there is a $\gamma > 0$ such that

$$\inf_{(q,\bar{q})\in P\times\mathbb{R}} \sup_{\boldsymbol{u}\in U} \frac{b((q,\bar{q}),\boldsymbol{u})}{\|(q,\bar{q})\|_{P\times\mathbb{R}}\|u\|_U} \geq \gamma > 0.$$

Proof. Let $(0,0) \neq (q,\bar{q}) \in P \times \mathbb{R}$ be given. Then, we have

$$\begin{aligned}\sup_{\boldsymbol{u}\in U} \frac{b((q,\bar{q}),\boldsymbol{u})}{\|u\|_U} &\geq \frac{b((q,\bar{q}),\boldsymbol{u}_{(-q,-\bar{q})})}{\|\boldsymbol{u}_{(-q,-\bar{q})}\|_U} = \frac{-\int_\Omega q\boldsymbol{\nabla}\cdot\boldsymbol{u}_{(-q,-\bar{q})} - \bar{q}\int_\Omega \boldsymbol{e}_1\cdot\boldsymbol{u}_{(-q,-\bar{q})}}{\|\boldsymbol{u}_{(-q,-\bar{q})}\|_U} \\ &= \frac{\bar{q}^2 + \int_\Omega q^2}{\|\boldsymbol{u}_{(q,\bar{q})}\|_U} = \frac{\|(q,\bar{q})\|^2_{P\times\mathbb{R}}}{\|\boldsymbol{u}_{(q,\bar{q})}\|_U} \geq \frac{1}{C(\alpha,L)}\|(q,\bar{q})\|_{P\times\mathbb{R}}.\end{aligned} \tag{1.61}$$

Note that in (1.61), we used the fact $\|\boldsymbol{u}_{(-q,-\bar{q})}\|_U = \|\boldsymbol{u}_{(q,\bar{q})}\|_U$. Then, it follows

$$\sup_{\boldsymbol{u}\in U} \frac{b((q,\bar{q}),\boldsymbol{u})}{\|u\|_U\|(q,\bar{q})\|_{P\times\mathbb{R}}} \geq \frac{1}{C(\alpha,L)}. \tag{1.62}$$

Since $(q,\bar{q}) \in P \times \mathbb{R}$ was arbitrary, we can take the infimum of (1.62) over $P \times \mathbb{R}$, which yields the inf-sup condition

$$\inf_{(q,\bar{q})\in P\times\mathbb{R}} \sup_{\boldsymbol{u}\in U} \frac{b((q,\bar{q}),\boldsymbol{u})}{\|(q,\bar{q})\|_{P\times\mathbb{R}}\|u\|_U} \geq \gamma$$

with $\gamma := C(\alpha,L)^{-1} > 0$. ☐

Note that Lemma 1.3 can be improved by exploiting that a needs only to be considered on $\ker B$. This then leads to the following lemma.

Lemma 1.6. *For all $\boldsymbol{u} \in \ker B \subset U$, it holds*

$$a(\boldsymbol{u},\boldsymbol{u}) = \frac{1}{2}\|\boldsymbol{u}\|^2_U. \tag{1.63}$$

Proof. For this proof, we essentially have to show that Korn's first inequality is valid on the space $\ker B$. This is done in three steps. First, we characterize the functions of $\ker B$. Second, we show that boundary integrals appearing during Korn's first inequality proof vanish for functions in $\ker B$. This unlocks the last step, in which we can directly apply the same steps of the proof as in the $H^1_0(\Omega)^d$-case.

Let $\boldsymbol{u} \in U$ such that $b((q,\bar{q}),u) = 0$ for all $(q,\bar{q}) \in P \times \mathbb{R}$. Choosing $(q,\bar{q}) = (\boldsymbol{\nabla}\cdot\boldsymbol{u}, 0)$, yields $b((\boldsymbol{\nabla}\cdot\boldsymbol{u},0),\boldsymbol{u}) = \|\boldsymbol{\nabla}\cdot\boldsymbol{u}\|^2_{L^2} = 0$ and thus $\boldsymbol{\nabla}\cdot\boldsymbol{u} = 0$. Setting $(q,\bar{q}) = (0, \int_\Omega \boldsymbol{e}_1\cdot\boldsymbol{u})$ in $b((q,\bar{q}),\boldsymbol{u}) = 0$, implies $\int_\Omega \boldsymbol{e}_1\cdot\boldsymbol{u} = 0$. Let $\boldsymbol{u} \in U$ with $\boldsymbol{\nabla}\cdot\boldsymbol{u} = 0$ and $\int_\Omega \boldsymbol{e}_1\cdot\boldsymbol{u} = 0$, then it holds

$$b((q,\bar{q}),u) = -\int_\Omega q\boldsymbol{\nabla}\cdot\boldsymbol{u} - \bar{q}\int_\Omega \boldsymbol{e}_1\cdot\boldsymbol{u} = 0 \tag{1.64}$$

for all $(q, \bar{q}) \in P \times \mathbb{R}$. Therefore, we have

$$\ker B := \left\{ \boldsymbol{u} \in U \mid \nabla \cdot \boldsymbol{u} = 0, \ \int_\Omega \boldsymbol{e}_1 \cdot \boldsymbol{u} = 0 \right\}. \tag{1.65}$$

In the next step, we take a closer look at the integral $\int_\Omega \nabla \boldsymbol{u} : (\nabla \boldsymbol{u})^\mathrm{T}$ for $\boldsymbol{u} \in \ker B$. Expressing it component-wise and applying partial integration twice yields

$$\begin{aligned}\sum_{i,j} \int_\Omega (\partial_i u_j)(\partial_j u_i) &= -\sum_{i,j} \int_\Omega (\partial_{ji}^2 u_j) u_i + \sum_{i,j} \int_{\partial\Omega} (\partial_i u_j) u_i n_j \\ &= \sum_{i,j} \int_\Omega (\partial_i u_i)(\partial_j u_j) + \sum_{i,j} \int_{\partial\Omega} \left[(\partial_i u_j) u_i n_j - (\partial_j u_j) u_i n_i \right] \\ &= \int_\Omega (\nabla \cdot \boldsymbol{u})^2 + \sum_{i,j} \int_{\partial\Omega} \left[(\partial_i u_j) u_i n_j - (\partial_j u_j) u_i n_i \right]. \end{aligned} \tag{1.66}$$

A priori, it is not clear that the two partial integration can be done for H^1-components, as second derivatives appear during the transformation process. However, via a standard density argument, it can be proven that this whole transformation still holds true for H^1-components.

Now, we examine the boundary integrals in (1.66). For $\boldsymbol{u} \in \ker B$, we have $\boldsymbol{u}_{|\Gamma_\mathrm{D}} = 0$, $\boldsymbol{u}_{|\Gamma_\mathrm{P}^\mathrm{left}} = \boldsymbol{u}_{|\Gamma_\mathrm{P}^\mathrm{right}}$, which also implies $\partial_2 \boldsymbol{u}_{|\Gamma_\mathrm{P}^\mathrm{left}} = \partial_2 \boldsymbol{u}_{|\Gamma_\mathrm{P}^\mathrm{right}}$, and $\nabla \cdot \boldsymbol{u} = 0 \Leftrightarrow \partial_1 u_1 = -\partial_2 u_2$ in 2D. With these properties, we can deduce that the boundary integrals from above vanish:

$$\sum_{i,j} \int_{\partial\Omega} (\partial_i u_j) u_i n_j = \sum_i -\int_{\Gamma_\mathrm{P}^\mathrm{left}} (\partial_i u_1) u_i + \int_{\Gamma_\mathrm{P}^\mathrm{right}} (\partial_i u_1) u_i \tag{1.67a}$$

$$= -\int_{\Gamma_\mathrm{P}^\mathrm{left}} (\partial_1 u_1) u_1 + \int_{\Gamma_\mathrm{P}^\mathrm{right}} (\partial_1 u_1) u_1 \tag{1.67b}$$

$$= \int_{\Gamma_\mathrm{P}^\mathrm{left}} (\partial_2 u_2) u_1 - \int_{\Gamma_\mathrm{P}^\mathrm{right}} (\partial_2 u_2) u_1 = 0. \tag{1.67c}$$

For the second boundary integral in (1.66), holds

$$-\sum_{i,j} \int_{\partial\Omega} (\partial_j u_j) u_i n_i = -\int_{\partial\Omega} (\nabla \cdot \boldsymbol{u})(\boldsymbol{u} \cdot \boldsymbol{n}) = 0. \tag{1.68}$$

For $\boldsymbol{u} \in \ker B$, it then holds

$$\int_\Omega \nabla \boldsymbol{u} : (\nabla \boldsymbol{u})^\mathrm{T} = 0, \tag{1.69}$$

which is obtained by combining (1.66), (1.67), and (1.68). This gives us immediately

$$a(\boldsymbol{u}, \boldsymbol{u}) = \int_\Omega \boldsymbol{D}(\boldsymbol{u}) : \boldsymbol{D}(\boldsymbol{u}) = \frac{1}{4} \int_\Omega (\nabla \boldsymbol{u} + (\nabla \boldsymbol{u}^\mathrm{T})) : (\nabla \boldsymbol{u} + (\nabla \boldsymbol{u}^\mathrm{T})) \tag{1.70}$$

$$= \frac{1}{2} \int_{\Omega} \nabla \boldsymbol{u} : \nabla \boldsymbol{u} + \frac{1}{2} \int_{\Omega} \nabla \boldsymbol{u} : (\nabla \boldsymbol{u})^{\mathrm{T}} \tag{1.71}$$

$$= \frac{1}{2} \|\boldsymbol{u}\|_U^2. \tag{1.72}$$

□

Theorem 1.7 (Well-posedness of System (1.46))**.** *For* $Q \in \mathbb{R}$ *and* $\boldsymbol{f} \in L^2(\Omega)^2$ *in System* (1.46)*, there is a unique solution* $(\boldsymbol{u}, p, \bar{p}) \in U \times P \times \mathbb{R}$*.*

Proof. In Lemma 1.5, we proved already the third condition of Theorem 1.1. The first and second condition can be deduced from Lemma 1.3 as proven in the following.

Let $\boldsymbol{u} \in \ker B \subset U$. Then we have

$$\sup_{\boldsymbol{v} \in \ker B} \frac{a(\boldsymbol{u}, \boldsymbol{v})}{\|\boldsymbol{u}\|_U \|\boldsymbol{v}\|_U} \geq \frac{a(\boldsymbol{u}, \boldsymbol{u})}{\|\boldsymbol{u}\|_U^2} \geq C. \tag{1.73}$$

In (1.73), we used Lemma 1.3 for the last inequality. Taking the infimum of (1.73) over $\ker B$ yields

$$\inf_{\boldsymbol{u} \in \ker B} \sup_{\boldsymbol{v} \in \ker B} \frac{a(\boldsymbol{u}, \boldsymbol{v})}{\|\boldsymbol{u}\|_U \|\boldsymbol{v}\|_U} \geq C, \tag{1.74}$$

which is the first condition of Theorem 1.1.

Let $\boldsymbol{v} \in \ker B$ and $a(\boldsymbol{u}, \boldsymbol{v}) = 0$ for all $\boldsymbol{u} \in \ker B$. Then, it also holds $a(\boldsymbol{v}, \boldsymbol{v}) = 0$, which implies $\boldsymbol{v} = 0$ due to the coercivity of a. With this, we have proven the last remaining condition of Theorem 1.1, which ensures the unique existence of solutions. □

2 Kinetic theory models

Kinetic theory models for polymers/macromolecules use mechanical models to describe the evolution of polymer configurations under fluid flow. For this, complex polymers with a huge number of degrees of freedom are approximated by coarse grained molecular models that use beads, which are connected by rods or springs. Figure 2.1 visualizes this coarse graining procedure. One possible approximation for a polymer is the freely jointed bead-rod chain, which is also known as Kramers chain (cf. [13]), where a polymer is represented by beads, which are connected by rods of constant length (cf. Figure 2.1b). The bead-rod chain mimics a polymer in the sense that it can be deformed, oriented, stretched, and still possess a constant length. Further details of this model are discussed in Section 2.2. Examples of fluids with macroscopic rod like structure, cf.[12, p. 111], are isotactic polypropylene, Poly(n-butyl isocyanate) [2], proteins in helical forms, DNA in helix configuration, or the tobacco mosaic virus.

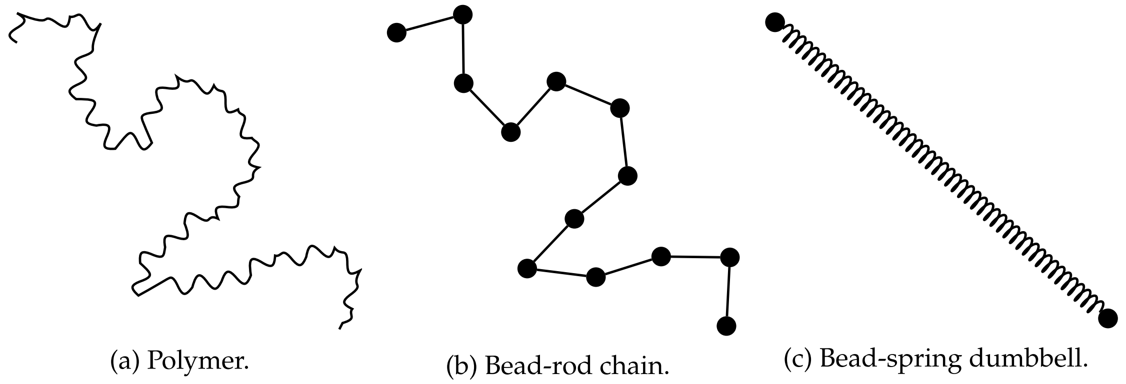
(a) Polymer. (b) Bead-rod chain. (c) Bead-spring dumbbell.

Figure 2.1. Approximation of a polymer with a bead-rod chain and a spring dumbbell.

The simplest class of polymer kinetic theory models are the spring dumbbell models, where a polymer is represented by two beads, which are connected by a single spring (cf. Figure 2.1c). In Section 2.1, the dumbbell model is derived for two types of springs: the Hookean spring and the *finitely extendable nonlinear elastic* (FENE) spring. The spring-dumbbell mimics a polymer in the sense that it can be stretched and oriented.

For the above mentioned class of bead-rod-spring models, it is possible to derive stochastic differential equations (SDEs) that describe trajectories of polymers in the fluid. Alternatively, the Fokker–Planck equation, which is the partial differential equation associated with the SDEs, can be used to gain insights into the temporal evolution of the probability density function in the polymer configuration space. Both approaches can be utilized for the evaluation of a polymeric stress tensor τ_p that enables the coupling to the Navier–Stokes equations (1.14). In the case of SDEs, the evaluation of τ_p results in an ensemble average and the Fokker–Planck approach leads to an integral over the polymer configuration space. Figure 2.2 visualizes these different approaches.

In some cases, it is possible to derive closed form constitutive equations for the

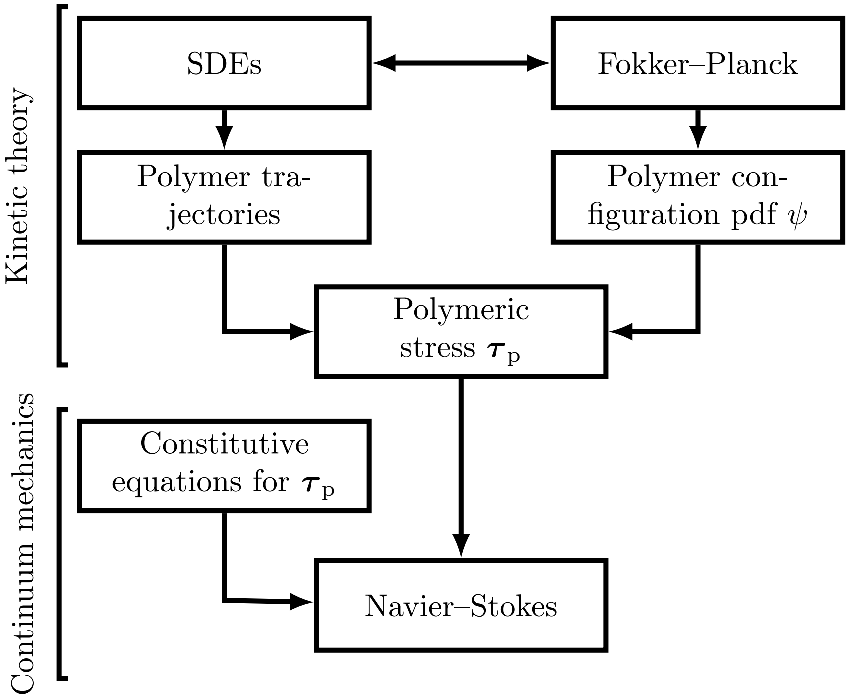

Figure 2.2. Visualization of connections to the polymeric stress tensor $\boldsymbol{\tau}_\mathrm{p}$.

polymeric stress tensor $\boldsymbol{\tau}_\mathrm{p}$. For the Hookean dumbbell model, it turns out that the Oldroyd-B model (cf. Section 1.4.3) is formally the macroscopic equivalent of the Hookean dumbbell model. There are rigorous proofs that show the equivalence of closely related models [9]. Such constitutive equations avoid the additional consideration of a SDE or Fokker–Planck equation for the evaluation of $\boldsymbol{\tau}_\mathrm{p}$, such that it is almost always more favorable to use a constitutive equation if available. However, the derivation of constitutive equations for kinetic models is not straight forward. For the FENE-dumbbell model, no equivalent constitutive equation is known yet. Currently, there are only constitutive equations that are approximations to the FENE-dumbbell model, e.g., the FENE-P model [14]. A starting point for more details and references about kinetic theory models for polymers can be found in [12]. More sophisticated models are the adaptive length scale (ALS) models [30, 38], which can be classified as a bead-spring (chain) model. There, the maximum spring extensions dynamically adapts to current flow situations.

2.1 Bead-spring dumbbell model

In this section, we approximate a polymer with a bead-spring dumbbell as visualized in Figure 2.1. At first, the governing equations are derived in Section 2.1.1. Afterwards, the equilibrium distribution function ψ_eq is derived, which is crucial for sampling bead-spring dumbbells in equilibrium (cf. Section 2.1.2). Section 2.1.3 gives an outlook to the associated Fokker–Plank equation and Section 2.1.4 derives the expression for the polymeric stress tensor $\boldsymbol{\tau}_\mathrm{p}$, which is used for the coupling to the Navier–Stokes equations (1.14). In the last Section 2.1.5, the equations of motion are non-dimensionalized.

2.1.1 Equations of motion

In order to derive the equations of motion for the bead-spring dumbbell model, we consider the following three forces on the beads:

- Hydrodynamic drag force $\boldsymbol{F}^{\mathrm{H}}$,
- Brownian force $\boldsymbol{F}^{\mathrm{B}}$,
- spring force $\boldsymbol{F}^{\mathrm{S}}$.

The hydrodynamic drag force $\boldsymbol{F}^{\mathrm{H}}$ models the resulting drag on beads in the fluid due to velocity differences. The expression of the *isotropic* drag force on bead i is given by

$$\boldsymbol{F}_i^{\mathrm{H}} = -\xi\left(\dot{\boldsymbol{r}}_i - \boldsymbol{u}_i\right), \quad i = 1, 2, \tag{2.1}$$

where ξ denotes the friction coefficient, $\dot{\boldsymbol{r}}_i$ the velocity of bead i, and $\boldsymbol{u}_i$ is the fluid velocity surrounding the ith bead.

The Brownian force $\boldsymbol{F}^{\mathrm{B}}$ models random collisions between beads and solvent molecules due to thermal fluctuations. It is described by a stochastic process with zero mean and a second moment given by

$$\langle \boldsymbol{F}_i^{\mathrm{B}}(t)\rangle = \boldsymbol{0}, \quad i = 1, 2, \tag{2.2a}$$

$$\langle \boldsymbol{F}_i^{\mathrm{B}}(t) \otimes \boldsymbol{F}_j^{\mathrm{B}}(t + \Delta t)\rangle = 2k_{\mathrm{B}}\vartheta\xi\delta_{ij}\delta(\Delta t)\boldsymbol{I}, \quad i, j = 1, 2. \tag{2.2b}$$

In (2.2b), k_{B} is the Boltzmann constant, ϑ the fluid temperature, ξ the friction coefficient from the drag force (2.1), δ_{ij} the Kronecker delta, $\delta(\Delta t)$ the Dirac delta function, and $\boldsymbol{I}$ is the unit tensor. The expectation value is denoted by $\langle\cdot\rangle$. The appearance of ξ in (2.2b) that connects drag and Brownian force is also known as fluctuation–dissipation theorem [63, p. 84]. Here, it is assumed that the Brownian forces are uncorrelated between two beads i, j, and two instants of time $t, t + \Delta t$ [63, p. 83]. Note that $\boldsymbol{F}_i^{\mathrm{B}}$ can be formally written as

$$\boldsymbol{F}_i^{\mathrm{B}}(t) = \sqrt{2k_{\mathrm{B}}\vartheta\xi}\,\frac{\mathrm{d}\boldsymbol{W}_i(t)}{\mathrm{d}t}, \tag{2.3}$$

where each component of $\boldsymbol{W}_i(t)$ is a scalar Wiener process [63, p. 68f]. Later on, we are interested in the formal integral $\int \boldsymbol{F}_i^{\mathrm{B}}(t)\,\mathrm{d}t$, which can interpreted as the well-defined stochastic Itô integral $\int \sqrt{2k_{\mathrm{B}}\vartheta\xi}\mathrm{d}\boldsymbol{W}_i(t)$.

The spring force $\boldsymbol{F}^{\mathrm{S}}$ models the spring that connects the two beads. It is characterized by a spring potential $U : \mathbb{R}^d \to \mathbb{R}$ and the resulting spring force $\boldsymbol{F}_i^{\mathrm{S}} : \mathbb{R}^d \to \mathbb{R}^d$ on bead i is given by

$$\boldsymbol{F}_i^{\mathrm{S}}(\boldsymbol{r}_2 - \boldsymbol{r}_1) = -\boldsymbol{\nabla}_{\boldsymbol{r}_i} U(\boldsymbol{r}_2 - \boldsymbol{r}_1) = \begin{cases} \boldsymbol{\nabla} U(\boldsymbol{r}_2 - \boldsymbol{r}_1), & i = 1, \\ -\boldsymbol{\nabla} U(\boldsymbol{r}_2 - \boldsymbol{r}_1), & i = 2, \end{cases} \tag{2.4}$$

where ∇_{r_i} denotes the gradient w.r.t. r_i. For the scope of this thesis, we consider two spring potentials. The Hookean spring potential with spring constant H is given by

$$U^{\text{Hookean}}(r_2 - r_1) = \frac{1}{2}H(r_2 - r_1)^2, \tag{2.5}$$

and the FENE (finitely extendable nonlinear elastic) spring potential by

$$U^{\text{FENE}}(r_2 - r_1) = \begin{cases} -\frac{1}{2}HQ_0^2 \ln\left(1 - \left[\frac{r_2 - r_1}{Q_0}\right]^2\right), & |r_2 - r_1| < Q_0, \\ \infty, & |r_2 - r_1| \geq Q_0, \end{cases} \tag{2.6}$$

with spring constant H and maximum spring length Q_0 [12, p. 21]. In contrast to the Hookean spring, the FENE-spring length is bounded by Q_0.

From Newton's second law of motion, we get

$$m\ddot{r}_i = F_i^{\text{H}} + F_i^{\text{S}} + F_i^{\text{B}}, \quad i = 1, 2, \tag{2.7}$$

and due to small bead masses, we neglect the inertia term, which yields

$$0 = F_i^{\text{H}} + F_i^{\text{S}} + F_i^{\text{B}}, \quad i = 1, 2. \tag{2.8}$$

In [72], the effects of not neglecting inertia are discussed in detail and material functions are derived for startup and steady shear flow. From (2.8), one can derive the Itô stochastic differential equations (SDEs)

$$\mathrm{d}r_1 = \left[u_1 - \frac{1}{\xi}\nabla_{r_1} U(r_2 - r_1)\right]\mathrm{d}t + \sqrt{\frac{2k_{\text{B}}\vartheta}{\xi}}\mathrm{d}W_1, \tag{2.9a}$$

$$\mathrm{d}r_2 = \left[u_2 - \frac{1}{\xi}\nabla_{r_2} U(r_2 - r_1)\right]\mathrm{d}t + \sqrt{\frac{2k_{\text{B}}\vartheta}{\xi}}\mathrm{d}W_2, \tag{2.9b}$$

which describe the evolution of a bead-spring dumbbell. Equation (2.9a) and (2.9b) are coupled with each other by the spring potential U.

Note that one can interpret an SDE in the sense of Itô or Stratonovich. In this thesis, we always have constant additive noise, where the two interpretations are equivalent. As in [63] described, the Stratonovich integral $\int_0^t \sigma(t', X_t) \odot \mathrm{d}W_{t'}$ is related to the Itô integral $\int_0^t \sigma(t', X_t)\,\mathrm{d}W_{t'}$ via

$$\int_0^t \sigma(t', X_t) \odot \mathrm{d}W_{t'} = \int_0^t \sigma(t', X_t)\,\mathrm{d}W_{t'} + \frac{1}{2}\int_0^t \sigma(t', X_t)\partial_x \sigma(t', X_t)\,\mathrm{d}t'. \tag{2.10}$$

The last integral in (2.10) vanishes for constant additive noise $\sigma \in \mathbb{R}$, which yields the equivalency of the Stratonovich and Itô integral.

Instead of considering the bead positions r_1 and r_2, we switch to the (Q, r_c)-formulation, where $Q := r_2 - r_1$ denotes the connector vector and $r_c := \frac{1}{2}(r_1 + r_2)$ the center of mass (cf. Figure 2.3). The (Q, r_c)-formulation turns out to be more

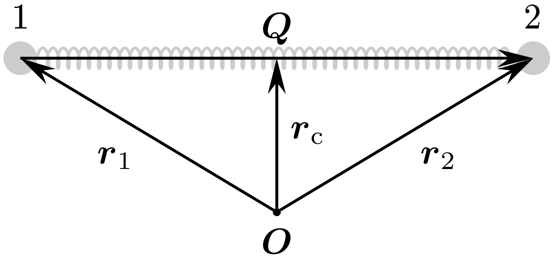

Figure 2.3. Visualization of a spring dumbbell with origin $\boldsymbol{O}$, vector $\boldsymbol{r}_\mathrm{c}$ pointing from $\boldsymbol{O}$ to the dumbbell center of mass, vector $\boldsymbol{r}_i$ pointing from $\boldsymbol{O}$ to bead i, and connector vector $\boldsymbol{Q} := \boldsymbol{r}_2 - \boldsymbol{r}_1$.

suitable for the discretization with Brownian configuration fields (cf. Section 3.1). From the definition of $\boldsymbol{Q}$ and $\boldsymbol{r}_\mathrm{c}$ follows

$$\mathrm{d}\boldsymbol{Q} = \left[\boldsymbol{u}_2 - \boldsymbol{u}_1 - \frac{2}{\xi}\nabla U(\boldsymbol{Q})\right]\mathrm{d}t + 2\sqrt{\frac{k_\mathrm{B}\vartheta}{\xi}}\mathrm{d}\boldsymbol{W}_{\boldsymbol{Q}}, \tag{2.11a}$$

$$\mathrm{d}\boldsymbol{r}_\mathrm{c} = \left[\frac{\boldsymbol{u}_1 + \boldsymbol{u}_2}{2}\right]\mathrm{d}t + \sqrt{\frac{k_\mathrm{B}\vartheta}{\xi}}\mathrm{d}\boldsymbol{W}_{\boldsymbol{r}_\mathrm{c}}. \tag{2.11b}$$

In (2.11a) and (2.11b), the relation $\sqrt{2}\boldsymbol{W}_{\boldsymbol{Q}} = \boldsymbol{W}_2 - \boldsymbol{W}_1$ and $\sqrt{2}\boldsymbol{W}_{\boldsymbol{r}_\mathrm{c}} = \boldsymbol{W}_1 + \boldsymbol{W}_2$ were used, where $\boldsymbol{W}_{\boldsymbol{Q}}$ and $\boldsymbol{W}_{\boldsymbol{r}_\mathrm{c}}$ are two independent Wiener processes. Approximating the velocity $\boldsymbol{u}_i$ at $\boldsymbol{r}_i$ by a first-order Taylor expansion at the center of mass $\boldsymbol{r}_\mathrm{c}$ yields

$$\boldsymbol{u}_i \approx \boldsymbol{u}_\mathrm{c} + \nabla\boldsymbol{u}_\mathrm{c}\left(\boldsymbol{r}_i - \boldsymbol{r}_\mathrm{c}\right), \quad i = 1, 2, \tag{2.12}$$

where $\boldsymbol{u}_\mathrm{c}$ denotes $\boldsymbol{u}(\boldsymbol{r}_\mathrm{c})$. Using (2.12) on $\boldsymbol{u}_2 - \boldsymbol{u}_1$ and $\boldsymbol{u}_1 + \boldsymbol{u}_2$, we obtain

$$\boldsymbol{u}_2 - \boldsymbol{u}_1 = \nabla\boldsymbol{u}(\boldsymbol{r}_\mathrm{c})\left(\boldsymbol{r}_2 - \boldsymbol{r}_1\right) = \nabla\boldsymbol{u}(\boldsymbol{r}_\mathrm{c})\boldsymbol{Q}, \tag{2.13a}$$

$$\boldsymbol{u}_1 + \boldsymbol{u}_2 = 2\boldsymbol{u}_\mathrm{c}. \tag{2.13b}$$

With (2.13) and a smallness assumption on the noise $\boldsymbol{W}_{\boldsymbol{r}_\mathrm{c}}$ (analog to [17])

$$\sqrt{\frac{k_\mathrm{B}\vartheta}{\xi}}\boldsymbol{W}_{\boldsymbol{r}_\mathrm{c}}(T) \ll \int_0^T \left[\frac{\boldsymbol{u}_1 + \boldsymbol{u}_2}{2}\right]\mathrm{d}t, \tag{2.14}$$

we obtain the simplified system

$$\mathrm{d}\boldsymbol{Q} = \left[\nabla\boldsymbol{u}_\mathrm{c}\boldsymbol{Q} - \frac{2}{\xi}\nabla U(\boldsymbol{Q})\right]\mathrm{d}t + 2\sqrt{\frac{k_\mathrm{B}\vartheta}{\xi}}\mathrm{d}\boldsymbol{W}_{\boldsymbol{Q}}, \tag{2.15a}$$

$$\mathrm{d}\boldsymbol{r}_\mathrm{c} = \boldsymbol{u}_\mathrm{c}\mathrm{d}t. \tag{2.15b}$$

For Hookean bead-spring dumbbells, we have

$$\nabla U^{\mathrm{Hookean}}(\boldsymbol{Q}) = H\boldsymbol{Q} =: \boldsymbol{F}^{\mathrm{S}}_{\mathrm{Hookean}}(\boldsymbol{Q}). \tag{2.16}$$

For FENE bead-spring dumbbells, we have

$$\nabla U^{\mathrm{FENE}}(\boldsymbol{Q}) = H \frac{\boldsymbol{Q}}{1 - (Q/Q_0)^2} =: \boldsymbol{F}^{\mathrm{S}}_{\mathrm{FENE}}(\boldsymbol{Q}). \tag{2.17}$$

System (2.15) is closed by prescribing initial conditions $\boldsymbol{r}_{\mathrm{c}}(0)$, $\boldsymbol{Q}(0)$. A common choice of initial conditions are configurations that are in thermal equilibrium. These need to be sampled according to a specific equilibrium probability distribution function. In Section 2.1.2, this distribution function is derived.

System (2.15) is currently formulated in the Lagrangian setting, i.e., we specify a single initial configuration $\boldsymbol{Q}_0$ and position $\boldsymbol{r}_{\mathrm{c},0}$ at t_0 and track the evolution of $\boldsymbol{Q}$ and its position $\boldsymbol{r}_{\mathrm{c}}$ over time, where $\boldsymbol{r}_{\mathrm{c}}$ follows the streamlines of $\boldsymbol{u}$ in the domain Ω. Instead of tracking the evolution of an individual dumbbell configuration along a streamline w.r.t. flow field $\boldsymbol{u}$, one could look at the dumbbell evolution at a point $\boldsymbol{x} \in \Omega$ over time, which leads to the Eulerian ansatz. The Eulerian formulation of System (2.15) is given by

$$\mathrm{d}\boldsymbol{Q} = \left[-\boldsymbol{u} \cdot \nabla \boldsymbol{Q} + (\nabla \boldsymbol{u})\boldsymbol{Q} - \frac{2}{\xi} \boldsymbol{F}^{\mathrm{S}}(\boldsymbol{Q}) \right] \mathrm{d}t + 2\sqrt{\frac{k_{\mathrm{B}}\vartheta}{\xi}} \mathrm{d}\boldsymbol{W}_{\boldsymbol{Q}}, \tag{2.18}$$

where the Wiener process $\boldsymbol{W}_{\boldsymbol{Q}}$ is constant in space and only allowed to vary in time. Note that in (2.18), the dumbbell connector vector $\boldsymbol{Q}$ is now a time-dependent vector field, i.e., $\boldsymbol{Q} : \Omega \times \mathbb{T} \longrightarrow \mathbb{D}_{\mathrm{BS}}$, where $\Omega \subset \mathbb{R}^d$ is the flow domain, $\mathbb{T} := (0, T)$ the time interval, and $\mathbb{D}_{\mathrm{BS}}$ the bead-spring dumbbell configuration space. The additional term $-\boldsymbol{u} \cdot \nabla \boldsymbol{Q}$ in (2.18) is due to the chain rule from computing the time derivative of $\boldsymbol{Q}(\boldsymbol{r}_{\mathrm{c}}(t), t)$. Note that for Hookean dumbbells, we have $\mathbb{D}^{\mathrm{H}}_{\mathrm{BS}} := \mathbb{R}^d$ and for FENE-dumbbells $\mathbb{D}^{\mathrm{F}}_{\mathrm{BS}} := \left\{ \boldsymbol{Q} \in \mathbb{R}^d \,|\, |\boldsymbol{Q}| < Q_0 \right\}$. Additional boundary conditions have to be specified at the inflow part of the domain Ω.

2.1.2 Equilibrium distribution

The derivation of the equilibrium distribution function of bead-spring dumbbells uses tools and ideas from statistical physics. Describing a fluid completely at microscopic level is in practice impossible due to the sheer number of degrees of freedom and the uncertainty of initial values. Statistical physics connects the microscopic equations of motion with elements from the probability theory. Typically results are then given in terms of means and distribution functions.

The following introduction is based on Chapter 1 in [61]. In statistical physics, one considers isolated systems with s degrees of freedom, where s is typically very large. In theory, such a system can be described with generalized coordinates $\boldsymbol{q} \in \mathbb{R}^s$ and generalized momenta $\boldsymbol{p} \in \mathbb{R}^s$, which are combined into a phase-vector $\boldsymbol{\pi} = (q_1, \ldots, q_s, p_1, \ldots, p_s) \in \Gamma := \mathbb{R}^{2s}$, where Γ denotes the phase-space. A microstate of such a system can then be characterized with a phase-vector $\boldsymbol{\pi} \in \Gamma$. If an initial value $\boldsymbol{\pi}(0)$ is known, the trajectory $\boldsymbol{\pi}(t)$, $t > 0$, in the phase-space Γ is described by the Hamilton equations of motion, which are given by

$$\dot{p}_i = -\frac{\partial \mathcal{H}}{\partial q_i}, \quad \dot{q}_i = \frac{\partial \mathcal{H}}{\partial p_i}, \quad i = 1, \ldots, s. \tag{2.19}$$

In (2.19), $\mathcal{H} : \mathbb{R}^{2s} \longrightarrow \mathbb{R}$ denotes the *Hamiltonian*, which is identical to the total energy E in a system if the following properties are satisfied:

(i) The system has to be isolated (no external forces) and conservative, i.e, internal forces $\boldsymbol{F}$ can be expressed with a gradient of a scalar-valued potential.
(ii) There are only time-independent constraints that can be written down as equation w.r.t. Cartesian coordinates in the system.

A trajectory $\boldsymbol{\pi}(t) = (\boldsymbol{q}(t), \boldsymbol{p}(t))$, which satisfies (2.19) stays on a $(2s-1)$-dimensional hypersurface in Γ that is characterized by

$$S_E := \{(\boldsymbol{q}, \boldsymbol{p}) \in \Gamma \,|\, \mathcal{H}(\boldsymbol{q}, \boldsymbol{p}) = E\}, \tag{2.20}$$

where E is given by $\mathcal{H}(\boldsymbol{q}(0), \boldsymbol{p}(0))$. This can be easily checked by computing

$$\frac{\mathrm{d}}{\mathrm{d}t}\mathcal{H}(\boldsymbol{q}(t), \boldsymbol{p}(t)) = \sum_{j=1}^{s} \left[\frac{\partial \mathcal{H}}{\partial q_j}\dot{q}_j + \frac{\partial \mathcal{H}}{\partial p_j}\dot{p}_j \right] \overset{(2.19)}{=} 0, \tag{2.21}$$

i.e., $\mathcal{H}(\boldsymbol{q}, \boldsymbol{p})$ is a first integral, since $\mathcal{H}(\boldsymbol{q}(t), \boldsymbol{p}(t)) = \mathcal{H}(\boldsymbol{q}(0), \boldsymbol{p}(0)) \equiv E$, $t > 0$.

Now, one is interested in observables $F(\boldsymbol{q}, \boldsymbol{p})$, which are physical quantities that can be measured. The exact evolution of F over time cannot be computed due to missing initial data $\boldsymbol{\pi}(0)$. Since measuring F takes a finite time in reality, one is interested in time averages

$$\bar{F}^{t_0} := \frac{1}{t_0} \int_0^{t_0} F(\boldsymbol{q}(t), \boldsymbol{p}(t)) \, \mathrm{d}t, \tag{2.22}$$

which unfortunately still depend on initial data $\boldsymbol{\pi}(0)$ for finite t_0. One postulate of statistical physics is that the limit

$$\lim_{t_0 \longrightarrow \infty} \bar{F}^{t_0} = \bar{F} \tag{2.23}$$

exists and is independent of the initial data $\boldsymbol{\pi}(0)$, which is a special formulation of the quasi-ergodic hypothesis [61, p. 17]. The aforementioned hypothesis states that a trajectory $\boldsymbol{\pi}(t)$, $t > 0$, on the hypersurface S_E (cf. (2.20)) reaches every point on S_E with arbitrary closeness over time. Thus it is possible to consider a probability density $\bar{\rho}(\boldsymbol{q}, \boldsymbol{p}, t_0)$ on the hypersurface S_E, which characterizes the probability of finding the trajectory $\boldsymbol{\pi}(t)$, $t > 0$, at $(\boldsymbol{q}, \boldsymbol{p})$ during the time interval $[0, t_0]$. Probability density $\bar{\rho}(\boldsymbol{q}, \boldsymbol{p}, t_0)$ can then be used to rewrite (2.22) to

$$\bar{F}^{t_0} = \iint_{S_E} F(\boldsymbol{q}, \boldsymbol{p}) \bar{\rho}(\boldsymbol{q}, \boldsymbol{p}, t_0) \, \mathrm{d}\boldsymbol{q}\mathrm{d}\boldsymbol{p}. \tag{2.24}$$

The quasi-ergodic hypothesis postulates now that for $t_0 \to \infty$, the probability density for macroscopic systems (systems with degrees of freedom $s \to \infty$) becomes independent of the initial value $\boldsymbol{\pi}(0)$, i.e,

$$\lim_{t_0 \to \infty} \bar{\rho}(\boldsymbol{q}, \boldsymbol{p}, t_0) = \bar{\rho}(\boldsymbol{q}, \boldsymbol{p}). \tag{2.25}$$

Note that (2.25) is a crucial requirement for statistical physics and cannot be mathematically proven. However, the quasi-ergodic hypothesis did not solve our problem to compute time averages $\bar{F}^{t_0}$ that are independent of initial data, as (2.23) requires an infinitely long observation time and the Hamilton equations (2.19) cannot be solved explicitly in general.

Instead of considering the trajectory of a single microstate $\boldsymbol{\pi}$ over time, the idea of statistical physics is now to consider statistical ensembles instead. Such an ensemble is a collection of all microstates $\boldsymbol{\pi}_i \in \Gamma$ that are a valid realization of a macroscopic system with a given set of properties, i.e., constant volume, constant number of particles, and constant temperature (*canonical ensemble*). Due to the quasi-ergodic hypothesis, we know that the actual system is at some point in time in one of these microstates of the statistical ensemble. Thus, the ensemble actually represents the states of the whole time evolution of the system. This idea is the motivation to use instant ensemble averages

$$\iint_{\Gamma} F(\boldsymbol{q}, \boldsymbol{p}) \rho(\boldsymbol{q}, \boldsymbol{p}) \, \mathrm{d}\boldsymbol{q} \mathrm{d}\boldsymbol{p} \tag{2.26}$$

instead of time averages (2.24) over a fixed trajectory. This shifts the problem of solving the Hamilton equations (2.19) and finding the correct initial value $\boldsymbol{\pi}(0)$ of a microstate to finding the probability distribution $\rho(\boldsymbol{q}, \boldsymbol{p})$ in (2.26), which describes the distribution of the microstates in Γ w.r.t. the statistical ensemble prescribed properties. In the case of a *canonical ensemble*, the properties are the prescribed constant volume, constant number of particles, and constant temperature (thermal equilibrium).

One major result of statistical physics is that for canonical ensembles, the distribution function $\rho(\boldsymbol{q}, \boldsymbol{p})$ in (2.26) is given by

$$\rho(\boldsymbol{q}, \boldsymbol{p}) \sim \exp\left(-\frac{\mathcal{H}(\boldsymbol{q}, \boldsymbol{p})}{k_{\mathrm{B}} \vartheta}\right), \tag{2.27}$$

where $\mathcal{H}$ is the Hamiltonian of the system, k_{B} denotes the Boltzmann constant, and ϑ the temperature of the system. For the derivation of (2.27) see Chapter 1.4 in [61].

In this section, we are interested in computing the probability distribution (2.27) w.r.t. one single bead-spring dumbbell. If the system consists of N non-interacting bead-spring dumbbells and $\mathcal{H}_i$, $i = 1, \ldots, N$, denotes the Hamiltonian w.r.t. the ith bead-spring dumbbell, the Hamiltonian of the full system is given by $\mathcal{H} = \sum_{i=1}^{N} \mathcal{H}_i$. The probability distribution (2.27), can then be rewritten to $\rho = \prod_{i=1}^{N} \rho_i$, where $\rho_i \sim \exp\left(-\mathcal{H}_i/(k_{\mathrm{B}}\vartheta)\right)$ is the single-molecule distribution function we are looking for.

The derivation of the equilibrium distribution function is based on [12, Ch. 12.3] and consists of multiple steps. At first, we derive the Hamiltonian $\mathcal{H}_i(\boldsymbol{r}_\mathrm{c}, \boldsymbol{Q}, \boldsymbol{p}_\mathrm{c}, \boldsymbol{P})$ for the bead-spring dumbbell, where $\boldsymbol{p}_\mathrm{c} \in \mathbb{R}^d$ and $\boldsymbol{P} \in \mathbb{R}^d$ denote the generalized momenta w.r.t. $\boldsymbol{r}_\mathrm{c} \in \Omega$ and $\boldsymbol{Q} \in \mathbb{D}_\mathrm{BS}$ with $\mathbb{D}_\mathrm{BS}$ denoting the dumbbell configuration space. In the following, we suppress the index i in $\mathcal{H}_i$ and just write $\mathcal{H}$. The single-molecule-phase-space distribution function $f_\mathrm{eq}(\boldsymbol{r}_\mathrm{c}, \boldsymbol{Q}, \boldsymbol{p}_\mathrm{c}, \boldsymbol{P})$ is given by

$$f_\mathrm{eq} = n|\Omega| \frac{\exp\left(-\frac{\mathcal{H}}{k_\mathrm{B}\vartheta}\right)}{\iiiint\limits_{\mathcal{P}} \exp\left(-\frac{\mathcal{H}}{k_\mathrm{B}\vartheta}\right) \mathrm{d}\boldsymbol{r}_\mathrm{c}\mathrm{d}\boldsymbol{Q}\mathrm{d}\boldsymbol{p}_\mathrm{c}\mathrm{d}\boldsymbol{P}}, \tag{2.28}$$

where n is the polymer number density in the domain $\Omega \subset \mathbb{R}^d$ with volume $|\Omega| > 0$, $\mathcal{H}$ the Hamiltonian of a single bead-spring dumbbell, k_B the Boltzmann constant, ϑ the temperature, and $\mathcal{P} := \Omega \times \mathbb{D}_\mathrm{BS} \times \mathbb{R}^d \times \mathbb{R}^d$ the phase-space. Note that in (2.28), the notation $\mathrm{d}\boldsymbol{P}$ is an abbreviation for $\mathrm{d}P_1 \ldots \mathrm{d}P_d$ and analog for $\mathrm{d}\boldsymbol{r}_\mathrm{c}$, $\mathrm{d}\boldsymbol{Q}$, $\mathrm{d}\boldsymbol{p}_\mathrm{c}$.

Let $\mathcal{A} \subset \mathcal{P}$. The integral

$$\iiiint\limits_{\mathcal{A}} f_\mathrm{eq} \mathrm{d}\boldsymbol{r}_\mathrm{c}\mathrm{d}\boldsymbol{Q}\mathrm{d}\boldsymbol{p}_\mathrm{c}\mathrm{d}\boldsymbol{P} \tag{2.29}$$

gives then the number of polymer molecules with phase-space configurations in $\mathcal{A}$. We are only interested in the configurational distribution function $\Psi_\mathrm{eq} : \Omega \times \mathbb{D}_\mathrm{BS} \to \mathbb{R}$ that is given by

$$\Psi_\mathrm{eq}(\boldsymbol{r}_\mathrm{c}, \boldsymbol{Q}) = \iint\limits_{\mathbb{R}^d \times \mathbb{R}^d} f_\mathrm{eq}(\boldsymbol{r}_\mathrm{c}, \boldsymbol{Q}, \boldsymbol{p}_\mathrm{c}, \boldsymbol{P}) \mathrm{d}\boldsymbol{p}_\mathrm{c}\mathrm{d}\boldsymbol{P}. \tag{2.30}$$

With $\mathcal{B} \subset \Omega \times \mathbb{D}_\mathrm{BS}$, the integral

$$\iint\limits_{\mathcal{B}} \Psi_\mathrm{eq}(\boldsymbol{r}_\mathrm{c}, \boldsymbol{Q}) \mathrm{d}\boldsymbol{r}_\mathrm{c}\mathrm{d}\boldsymbol{Q} \tag{2.31}$$

gives the number of polymer molecules with configurations in $\mathcal{B}$ (independent of their momenta). The goal of this section is to compute Ψ_eq.

Derivation of $\mathcal{H}$ Since we have no explicit time-dependent constraints (rheonomic constraints), it holds for the Hamiltonian

$$\mathcal{H}(\boldsymbol{r}_\mathrm{c}, \boldsymbol{Q}, \boldsymbol{p}_\mathrm{c}, \boldsymbol{P}) = T_\mathcal{H}(\boldsymbol{r}_\mathrm{c}, \boldsymbol{Q}, \boldsymbol{p}_\mathrm{c}, \boldsymbol{P}) + U(\boldsymbol{Q}), \tag{2.32}$$

where $T_\mathcal{H}$ is the kinetic energy and U the potential energy of the bead-spring dumbbell, which needs to be expressed in terms of $\boldsymbol{r}_\mathrm{c}$, $\boldsymbol{Q}$, and their corresponding conjugate generalized momenta $\boldsymbol{p}_\mathrm{c}$, $\boldsymbol{P}$. The momenta are given by

$$\boldsymbol{p}_\mathrm{c} := \frac{\partial}{\partial \dot{\boldsymbol{r}}_\mathrm{c}} \mathcal{L}(\boldsymbol{r}_\mathrm{c}, \boldsymbol{Q}, \dot{\boldsymbol{r}}_\mathrm{c}, \dot{\boldsymbol{Q}}), \quad \boldsymbol{P} := \frac{\partial}{\partial \dot{\boldsymbol{Q}}} \mathcal{L}(\boldsymbol{r}_\mathrm{c}, \boldsymbol{Q}, \dot{\boldsymbol{r}}_\mathrm{c}, \dot{\boldsymbol{Q}}), \tag{2.33}$$

where

$$\mathcal{L}(\boldsymbol{r}_\mathrm{c}, \boldsymbol{Q}, \dot{\boldsymbol{r}}_\mathrm{c}, \dot{\boldsymbol{Q}}) = T_\mathcal{L}(\boldsymbol{r}_\mathrm{c}, \boldsymbol{Q}, \dot{\boldsymbol{r}}_\mathrm{c}, \dot{\boldsymbol{Q}}) - U(\boldsymbol{Q}) \tag{2.34}$$

is the Lagrangian of the bead-spring dumbbell [60]. In (2.34), the kinetic energy $T_\mathcal{L}$ is expressed in terms of $\boldsymbol{r}_\mathrm{c}$, $\boldsymbol{Q}$, and their corresponding velocities $\dot{\boldsymbol{r}}_\mathrm{c}$, $\dot{\boldsymbol{Q}}$. In order to avoid confusion, the kinetic energies in (2.32) and (2.34), which are expressed in different coordinates, are annotated by $\mathcal{H}$ or $\mathcal{L}$ in their index.

The Lagrangian in the standard coordinates $\boldsymbol{r}_1$, $\boldsymbol{r}_2$, $\dot{\boldsymbol{r}}_1$, and $\dot{\boldsymbol{r}}_2$ is given by

$$\mathcal{L}(\boldsymbol{r}_1, \boldsymbol{r}_2, \dot{\boldsymbol{r}}_1, \dot{\boldsymbol{r}}_2) = \frac{1}{2} m \left(\dot{\boldsymbol{r}}_1^2 + \dot{\boldsymbol{r}}_2^2 \right) - U(\boldsymbol{r}_2 - \boldsymbol{r}_1). \tag{2.35}$$

Substituting $\dot{\boldsymbol{r}}_1 = \dot{\boldsymbol{r}}_\mathrm{c} - \frac{1}{2}\dot{\boldsymbol{Q}}$ and $\dot{\boldsymbol{r}}_2 = \dot{\boldsymbol{r}}_\mathrm{c} + \frac{1}{2}\dot{\boldsymbol{Q}}$ in (2.35) yields

$$\mathcal{L}(\boldsymbol{r}_\mathrm{c}, \boldsymbol{Q}, \dot{\boldsymbol{r}}_\mathrm{c}, \dot{\boldsymbol{Q}}) = m \left(\dot{\boldsymbol{r}}_\mathrm{c}^2 + \frac{1}{4} \dot{\boldsymbol{Q}}^2 \right) - U(\boldsymbol{Q}), \tag{2.36}$$

from which the generalized momenta

$$\boldsymbol{p}_\mathrm{c} = \frac{\partial}{\partial \dot{\boldsymbol{r}}_\mathrm{c}} \mathcal{L}(\boldsymbol{r}_\mathrm{c}, \boldsymbol{Q}, \dot{\boldsymbol{r}}_\mathrm{c}, \dot{\boldsymbol{Q}}) = 2m\dot{\boldsymbol{r}}_\mathrm{c}, \tag{2.37a}$$

$$\boldsymbol{P} = \frac{\partial}{\partial \dot{\boldsymbol{Q}}} \mathcal{L}(\boldsymbol{r}_\mathrm{c}, \boldsymbol{Q}, \dot{\boldsymbol{r}}_\mathrm{c}, \dot{\boldsymbol{Q}}) = \frac{1}{2} m \dot{\boldsymbol{Q}} \tag{2.37b}$$

can be derived. From (2.36), we read off

$$T_\mathcal{L}(\boldsymbol{r}_\mathrm{c}, \boldsymbol{Q}, \dot{\boldsymbol{r}}_\mathrm{c}, \dot{\boldsymbol{Q}}) = m \left(\dot{\boldsymbol{r}}_\mathrm{c}^2 + \frac{1}{4} \dot{\boldsymbol{Q}}^2 \right) \tag{2.38}$$

and together with (2.37), we deduce

$$T_\mathcal{H}(\boldsymbol{r}_\mathrm{c}, \boldsymbol{Q}, \boldsymbol{p}_\mathrm{c}, \boldsymbol{P}) = \frac{1}{4m} \boldsymbol{p}_\mathrm{c}^2 + \frac{1}{m} \boldsymbol{P}^2. \tag{2.39}$$

The expression (2.39) for the kinetic energy $T_\mathcal{H}$ gives us directly the required Hamiltonian

$$\mathcal{H}(\boldsymbol{r}_\mathrm{c}, \boldsymbol{Q}, \boldsymbol{p}_\mathrm{c}, \boldsymbol{P}) = \frac{1}{4m} \boldsymbol{p}_\mathrm{c}^2 + \frac{1}{m} \boldsymbol{P}^2 + U(\boldsymbol{Q}), \tag{2.40}$$

which is required for the computation of the configurational distribution function (2.30).

Computation of Ψ_eq Inserting the Hamiltonian (2.40) in the definition (2.28) of f_eq yields the expression

$$\Psi_\mathrm{eq}(\boldsymbol{r}_\mathrm{c}, \boldsymbol{Q}) = n|\Omega| \frac{\displaystyle\iint\limits_{\mathbb{R}^d \times \mathbb{R}^d} \exp\left(-\frac{\frac{1}{4m}\boldsymbol{p}_\mathrm{c}^2 + \frac{1}{m}\boldsymbol{P}^2 + U(\boldsymbol{Q})}{k_\mathrm{B}\vartheta} \right) \mathrm{d}\boldsymbol{p}_\mathrm{c} \mathrm{d}\boldsymbol{P}}{\displaystyle\iiiint\limits_{\mathcal{P}} \exp\left(-\frac{\frac{1}{4m}\boldsymbol{p}_\mathrm{c}^2 + \frac{1}{m}\boldsymbol{P}^2 + U(\boldsymbol{Q}')}{k_\mathrm{B}\vartheta} \right) \mathrm{d}\boldsymbol{r}_\mathrm{c}' \mathrm{d}\boldsymbol{Q}' \mathrm{d}\boldsymbol{p}_\mathrm{c} \mathrm{d}\boldsymbol{P}}. \tag{2.41}$$

In (2.41), the integrals can be simplified with the following observations: The integrals w.r.t. $\boldsymbol{p}_{\mathrm{c}}$ and $\boldsymbol{P}$ in the numerator and denominator cancel each other out. Integration w.r.t. $\boldsymbol{r}_{\mathrm{c}}$ in the denominator yields the factor $|\Omega|$, since there is no dependency on $\boldsymbol{r}_{\mathrm{c}}$ in (2.40). Applying the observations from above on (2.41) gives us

$$\Psi_{\mathrm{eq}}(\boldsymbol{r}_{\mathrm{c}}, \boldsymbol{Q}) = n \frac{\exp\left(-\frac{U(\boldsymbol{Q})}{k_{\mathrm{B}}\vartheta}\right)}{\int\limits_{\mathbb{D}_{\mathrm{BS}}} \exp\left(-\frac{U(\boldsymbol{Q}')}{k_{\mathrm{B}}\vartheta}\right) \mathrm{d}\boldsymbol{Q}'} = n\psi_{\mathrm{eq}}(\boldsymbol{Q}). \tag{2.42}$$

Note that in (2.42), there is no dependency on $\boldsymbol{r}_{\mathrm{c}}$ on the right hand side, i.e., the polymer molecules center of masses $\boldsymbol{r}_{\mathrm{c}}$ are uniformly distributed in volume Ω. The probability density function $\psi_{\mathrm{eq}} : \mathbb{D}_{\mathrm{BS}} \to \mathbb{R}$, defined by

$$\psi_{\mathrm{eq}}(\boldsymbol{Q}) = \frac{\exp\left(-\frac{U(\boldsymbol{Q})}{k_{\mathrm{B}}\vartheta}\right)}{\int\limits_{\mathbb{D}_{\mathrm{BS}}} \exp\left(-\frac{U(\boldsymbol{Q}')}{k_{\mathrm{B}}\vartheta}\right) \mathrm{d}\boldsymbol{Q}'}, \tag{2.43}$$

is the distribution function that we are interested in. Let $C \subset \mathbb{D}_{\mathrm{BS}}$. The integral $\int_C \psi_{\mathrm{eq}}(\boldsymbol{Q}')\,\mathrm{d}\boldsymbol{Q}'$ is then the probability of finding a configuration $\boldsymbol{Q} \in C$.

In the next step, we insert the spring-potential expressions (2.5) and (2.6) for Hookean and FENE springs in (2.43) and finally obtain the required distribution function for sampling initial spring configurations. After evaluating the integral in (2.43), we get

$$\psi_{\mathrm{eq}}^{\mathrm{Hookean}}(\boldsymbol{Q}) = \left(\frac{2\pi k_{\mathrm{B}}\vartheta}{H}\right)^{-\frac{d}{2}} \exp\left(-\frac{H\boldsymbol{Q}^2}{2k_{\mathrm{B}}\vartheta}\right), \tag{2.44a}$$

$$\psi_{\mathrm{eq}}^{\mathrm{FENE}}(\boldsymbol{Q}) = \begin{cases} C(d)^{-1}\left[1 - \left(\frac{Q}{Q_0}\right)^2\right]^{\frac{HQ_0^2}{2k_{\mathrm{B}}\vartheta}}, & |\boldsymbol{Q}| < Q_0, \\ 0, & |\boldsymbol{Q}| \geq Q_0, \end{cases} \tag{2.44b}$$

where the normalization factor $C(d)$ (cf. [12, p. 21]) for $d = 2, 3$ is given by

$$C(d) = \begin{cases} \pi Q_0^2 \left(\frac{HQ_0^2}{2k_{\mathrm{B}}\vartheta} + 1\right)^{-1}, & d = 2, \\ 2\pi Q_0^3 B(\frac{3}{2}, \frac{HQ_0^2}{2k_{\mathrm{B}}\vartheta} + 1) & d = 3. \end{cases} \tag{2.45}$$

In (2.45), $B : \mathbb{R}^+ \times \mathbb{R}^+ \to \mathbb{R}$ denotes the Beta function

$$B(x, y) = \int_0^1 t^{x-1}(1-t)^{y-1}\,\mathrm{d}t. \tag{2.46}$$

2.1.3 Fokker–Planck equation

Associated to System (2.15), there exists a distribution function $\psi : \mathbb{D}_{\mathrm{BS}} \times \Omega \times \mathbb{T} \to \mathbb{R}$ that satisfies a Fokker–Planck equation [63, Ch. 3.3.3], which is given by

$$\begin{aligned}\frac{\partial}{\partial t}\psi(\boldsymbol{Q},\boldsymbol{r}_{\mathrm{c}},t) = &-\nabla_{\boldsymbol{Q}} \cdot \left(\left[\nabla \boldsymbol{u}(\boldsymbol{r}_{\mathrm{c}})\boldsymbol{Q} - \frac{2}{\xi}\boldsymbol{F}^{\mathrm{S}}(\boldsymbol{Q})\right]\psi(\boldsymbol{Q},\boldsymbol{r}_{\mathrm{c}},t)\right) \\ &- \nabla_{\boldsymbol{r}_{\mathrm{c}}} \cdot (\boldsymbol{u}(\boldsymbol{r}_{\mathrm{c}})\psi(\boldsymbol{Q},\boldsymbol{r}_{\mathrm{c}},t)) + \frac{2k_{\mathrm{B}}\vartheta}{\xi}\Delta_{\boldsymbol{Q}}\psi(\boldsymbol{Q},\boldsymbol{r}_{\mathrm{c}},t),\end{aligned} \tag{2.47}$$

where $\boldsymbol{F}^{\mathrm{S}}$ is the spring force (2.16) or (2.17), $\boldsymbol{u}$ the fluid velocity, ξ the friction coefficient, k_{B} the Boltzmann constant, and ϑ the fluid temperature. The partial differential equation (2.47) describes the evolution of the function $\psi(\boldsymbol{Q},\boldsymbol{r}_{\mathrm{c}},t)$ in $\mathbb{D}_{\mathrm{BS}} \times \Omega \times \mathbb{T}$, which is related to the stochastic process $\boldsymbol{Q}$ from System (2.15). Note that $\psi_{\mathrm{eq}} : \mathbb{D}_{\mathrm{BS}} \to \mathbb{R}$ from (2.43) is a solution of (2.47) in the equilibrium case $\boldsymbol{u} = \boldsymbol{0}$. This can be easily verified by setting $\boldsymbol{u} = \boldsymbol{0}$ in (2.47), observing (2.43), and using the identity

$$\Delta_{\boldsymbol{Q}}\psi_{\mathrm{eq}}(\boldsymbol{Q}) = \sum_{i=1}^{d} \frac{\partial}{\partial Q_i}\left(-\frac{1}{k_{\mathrm{B}}\vartheta}\left(\frac{\partial}{\partial Q_i}U(\boldsymbol{Q})\right)\psi_{\mathrm{eq}}(\boldsymbol{Q})\right), \tag{2.48a}$$

$$\Leftrightarrow \quad \frac{2k_{\mathrm{B}}\vartheta}{\xi}\Delta_{\boldsymbol{Q}}\psi_{\mathrm{eq}}(\boldsymbol{Q}) = \nabla_{\boldsymbol{Q}} \cdot \left(-\frac{2}{\xi}\boldsymbol{F}^{\mathrm{S}}(Q)\psi_{\mathrm{eq}}(\boldsymbol{Q})\right). \tag{2.48b}$$

For each $(\boldsymbol{r}_{\mathrm{c}},t) \in \Omega \times \mathbb{T}$, function $\psi(\cdot,\boldsymbol{r}_{\mathrm{c}},t) : \mathbb{D}_{\mathrm{BS}} \to \mathbb{R}$ is a probability density function. A common choice for the initial condition ψ_0 of (2.47) is the equilibrium distribution function (2.43). Concerning boundary conditions w.r.t. a channel scenario with periodic BC (cf. Figure 1.10), we have

$$\psi(\boldsymbol{Q},\cdot,t)_{|\Gamma_{\mathrm{P}}^{\mathrm{left}}} = \psi(\boldsymbol{Q},\cdot,t)_{|\Gamma_{\mathrm{P}}^{\mathrm{right}}} \quad \forall(\boldsymbol{Q},t) \in \mathbb{D}_{\mathrm{BS}} \times \mathbb{T}, \tag{2.49}$$

and $\psi = 0$ on $\partial\mathbb{D}_{\mathrm{BS}}^{\mathrm{F}} \times \Omega \times \mathbb{T}$ for FENE dumbbells or a decay condition

$$\left|\left[\nabla \boldsymbol{u}(\boldsymbol{r}_{\mathrm{c}})\boldsymbol{Q} - \frac{2}{\xi}\boldsymbol{F}^{\mathrm{S}}(\boldsymbol{Q})\right]\psi(\boldsymbol{Q},\boldsymbol{r}_{\mathrm{c}},t)\right| \to 0 \quad \text{as} \quad |\boldsymbol{Q}| \to \infty \quad \forall(\boldsymbol{r}_{\mathrm{c}},t) \in \Omega \times \mathbb{T} \tag{2.50}$$

for Hookean dumbbells due to the unboundedness of the configuration space $\mathbb{D}_{\mathrm{BS}}^{\mathrm{H}}$. Function ψ plays a crucial role for the derivation of the polymeric stress tensor $\boldsymbol{\tau}_{\mathrm{p}}$ in the next section. After $\boldsymbol{\tau}_{\mathrm{p}}$ is derived, the Navier–Stokes equations (1.14) could be coupled to (2.47) over $\boldsymbol{\tau}_{\mathrm{p}}$. This approach is considered in the series of papers by Barrett and Süli [5–8, 81], where the existence of weak solutions of the coupled system is analyzed w.r.t. different spring forces and regularized versions of (2.47).

2.1.4 Polymeric stress tensor

In order to couple the bead-spring model to the Navier–Stokes equations (1.14), we need an expression for the polymeric stress tensor $\boldsymbol{\tau}_{\mathrm{p}}$. In the literature, there

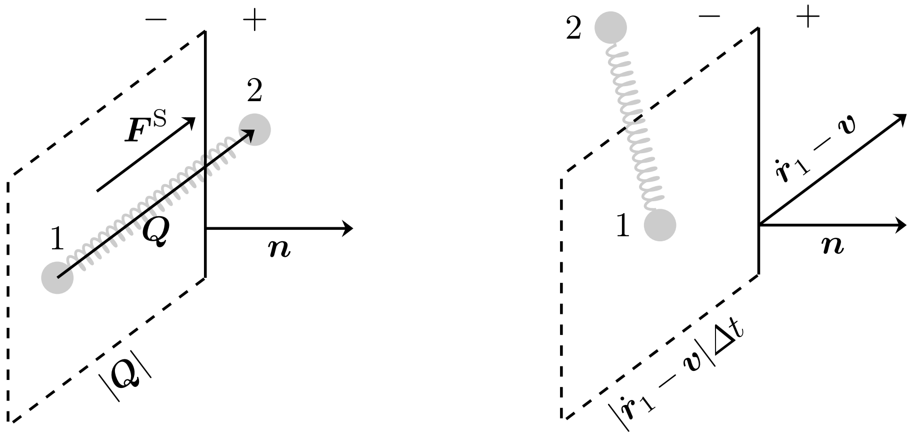

(a) Volume shape for given vector Q that must contain bead 1.

(b) Volume shape for given bead velocity $\dot{r}_1$ and plane velocity v.

Figure 2.4. Side view of the plane with normal vector n, which determines the negative and positive side of the plane (marked with ±).

are several equivalent expressions for τ_p (cf. Tab. 13.3-1 in [12]). Here, we use Kramers expression, which is given by the symmetric tensor

$$\tau_p = n\langle Q \otimes F^S(Q)\rangle - nk_B\vartheta I, \tag{2.51}$$

where n is the polymer number density, Q the dumbbell connector vector, F^S the spring force given by (2.16) or (2.17), k_B the Boltzmann constant, I the identity tensor. The expectation value $\langle \ldots \rangle$ in (2.51) for a function $B(Q, r_c, t)$ at $(r_c, t) \in \Omega \times \mathbb{T}$ is defined w.r.t. distribution function $\psi(Q, r_c, t)$ of the previous Section 2.1.3, i.e.

$$\langle B\rangle(r_c, t) := \int_{\mathbb{D}_{BS}} B(Q, r_c, t)\psi(Q, r_c, t)\,\mathrm{d}Q. \tag{2.52}$$

Note that in (2.51), we neglected the consideration of external forces on the beads.

The derivation of (2.51) is based on [12, Ch. 13.3]. In order to derive (2.51) at arbitrary but fixed $(r_c, t) \in \Omega \times \mathbb{T}$, we look at two effects: the contribution due to spring force and due to bead motion. For the spring force contribution, we consider a plane with area S and normal vector $n \in \mathbb{R}^d$. Now, we need to know how many beads with dumbbell configuration $Q \in \mathbb{D}_{BS}$ cross the plane with r_1 on the negative side and r_2 on the positive side of the plane, i.e., $Q \cdot n > 0$. This quantity is given by

$$\int_{\{Q \in \mathbb{D}_{BS} \,|\, n \cdot Q > 0\}} n(n \cdot Q)S\psi(Q, r_c, t)\mathrm{d}Q, \tag{2.53}$$

where n is the polymer number density and $(n \cdot Q)S$ the volume that must contain r_1 (cf. Figure 2.4a for a visualization of this volume). Dividing (2.53) through the surface area S, yields the corresponding area number density, i.e., the number of dumbbells at $(\boldsymbol{r}_\mathrm{c}, t)$ with $\boldsymbol{Q} \cdot \boldsymbol{n} > 0$ per unit area. Thus, dumbbells with arbitrary configuration and $\boldsymbol{r}_1$ on the negative side of the plane contribute

$$\int_{\{\boldsymbol{Q} \in \mathbb{D}_\mathrm{BS} \,|\, \boldsymbol{n} \cdot \boldsymbol{Q} > 0\}} n\,(\boldsymbol{n} \cdot \boldsymbol{Q})\,(-\boldsymbol{F}^\mathrm{S}(\boldsymbol{Q}))\psi(\boldsymbol{Q}, \boldsymbol{r}_\mathrm{c}, t)\mathrm{d}\boldsymbol{Q} \tag{2.54}$$

to the stress with their spring-force $\boldsymbol{F}^\mathrm{S}$ on the positive side of the plane. The analog computation can be done for dumbbells with $\boldsymbol{r}_2$ on the negative side of the plane, which gives the contribution

$$\int_{\{\boldsymbol{Q} \in \mathbb{D}_\mathrm{BS} \,|\, \boldsymbol{n} \cdot \boldsymbol{Q} < 0\}} n\,(-\boldsymbol{n} \cdot \boldsymbol{Q})\,\boldsymbol{F}^\mathrm{S}(\boldsymbol{Q})\psi(\boldsymbol{Q}, \boldsymbol{r}_\mathrm{c}, t)\mathrm{d}\boldsymbol{Q}. \tag{2.55}$$

The sum of (2.54) and (2.55) gives

$$-n\boldsymbol{n} \int_{\mathbb{D}_\mathrm{BS}} (\boldsymbol{Q} \otimes \boldsymbol{F}^\mathrm{S}(\boldsymbol{Q}))\psi(\boldsymbol{Q}, \boldsymbol{r}_\mathrm{c}, t)\mathrm{d}\boldsymbol{Q}, \tag{2.56}$$

from which the first contribution of (2.51) can be obtained due to Cauchy's stress theorem. The sign-switch in (2.51) is due to the sign-convention of the stress tensor in this thesis. Note that $\boldsymbol{Q} \otimes \boldsymbol{F}^\mathrm{S}(\boldsymbol{Q})$ is symmetric since $\boldsymbol{F}^\mathrm{S}(\boldsymbol{Q}) = F(\boldsymbol{Q})\boldsymbol{Q}$, where $F(\boldsymbol{Q})$ is a scalar-valued function (cf. (2.16) and (2.17)).

To obtain the second contribution of (2.51), we need to look at the transported momentum by beads with velocity $\dot{\boldsymbol{r}}_i$, $i = 1, 2$, through an arbitrary plane with surface S, normal $\boldsymbol{n}$, and velocity $\boldsymbol{v}$ (cf. Figure 2.4b). Analog to the considerations from above, the transported momentum across the plane is the product of the number of dumbbells that cross the plane during Δt and the momentum of bead i, which leads to

$$n(\dot{\boldsymbol{r}}_i - \boldsymbol{v}) \cdot \boldsymbol{n} S \Delta t m(\dot{\boldsymbol{r}}_i - \boldsymbol{v}), \quad i = 1, 2. \tag{2.57}$$

Thus, due to bead motion, the total average momentum flux for arbitrary $\dot{\boldsymbol{r}}_i$, $i = 1, 2$, and $\boldsymbol{Q}$ is given by

$$n\boldsymbol{n} \int_{\mathbb{D}_\mathrm{BS}} \left[\!\!\left[\sum_{i=1}^{2} m(\dot{\boldsymbol{r}}_i - \boldsymbol{v}) \otimes (\dot{\boldsymbol{r}}_i - \boldsymbol{v}) \right]\!\!\right] \psi(\boldsymbol{Q}, \boldsymbol{r}_\mathrm{c}, t)\mathrm{d}\boldsymbol{Q}, \tag{2.58}$$

where

$$\left[\!\!\left[\sum_{i=1}^{2} m(\dot{\boldsymbol{r}}_i - \boldsymbol{v}) \otimes (\dot{\boldsymbol{r}}_i - \boldsymbol{v}) \right]\!\!\right] := \iint_{\mathbb{R}^d \times \mathbb{R}^d} \sum_{i=1}^{2} m(\dot{\boldsymbol{r}}_i - \boldsymbol{v}) \otimes (\dot{\boldsymbol{r}}_i - \boldsymbol{v}) \varXi(\dot{\boldsymbol{r}}_1, \dot{\boldsymbol{r}}_2)\,\mathrm{d}\dot{\boldsymbol{r}}_1 \mathrm{d}\dot{\boldsymbol{r}}_2 \tag{2.59}$$

is the velocity-space average with $\varXi(\dot{\boldsymbol{r}}_1, \dot{\boldsymbol{r}}_2)$ denoting the velocity-space distribution. Assuming in (2.59) the distribution $\varXi(\dot{\boldsymbol{r}}_1, \dot{\boldsymbol{r}}_2)$ to be Maxwellian, i.e.,

$$\varXi(\dot{\boldsymbol{r}}_1, \dot{\boldsymbol{r}}_2) = \frac{\exp\left(-\frac{m(\dot{\boldsymbol{r}}_1 - \boldsymbol{v})^2 + m(\dot{\boldsymbol{r}}_2 - \boldsymbol{v})^2}{2k_\mathrm{B}\vartheta}\right)}{\iint_{\mathbb{R}^d \times \mathbb{R}^d} \exp\left(-\frac{m(\dot{\boldsymbol{r}}_1 - \boldsymbol{v})^2 + m(\dot{\boldsymbol{r}}_2 - \boldsymbol{v})^2}{2k_\mathrm{B}\vartheta}\right) \mathrm{d}\dot{\boldsymbol{r}}_1 \mathrm{d}\dot{\boldsymbol{r}}_2}, \tag{2.60}$$

one can further simplify (2.58) to

$$nn \int_{\mathbb{D}_{\mathrm{BS}}} \left[\!\!\left[\sum_{i=1}^{2} m(\dot{\boldsymbol{r}}_i - v) \otimes (\dot{\boldsymbol{r}}_i - v) \right]\!\!\right] \psi(\boldsymbol{Q}, \boldsymbol{r}_{\mathrm{c}}, t) \mathrm{d}\boldsymbol{Q} = 2nk_{\mathrm{B}}\vartheta \boldsymbol{n}, \tag{2.61}$$

from which the isotropic contribution in (2.51) with a switched sign (convention) is obtained due to Cauchy's stress theorem. The assumption (2.60) is equivalent to assuming that the velocity-space distribution in a flow system is the same as that in a solution at equilibrium (*equilibration in momentum space*) [12, p. 57]. In (2.51), the factor 2 is missing. This is due to the demand of having a vanishing polymeric stress $\boldsymbol{\tau}_{\mathrm{p}} = \boldsymbol{0}$ in equilibrium. Since $\langle \boldsymbol{Q} \otimes \boldsymbol{F}^{\mathrm{S}}(\boldsymbol{Q}) \rangle = k_{\mathrm{B}}\vartheta \boldsymbol{I}$ in equilibrium (cf. (12B.1-9) in [12]), we only need one half of the constant isotropic contribution $2nk_{\mathrm{B}}\vartheta \boldsymbol{I}$ in (2.51). The remaining part of $2nk_{\mathrm{B}}\vartheta \boldsymbol{I}$ is absorbed into the pressure. This can be done since adding a constant to the pressure does only result in a shift and does not change pressure gradients, which are relevant in the Navier–Stokes equations (1.14).

2.1.5 Units and non-dimensionalization

In this section, we non-dimensionalize the relevant equations of Sections 2.1.1, 2.1.2 and 2.1.4. The non-dimensionalized equations are then used in Sections 3.3 and 5 for discretization and simulations. The characteristic quantities are chosen as done in [17]. Dimensionless quantities are marked with *. Table 2.1 summarizes

Symbol	Unit	Name
k_{B}	$\mathrm{kg\,m^2/(K\,s^2)}$	Boltzmann constant
n	$1/\mathrm{m}^3$	Polymer number density
λ	s	Polymer relaxation time
H	$\mathrm{kg/s^2}$	Spring constant
Q_0	m	Maximum spring extension
ξ	kg/s	Friction coefficient
ϑ	K	Temperature
η_{p}	kg/(m s)	Polymeric viscosity
η_{s}	kg/(m s)	Solvent viscosity
U_{c}	m/s	Characteristic velocity
L_{c}	m	Characteristic length
T_{c}	s	Characteristic time
$\tau_{\mathrm{c}}^{\mathrm{p}}$	$\mathrm{kg/(m\,s^2)}$	Characteristic stress
l_{c}	m	Micr. char. length
ϵ	1	Polymeric viscosity ratio
Wi	1	Weissenberg number
b	1	Sq. max. extension of FENE spring

Table 2.1. Collection of symbols, units, and names

the physical parameters, characteristic quantities, dimensionless numbers, and their corresponding units that are used in the following.

For the non-dimensionalization of SDE (2.18), we introduce the Weissenberg number $\mathrm{Wi} \in \mathbb{R}$, which is defined by

$$\mathrm{Wi} := \lambda \frac{U_\mathrm{c}}{L_\mathrm{c}}, \tag{2.62}$$

where λ is the characteristic longest relaxation time of the polymer and U_c, L_c are the characteristic velocity and length-scale from Section 1.6. The Weissenberg number is a measure for the ratio of elastic forces to viscous forces in the fluid. For bead-spring dumbbells, one chooses $\lambda = \xi/(4H)$ with ξ denoting the friction coefficient and H the spring constant. The microscopic characteristic length scale is given by $l_\mathrm{c} = \sqrt{k_\mathrm{B}\vartheta/H}$. For the macroscopic characteristic time scale, we choose $T_\mathrm{c} = L_\mathrm{c}/U_\mathrm{c}$. Non-dimensionalization of (2.18) with the quantities from above leads to

$$\begin{aligned} l_\mathrm{c}\mathrm{d}\boldsymbol{Q}^* &= \left[-\frac{U_\mathrm{c} l_\mathrm{c}}{L_\mathrm{c}}\boldsymbol{u}^* \cdot \boldsymbol{\nabla}^*\boldsymbol{Q}^* + \frac{l_\mathrm{c} U_\mathrm{c}}{L_\mathrm{c}}(\boldsymbol{\nabla}^*\boldsymbol{u}^*)\boldsymbol{Q}^* - \frac{2Hl_\mathrm{c}}{\xi}\boldsymbol{F}^{\mathrm{S}*}(\boldsymbol{Q}^*)\right] T_\mathrm{c}\mathrm{d}t^* \\ &\quad + \sqrt{\frac{4k_\mathrm{B}\vartheta T_\mathrm{c}}{\xi}}\mathrm{d}\boldsymbol{W}_{\boldsymbol{Q}}^*, \end{aligned} \tag{2.63a}$$

$$\Leftrightarrow \mathrm{d}\boldsymbol{Q}^* = \left[-\boldsymbol{u}^* \cdot \boldsymbol{\nabla}^*\boldsymbol{Q}^* + (\boldsymbol{\nabla}^*\boldsymbol{u}^*)\boldsymbol{Q}^* - \frac{2HL_\mathrm{c}}{\xi U_\mathrm{c}}\boldsymbol{F}^{\mathrm{S}*}(\boldsymbol{Q}^*)\right] \mathrm{d}t^* + \sqrt{\frac{4k_\mathrm{B}\vartheta T_\mathrm{c}}{\xi l_\mathrm{c}^2}}\mathrm{d}\boldsymbol{W}_{\boldsymbol{Q}}^*, \tag{2.63b}$$

$$\Leftrightarrow \mathrm{d}\boldsymbol{Q}^* = \left[-\boldsymbol{u}^* \cdot \boldsymbol{\nabla}^*\boldsymbol{Q}^* + (\boldsymbol{\nabla}^*\boldsymbol{u}^*)\boldsymbol{Q}^* - \frac{1}{2\mathrm{Wi}}\boldsymbol{F}^{\mathrm{S}*}(\boldsymbol{Q}^*)\right] \mathrm{d}t^* + \sqrt{\frac{1}{\mathrm{Wi}}}\mathrm{d}\boldsymbol{W}_{\boldsymbol{Q}}^*, \tag{2.63c}$$

where $\boldsymbol{\nabla}^*$ denotes the gradient w.r.t. the dimensionless unknowns and $\boldsymbol{W}_{\boldsymbol{Q}}^*$ denotes the Wiener process w.r.t. t^*. Wiener processes $\boldsymbol{W}_{\boldsymbol{Q}}^*$ and $\boldsymbol{W}_{\boldsymbol{Q}}$ are connected via relation $\sqrt{T_\mathrm{c}}\boldsymbol{W}_{\boldsymbol{Q}}^*(t^*) = \boldsymbol{W}_{\boldsymbol{Q}}(t)$. The dimensionless spring forces $\boldsymbol{F}^{\mathrm{S}*}(\boldsymbol{Q}^*)$ are given by

$$\boldsymbol{F}^{\mathrm{S}*}_{\mathrm{Hookean}}(\boldsymbol{Q}^*) = \boldsymbol{Q}^* \tag{2.64}$$

for Hookean dumbbells and

$$\boldsymbol{F}^{\mathrm{S}*}_{\mathrm{FENE}}(\boldsymbol{Q}^*) = \frac{\boldsymbol{Q}^*}{1 - (\boldsymbol{Q}^*)^2/b} \tag{2.65}$$

for FENE dumbbells, where $b = (Q_0/l_\mathrm{c})^2 = Q_0 H/(k_\mathrm{B}\vartheta)$ denotes the dimensionless squared maximum extension of the FENE-spring.

For the non-dimensionalization of the polymeric stress tensor (2.51), we use the characteristic stress $\tau_\mathrm{c}^\mathrm{p} = U_\mathrm{c}(\eta_\mathrm{s} + \eta_\mathrm{p})/L_\mathrm{c}$ from Section 1.6 and for the polymeric viscosity, we have

$$\eta_\mathrm{p} := n k_\mathrm{B}\vartheta\lambda\alpha_{b,d}, \tag{2.66}$$

where the parameter $\alpha_{b,d}$ (cf. (1.40) in [56]) is given by

$$\alpha_{b,d} := \begin{cases} 1, & \text{Hookean}, \\ \frac{b}{b+d+2}, & \text{FENE}. \end{cases} \tag{2.67}$$

The non-dimensional stress tensor $\boldsymbol{\tau}_{\mathrm{p}}^{*} = \boldsymbol{\tau}_{\mathrm{p}}/\tau_{\mathrm{c}}^{\mathrm{p}}$ is then given by

$$\boldsymbol{\tau}_{\mathrm{p}}^{*} = \frac{n}{\tau_{\mathrm{c}}^{\mathrm{p}}} \left(l_{\mathrm{c}}^{2} H \langle \boldsymbol{Q}^{*} \otimes \boldsymbol{F}^{*\mathrm{S}}(\boldsymbol{Q}^{*}) \rangle - k_{\mathrm{B}} \vartheta \boldsymbol{I} \right), \tag{2.68a}$$

$$\Leftrightarrow \boldsymbol{\tau}_{\mathrm{p}}^{*} = \frac{L_{\mathrm{c}} n k_{\mathrm{B}} \vartheta}{U_{\mathrm{c}}(\eta_{\mathrm{s}} + \eta_{\mathrm{p}})} \left(\langle \boldsymbol{Q}^{*} \otimes \boldsymbol{F}^{*\mathrm{S}}(\boldsymbol{Q}^{*}) \rangle - \boldsymbol{I} \right), \tag{2.68b}$$

$$\Leftrightarrow \boldsymbol{\tau}_{\mathrm{p}}^{*} = \frac{\epsilon}{\alpha_{b,d} \mathrm{Wi}} \left(\langle \boldsymbol{Q}^{*} \otimes \boldsymbol{F}^{*\mathrm{S}}(\boldsymbol{Q}^{*}) \rangle - \boldsymbol{I} \right). \tag{2.68c}$$

The step from (2.68b) to (2.68c) is done by using (2.62) and (2.66) in combination with the polymeric viscosity ratio $\epsilon = \eta_{\mathrm{p}}/(\eta_{\mathrm{p}} + \eta_{\mathrm{s}})$, which was already used for the non-dimensionalization of the Navier–Stokes equations in Section 1.6.

The equilibrium distribution functions (2.44a) and (2.44b) in the non-dimensional setting are given by

$$\psi_{\mathrm{eq}}^{*\mathrm{Hookean}}(\boldsymbol{Q}^{*}) = (2\pi)^{-\frac{d}{2}} \exp\left(-\frac{(\boldsymbol{Q}^{*})^{2}}{2} \right), \tag{2.69a}$$

$$\psi_{\mathrm{eq}}^{*\mathrm{FENE}}(\boldsymbol{Q}^{*}) = \begin{cases} C(d)^{-1} \left[1 - \frac{(\boldsymbol{Q}^{*})^{2}}{b} \right]^{\frac{b}{2}}, & |\boldsymbol{Q}^{*}| < \sqrt{b}, \\ 0, & |\boldsymbol{Q}^{*}| \geq \sqrt{b}, \end{cases} \tag{2.69b}$$

where the normalization constants are now given by

$$C(d) = \begin{cases} \frac{2\pi b}{b+2}, & d = 2, \\ 2\pi b^{\frac{3}{2}} B(\frac{3}{2}, \frac{b+2}{b}) & d = 3. \end{cases} \tag{2.70}$$

In (2.70), $B : \mathbb{R}^{+} \times \mathbb{R}^{+} \longrightarrow \mathbb{R}$ denotes the Beta function (2.46).

2.2 Bead-rod chain model

In this section, we approximate a polymer molecule with a bead-rod chain as visualized in Figure 2.1b. At first, the governing equations of the bead-rod chain model are derived in Section 2.2.1. Afterwards, we make some remarks to the equilibrium distribution function and Fokker–Planck equation w.r.t. bead-rod chains in Section 2.2.2. Section 2.2.3 presents the expression for the polymeric stress tensor and Section 2.2.4 discusses the non-dimensionalization of the governing equations and stress tensor.

2.2.1 Equations of motion

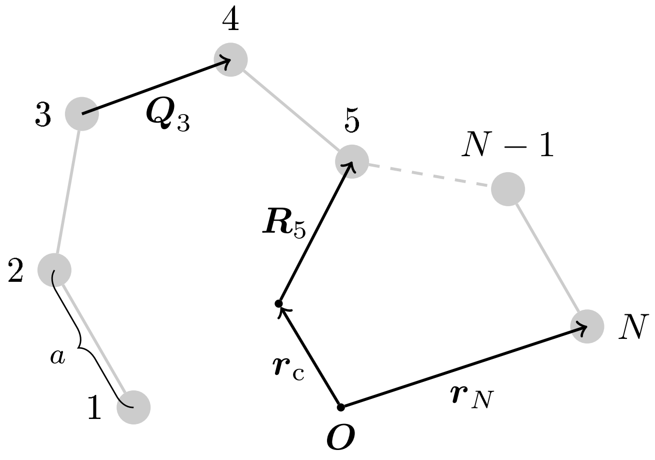

Figure 2.5. Bead-rod chain with visualization of the rod length a, origin $\boldsymbol{O}$, vector $\boldsymbol{r}_\mathrm{c}$ pointing from $\boldsymbol{O}$ to the beads center of mass, vector $\boldsymbol{r}_N$ pointing from $\boldsymbol{O}$ to bead N, relative bead position $\boldsymbol{R}_5 := \boldsymbol{r}_5 - \boldsymbol{r}_\mathrm{c}$ w.r.t. $\boldsymbol{r}_\mathrm{c}$, and connector vector $\boldsymbol{Q}_3 := \boldsymbol{r}_4 - \boldsymbol{r}_3$.

We model polymer chains by freely jointed bead-rod chains. Two neighboring beads are connected by a rod of fixed length a (cf. Fig. 2.5). We follow [75] for the derivation of the stochastic differential equation w.r.t. the bead position vectors $\boldsymbol{r}_i$, $i = 1, \ldots, N$, for a chain with N beads. For a more detailed derivation of the model see [12, 63]. Similar to the bead-spring model from Section 2.1, the model takes three forces on the beads into account. The hydrodynamic drag force $\boldsymbol{F}_i^\mathrm{H}$ and Brownian force $\boldsymbol{F}_i^\mathrm{B}$ are already defined in (2.1) and (2.2). The range of the bead index i is extended to the set $\{1, \ldots, N\}$. Instead of the spring force, the third force is now a constraint force $\boldsymbol{F}_i^\mathrm{C}$, which ensure that two neighboring beads keep a constant distance a. Analog to Section 2.1.1, we apply Newton's second law of motion and neglect again the inertia term due to small beads masses, which yields the ansatz

$$\boldsymbol{F}_i^\mathrm{H} + \boldsymbol{F}_i^\mathrm{B} + \boldsymbol{F}_i^\mathrm{C} = \boldsymbol{0}, \quad i = 1, \ldots, N. \tag{2.71}$$

Inserting the expressions for the various forces in (2.71) yields the stochastic differential equations

$$\mathrm{d}\boldsymbol{r}_i = \left[\boldsymbol{u}_i + \frac{\boldsymbol{F}_i^\mathrm{C}}{\xi}\right]\mathrm{d}t + \sqrt{\frac{2k_\mathrm{B}\vartheta}{\xi}}\mathrm{d}\boldsymbol{W}_i, \quad i = 1, \ldots, N, \tag{2.72a}$$

$$(\boldsymbol{r}_{i+1} - \boldsymbol{r}_i) \cdot (\boldsymbol{r}_{i+1} - \boldsymbol{r}_i) - a^2 = 0, \quad i = 1, \ldots, N-1. \tag{2.72b}$$

Eq. (2.72b) are the equations for the constant rod length constraint. The Wiener process $\boldsymbol{W}_i$ is characterized by $\boldsymbol{W}_i(0) = \boldsymbol{0}$, has zero mean and normally distributed increments $\boldsymbol{W}_i(t+\Delta t) - \boldsymbol{W}_i(t) = \Delta \boldsymbol{W}_i(t) \sim \mathcal{N}(0, \Delta t)^d$ with zero mean and variance Δt.

The constraint forces $\boldsymbol{F}_i^{\mathrm{C}}$ are expressed in terms of *tensions* T_i:

$$\boldsymbol{F}_i^{\mathrm{C}} = \begin{cases} T_1(\boldsymbol{r}_2 - \boldsymbol{r}_1)/a, & i = 1, \\ T_i(\boldsymbol{r}_{i+1} - \boldsymbol{r}_i)/a - T_{i-1}(\boldsymbol{r}_i - \boldsymbol{r}_{i-1})/a, & i = 2, \dots, N-1, \\ -T_{N-1}(\boldsymbol{r}_N - \boldsymbol{r}_{N-1})/a, & i = N. \end{cases} \tag{2.73}$$

In order to derive expression (2.73), we recall that the constraint force $\boldsymbol{F}_i^{\mathrm{C}}$ is given by the general expression

$$\boldsymbol{F}_i^{\mathrm{C}} := \sum_{j=1}^{N-1} \lambda_j \boldsymbol{\nabla}_{\boldsymbol{r}_i} f_j, \tag{2.74}$$

where λ_j are Lagrangian multipliers and functions f_j, $j = 1, \dots, N-1$, describe the constraint equations $f_j = 0$. For the derivation of (2.74) see [60, Ch. 1.2.5], where ideas of the d'Alembert principle are applied. In order to get (2.73), where tension T_j can be identified with λ_j, one has to specifically choose

$$f_j := -\frac{1}{2a}\left[\left(\boldsymbol{r}_{j+1} - \boldsymbol{r}_j\right) \cdot \left(\boldsymbol{r}_{j+1} - \boldsymbol{r}_j\right) - a^2\right], \quad j = 1, \dots, N-1. \tag{2.75}$$

Note that (2.75) vanishes if and only if $|\boldsymbol{r}_{j+1} - \boldsymbol{r}_j| = a$, i.e., the rod length of rod j is a. In [21], the constraint force (2.73) is derived by approximating the chain with a flexible inextensible string, where the constraint force per unit length is equivalent to the tension gradient. Integrating this tension gradient over a single rod yields (2.73). Hence the name *tension* for T_i.

In order to apply the Brownian configuration fields ansatz, it is useful to transfer the bead-position formulation (2.72) into a connector-vector formulation. Let $\boldsymbol{Q}_i := \boldsymbol{r}_{i+1} - \boldsymbol{r}_i$, $i = 1, \dots, N-1$, be the connector vector pointing from bead position $\boldsymbol{r}_i$ to $\boldsymbol{r}_{i+1}$ (cf. Fig. 2.5). System (2.72) can be rewritten to

$$\mathrm{d}\boldsymbol{Q}_i = \left[\boldsymbol{u}_{i+1} - \boldsymbol{u}_i + \frac{\boldsymbol{F}_{i+1}^{\mathrm{C}} - \boldsymbol{F}_i^{\mathrm{C}}}{\xi}\right]\mathrm{d}t + \sqrt{\frac{2k_{\mathrm{B}}\vartheta}{\xi}}(\mathrm{d}\boldsymbol{W}_{i+1} - \mathrm{d}\boldsymbol{W}_i), \tag{2.76a}$$

$$\boldsymbol{Q}_i \cdot \boldsymbol{Q}_i - a^2 = 0, \tag{2.76b}$$

$$\mathrm{d}\boldsymbol{r}_{\mathrm{c}} = \left[\frac{1}{N}\sum_{j=1}^{N} \boldsymbol{u}_j\right]\mathrm{d}t + \frac{1}{N}\sum_{j=1}^{N}\sqrt{\frac{2k_{\mathrm{B}}\vartheta}{\xi}}\mathrm{d}\boldsymbol{W}_j, \tag{2.76c}$$

where $i = 1, \dots, N-1$, and the chain's center of mass is given by

$$\boldsymbol{r}_{\mathrm{c}} := \frac{1}{N}\sum_{i=1}^{N} \boldsymbol{r}_i. \tag{2.77}$$

In (2.76c), we used $\sum_{j=1}^{N} \boldsymbol{F}_j^{\mathrm{C}} = \boldsymbol{0}$ due to (2.73). Analog to the bead-spring model, we use a first order Taylor approximation

$$\boldsymbol{u}_i \approx \boldsymbol{u}_{\mathrm{c}} + \boldsymbol{\nabla}\boldsymbol{u}_{\mathrm{c}}\left(\boldsymbol{r}_i - \boldsymbol{r}_{\mathrm{c}}\right), \quad i = 1, \dots, N, \tag{2.78}$$

where $\boldsymbol{u}_{\mathrm{c}}$ denotes $\boldsymbol{u}(\boldsymbol{r}_{\mathrm{c}})$. Using (2.78) to simplify the velocity term $\boldsymbol{u}_{i+1} - \boldsymbol{u}_i$ in (2.76a) and $\frac{1}{N}\sum_{j=1}^{N}\boldsymbol{u}_j$ in (2.76c) together with the smallness assumption on the noise (analog to [17])

$$\left|\frac{1}{N}\sum_{i=1}^{N}\sqrt{\frac{2k_{\mathrm{B}}\vartheta}{\xi}}\boldsymbol{W}_i(T)\right| \ll \left|\int_0^T\left[\frac{1}{N}\sum_{i=1}^{N}\boldsymbol{u}_i\right]\mathrm{d}t\right|, \tag{2.79}$$

yields the simplified system

$$\mathrm{d}\boldsymbol{Q}_i = \left[\nabla\boldsymbol{u}_{\mathrm{c}}(\boldsymbol{Q}_i) + \frac{\boldsymbol{F}_{i+1}^{\mathrm{C}} - \boldsymbol{F}_i^{\mathrm{C}}}{\xi}\right]\mathrm{d}t + \sqrt{\frac{2k_{\mathrm{B}}\vartheta}{\xi}}(\mathrm{d}\boldsymbol{W}_{i+1} - \mathrm{d}\boldsymbol{W}_i), \tag{2.80a}$$

$$\boldsymbol{Q}_i \cdot \boldsymbol{Q}_i - a^2 = 0, \tag{2.80b}$$

$$\frac{\mathrm{d}\boldsymbol{r}_{\mathrm{c}}}{\mathrm{d}t} = \boldsymbol{u}_{\mathrm{c}}. \tag{2.80c}$$

System (2.80) is currently formulated in the Lagrangian setting. The corresponding Eulerian formulation is given by

$$\mathrm{d}\boldsymbol{Q}_i = \left[-\boldsymbol{u}\cdot\nabla\boldsymbol{Q}_i + (\nabla\boldsymbol{u})\boldsymbol{Q}_i + \frac{\boldsymbol{F}_{i+1}^{\mathrm{C}} - \boldsymbol{F}_i^{\mathrm{C}}}{\xi}\right]\mathrm{d}t + \sqrt{\frac{2k_{\mathrm{B}}\vartheta}{\xi}}(\mathrm{d}\boldsymbol{W}_{i+1} - \mathrm{d}\boldsymbol{W}_i), \tag{2.81a}$$

$$\boldsymbol{Q}_i \cdot \boldsymbol{Q}_i - a^2 = 0, \tag{2.81b}$$

where the Wiener processes $\boldsymbol{W}_i$ are constant in space and only allowed to vary in time. Note that in (2.81), the connector vectors $\boldsymbol{Q}_i$ are now time-dependent vector fields, i.e., $\boldsymbol{Q}_i : \Omega \times \mathbb{T} \to \mathbb{D}_{\mathrm{BR}}$, where $\Omega \subset \mathbb{R}^d$ is the flow domain, $\mathbb{T} := (0, T)$ the time interval, and $\mathbb{D}_{\mathrm{BR}} := \left\{\boldsymbol{Q} \in \mathbb{R}^d \,|\, |\boldsymbol{Q}| = a\right\}$ the bead-rod connector vector configuration space.

2.2.2 Equilibrium distribution and Fokker–Planck equation

In order to derive an explicit expression for the bead-rod chain equilibrium distribution, one switches to generalized coordinates. Each connector vector $\boldsymbol{Q}_i$, $i = 1, \dots, N-1$, has a priori d degrees of freedom (DOF) and there are $N-1$ additional constraints due to constant rod lengths, where $N \geq 2$ is the number of beads. Thus, we are able to eliminate $N-1$ DOF via switching to generalized coordinates. As the connector vectors $\boldsymbol{Q}_i$ are enforced to have a constant length a, it suffices to describe $\boldsymbol{Q}_i$ by $d-1$ angles. For example in $d = 2$, the expression for $\boldsymbol{Q}_i$ is then given by

$$\boldsymbol{Q}_i = a\begin{pmatrix}\cos(\phi_i)\\ \sin(\phi_i)\end{pmatrix} \tag{2.82}$$

with $0 \leq \phi_i < 2\pi$. For $d = 3$, one uses the additional polar angle $\theta_i \in [0, \pi)$ next to the azimuthal angle ϕ_i.

Analog to Section 2.1.2, one could try to derive an explicit expression for ψ_{eq} for a given N, which is a very lengthy process that we avoid here. In [12], an explicit expression of ψ_{eq} for $N = 3$ and $d = 3$ is computed and is given by

$$\psi_{\text{eq}}(\theta_1, \phi_1, \theta_2, \phi_2) = \frac{\sin(\theta_1)\sin(\theta_2)}{(4\pi)^2}\left[\frac{\sqrt{1 - \frac{1}{4}\cos(\xi_2)^2}}{\frac{1}{4}\sqrt{3} + \frac{1}{6}\pi}\right], \tag{2.83}$$

where ξ_2 is the angle between the two vectors described by (θ_i, ϕ_i), $i = 1, 2$. With (2.83), one can observe that the two orientations are not independent from each other due to the presence of ξ_2. Distribution (2.83) is not the random-walk distribution, which is given by

$$\psi_{\text{eq}}^{\text{RW}}(\theta_1, \phi_1, \theta_2, \phi_2) = \frac{\sin(\theta_1)\sin(\theta_2)}{(4\pi)^2}. \tag{2.84}$$

The random-walk distribution (2.84) assumes that each rod is oriented independently from each other. For a bead-spring chain with infinitely stiff Fraenkel springs that could be interpreted as a bead-rod chain, the equilibrium distribution is of random-walk type. This was computed in [47], where a possible explanation of the deviation for the different distributions is given. Their main argument lies in the different phase-spaces. Using constraints to enforce the bead motion yields a 7-dimensional manifold in a 9-dimensional space. Using a potential to confine the motion of beads, such that they stay at a constant distance, results in potential gullies with varying widths in the 9-dimensional space.

In practice, it is not straightforward to get explicit expressions for ψ_{eq} in the case of bead-rod chains with arbitrary N. Instead, we will use a different technique for the generation of bead-rod chains in equilibrium. The idea is to sample initial chains w.r.t. the random-walk distribution and then drive them into equilibrium. A detailed description of this procedure is given in Section 3.4.1.

In the case of the Fokker–Planck (FP) equation for bead-rod chains, similar problems arise as above. There is no easy-to-work-with explicit expression. In [55], an abstract expression of the FP equation is given that has no practical use. The FP equation is a $((N-1)(d-1) + d + 1)$-dimensional partial differential equation. Note that the dimension gets very large if the number of beads N is increased. In Section 3.1, where the Brownian configuration field method is introduced, it will be made clear that we don't need the FP equation for simulations at all.

2.2.3 Polymeric stress tensor

In order to couple the bead-rod chain model to the Navier–Stokes equations, an expression for the polymeric stress contribution $\boldsymbol{\tau}_{\text{p}}$ in (1.14a) is required. There exist several in theory equivalent expressions for $\boldsymbol{\tau}_{\text{p}}$ in the literature [12]. In [75], the Kramers–Kirkwood expression

$$\boldsymbol{\tau}_{\text{p}} := n\sum_{i=1}^{N}\langle \boldsymbol{R}_i \otimes \boldsymbol{F}_i^{\text{H}}\rangle - nk_{\text{B}}\vartheta\boldsymbol{I} \tag{2.85}$$

is compared to the modified Giesekus expression

$$\boldsymbol{\tau}_\mathrm{p} := \frac{1}{2} n \left[\sum_{i=1}^{N} \langle \boldsymbol{R}_i \otimes \boldsymbol{R}_i \rangle \right]^{(1)} - n k_\mathrm{B} \vartheta \boldsymbol{I} \tag{2.86}$$

in a start-up of extensional flow scenario. In (2.85), $\boldsymbol{R}_i$ denotes the relative bead position w.r.t. the chain's center of mass $\boldsymbol{r}_\mathrm{c}$ (see Fig. 2.5), $\boldsymbol{F}_i^\mathrm{H}$ the drag force (2.1), and n is the number density, i.e., n polymer molecules per unit volume. In (2.86), superscript (1) denotes the upper convected derivative

$$\boldsymbol{\Lambda}^{(1)} := \frac{\partial \boldsymbol{\Lambda}}{\partial t} - (\nabla \boldsymbol{u})^\mathrm{T} \boldsymbol{\Lambda} - \boldsymbol{\Lambda} \nabla \boldsymbol{u}. \tag{2.87}$$

Both expressions have their advantages and disadvantages. In Section 4.1 of [75], the main findings are the following: Both expressions produce almost identical results. The Kramers–Kirkwood expression requires an additional noise reduction technique [21] to filter out statistical noise of order $(\Delta t)^{-0.5}$. In transient regimes, the modified Giesekus expression contains a time derivative that is non–trivial to evaluate due to rapidly fluctuating results, which requires additional smoothing. The smoothing introduces additional numerical errors and is memory-consuming as several previous solutions need to be stored, especially when fine meshes are considered. In steady–state regimes, the modified Giesekus expression is simpler to evaluate and produces less noisy results compared to the Kramers–Kirkwood expression. In this thesis, we consider time-dependent problems in complex flow geometries, therefore we use the Kramers–Kirkwood expression with noise filtering for the evaluation of the polymeric stress tensor $\boldsymbol{\tau}_\mathrm{p}$. Details concerning the noise-filtering are discussed in Section 3.4.2. See [12] for a detailed derivation of Kramers–Kirkwood expression (2.85).

Evaluating the stress tensor (2.85) requires the relative bead position $\boldsymbol{R}_i$. The relation between $\boldsymbol{R}_i$ and the connector vectors $\boldsymbol{Q}_i$ is given by

$$\boldsymbol{R}_k = \sum_{i=1}^{N-1} B_{ki} \boldsymbol{Q}_i, \tag{2.88}$$

where $B_{ki} = i/N, i < k$ and $B_{ki} = -(1 - i/N) = -(N-i)/N, i \geq k$, which we proof in the following lemma.

Lemma 2.1. *Let $\boldsymbol{R}_k := \boldsymbol{r}_k - \boldsymbol{r}_\mathrm{c}$, $k = 1, \ldots, N$, be the relative bead position w.r.t. center of mass $\boldsymbol{r}_\mathrm{c} = \frac{1}{N} \sum_{i=1}^{N} \boldsymbol{r}_i$ and let $\boldsymbol{Q}_i := \boldsymbol{r}_{i+1} - \boldsymbol{r}_i$, $i = 1, \ldots, N-1$, be the connector vector. Vector $\boldsymbol{R}_k$ is then related to the connector vectors $\boldsymbol{Q}_i$ via (2.88).*

Proof. First, we use the definition of the B_{ki} and $\boldsymbol{Q}_i$ in (2.88) to get

$$\sum_{i=1}^{N-1} B_{ki} \boldsymbol{Q}_i = \frac{1}{N} \left[\sum_{1 \leq i < k} i \boldsymbol{r}_{i+1} - i \boldsymbol{r}_i + \sum_{k \leq i < N} -(N-i) \boldsymbol{r}_{i+1} + (N-i) \boldsymbol{r}_i \right] \tag{2.89}$$

and take a closer look at the two sums of the right hand side of (2.89). The first sum can be transformed to

$$\begin{aligned}\sum_{1\le i<k} i\boldsymbol{r}_{i+1} - i\boldsymbol{r}_i &= \sum_{2\le i<k+1} (i-1)\boldsymbol{r}_i - \sum_{1\le i<k} i\boldsymbol{r}_i \\ &= -\boldsymbol{r}_1 + (k-1)\boldsymbol{r}_k + \sum_{2\le i<k} (i-1)\boldsymbol{r}_i - \sum_{2\le i<k} i\boldsymbol{r}_i \\ &= (k-1)\boldsymbol{r}_k - \sum_{1\le i<k} \boldsymbol{r}_i. \end{aligned} \tag{2.90}$$

The second sum can be transformed to

$$\begin{aligned}\sum_{k\le i<N} -(N-i)\boldsymbol{r}_{i+1} + (N-i)\boldsymbol{r}_i &= \sum_{k+1\le i<N+1} -(N-i+1)\boldsymbol{r}_i + \sum_{k\le i<N} (N-i)\boldsymbol{r}_i \\ &= -\boldsymbol{r}_N + (N-k)\boldsymbol{r}_k - \sum_{k+1\le i<N} (N-i+1)\boldsymbol{r}_i + \sum_{k+1\le i<N} (N-i)\boldsymbol{r}_i \\ &= (N-k)\boldsymbol{r}_k - \sum_{k+1\le i\le N} \boldsymbol{r}_i. \end{aligned} \tag{2.91}$$

Using the expression (2.90) and (2.91) in (2.89) then gives the result

$$\sum_{i=1}^{N-1} B_{ki}\boldsymbol{Q}_i = \frac{1}{N}\left[(N-1)\boldsymbol{r}_k - \sum_{1\le i\le N,\ i\ne k} \boldsymbol{r}_i\right] = \frac{1}{N}\left[N\boldsymbol{r}_k - \sum_{i=1}^{N} \boldsymbol{r}_i\right] \tag{2.92a}$$

$$= \boldsymbol{r}_k - \frac{1}{N}\sum_{i=1}^{N} \boldsymbol{r}_i = \boldsymbol{r}_k - \boldsymbol{r}_\mathrm{c} = \boldsymbol{R}_k. \tag{2.92b}$$

□

2.2.4 Units and non-dimensionalization

In the following section, we mark dimensionless quantities with *. Table 2.2 lists physical parameters, characteristic quantities, dimensionless numbers, and their corresponding units that are used during the non-dimensionalization process. For the numerical simulation in Section 5, it is convenient to consider the non-dimensionalized formulation of System (2.80) or (2.81). The characteristic scales are as follows: microscopic length scale $l_\mathrm{c} = a$, microscopic time scale $t_\mathrm{c} = \xi a^2/(k_\mathrm{B}\vartheta)$, and characteristic force $F_\mathrm{c} = k_\mathrm{B}\vartheta/a$. This choice leads to

$$\mathrm{d}\boldsymbol{Q}_i = \left[(\nabla\boldsymbol{u}_\mathrm{c})\boldsymbol{Q}_i + \frac{\boldsymbol{F}^\mathrm{C}_{i+1} - \boldsymbol{F}^\mathrm{C}_i}{\xi}\right]\mathrm{d}t + \sqrt{\frac{2k_\mathrm{B}\vartheta}{\xi}}(\mathrm{d}\boldsymbol{W}_{i+1} - \mathrm{d}\boldsymbol{W}_i), \tag{2.93a}$$

$$\begin{aligned}\Leftrightarrow\quad l_\mathrm{c}\mathrm{d}\boldsymbol{Q}^*_i = &\left[\frac{U_\mathrm{c}l_\mathrm{c}}{L_\mathrm{c}}(\nabla^*\boldsymbol{u}^*_\mathrm{c})\boldsymbol{Q}^*_i + \frac{F_\mathrm{c}}{\xi}(\boldsymbol{F}^{*\mathrm{C}}_{i+1} - \boldsymbol{F}^{*\mathrm{C}}_i)\right]\frac{L_\mathrm{c}}{U_\mathrm{c}}\mathrm{d}t^* \\ &+ \sqrt{\frac{2k_\mathrm{B}\vartheta L_\mathrm{c}}{\xi U_\mathrm{c}}}(\mathrm{d}\boldsymbol{W}^*_{i+1} - \mathrm{d}\boldsymbol{W}^*_i),\end{aligned} \tag{2.93b}$$

Symbol	**Unit**	**Name**
k_B	$\mathrm{kg\,m^2/(K\,s^2)}$	Boltzmann constant
n	$1/\mathrm{m}^3$	Polymer number density
λ	s	Polymer relaxation time
ξ	kg/s	Friction coefficient
ϑ	K	Temperature
η_p	$\mathrm{kg/(m\,s)}$	Polymeric viscosity
η_s	$\mathrm{kg/(m\,s)}$	Solvent viscosity
U_c	m/s	Characteristic velocity
L_c	m	Characteristic length
T_c	s	Macr. characteristic time
t_c	s	Micr. characteristic time
$F_\mathrm{c} = k_\mathrm{B}\vartheta/a$	$\mathrm{kg\,m/s^2}$	Characteristic force
$l_\mathrm{c} = a$	m	Micr. char. length (rod length)
$\tau_\mathrm{c}^\mathrm{p}$	$\mathrm{kg/(m\,s^2)}$	Characteristic stress
ϵ	1	Polymeric viscosity ratio
Wi	1	Weissenberg number

Table 2.2. Collection of symbols, units, and names.

$$\begin{aligned}\Leftrightarrow\quad \mathrm{d}\boldsymbol{Q}_i^* &= \left[(\nabla^*\boldsymbol{u}_\mathrm{c}^*)\boldsymbol{Q}_i^* + \frac{F_\mathrm{c}L_\mathrm{c}}{l_\mathrm{c}\xi U_\mathrm{c}}(\boldsymbol{F}_{i+1}^{*\mathrm{C}} - \boldsymbol{F}_i^{*\mathrm{C}})\right]\mathrm{d}t^* \\ &\quad + \sqrt{\frac{2k_\mathrm{B}\vartheta L_\mathrm{c}}{\xi U_\mathrm{c} l_\mathrm{c}^2}}(\mathrm{d}\boldsymbol{W}_{i+1}^* - \mathrm{d}\boldsymbol{W}_i^*),\end{aligned} \tag{2.93c}$$

$$\begin{aligned}\Leftrightarrow\quad \mathrm{d}\boldsymbol{Q}_i^* &= \left[(\nabla^*\boldsymbol{u}_\mathrm{c}^*)\boldsymbol{Q}_i^* + \frac{L_\mathrm{c}}{t_\mathrm{c}U_\mathrm{c}}(\boldsymbol{F}_{i+1}^{*\mathrm{C}} - \boldsymbol{F}_i^{*\mathrm{C}})\right]\mathrm{d}t^* \\ &\quad + \sqrt{\frac{2L_\mathrm{c}}{t_\mathrm{c}U_\mathrm{c}}}(\mathrm{d}\boldsymbol{W}_{i+1}^* - \mathrm{d}\boldsymbol{W}_i^*).\end{aligned} \tag{2.93d}$$

The factor $L_\mathrm{c}/(t_\mathrm{c}U_\mathrm{c})$ in front of the dimensionless constraint force expression in (2.93d) can be absorbed in $\boldsymbol{F}^{*\mathrm{C}}$ by defining the rescaled dimensionless tension

$$\hat{T}_i^* := \frac{L_\mathrm{c}}{t_\mathrm{c}U_\mathrm{c}}T_i^*, \tag{2.94}$$

which will be just a Lagrange multiplier in the end. The expression for the rescaled dimensionless constraint force $\hat{\boldsymbol{F}}_i^{*\mathrm{C}}$ is then

$$\hat{\boldsymbol{F}}_i^{*\mathrm{C}} := \frac{L_\mathrm{c}}{t_\mathrm{c}U_\mathrm{c}}\boldsymbol{F}_i^{*\mathrm{C}} = \begin{cases}\hat{T}_1^*\boldsymbol{Q}_1^*, & i = 1,\\ \hat{T}_i^*\boldsymbol{Q}_i^* - \hat{T}_{i-1}^*\boldsymbol{Q}_{i-1}^*, & i = 2,\ldots,N-1,\\ -\hat{T}_{N-1}^*\boldsymbol{Q}_{N-1}^*, & i = N.\end{cases} \tag{2.95}$$

Let $\mathrm{Wi}(N)$ denote the bead-dependent Weissenberg number

$$\mathrm{Wi}(N) := \frac{\lambda U_\mathrm{c}}{L_\mathrm{c}} = \frac{\alpha(N) t_\mathrm{c} U_\mathrm{c}}{L_\mathrm{c}}, \tag{2.96}$$

where the physical parameter λ denotes the longest relaxation time scale of the polymer chains. Non-dimensionalizing the longest relaxation time λ with t_c yields

$$\lambda^*(N) = \lambda / t_\mathrm{c} = \alpha(N). \tag{2.97}$$

In (2.97), the factor $\alpha(N)$ depends on the number of beads N. The factor $1/\alpha$ is defined as the stress decay rate of an initially perturbed chain towards its equilibrium state, see Figure 3.10 in Section 3.4.3. In [21], the approximation $\alpha(N) \approx 0.0142N^2$ is computed via a fit for large N. The final form of the dimensionless version of System (2.80) is then given by

$$\begin{aligned} \mathrm{d}\boldsymbol{Q}_i^* &= \left[(\nabla^* \boldsymbol{u}_\mathrm{c}^*)\boldsymbol{Q}_i^* + \boldsymbol{F}_i^*\right] \mathrm{d}t^* \\ &\qquad + \sqrt{\frac{2\alpha(N)}{\mathrm{Wi}(N)}}(\mathrm{d}\boldsymbol{W}_{i+1}^* - \mathrm{d}\boldsymbol{W}_i^*), \quad i = 1, \dots, N-1, && \text{(2.98a)} \\ \boldsymbol{Q}_i^* \cdot \boldsymbol{Q}_i^* - 1 &= 0, \quad i = 1, \dots, N-1, && \text{(2.98b)} \\ \frac{\mathrm{d}\boldsymbol{r}_\mathrm{c}^*}{\mathrm{d}t^*} &= \boldsymbol{u}_\mathrm{c}^*, && \text{(2.98c)} \end{aligned}$$

where

$$\boldsymbol{F}_i^* = \begin{cases} \hat{T}_2^* \boldsymbol{Q}_2^* - 2\hat{T}_1^* \boldsymbol{Q}_1^*, & i = 1, \\ \hat{T}_{i+1}^* \boldsymbol{Q}_{i+1}^* - 2\hat{T}_i^* \boldsymbol{Q}_i^* + \hat{T}_{i-1}^* \boldsymbol{Q}_{i-1}^*, & i = 2, \dots, N-2 \\ -2\hat{T}_{N-1}^* \boldsymbol{Q}_{N-1}^* + \hat{T}_{N-2}^* \boldsymbol{Q}_{N-2}^*, & i = N-1. \end{cases} \tag{2.99}$$

The Eulerian formulation of System (2.98) is given by

$$\begin{aligned} \mathrm{d}\boldsymbol{Q}_i^* &= \left[-\boldsymbol{u}^* \cdot \nabla^* \boldsymbol{Q}_i^* + (\nabla^* \boldsymbol{u}^*)\boldsymbol{Q}_i^* + \boldsymbol{F}_i^*\right] \mathrm{d}t^* \\ &\qquad + \sqrt{\frac{2\alpha(N)}{\mathrm{Wi}(N)}}(\mathrm{d}\boldsymbol{W}_{i+1}^* - \mathrm{d}\boldsymbol{W}_i^*), \quad i = 1, \dots, N-1, && \text{(2.100a)} \\ \boldsymbol{Q}_i^* \cdot \boldsymbol{Q}_i^* - 1 &= 0, \quad i = 1, \dots, N-1. && \text{(2.100b)} \end{aligned}$$

In System (2.100), quantities $\boldsymbol{Q}_i$, $\boldsymbol{F}_i^*$, and $\boldsymbol{W}_i^*$ are now vector fields and the Wiener process $\boldsymbol{W}_i^*$ is constant in space and only allowed to vary in time.

The polymeric stress tensor $\boldsymbol{\tau}_\mathrm{p}$ is non-dimensionalized by $\boldsymbol{\tau}_\mathrm{p}^* = \boldsymbol{\tau}_\mathrm{p} / \tau_\mathrm{c}^\mathrm{p}$ and the hydrodynamic drag force $\boldsymbol{F}_\nu^\mathrm{H}$ by $\boldsymbol{F}_\nu^{\mathrm{H}*} = \boldsymbol{F}_\nu^\mathrm{H} / F_\mathrm{c}$ with $\tau_\mathrm{c}^\mathrm{p} = U_\mathrm{c}(\eta_\mathrm{p} + \eta_\mathrm{s}) / L_\mathrm{c}$ and $F_\mathrm{c} = k_\mathrm{B}\vartheta / a$. This leads to

$$\boldsymbol{\tau}_\mathrm{p}^* = \frac{n}{\tau_\mathrm{c}^\mathrm{p}} \sum_{\nu=1}^{N} \langle \boldsymbol{R}_\nu \otimes \boldsymbol{F}_\nu^\mathrm{H} \rangle - \frac{n k_\mathrm{B} \vartheta}{\tau_\mathrm{c}^\mathrm{p}} \boldsymbol{I} = \frac{n k_\mathrm{B} \vartheta L_\mathrm{c}}{U_\mathrm{c}(\eta_\mathrm{p} + \eta_\mathrm{s})} \left(\sum_{\nu=1}^{N} \langle \boldsymbol{R}_\nu^* \otimes \boldsymbol{F}_\nu^{\mathrm{H}*} \rangle - \boldsymbol{I} \right). \tag{2.101}$$

The factor in front of the braces in (2.101) together with (2.96) can be further transformed to

$$\frac{nk_\mathrm{B}\vartheta L_\mathrm{c}}{U_\mathrm{c}(\eta_\mathrm{p}+\eta_\mathrm{s})}=\frac{nk_\mathrm{B}\vartheta\lambda}{(\eta_\mathrm{p}+\eta_\mathrm{s})\mathrm{Wi}(N)}. \tag{2.102}$$

In Table 2.5-1 in [11], the polymeric viscosity is given by

$$\eta_\mathrm{p}(N)=\frac{1}{36}(N^2-1)n\xi a^2=\beta(N)n\xi a^2 \tag{2.103}$$

with $\beta=\frac{1}{36}(N^2-1)$. Together with $\lambda=\alpha(N)\frac{\xi a^2}{k_\mathrm{B}\vartheta}$ one obtains

$$\frac{nk_\mathrm{B}\vartheta\lambda}{(\eta_\mathrm{p}(N)+\eta_\mathrm{s})\mathrm{Wi}(N)}=\frac{\alpha(N)\eta_\mathrm{p}(N)}{\beta(N)(\eta_\mathrm{s}+\eta_\mathrm{p}(N))\mathrm{Wi}(N)}=\frac{\alpha(N)\epsilon(N)}{\beta(N)\mathrm{Wi}(N)} \tag{2.104}$$

and therefore

$$\boldsymbol{\tau}_\mathrm{p}^*=\frac{\alpha(N)\epsilon(N)}{\beta(N)\mathrm{Wi}(N)}\left(\sum_{\nu=1}^{N}\langle\boldsymbol{R}_\nu^*\otimes\boldsymbol{F}_\nu^{\mathrm{H}*}\rangle-\boldsymbol{I}\right). \tag{2.105}$$

3 Discretization

In the following sections, we present the various discretization schemes that are used in the simulations of the models from Section 2. At first, we discuss the Brownian configuration field method in Section 3.1. In Section 3.2, the finite element scheme for the Navier–Stokes equations is stated. Afterwards, our discretization of the bead-spring dumbbell model (cf. Section 2.1) is presented in Section 3.3. Section 3.4 discusses the bead-rod chain discretization.

3.1 Brownian configuration field method

There are in principle two approaches for the evaluation of the polymeric stress tensor $\boldsymbol{\tau}_\mathrm{p}$ as visualized in Figure 2.2 for kinetic theory models. The SDE or Fokker–Planck approach. We neglect the constitutive approach here, since there is not always an equivalent constitutive equation for polymeric fluid models that are derived with kinetic theory. If the SDE path is pursued, a finite number $N_f > 0$ of trajectories are simulated and an ensemble average is performed to approximate the expectation value in (2.51) or (2.85). The approximation of an expectation value with a finite number of realizations introduces a stochastic error, which scales with $N_f^{-1/2}$ (central limit theorem). In the case of bead-spring dumbbells, the approximation of the polymeric stress tensor (2.51) with N_f trajectories would be

$$\boldsymbol{\tau}_\mathrm{p} \approx \frac{n}{N_f} \sum_{k=1}^{N_f} \left(\boldsymbol{Q}^k \otimes \boldsymbol{F}^\mathrm{S}(\boldsymbol{Q}^k) \right) - n k_\mathrm{B} \vartheta \boldsymbol{I}, \tag{3.1}$$

where $\boldsymbol{Q}^k$, $k = 1, \dots, N_f$, denotes the sampled trajectory of SDE (2.15). Such an approach is of Monte–Carlo type and is computationally expensive but consists of many small and easily solvable problems. The computation of the individual trajectories can be easily parallelized as they are independent from each other. Alternatively, the Fokker–Planck equation associated with the SDE can be solved. This enables a deterministic evaluation of the expectation value in (2.51) or (2.85) by an integration over the polymer configuration space. For bead-spring dumbbells, this would be

$$\boldsymbol{\tau}_\mathrm{p}(\boldsymbol{r}_\mathrm{c}, t) = n \int_{\mathbb{D}} \boldsymbol{Q} \otimes \boldsymbol{F}^\mathrm{S}(\boldsymbol{Q}) \psi(\boldsymbol{Q}, \boldsymbol{r}_\mathrm{c}, t) \,\mathrm{d}\boldsymbol{Q} - n k_\mathrm{B} \vartheta \boldsymbol{I}. \tag{3.2}$$

Solving the Fokker–Planck equation for high-dimensional models, is in practice not feasible. In the case of bead-rod chains with N beads in d dimensions, the number of unknowns in the Fokker–Planck equation w.r.t. generalized coordinates would be $(d-1)(N-1) + d + 1$. In Section 5, we simulate bead-rod chains with up to 17 beads in 2D, i.e., the corresponding Fokker–Planck equation would be 19-dimensional, which cannot be solved on sufficiently fine meshes with current computational resources.

The SDE approach can be tackled from two points of view. The Lagrangian approach leads to CONNFESSIT (Calculation of Non-Newtonian Flow: Finite

Elements & Stochastic Simulation Techniques) [52], where individual particle trajectories are simulated by solving SDE (2.15) or (2.80). For bead-spring dumbbells, the trajectories are $(\boldsymbol{Q}(t), \boldsymbol{r}_c(t)) \in \mathbb{D}_{\mathrm{BS}} \times \Omega$, $t \in \mathbb{T}$. The bead-rod chain trajectories are given by $(\boldsymbol{Q}_1(t), \dots, \boldsymbol{Q}_{N-1}, \boldsymbol{r}_c(t)) \in \mathbb{D}_{\mathrm{BR}}^{N-1} \times \Omega$, $t \in \mathbb{T}$. This leads to multiple challenges. Performing an ensemble average in a point $\boldsymbol{x} \in \Omega$, requires knowledge of the particles associated to that point. This can be realized by individual particle tracking. Additionally, the particle distribution in Ω deteriorates over time, such that in certain regions of Ω, the amount of particles, which is used for the ensemble average in a point, is not high enough for a good approximations of $\boldsymbol{\tau}_{\mathrm{p}}$ (cf. Figure 3.1).

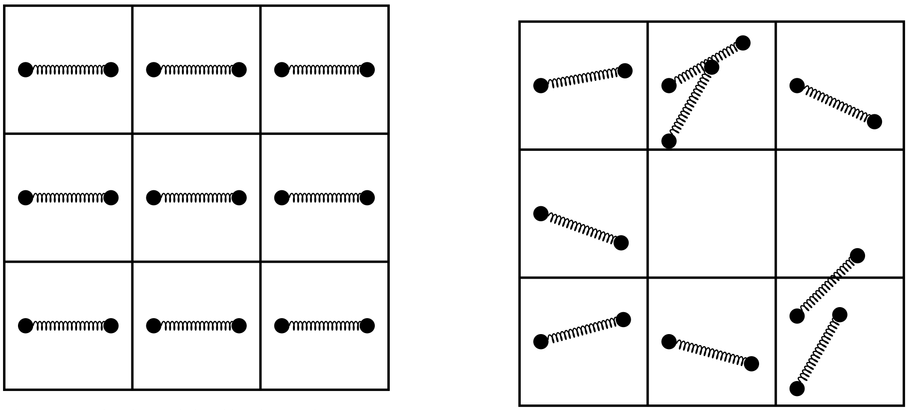

(a) Initial dumbbell distribution at t_0.

(b) Dumbbell distribution at $t_0+\Delta t$.

Figure 3.1. Visualization of particle distribution deterioration over time with CONNFESSIT approach.

The Eulerian approach leads to the Brownian configuration field (BCF) method [40], where continuous vector fields are considered that describe the polymer configuration over time in the whole domain Ω instead of single particles. This approach prevents the need of individual particle tracking and simultaneously ensures a homogeneous particle distribution as the number of configuration fields stays constant in each point (cf. Figure 3.2). These advantages come with price that now N_f realizations of stochastic PDE (2.18) or (2.81) need to be solved. Note that the Wiener processes in (2.18) or (2.81) are constant in space and vary only over time. This leads to strong spatial correlations of stress fluctuations, which results in an enormous variance reduction. The bead-spring dumbbell trajectories are now given by time dependent vector fields $\boldsymbol{Q} : \Omega \times \mathbb{T} \to \mathbb{D}_{\mathrm{BS}}$ and the bead-rod chain trajectories by $\boldsymbol{Q}_i : \Omega \times \mathbb{T} \to \mathbb{D}_{\mathrm{BR}}$, $i = 1, \dots, N-1$. In the bead-rod chain case with N beads in d dimensions, the BCF method requires the simulation of N_f realizations of a system of $N-1$ coupled $(d+1)$-dimensional PDEs, which is computationally more viable compared to the high dimensional Fokker–Planck approach. The number of realizations N_f is typically $\mathcal{O}(10^3)$.

A possible BCF generalization is presented in [73], where a method for including center of mass diffusion is described. In [76], a multi level Monte–Carlo method for BCF is presented, which can improve the total computation costs of

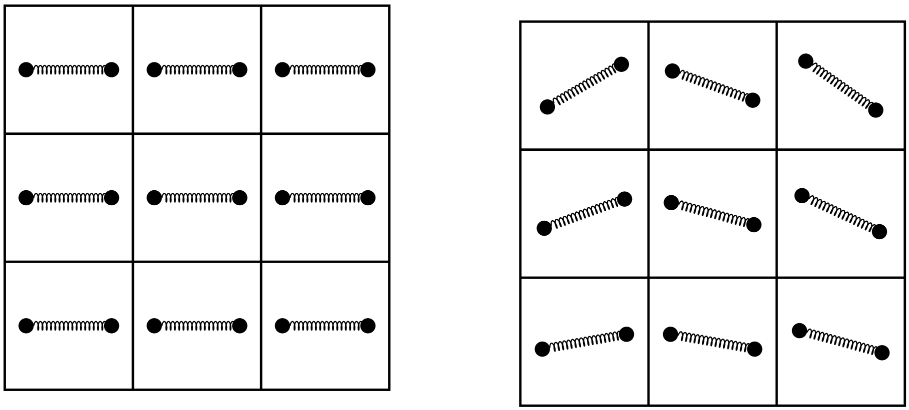

(a) Initial dumbbell distribution at t_0.

(b) Dumbbell distribution at $t_0+\Delta t$.

Figure 3.2. Visualization of particle distribution over time with BCF approach.

the standard BCF method from above.

3.2 Numerical scheme for the Navier–Stokes equations

In the following subsections, we present the temporal and spatial discretization of the non-dimensional Navier–Stokes equations

$$\partial_t \boldsymbol{u} + \boldsymbol{u} \cdot \nabla \boldsymbol{u} - 2\frac{1-\epsilon}{\mathrm{Re}} \nabla \cdot \boldsymbol{D}(\boldsymbol{u}) - \frac{1}{\mathrm{Re}} \nabla \cdot \boldsymbol{\tau}_{\mathrm{p}} + \nabla p = 0, \tag{3.3a}$$

$$- \nabla \cdot \boldsymbol{u} = 0, \tag{3.3b}$$

formulated for the symmetric flow around a cylinder scenario (cf. Figure 3.3) with homogeneous Dirichlet BC (1.36), periodic BC (1.39), symmetric BC (1.38), and constant flow rate condition (1.40) with flow rate $Q > 0$. In (3.3), $\boldsymbol{u}$ is the velocity, p the pressure, $\boldsymbol{\tau}_{\mathrm{p}}$ the polymeric stress tensor, $\boldsymbol{D}(\boldsymbol{u})$ the symmetrized gradient of $\boldsymbol{u}$, ϵ the polymeric viscosity ratio, and Re denotes the Reynolds number. Note that the * in (3.3) was dropped for ease of notation. For the weak formulation of System (3.3), we define the following spaces

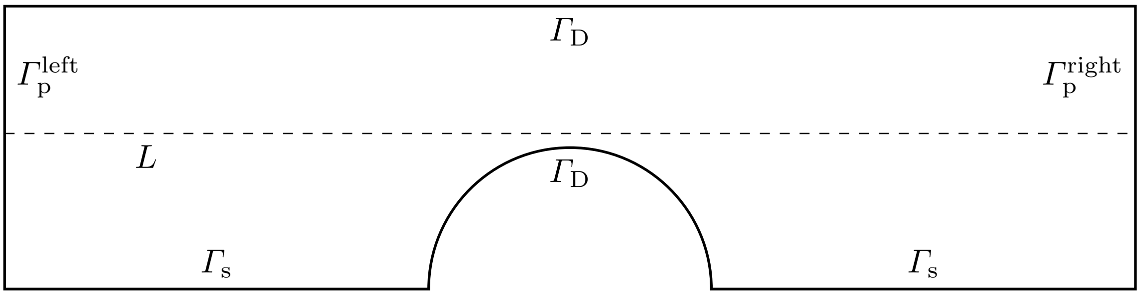

Figure 3.3. Flow around a cylinder domain with boundary condition information.

$$U := \{\boldsymbol{v} \in H^1(\Omega)^2 \mid \boldsymbol{v} \text{ satisfying } (1.36), (1.38a), (1.39a)\}, \tag{3.4a}$$

$$P := L_0^2(\Omega), \tag{3.4b}$$

$$\Sigma := L^2(\Omega)^{2\times 2}. \tag{3.4c}$$

In order to include the constant flow rate condition (1.40) into the weak formulation of System (3.3), we test (3.3b) with $q = q_p - \bar{q}x$, $q_p \in P$, $\bar{q} \in \mathbb{R}$, which leads to the two equations

$$-\int_\Omega q_p \boldsymbol{\nabla} \cdot \boldsymbol{u} = 0 \quad \forall q_p \in P, \tag{3.5a}$$

$$\bar{q}\int_\Omega x \boldsymbol{\nabla} \cdot \boldsymbol{u} = 0 \quad \forall \bar{q} \in \mathbb{R}. \tag{3.5b}$$

Applying partial integration on (3.5b), yields

$$\Leftrightarrow \quad \bar{q}\left(-\int_\Omega \boldsymbol{\nabla} x \cdot \boldsymbol{u} + \int_{\partial\Omega} x\boldsymbol{u}\cdot\boldsymbol{n}\right) = 0, \tag{3.6a}$$

$$\Leftrightarrow \quad \bar{q}\left(-\int_\Omega \boldsymbol{e}_1 \cdot \boldsymbol{u} + L\int_{\Gamma_{\mathrm{P}}^{\mathrm{right}}} \boldsymbol{u}\cdot\boldsymbol{n}\right) = 0, \tag{3.6b}$$

$$\Leftrightarrow \quad \bar{q}\int_\Omega \boldsymbol{e}_1 \cdot \boldsymbol{u} = LQ\bar{q}, \tag{3.6c}$$

where L denotes the length of the domain in flow direction and Q the prescribed flow rate over the boundary $\Gamma_{\mathrm{P}}^{\mathrm{right}}$ (cf. Figure 3.3). In the following, we abbreviate quantities $\xi(t_n)$ with ξ^n, where $t_n := T_0 + n\Delta t$ is the time after n steps with step size Δt. With the knowledge of (3.5a) and (3.6c), our weak formulation of the time-discretized version of (3.3) with constant flow rate condition (1.40) is given by:

For given $Q \in \mathbb{R}$, $\boldsymbol{u}^n \in U$, and $\boldsymbol{\tau}_{\mathrm{p}}^n \in \Sigma$, find $\boldsymbol{u}^{n+1} \in U$, $p_p^{n+1} \in P$, and $\bar{p}^{n+1} \in \mathbb{R}$ such that

$$\begin{aligned}\frac{1}{\Delta t}\left(\boldsymbol{u}^{n+1}, \boldsymbol{v}\right) + 2\frac{1-\epsilon}{\mathrm{Re}}\left(\boldsymbol{D}(\boldsymbol{u}^{n+1}), \boldsymbol{D}(\boldsymbol{v})\right) - \left(p_p^{n+1}, \boldsymbol{\nabla}\cdot\boldsymbol{v}\right) - \bar{p}^{n+1}\left(\boldsymbol{e}_1, \boldsymbol{v}\right) \\ = \frac{1}{\Delta t}\left(\boldsymbol{u}^n, \boldsymbol{v}\right) - \left(\boldsymbol{u}^n \cdot \boldsymbol{\nabla}\boldsymbol{u}^n, \boldsymbol{v}\right) - \frac{1}{\mathrm{Re}}\left(\boldsymbol{\tau}_{\mathrm{p}}^n, \boldsymbol{\nabla}\boldsymbol{v}\right) \quad \forall \boldsymbol{v} \in U,\end{aligned} \tag{3.7a}$$

$$-\left(\boldsymbol{\nabla}\cdot\boldsymbol{u}^{n+1}, q_p\right) = 0 \quad \forall q_p \in P, \tag{3.7b}$$

$$-\left(\boldsymbol{e}_1, \boldsymbol{u}^{n+1}\right)\bar{q} = -QL\bar{q} \quad \forall \bar{q} \in \mathbb{R}. \tag{3.7c}$$

In System (3.7), $(\cdot,\cdot)$ denotes the L^2-inner product w.r.t. scalars, vectors, or matrices, i.e.,

$$(v, w) := \int_\Omega vw, \quad v, w \in L^2(\Omega), \tag{3.8a}$$

$$(\boldsymbol{v}, \boldsymbol{w}) := \int_\Omega \sum_{i=1}^d v_i w_i, \quad \boldsymbol{v}, \boldsymbol{w} \in L^2(\Omega)^d, \tag{3.8b}$$

$$(\boldsymbol{V}, \boldsymbol{W}) := \int_\Omega \sum_{i=1}^{d} \sum_{j=1}^{d} V_{ij} W_{ij}, \quad \boldsymbol{V}, \boldsymbol{W} \in L^2(\Omega)^{d \times d}. \tag{3.8c}$$

For the discretization in time, all terms are treated implicitly (implicit Euler) with the two exceptions $\boldsymbol{u} \cdot \nabla \boldsymbol{u}$ (only small Re are considered) and $\boldsymbol{\tau}_\mathrm{p}$, which are treated explicitly. An equivalent formulation of (3.7) without $\boldsymbol{\tau}_\mathrm{p}$ and full homogeneous Dirichlet BC is analyzed in [77, Ch. 5.3], where (3.7b) is included into the velocity space U. The weak formulation (3.7) is the basis for the spatial discretization with finite elements. An alternative approach is the finite volume method, which is presented in the overview paper [1] for viscoelastic fluids.

3.2.1 DEVSS stabilization

Concerning the spatial discretization of System (3.7) with finite elements, it is a priori not clear how to choose compatible inf-sup stable elements for the finite dimensional ansatz spaces $U_h \subset U$, $P_h \subset P$, and $\Sigma_h \subset \Sigma$. The DEVSS (discrete elastic viscous stress split) stabilization is an established stabilization technique for FEM discretizations of viscoelastic fluid models [33]. It enables a flexible finite element choice for velocity $\boldsymbol{u}$, pressure p, polymeric stress $\boldsymbol{\tau}_\mathrm{p}$, and additionally introduces more robustness w.r.t. the polymeric viscosity ratio ϵ. For polymeric viscosity ratios ϵ near 1, equation (3.3a) gets convection dominated due to the vanishing elliptic term

$$2\frac{1-\epsilon}{\mathrm{Re}} \nabla \cdot \boldsymbol{D}(\boldsymbol{u}). \tag{3.9}$$

In the case of stationary Stokes, i.e., dropping the term $\partial_t \boldsymbol{u} + \boldsymbol{u} \cdot \nabla \boldsymbol{u}$ in (3.3a), coupled with the upper convected Maxwell model (1.29), the following compatibility conditions between U_h, P_h, and Σ_h for well-posedness are stated in [4] for Lagrangian elements. If $\eta_\mathrm{s} = 0$, i.e., $\epsilon = 1$:

(i) U_h and P_h need to satisfy the inf-sup condition

$$\inf_{q_h \in P_h} \sup_{\boldsymbol{u}_h \in U_h} \frac{\int q_h \nabla \cdot \boldsymbol{u}_h}{\|q_h\|_{P_h} \|\boldsymbol{u}_h\|_{U_h}} \geq \gamma \tag{3.10}$$

uniformly in h for a $\gamma > 0$,

(ii) if $\Sigma_h \not\subset C^0(\bar{\Omega})$, $\boldsymbol{D}(\boldsymbol{u}_h) \in \Sigma_h$ for $\boldsymbol{u}_h \in U_h$,

(iii) if $\Sigma_h \subset C^0(\bar{\Omega})$, the number of internal nodes for an Σ_h-element must be larger than the number of nodes on the boundary of an U_h-element (cf. Figure 3.4).

If $\eta_\mathrm{s} > 0$, i.e., $0 < \epsilon < 1$, the third condition from above is not required. Especially the third condition is very restrictive in the case $\eta_\mathrm{s} = 0$. In [57], the following choice is suggested:

$$U_h := \left\{ \boldsymbol{u}_h \in C(\bar{\Omega})^2 \mid \forall K \in \mathcal{T}_h, \boldsymbol{u}_{h|K} \in \mathbb{Q}_2^2(K) \right\} \cap U \subset U, \tag{3.11a}$$

$$\Sigma_h := \left\{ \boldsymbol{d}_h \in C(\bar{\Omega})^{2 \times 2} \mid \forall K \in \mathcal{T}_h, \boldsymbol{d}_{h|K} \in (\mathbb{Q}_1^m(K))^{2 \times 2} \right\} \subset \Sigma, \tag{3.11b}$$

$$P_h := \left\{p_h \in C(\bar{\Omega}) \mid \forall K \in \mathcal{T}_h, p_{h|K} \in \mathbb{Q}_1(K)\right\} \cap L^2_0(\Omega) \subset P, \tag{3.11c}$$

where $\mathcal{T}_h$ is a regular family of non-overlapping partitions of Ω into quadrilaterals $K \in \mathcal{T}_h$ with characteristic size h. The polynomial space $\mathbb{Q}_k$ is then given by

$$\mathbb{Q}_k(K) := \left\{ p : K \to \mathbb{R},\ p(\boldsymbol{x}) = \sum_{0 \le i_1,\dots,i_d \le k} \alpha_{i_1,\dots,i_d} x_1^{i_1} \cdots x_d^{i_d}, \quad \alpha_{i_1,\dots,i_d} \in \mathbb{R} \right\}. \tag{3.12}$$

This choice satisfies the conditions from above in the case $\epsilon = 1$. Figure 3.4 visualizes the reference elements of the polynomial spaces, which are used in (3.11). For the definition of $\mathbb{Q}_1^m(\hat{K})$ on the reference square $\hat{K} := [0,1]^2$, one subdivides $\hat{K}$ into 16 equal squares $\hat{K}_i$, $i = 1, \dots, 16$, as visualized in Figure 3.4c. The space $\mathbb{Q}_1^m(\hat{K})$ is then given by

$$\mathbb{Q}_1^m(\hat{K}) := \left\{ p \in C(\hat{K}) \,|\, p_{|\hat{K}_i} \in \mathbb{Q}_1(\hat{K}_i),\ i = 1, \dots, 16 \right\}. \tag{3.13}$$

Note that the reference element in Figure 3.4c satisfies the third condition from above, i.e., the number of internal nodes, here 9, is larger than the number of nodes on the boundary of Figure 3.4b. The idea of DEVSS [28], is to retain the elliptic operator $\left(\boldsymbol{D}(\boldsymbol{u}^{n+1}), \boldsymbol{D}(\boldsymbol{v})\right)$ in (3.7a) in the case of $\epsilon = 1$ and to enable a more flexible and cheaper choice of finite elements compared to the suggestion from above in (3.11). This is done by introducing a new unknown tensor $\boldsymbol{d}_h \in \Sigma_h$ together with the equation

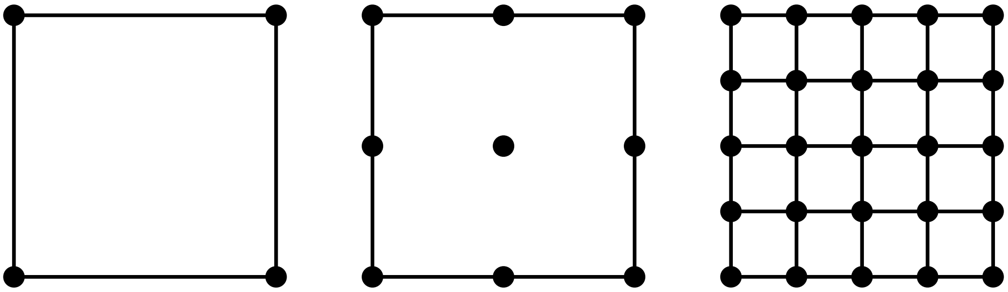

(a) $\mathbb{Q}_1$-reference element for pressure $p_h \in P_h$.

(b) $\mathbb{Q}_2$-reference element for velocity $\boldsymbol{u}_h \in U_h$.

(c) $\mathbb{Q}_1^m$-reference element for stress $\boldsymbol{\tau}_{\mathrm{p},h} \in \Sigma_h$.

Figure 3.4. Visualization of the degrees of freedom for the reference elements from the spaces (3.11), which are used in [57].

$$\left(\boldsymbol{d}_h - \boldsymbol{D}(\boldsymbol{u}_h^{n+1}), \boldsymbol{f}_h\right) = 0 \quad \forall \boldsymbol{f}_h \in \Sigma_h. \tag{3.14}$$

Additionally, the stabilizing term

$$2\frac{\epsilon}{\mathrm{Re}} \left(\boldsymbol{D}(\boldsymbol{u}_h^{n+1}) - \boldsymbol{d}_h, \boldsymbol{D}(\boldsymbol{v}_h)\right) \tag{3.15}$$

is added to the discrete momentum equation of (3.7a), where the finite dimensional ansatz spaces $\Sigma_h \subset \Sigma$ and $U_h \subset U$ have to be chosen such that $\boldsymbol{D}(\boldsymbol{u}_h) \notin \Sigma_h$

for $\boldsymbol{u}_h \in U_h$, otherwise (3.14) can be trivially satisfied by choosing $\boldsymbol{d}_h = \boldsymbol{D}(\boldsymbol{u}_h^{n+1})$ and the stabilizing term (3.15) would be zero. Note that the spaces U_h and P_h should satisfy the inf-sup condition (3.10). The unknown $\boldsymbol{d}_h$ can be interpreted as the L^2-projection of $\boldsymbol{D}(\boldsymbol{u}_h^{n+1})$ with $\boldsymbol{u}_h^{n+1} \in U_h$ into the space Σ_h. Adding (3.15) to the discrete momentum equation of (3.7a) together with (3.14), leads to the following weak formulation:

For given $Q \in \mathbb{R}$, $\boldsymbol{u}_h^n \in U_h$, and $\boldsymbol{\tau}_{\mathrm{p},h}^n \in \Sigma_h$ find $\boldsymbol{u}_h^{n+1} \in U_h$, $\boldsymbol{d}_h^{n+1} \in \Sigma_h$, $\bar{p}_h^{n+1} \in \mathbb{R}$, and $p_{p,h}^{n+1} \in P_h$ such that

$$\begin{aligned}\frac{1}{\Delta t}\left(\boldsymbol{u}_h^{n+1}, \boldsymbol{v}_h\right) + \frac{2}{\mathrm{Re}}\left(\boldsymbol{D}(\boldsymbol{u}_h^{n+1}), \boldsymbol{D}(\boldsymbol{v}_h)\right) - \left(\boldsymbol{d}_h^{n+1}, \boldsymbol{D}(\boldsymbol{v}_h)\right)&\\ - \left(p_{p,h}^{n+1}, \nabla \cdot \boldsymbol{v}_h\right) - \bar{p}_h^{n+1}\left(\boldsymbol{e}_1, \boldsymbol{v}_h\right) = \frac{1}{\Delta t}\left(\boldsymbol{u}_h^n, \boldsymbol{v}_h\right)&\\ - \left(\boldsymbol{u}_h^n \cdot \nabla \boldsymbol{u}_h^n, \boldsymbol{v}_h\right) - \frac{1}{\mathrm{Re}}\left(\boldsymbol{\tau}_{\mathrm{p},h}^n, \nabla \boldsymbol{v}_h\right) \quad \forall \boldsymbol{v}_h \in U_h,&\end{aligned} \tag{3.16a}$$

$$-\left(\nabla \cdot \boldsymbol{u}_h^{n+1}, q_h\right) = 0 \quad \forall q_h \in P_h, \tag{3.16b}$$

$$-\left(\boldsymbol{D}(\boldsymbol{u}_h^{n+1}), \boldsymbol{f}_h\right) + \frac{\mathrm{Re}}{2\epsilon}\left(\boldsymbol{d}_h^{n+1}, \boldsymbol{f}_h\right) = 0 \quad \forall \boldsymbol{f}_h \in \Sigma_h, \tag{3.16c}$$

$$-\left(\boldsymbol{e}_1, \boldsymbol{u}_h^{n+1}\right)\bar{q}_h = -QL\bar{q}_h \quad \forall \bar{q}_h \in \mathbb{R}. \tag{3.16d}$$

In (3.16a), the ϵ in front of the elliptic term $(\boldsymbol{D}(\boldsymbol{u}_h^{n+1}), \boldsymbol{D}(\boldsymbol{v}_h))$ was eliminated at the cost of an additional unknown $\boldsymbol{d}_h^{n+1} \in \Sigma_h$ and equation (3.16c), which results in a larger linear system of equations.

In this thesis, we choose

$$U_h := \left\{\boldsymbol{u}_h \in C(\bar{\Omega})^2 \mid \forall K \in \mathcal{T}_h, \boldsymbol{u}_{h|K} \in \mathbb{Q}_2^2(K)\right\} \cap U \subset U, \tag{3.17a}$$

$$\Sigma_h := \left\{\boldsymbol{d}_h \in C(\bar{\Omega})^{2\times 2} \mid \forall K \in \mathcal{T}_h, \boldsymbol{d}_{h|K} \in \mathbb{Q}_1^{2\times 2}(K)\right\} \subset \Sigma, \tag{3.17b}$$

$$P_h := \left\{p_h \in C(\bar{\Omega}) \mid \forall K \in \mathcal{T}_h, p_{h|K} \in \mathbb{Q}_1(K)\right\} \cap L_0^2(\Omega) \subset P, \tag{3.17c}$$

for quadrilaterals or analogously defined with $\mathbb{P}_2^2/\mathbb{P}_1^{2\times 2}/\mathbb{P}_1$ for triangles, where $\mathbb{P}_k$ is given by

$$\mathbb{P}_k(K) := \left\{p : K \to \mathbb{R},\ p(\boldsymbol{x}) = \sum_{\substack{0 \le i_1,\ldots,i_d \le k\\ i_1+\ldots+i_d \le k}} \alpha_{i_1,\ldots,i_d} x_1^{i_1} \cdots x_d^{i_d}, \quad \alpha_{i_1,\ldots,i_d} \in \mathbb{R}\right\}. \tag{3.18}$$

The choice of spaces (3.17) is motivated by [28], where well-posedness for a DEVSS stabilized stationary Stokes problem is proven, which is coupled with a generic linear viscoelastic model. Note that in the case $\epsilon = 1$ with DEVSS stabilization, the finite dimensional ansatz spaces (3.17) are more economical compared to the expensive choice from (3.11) w.r.t. the number of degrees of freedom.

Theorem 3.1 (Unique existence of solutions). *With the spaces* (3.17)*, there exist unique solutions* $\boldsymbol{u}_h^{n+1} \in U_h$*,* $\boldsymbol{d}_h^{n+1} \in \Sigma_h$*,* $\bar{p}_h^{n+1} \in \mathbb{R}$*, and* $p_{p,h}^{n+1} \in P_h$ *such that* (3.16) *is satisfied for given* $Q \in \mathbb{R}$*,* $\boldsymbol{u}_h^n \in U_h$*, and* $\boldsymbol{\tau}_{\mathrm{p},h}^n \in \Sigma_h$*.*

Proof. System (3.16) can be viewed as a modified Stokes problem with additional DEVSS stabilization. This can be revealed by collecting all the explicit terms on the right hand side of (3.16a). The proof for well-posedness of System (3.16) is the same as in [28]. Instead of rewriting the whole proof of [28], we just state the modified spaces and bilinear forms, which need to be used for the proof. The infinite and finite dimensional spaces are given by

$$X = X_i := \Sigma \times U, \quad i = 1,2, \tag{3.19a}$$

$$X_h = X_{i,h} := \Sigma_h \times U_h, \quad i = 1,2, \tag{3.19b}$$

$$M = M_i := \Sigma \times P \times \mathbb{R}, \quad i = 1,2, \tag{3.19c}$$

$$M_h = M_{i,h} := \Sigma_h \times P_h \times \mathbb{R}, \quad i = 1,2, \tag{3.19d}$$

and the modified bilinear forms $a : X \times X \to \mathbb{R}$, $b_i : X \times M \to \mathbb{R}$, $i = 1,2$, are defined by

$$a((\boldsymbol{\sigma},\boldsymbol{u}),(\boldsymbol{\tau},\boldsymbol{v})) := \frac{1}{\Delta t}(\boldsymbol{u},\boldsymbol{v}) + \left(\boldsymbol{\sigma} + \frac{2}{\mathrm{Re}}\boldsymbol{D}(\boldsymbol{u}),\boldsymbol{D}(\boldsymbol{v})\right) - (\boldsymbol{D}(\boldsymbol{u}),\boldsymbol{\tau}), \tag{3.20}$$

$$b_1((\boldsymbol{\tau},\boldsymbol{v}),(\boldsymbol{e},q,\bar{q})) := \left(\boldsymbol{\tau} - \frac{2\epsilon}{\mathrm{Re}}\boldsymbol{D}(\boldsymbol{v}),\boldsymbol{e}\right) - (q\boldsymbol{I},\boldsymbol{D}(\boldsymbol{v})) - \bar{q}\,(\boldsymbol{e}_1,\boldsymbol{v}), \tag{3.21}$$

$$b_2((\boldsymbol{\tau},\boldsymbol{v}),(\boldsymbol{e},q,\bar{q})) := (\boldsymbol{\tau},\boldsymbol{e}) - (q\boldsymbol{I},\boldsymbol{D}(\boldsymbol{v})) - \bar{q}\,(\boldsymbol{e}_1,\boldsymbol{v}). \tag{3.22}$$

Together with the results from Section 1.7, the proof of [28] yields the well-posedness of System (3.16). □

Note that System (3.16) without the constant flowrate condition, i.e, dropping the term with $\bar{p}_h^{n+1}$ in (3.16a) and discarding (3.16d), is also well-posed. This fact is exploited in the next section to solve (3.16) more effectively. Problem (3.16) without the constant flowrate condition is given by:

For given $\boldsymbol{u}_h^n \in U_h$, $\boldsymbol{\tau}_{\mathrm{p},h}^n \in \Sigma_h$ find $\boldsymbol{u}_h^{n+1} \in U_h$, $\boldsymbol{d}_h^{n+1} \in \Sigma_h$, and $p_{p,h}^{n+1} \in P_h$ such that

$$\begin{aligned}\frac{1}{\Delta t}\left(\boldsymbol{u}_h^{n+1},\boldsymbol{v}_h\right) + \frac{2}{\mathrm{Re}}\left(\boldsymbol{D}(\boldsymbol{u}_h^{n+1}),\boldsymbol{D}(\boldsymbol{v}_h)\right) - \left(\boldsymbol{d}_h^{n+1},\boldsymbol{D}(\boldsymbol{v}_h)\right) - \left(p_{p,h}^{n+1},\nabla\cdot\boldsymbol{v}_h\right)\\ = \frac{1}{\Delta t}\left(\boldsymbol{u}_h^n,\boldsymbol{v}_h\right) - \left(\boldsymbol{u}_h^n\cdot\nabla\boldsymbol{u}_h^n,\boldsymbol{v}_h\right) - \frac{1}{\mathrm{Re}}\left(\boldsymbol{\tau}_{\mathrm{p},h}^n,\nabla\boldsymbol{v}_h\right) \quad \forall\boldsymbol{v}_h \in U_h,\end{aligned} \tag{3.23a}$$

$$-\left(\nabla\cdot\boldsymbol{u}_h^{n+1},q_h\right) = 0 \quad \forall q_h \in P_h, \tag{3.23b}$$

$$-\left(\boldsymbol{D}(\boldsymbol{u}_h^{n+1}),\boldsymbol{f}_h\right) + \frac{\mathrm{Re}}{2\epsilon}\left(\boldsymbol{d}_h^{n+1},\boldsymbol{f}_h\right) = 0 \quad \forall\boldsymbol{f}_h \in \Sigma_h. \tag{3.23c}$$

Theorem 3.2 (Unique existence of solutions). *With the spaces* (3.17)*, there exist unique solutions* $\boldsymbol{u}_h^{n+1} \in U_h$*,* $\boldsymbol{d}_h^{n+1} \in \Sigma_h$*, and* $p_{p,h}^{n+1} \in P_h$ *such that* (3.23) *is satisfied for given* $\boldsymbol{u}_h^n \in U_h$ *and* $\boldsymbol{\tau}_{\mathrm{p},h}^n \in \Sigma_h$*.*

Proof. The idea of the proof is the same as in Theorem 3.1, i.e., use the proof of [28] with the following spaces and bilinear forms. The infinite and finite dimensional spaces are given by

$$X = X_i \coloneqq \Sigma \times U, \quad i = 1,2, \tag{3.24a}$$

$$X_h = X_{i,h} \coloneqq \Sigma_h \times U_h, \quad i = 1,2, \tag{3.24b}$$

$$M = M_i \coloneqq \Sigma \times P, \quad i = 1,2, \tag{3.24c}$$

$$M_h = M_{i,h} \coloneqq \Sigma_h \times P_h, \quad i = 1,2, \tag{3.24d}$$

and the modified bilinear forms $a : X \times X \to \mathbb{R}$, $b_i : X \times M \to \mathbb{R}$, $i = 1,2$, are defined by

$$a((\boldsymbol{\sigma},\boldsymbol{u}),(\boldsymbol{\tau},\boldsymbol{v})) \coloneqq \frac{1}{\Delta t}(\boldsymbol{u},\boldsymbol{v}) + \left(\boldsymbol{\sigma} + \frac{2}{\mathrm{Re}}\boldsymbol{D}(\boldsymbol{u}),\boldsymbol{D}(\boldsymbol{v})\right) - (\boldsymbol{D}(\boldsymbol{u}),\boldsymbol{\tau}), \tag{3.25}$$

$$b_1((\boldsymbol{\tau},\boldsymbol{v}),(\boldsymbol{e},q)) \coloneqq \left(\boldsymbol{\tau} - \frac{2\epsilon}{\mathrm{Re}}\boldsymbol{D}(\boldsymbol{v}),\boldsymbol{e}\right) - (q\boldsymbol{I},\boldsymbol{D}(\boldsymbol{v})), \tag{3.26}$$

$$b_2((\boldsymbol{\tau},\boldsymbol{v}),(\boldsymbol{e},q)) \coloneqq (\boldsymbol{\tau},\boldsymbol{e}) - (q\boldsymbol{I},\boldsymbol{D}(\boldsymbol{v})). \tag{3.27}$$

□

3.2.2 Linear system of equations

In order to solve (3.16) numerically, one transforms the weak formulation into an equivalent linear system of equations

$$\mathcal{A}\boldsymbol{x} = \boldsymbol{b}, \tag{3.28}$$

where the entries of matrix $\mathcal{A}$ and vectors $\boldsymbol{x}, \boldsymbol{b}$ are specified in the following.

At first, we represent $(\boldsymbol{u}_h^{n+1}, p_h^{n+1}, \boldsymbol{d}_h^{n+1}, \bar{p}_h^{n+1}) \in U_h \times P_h \times \Sigma_h \times \mathbb{R}$ with degree-of-freedom vectors $\boldsymbol{x}^{u,n+1} \in \mathbb{R}^{n_u}$, $\boldsymbol{x}^{p,n+1} \in \mathbb{R}^{n_p}$, $\boldsymbol{x}^{d,n+1} \in \mathbb{R}^{n_\Sigma}$, and $x^{\bar{p},n+1} \in \mathbb{R}$, where $n_u, n_p, n_\Sigma \in \mathbb{N}$ are the dimensions of the spaces U_h, P_h, Σ_h, respectively. The representations are then given by

$$\boldsymbol{u}_h^{n+1} = \sum_{i=1}^{n_u} x_i^{u,n+1}\boldsymbol{\phi}_i^{U_h}, \quad p_h^{n+1} = \sum_{i=1}^{n_p} x_i^{p,n+1}\phi_i^{P_h}, \quad \boldsymbol{d}_h^{n+1} = \sum_{i=1}^{n_\Sigma} x_i^{d,n+1}\boldsymbol{\phi}_i^{\Sigma_h}, \tag{3.29}$$

and $\bar{p}_h^{n+1} \equiv x^{\bar{p},n+1}$, where $\boldsymbol{\phi}_i^{U_h}$, $\phi_i^{P_h}$, $\boldsymbol{\phi}_i^{\Sigma_h}$ are basis functions with the property $U_h = \operatorname{span}\{\boldsymbol{\phi}_i^{U_h}\}_{i=1}^{n_u}$, $P_h = \operatorname{span}\{\phi_i^{P_h}\}_{i=1}^{n_p}$, and $\Sigma_h = \operatorname{span}\{\boldsymbol{\phi}_i^{\Sigma_h}\}_{i=1}^{n_\Sigma}$. In this thesis, Lagrangian finite elements are used (cf. (3.17)).

The linear system (3.28) takes then the shape

$$\begin{bmatrix} \frac{1}{\Delta t}\boldsymbol{M} + \frac{2}{\mathrm{Re}}\boldsymbol{A} & \boldsymbol{B}^{\mathrm{T}} & \boldsymbol{L}^{\mathrm{T}} & \boldsymbol{G}^{\mathrm{T}} \\ \boldsymbol{B} & & & \\ \boldsymbol{L} & & \frac{\mathrm{Re}}{2\epsilon}\boldsymbol{E} & \\ \boldsymbol{G} & & & \end{bmatrix} \begin{bmatrix} \boldsymbol{x}^{u,n+1} \\ \boldsymbol{x}^{p,n+1} \\ \boldsymbol{x}^{d,n+1} \\ x^{\bar{p},n+1} \end{bmatrix} = \begin{bmatrix} \boldsymbol{f}(\boldsymbol{u}_h^n, \boldsymbol{\tau}_{\mathrm{p},h}^n) \\ \boldsymbol{0} \\ \boldsymbol{0} \\ -QL \end{bmatrix}. \tag{3.30}$$

In (3.30), entries of the matrices $\boldsymbol{M}, \boldsymbol{A} \in \mathbb{R}^{n_u \times n_u}$, $\boldsymbol{B} \in \mathbb{R}^{n_p \times n_u}$, $\boldsymbol{L} \in \mathbb{R}^{n_u \times n_\Sigma}$, $\boldsymbol{G} \in \mathbb{R}^{1 \times n_u}$ and $\boldsymbol{E} \in \mathbb{R}^{n_\Sigma \times n_\Sigma}$ are specified by

$$\boldsymbol{M}_{ij} := \int_\Omega \boldsymbol{\phi}_j^{U_h} \cdot \boldsymbol{\phi}_i^{U_h}, \qquad \boldsymbol{A}_{ij} := \int_\Omega \boldsymbol{D}(\boldsymbol{\phi}_j^{U_h}) : \boldsymbol{D}(\boldsymbol{\phi}_i^{U_h}), \tag{3.31a}$$

$$\boldsymbol{B}_{ij} := -\int_\Omega \phi_i^{P_h} \nabla \cdot \boldsymbol{\phi}_j^{U_h}, \qquad \boldsymbol{L}_{ij} := -\int_\Omega \boldsymbol{D}(\boldsymbol{\phi}_i^{U_h}) : \boldsymbol{\phi}_j^{\Sigma_h}, \tag{3.31b}$$

$$\boldsymbol{E}_{ij} := \int_\Omega \boldsymbol{\phi}_i^{\Sigma_h} : \boldsymbol{\phi}_j^{\Sigma_h}, \qquad \boldsymbol{G}_i := -\int_\Omega e_1 \cdot \boldsymbol{\phi}_i^{U_h}. \tag{3.31c}$$

In (3.30), entries of the right hand side vector $\boldsymbol{f}(\boldsymbol{u}_h^n, \boldsymbol{\tau}_{\mathrm{p},h}^n) \in \mathbb{R}^{n_u}$, which depends on $\boldsymbol{u}_h^n \in U_h$ and $\boldsymbol{\tau}_{\mathrm{p},h}^n \in \Sigma_h$, are defined by

$$f_i(\boldsymbol{u}_h^n, \boldsymbol{\tau}_{\mathrm{p},h}^n) := \frac{1}{\Delta t} \int_\Omega \boldsymbol{u}_h^n \cdot \boldsymbol{\phi}_i^{U_h} - \int_\Omega \left(\boldsymbol{u}_h^n \cdot \nabla \boldsymbol{u}_h^n\right) \boldsymbol{\phi}_i^{U_h} - \frac{1}{\mathrm{Re}} \int_\Omega \boldsymbol{\tau}_{\mathrm{p},h}^n : \nabla \boldsymbol{\phi}_i^{U_h}. \tag{3.32}$$

The constants Q and L in the right hand side of (3.30), are the prescribed constant flow rate (cf. (1.40)) and the length of the domain in flow direction (cf. Figure 3.3). From Theorem 3.1, we know that (3.30) has a unique solution.

For abbreviation of notation, let

$$\boldsymbol{K} := \frac{1}{\Delta t}\boldsymbol{M} + \frac{2}{\mathrm{Re}}\boldsymbol{A}. \tag{3.33}$$

The solution of linear system (3.30) can be obtained in three steps:

- Step 1: Solve

$$\begin{bmatrix} \boldsymbol{K} & \boldsymbol{B}^{\mathrm{T}} & \boldsymbol{L}^{\mathrm{T}} \\ \boldsymbol{B} & & \\ \boldsymbol{L} & & \frac{\mathrm{Re}}{2\epsilon}\boldsymbol{E} \end{bmatrix} \begin{bmatrix} \boldsymbol{x}^u \\ \boldsymbol{x}^p \\ \boldsymbol{x}^d \end{bmatrix} = \begin{bmatrix} \boldsymbol{f}(\boldsymbol{u}_h^n, \boldsymbol{\tau}_{\mathrm{p},h}^n) \\ 0 \\ 0 \end{bmatrix}. \tag{3.34}$$

- Step 2: Solve

$$\begin{bmatrix} \boldsymbol{K} & \boldsymbol{B}^{\mathrm{T}} & \boldsymbol{L}^{\mathrm{T}} \\ \boldsymbol{B} & & \\ \boldsymbol{L} & & \frac{\mathrm{Re}}{2\epsilon}\boldsymbol{E} \end{bmatrix} \begin{bmatrix} \hat{\boldsymbol{x}}^u \\ \hat{\boldsymbol{x}}^p \\ \hat{\boldsymbol{x}}^d \end{bmatrix} = \begin{bmatrix} -\boldsymbol{G}^{\mathrm{T}} \\ 0 \\ 0 \end{bmatrix}. \tag{3.35}$$

- Step 3: Compute

$$x^{\bar{p},n+1} := \frac{-QL - \boldsymbol{G}\boldsymbol{x}^u}{\boldsymbol{G}\hat{\boldsymbol{x}}^u}, \qquad \begin{bmatrix} \boldsymbol{x}^{u,n+1} \\ \boldsymbol{x}^{p,n+1} \\ \boldsymbol{x}^{d,n+1} \end{bmatrix} := \begin{bmatrix} \boldsymbol{x}^u \\ \boldsymbol{x}^p \\ \boldsymbol{x}^d \end{bmatrix} + x^{\bar{p},n+1} \begin{bmatrix} \hat{\boldsymbol{x}}^u \\ \hat{\boldsymbol{x}}^p \\ \hat{\boldsymbol{x}}^d \end{bmatrix}. \tag{3.36}$$

Note that the solution of linear system (3.35) has to be computed only once, as the system matrix and right hand side stays constant over time. As a result, only the solution of (3.34) has to be obtained in each time step. In order to solve (3.34) and (3.35) numerically, a suitable solver has to be chosen. The choice is based on the matrix properties of the corresponding system matrix in (3.34) and (3.35). As a next step, the matrix properties need to be examined. This is done in Theorem 3.3. In Step 3, a division by $\boldsymbol{G}\hat{\boldsymbol{x}}^u$ is performed. Theorem 3.4 proofs that $\boldsymbol{G}\hat{\boldsymbol{x}}^u$ cannot be zero.

Theorem 3.3 (Matrix properties)**.** *The block matrix*

$$\mathcal{B} := \begin{bmatrix} \boldsymbol{K} & \boldsymbol{B}^{\mathrm{T}} & \boldsymbol{L}^{\mathrm{T}} \\ \boldsymbol{B} & & \\ \boldsymbol{L} & & \frac{\mathrm{Re}}{2\epsilon}\boldsymbol{E} \end{bmatrix} \in \mathbb{R}^{(n_u+n_p+n_\Sigma)\times(n_u+n_p+n_\Sigma)} \tag{3.37}$$

with entries defined in (3.31) *is symmetric indefinite and regular.*

Proof. Due to Theorem 3.2, we know that $\mathcal{B}$ is regular as it is the equivalent finite dimensional formulation of (3.23). The symmetry follows directly from the symmetry of the diagonal blocks $\mathbf{K}$, i.e., $\mathbf{A}$ and $\mathbf{M}$, and $\mathbf{E}$. For the indefiniteness, we factorize $\mathcal{B}$ into $\mathcal{L}\mathcal{D}\mathcal{L}^{\mathrm{T}}$, where $\mathcal{L}$ is a lower triangular block matrix with identity blocks on the diagonal and $\mathcal{D}$ is a block diagonal matrix. Note that the matrix $\boldsymbol{K}$ is symmetric positive definite, i.e., the inverse $\boldsymbol{K}^{-1}$ exists. Let $\boldsymbol{x} \in \mathbb{R}^{n_p}$. Due to the positive definiteness of $\boldsymbol{K}$, we have

$$\boldsymbol{x} \cdot \left(\boldsymbol{B}\boldsymbol{K}^{-1}\boldsymbol{B}^{\mathrm{T}}\boldsymbol{x}\right) = (\boldsymbol{B}^{\mathrm{T}}\boldsymbol{x}) \cdot \left(\boldsymbol{K}^{-1}\boldsymbol{B}^{\mathrm{T}}\boldsymbol{x}\right) > 0 \tag{3.38}$$

for $\boldsymbol{x} \notin \ker(\boldsymbol{B}^{\mathrm{T}})$. Due to the inf-sup stability of U_h and P_h, only constant pressures $p_h = C \in P_h$ are in $\ker(\boldsymbol{B}^{\mathrm{T}})$. As a consequence of the zero mean condition $\int_\Omega p_h = 0$ (cf. (3.17c)), we deduce $C = 0$, i.e., $\ker(\boldsymbol{B}^{\mathrm{T}}) = \{\boldsymbol{0}\}$. Together with (3.38), we get the positive definiteness of $\boldsymbol{B}\boldsymbol{K}^{-1}\boldsymbol{B}^{\mathrm{T}}$ and thus the justification to write $\left(\boldsymbol{B}\boldsymbol{K}^{-1}\boldsymbol{B}^{\mathrm{T}}\right)^{-1}$ in the following. The $\mathcal{L}\mathcal{D}\mathcal{L}^{\mathrm{T}}$-factorization of $\mathcal{B}$ is given by

$$\mathcal{L} := \begin{bmatrix} \mathbf{1} & & \\ \boldsymbol{B}K^{-1} & \mathbf{1} & \\ \boldsymbol{L}K^{-1} & \left(\boldsymbol{L}\boldsymbol{K}\boldsymbol{B}^{\mathrm{T}}\right)\left(\boldsymbol{B}\boldsymbol{K}^{-1}\boldsymbol{B}^{\mathrm{T}}\right)^{-1} & \mathbf{1} \end{bmatrix}, \tag{3.39}$$

$$\mathcal{D} := \begin{bmatrix} \boldsymbol{K} & & \\ & -\boldsymbol{B}\boldsymbol{K}^{-1}\boldsymbol{B}^{\mathrm{T}} & \\ & & \frac{\mathrm{Re}}{2\epsilon}\boldsymbol{E} - \boldsymbol{L}\boldsymbol{K}^{-1}\boldsymbol{L}^{\mathrm{T}} + \left(\boldsymbol{L}\boldsymbol{K}^{-1}\boldsymbol{B}^{\mathrm{T}}\right)\left(\boldsymbol{B}\boldsymbol{K}^{-1}\boldsymbol{B}^{\mathrm{T}}\right)^{-1}\left(\boldsymbol{B}\boldsymbol{K}^{-1}\boldsymbol{L}^{\mathrm{T}}\right) \end{bmatrix}. \tag{3.40}$$

One property of the $\mathcal{L}\mathcal{D}\mathcal{L}^{\mathrm{T}}$-factorization of $\mathcal{B}$ is that $\mathcal{B}$ and $\mathcal{D}$ have the same number of positive, negative, and zero eigenvalues (cf. Sylvester's law of inertia in [49, Thm. 5.35]). Since $\mathcal{B}$ is regular, there are no zero eigenvalues. Due to the first diagonal block $\boldsymbol{K}$ of $\mathcal{D}$, which is symmetric positive definite, matrix $\mathcal{B}$ has at least n_u positive eigenvalues. From the symmetric negative definite second block $-\boldsymbol{B}\boldsymbol{K}^{-1}\boldsymbol{B}^{\mathrm{T}}$, matrix $\mathcal{B}$ gets n_p negative eigenvalues. As $\mathcal{B}$ has at least n_u positive, at least n_p negative, and zero 0 eigenvalues, the indefiniteness property is obtained. □

Theorem 3.4. *In (3.36), it holds* $\boldsymbol{G}\hat{\boldsymbol{x}}^u \neq 0$.

Proof. From Theorem 3.3, we know that System (3.35) has a unique solution denoted by $[\hat{\boldsymbol{x}}^u, \hat{\boldsymbol{x}}^p, \hat{\boldsymbol{x}}^d]^{\mathrm{T}}$. One can easily check that $[\hat{\boldsymbol{x}}^u, \hat{\boldsymbol{x}}^p, \hat{\boldsymbol{x}}^d, \hat{x}^{\bar{p}}]^{\mathrm{T}}$ with $\hat{x}^{\bar{p}} := 1$ is a solution of

$$\begin{bmatrix} \boldsymbol{K} & \boldsymbol{B}^{\mathrm{T}} & \boldsymbol{L}^{\mathrm{T}} & \boldsymbol{G}^{\mathrm{T}} \\ \boldsymbol{B} & & & \\ \boldsymbol{L} & & \frac{\mathrm{Re}}{2\epsilon}\boldsymbol{E} & \\ \boldsymbol{G} & & & \end{bmatrix} \begin{bmatrix} \boldsymbol{x}^u \\ \boldsymbol{x}^p \\ \boldsymbol{x}^d \\ x^{\bar{p}} \end{bmatrix} = \begin{bmatrix} \boldsymbol{0} \\ \boldsymbol{0} \\ \boldsymbol{0} \\ \boldsymbol{G}\hat{\boldsymbol{x}}^u \end{bmatrix}. \tag{3.41}$$

Since the system matrix in (3.41) is regular (cf. Theorem 3.1), one can deduce $[\hat{\boldsymbol{x}}^u, \hat{\boldsymbol{x}}^p, \hat{\boldsymbol{x}}^d, \hat{x}^{\bar{p}}]^{\mathrm{T}} = [\boldsymbol{x}^u, \boldsymbol{x}^p, \boldsymbol{x}^d, x^{\bar{p}}]^{\mathrm{T}}$ due to the uniqueness of solutions.

Assume $\boldsymbol{G}\hat{\boldsymbol{x}}^u = 0$. This leads to a vanishing right hand side in (3.41), which yields the trivial solution $[\boldsymbol{x}^u, \boldsymbol{x}^p, \boldsymbol{x}^d, x^{\bar{p}}]^{\mathrm{T}} = [\boldsymbol{0}, \boldsymbol{0}, \boldsymbol{0}, 0]^{\mathrm{T}}$. From above, we know that it must hold $x^{\bar{p}} = \hat{x}^{\bar{p}}$, which leads to the contradiction

$$0 = x^{\bar{p}} = \hat{x}^{\bar{p}} = 1, \tag{3.42}$$

i.e., the assumption $\boldsymbol{G}\hat{\boldsymbol{x}}^u = 0$ is false and it must hold $\boldsymbol{G}\hat{\boldsymbol{x}}^u \neq 0$. $\square$

3.2.3 Iterative solvers and preconditioning

In this thesis, we choose the preconditioned MINRES solver for the numerical approximation of solutions for the linear system of equations

$$\mathcal{B}\boldsymbol{x} = \boldsymbol{b}, \tag{3.43}$$

where $\mathcal{B} \in \mathbb{R}^{n \times n}$ is symmetric indefinite (cf. Theorem 3.3). The following introduction to (preconditioned) MINRES is based on Chapter 4 of [23]. MINRES is a Krylov subspace method, where the kth iterate $\boldsymbol{x}^{(k)}$ minimizes the residual

$$\boldsymbol{r}^{(k)} := \boldsymbol{b} - \mathcal{B}\boldsymbol{x}^{(k)} \tag{3.44}$$

in the Euclidean norm $\|\boldsymbol{r}^{(k)}\|_2 := \sqrt{\boldsymbol{r}^{(k)} \cdot \boldsymbol{r}^{(k)}}$ over the affine Krylov space

$$\boldsymbol{x}^{(0)} + \operatorname{span}\{\boldsymbol{r}^{(0)}, \mathcal{B}\boldsymbol{r}^{(0)}, \dots, \mathcal{B}^{k-1}\boldsymbol{r}^{(0)}\} \tag{3.45}$$

in an iterative way. The clustering of the spectrum $\sigma(\mathcal{B})$ plays a crucial role in the MINRES convergence behavior due to the estimate

$$\frac{\|\boldsymbol{r}^{(k)}\|_2}{\|\boldsymbol{r}^{(0)}\|_2} \leq \min_{q_k \in \Pi_k, q_k(0)=1} \max_{\lambda \in \sigma(\mathcal{B})} |q_k(\lambda)|, \tag{3.46}$$

where Π_k is the set of polynomials of degree less than or equal to k. From (3.46), one can deduce the theoretical finite termination property of MINRES. Let $n \in \mathbb{N}$ denote the number of rows/columns of $\mathcal{B}$. After at most n iterations, we have $\|\boldsymbol{r}^{(n)}\|_2 = 0$, i.e., the exact solution $\boldsymbol{x}^{(n)} = \boldsymbol{x}$ of (3.43), since one can find a $q_n \in \Pi_n$ in (3.46) such that $q_n(0) = 1$ and $q_n(\lambda_i) = 0$, $i = 1, \dots, n$. However, this property is of little use in practice due to the finite precision arithmetic of computers and the size of n.

The idea of preconditioning is now to use a symmetric positive definite matrix $\mathcal{P} = \mathcal{H}\mathcal{H}^{\mathrm{T}}$ and apply MINRES to

$$\mathcal{H}^{-1}\mathcal{B}\mathcal{H}^{-\mathrm{T}}\boldsymbol{y} = \mathcal{H}^{-1}\boldsymbol{b} \tag{3.47}$$

instead of (3.43). The solutions $\boldsymbol{y}, \boldsymbol{x}$ of (3.47) and (3.43) are connected via $\boldsymbol{y} = \mathcal{H}^{\mathrm{T}}\boldsymbol{x}$. The residual estimate (3.46) for preconditioned MINRES transforms to

$$\frac{\|\boldsymbol{r}^{(k)}\|_{\mathcal{P}^{-1}}}{\|\boldsymbol{r}^{(0)}\|_{\mathcal{P}^{-1}}} \leq \min_{q_k \in \Pi_k, q_k(0)=1} \max_{\lambda \in \sigma(\mathcal{P}^{-1}\mathcal{B})} |q_k(\lambda)|, \tag{3.48}$$

where $\|\boldsymbol{r}^{(k)}\|_{\mathcal{P}^{-1}} := \sqrt{\boldsymbol{r}^{(k)} \cdot \mathcal{P}^{-1}\boldsymbol{r}^{(k)}}$ and $\boldsymbol{r}^{(k)}$ is the residual from (3.44). In practice, only the actions $\boldsymbol{z} \mapsto \mathcal{B}\boldsymbol{z}$ and $\boldsymbol{z} \mapsto \mathcal{P}^{-1}\boldsymbol{z}$ are required in the preconditioned MINRES algorithm, i.e., the factorization of $\mathcal{P}$ into $\mathcal{H}\mathcal{H}^{\mathrm{T}}$ is not required and has only a theoretical background. During the iterations of preconditioned MINRES, only two scalar products and two matrix vector products are required next to minor SAXPY operations. The required memory is very limited, as only 6 additional vectors are used for the computation of the iterates $\boldsymbol{x}^{(k)}$ (cf. implementation from [59]). The preconditioning matrix $\mathcal{P}$ should be chosen such that the clustering of the spectrum $\sigma(\mathcal{P}^{-1}\mathcal{B})$ in (3.48) is better compared to $\sigma(\mathcal{B})$ and thus enabling faster convergence. An ideal $\mathcal{P}$ would cluster the spectrum $\sigma(\mathcal{P}^{-1}\mathcal{B})$ in two intervals $[-a, -b] \cup [c, d]$ with $a, b, c, d > 0$ independent on the discretization parameters Δt and h. This would lead to upper bounds on the required number of iterations it takes to reach a certain reduction of the initial residual, which are independent on $h, \Delta t$.

Here, we choose

$$\mathcal{P}^{-1} := \begin{pmatrix} \hat{\boldsymbol{K}}^{-1} & & \\ & \Delta t \hat{\boldsymbol{A}}_p^{-1} + \frac{\mathrm{Re}}{2}\hat{\boldsymbol{M}}_p^{-1} & \\ & & \frac{2\epsilon}{\mathrm{Re}}\hat{\boldsymbol{E}}^{-1} \end{pmatrix}, \tag{3.49}$$

where

$$(\boldsymbol{A}_p)_{ij} := \int_\Omega \nabla\phi_i^{P_h} \cdot \nabla\phi_j^{P_h}, \qquad (\boldsymbol{M}_p)_{ij} := \int_\Omega \phi_i^{P_h}\phi_j^{P_h}, \tag{3.50}$$

$\boldsymbol{K}$ defined in (3.33), and $\boldsymbol{E}$ in (3.31). The hat above $\boldsymbol{K}^{-1}$, $\boldsymbol{A}_p^{-1}$, $\boldsymbol{M}_p^{-1}$, and $\boldsymbol{E}^{-1}$ in (3.49) indicates that the actions on a vector, e.g. $\boldsymbol{z} \mapsto \boldsymbol{K}^{-1}\boldsymbol{z}$, are approximated with an algebraic multigrid (AMG) approach [69]. Preconditioner (3.49) is a combination of the generalized Stokes preconditioner from [74] and the DEVSS preconditioner presented in [42]. Here, we used the AMG implementation from the library Hypre [27] with the options summarized in Table 3.1. In this thesis, the number of AMG V-cycles is always one. Increasing the number of V-cycles leads to longer computation times for each MINRES iteration and a slight decrease in the total number of MINRES iterations required to reach a certain error tolerance. However, while theoretically there may be a reduction in computation time due to fewer MINRES iterations, this is partially compensated by the increased computation time per iteration required for more V-cycles. In the worst case, choosing a number of V-cycles that is too large can result in poorer performance w.r.t. total computation time. In our simulations, we found that using one V-cycle as default is a sufficiently good choice.

In the following test, the linear system of equations (3.35) is solved with the preconditioned MINRES solver from above. The flow scenario is the periodic 4:1

Option	Value
HYPRE_BoomerAMGSetCoarsenType	8 (PMIS)
HYPRE_BoomerAMGSetAggNumLevels	0
HYPRE_BoomerAMGSetRelaxType	18 (l1-Jacobi)
HYPRE_BoomerAMGSetNumSweeps	1
HYPRE_BoomerAMGSetStrongThreshold	0.25
HYPRE_BoomerAMGSetInterpType	6 (extended+i)
HYPRE_BoomerAMGSetPMaxElmts	4
HYPRE_BoomerAMGSetMaxLevels	25
HYPRE_BoomerAMGSetMaxIter	1 (V-cycle)

Table 3.1. Options used for the setup of Hypres BoomerAMG PC [27].

contraction flow from Section 5. Table 3.2 lists the required number of iterations for varying parameters. Here, we varied the number of uniform mesh refinements, polymeric viscosity ratios ϵ, and time step sizes $\varDelta t$. The initial iterate is $\boldsymbol{x}^{(0)} := \boldsymbol{0}$ and MINRES stops after the relative residual $\|\boldsymbol{r}\|_{\hat{\mathcal{P}}^{-1}}/\|\boldsymbol{b}\|_{\hat{\mathcal{P}}^{-1}}$ falls below 10^{-7}. The Reynolds number Re is kept fixed at 1. In Table 3.2, one can observe a strong dependence of the polymeric viscosity ϵ on the number of iterations. For $\epsilon = 0.9$ and $\varDelta t = 0.001$, the number of iterations more then doubles when going from the coarsest to the finest mesh. For $\epsilon = 0.1$ and $\varDelta t = 0.001$, the number of iterations stays almost constant. A similar behavior for large ϵ was observed in [42], where a stationary lid-driven cavity flow scenario was considered. Dirichlet BC for the velocity are typically applied by replacing the corresponding diagonal entries in the system matrix by 1 and the off-diagonal entries in the row/column by 0 together with a modification of the right-hand-side. The performance of AMG could be further increased by proper reordering of the unknowns such that all eliminated DOFs are moved to the end and applying AMG only on the unmodified sets of equations. This reordering was done in [42] such that they get a better behavior for varying mesh sizes h.

	$\epsilon = 0.1$		$\epsilon = 0.5$		$\epsilon = 0.9$	
DOF	$\varDelta t = 0.1$	$\varDelta t = 0.001$	$\varDelta t = 0.1$	$\varDelta t = 0.001$	$\varDelta t = 0.1$	$\varDelta t = 0.001$
19408	58	53	88	61	175	73
74528	64	49	97	65	193	92
291904	70	52	106	73	216	124
1155200	80	55	121	85	251	168

Table 3.2. Required number of iterations for preconditioned MINRES with preconditioner (3.49) to solve (3.35) for varying numbers of uniform mesh refinements, time step sizes $\varDelta t$, and polymeric viscosity ratios ϵ. Reynolds number is kept fixed at Re = 1. The stopping criterion of the solver is set to $\|\boldsymbol{r}\|_{\hat{\mathcal{P}}^{-1}}/\|\boldsymbol{b}\|_{\hat{\mathcal{P}}^{-1}} < 10^{-7}$.

3.3 Numerical scheme for bead-spring dumbbells

This section covers all aspects that are required for the discretization of bead-spring dumbbells. At first, the time-discretized weak formulations of the stochastic differential equation (2.63c) are presented. Afterwards, corresponding (non) linear systems of equations are derived together with well-suited solving approaches. At last, an algorithm is stated that generates bead-spring dumbbell configurations in equilibrium, which are required for meaningful initial conditions.

The temporal discretization uses the semi-implicit Euler-Maruyama method, where the deterministic part is treated implicitly and the stochastic part explicitly. For the discretization in space, the finite element method is utilized with additional SUPG stabilization [45], as there is no diffusion present in (2.63c). Here, we choose

$$Q_h := \left\{ \boldsymbol{q}_h \in C(\bar{\Omega})^2 \mid \forall K \in \mathcal{T}_h, \boldsymbol{q}_{h|K} \in \mathbb{Q}_1^2(K) \right\} \tag{3.51}$$

for the finite dimensional spring-dumbbell ansatz space.

Hookean dumbbells In the case of Hookean dumbbells, the weak formulation with additional SUPG stabilization is given by:

For given velocity $\boldsymbol{u}_h \in U_h$ and $\boldsymbol{Q}_h^n \in Q_h$, find $\boldsymbol{Q}_h^{n+1} \in Q_h$ such that

$$\begin{aligned} &\left(\boldsymbol{Q}_h^{n+1}, \boldsymbol{q}_h^{\mathrm{SUPG}}\right) + \frac{\Delta t}{2\mathrm{Wi}} \left(\boldsymbol{Q}_h^{n+1}, \boldsymbol{q}_h^{\mathrm{SUPG}}\right) - \Delta t \left(\nabla \boldsymbol{u}_h \boldsymbol{Q}_h^{n+1}, \boldsymbol{q}_h^{\mathrm{SUPG}}\right) \\ &\quad + \Delta t \left(\boldsymbol{u}_h \cdot \nabla \boldsymbol{Q}_h^{n+1}, \boldsymbol{q}_h^{\mathrm{SUPG}}\right) = \left(\boldsymbol{Q}_h^n, \boldsymbol{q}_h^{\mathrm{SUPG}}\right) + \sqrt{\frac{\Delta t}{\mathrm{Wi}}} \left(\Delta \boldsymbol{W}, \boldsymbol{q}_h^{\mathrm{SUPG}}\right), \end{aligned} \tag{3.52}$$

for all SUPG test functions $\boldsymbol{q}_h^{\mathrm{SUPG}}$ given by

$$\boldsymbol{q}_h^{\mathrm{SUPG}} := \boldsymbol{q}_h + \frac{h_K}{|\boldsymbol{u}_h|} \boldsymbol{u}_h \cdot \nabla \boldsymbol{q}_h, \quad \boldsymbol{q}_h \in Q_h. \tag{3.53}$$

In (3.53), h_K denotes the diameter of a mesh element $K \in \mathcal{T}_h$.

FENE dumbbells In contrast to Hookean dumbbells, the FENE dumbbells exhibit a non linear spring force. This leads to the following non linear weak formulation:

For given velocity $\boldsymbol{u}_h \in U_h$ and $\boldsymbol{Q}_h^n \in Q_h$, find $\boldsymbol{Q}_h^{n+1} \in Q_h$ such that

$$\begin{aligned} &\left(\boldsymbol{Q}_h^{n+1}, \boldsymbol{q}_h^{\mathrm{SUPG}}\right) + \frac{\Delta t}{2\mathrm{Wi}} \left(\boldsymbol{F}_{\mathrm{FENE}}^{\mathrm{S}}(\boldsymbol{Q}_h^{n+1}), \boldsymbol{q}_h^{\mathrm{SUPG}}\right) - \Delta t \left(\nabla \boldsymbol{u}_h \boldsymbol{Q}_h^{n+1}, \boldsymbol{q}_h^{\mathrm{SUPG}}\right) \\ &\quad + \Delta t \left(\boldsymbol{u}_h \cdot \nabla \boldsymbol{Q}_h^{n+1}, \boldsymbol{q}_h^{\mathrm{SUPG}}\right) = \left(\boldsymbol{Q}_h^n, \boldsymbol{q}_h^{\mathrm{SUPG}}\right) + \sqrt{\frac{\Delta t}{\mathrm{Wi}}} \left(\Delta \boldsymbol{W}, \boldsymbol{q}_h^{\mathrm{SUPG}}\right), \end{aligned} \tag{3.54}$$

The non linear FENE spring force $\boldsymbol{F}_{\mathrm{FENE}}^{\mathrm{S}}$ is defined in (2.65). The bound of the maximum spring extension is preserved by this temporal discretization as $\boldsymbol{F}_{\mathrm{FENE}}^{\mathrm{S}}(\boldsymbol{Q}_h^{n+1})$ is treated implicitly.

Polymeric stress tensor In order to evaluate the polymeric stress tensor $\boldsymbol{\tau}^n_{\mathrm{p},h} \in \Sigma_h$ with the help of Kramers expression (2.68c) and the use of Brownian configurations fields (cf. Section 3.1), we sample $N_f \in \mathbb{N}$ realizations of (3.52) or (3.54). This then gives $\boldsymbol{Q}^{n,j}_h \in Q_h$, $j = 1, \ldots, N_f$, where $\boldsymbol{Q}^{n,j}_h$ denotes the jth realization of $\boldsymbol{Q}^n_h$. The weak formulation of Kramers expression (2.68c) adapted to the BCF ansatz (cf. (3.1)) is then:

For given $\boldsymbol{Q}^{n,j}_h \in Q_h$, $j = 1, \ldots, N_f$, find $\boldsymbol{\tau}^n_{\mathrm{p},h} \in \Sigma_h$ such that

$$\left(\boldsymbol{\tau}^n_{\mathrm{p},h}, \boldsymbol{f}_h\right) = \frac{\epsilon}{\mathrm{Wi}\alpha_{b,d} N_f} \sum_{j=1}^{N_f} \left(\boldsymbol{Q}^{n,j}_h \otimes \boldsymbol{F}^{*\mathrm{S}}(\boldsymbol{Q}^{n,j}_h) - \boldsymbol{I}, \boldsymbol{f}_h\right) \quad \forall \boldsymbol{f}_h \in \Sigma_h, \tag{3.55}$$

where the dimensionless spring force $\boldsymbol{F}^{*\mathrm{S}}$ is defined in (2.64) and (2.65), the finite dimensional ansatz space Σ_h in (3.17b), and the expression of the model dependent parameter $\alpha_{b,d}$ in (2.67).

3.3.1 (Non) linear system of equations

Again, one represents an element $\boldsymbol{Q}^{n+1}_h \in Q_h$ with a degree-of-freedom vector $\boldsymbol{x}^{Q,n+1} \in \mathbb{R}^{n_Q}$, where $n_Q \in \mathbb{N}$ is the dimension of the space Q_h. The representation is then given by

$$\boldsymbol{Q}^{n+1}_h = \sum_{i=1}^{n_Q} x^{Q,n+1}_i \boldsymbol{\phi}^{Q_h}_i, \tag{3.56}$$

where $\boldsymbol{\phi}^{Q_h}_i$ are the basis functions of the space Q_h, i.e., $Q_h = \mathrm{span}\{\boldsymbol{\phi}^{Q_h}_i\}_{i=1}^{n_Q}$.

Hookean dumbbells In order to transform the weak formulations (3.52) into a linear system of equations, we define the matrices

$$(\boldsymbol{M}^{\boldsymbol{u}_h}_{\boldsymbol{F}})_{i,j} = \sum_{K \in \mathcal{T}_h} \int_K \boldsymbol{F}\boldsymbol{\phi}^{Q_h}_j \cdot \left(\boldsymbol{\phi}^{Q_h}_i + \frac{h_K}{|\boldsymbol{u}_h|}\left(\boldsymbol{u}_h \cdot \nabla \boldsymbol{\phi}^{Q_h}_i\right)\right), \tag{3.57}$$

$$(\boldsymbol{C}^{\boldsymbol{u}_h})_{i,j} = \sum_{K \in \mathcal{T}_h} \int_K \left(\boldsymbol{u}_h \cdot \nabla \boldsymbol{\phi}^{Q_h}_j\right) \cdot \left(\boldsymbol{\phi}^{Q_h}_i + \frac{h_K}{|\boldsymbol{u}_h|}\left(\boldsymbol{u}_h \cdot \nabla \boldsymbol{\phi}^{Q_h}_i\right)\right). \tag{3.58}$$

In (3.57), $\boldsymbol{F}$ denotes a matrix coefficient, i.e., $\boldsymbol{F} : K \subset\!\!\longrightarrow \mathbb{R}^{2\times 2}$, where $K \in \mathcal{T}_h$ denotes a mesh element (triangle or quadrilateral). The linear system of equations, associated to (3.52), is

$$\left(\boldsymbol{M}^{\boldsymbol{u}_h}_{\boldsymbol{F}_1} + \Delta t \boldsymbol{C}^{\boldsymbol{u}_h}\right) \boldsymbol{x}^{Q,n+1} = \boldsymbol{g}(\boldsymbol{Q}^n_h, \boldsymbol{u}_h), \tag{3.59}$$

where the coefficient matrix in $\boldsymbol{M}^{\boldsymbol{u}_h}_{\boldsymbol{F}_1}$ is given by

$$\boldsymbol{F}_1 := \left(1 + \frac{\Delta t}{2\mathrm{Wi}}\right)\boldsymbol{I} - \Delta t \nabla \boldsymbol{u}_h. \tag{3.60}$$

The entries of the right hand side $\boldsymbol{g}(\boldsymbol{Q}_h^n, \boldsymbol{u}_h)$ are

$$g_i(\boldsymbol{Q}_h^n, \boldsymbol{u}_h) = \sum_{K \in \mathcal{T}_h} \int_K \left(\boldsymbol{Q}_h^n + \sqrt{\frac{\Delta t}{\mathrm{Wi}}} \Delta \boldsymbol{W} \right) \cdot \left(\boldsymbol{\phi}_i^{Q_h} + \frac{h_K}{|\boldsymbol{u}_h|} \left(\boldsymbol{u}_h \cdot \nabla \boldsymbol{\phi}_i^{Q_h} \right) \right). \tag{3.61}$$

The system matrix in (3.59) is in general non symmetric.

FENE dumbbells In the case of FENE dumbbells, we have a non linear system of equations, due to the non linear spring force $\boldsymbol{F}_{\mathrm{FENE}}^{\mathrm{S}}$ in the weak formulation (3.54). The corresponding non linear system of equation is then given by

$$\boldsymbol{S}\boldsymbol{x}^{\mathrm{Q},n+1} + \boldsymbol{N}(\boldsymbol{x}^{\mathrm{Q},n+1}) = \boldsymbol{g}(\boldsymbol{Q}_h^n, \boldsymbol{u}_h), \tag{3.62}$$

with matrices

$$\boldsymbol{S} := \boldsymbol{M}_{\boldsymbol{F}_2}^{\boldsymbol{u}_h} + \Delta t \boldsymbol{C}^{\boldsymbol{u}_h}, \tag{3.63a}$$

$$\boldsymbol{F}_2 := \boldsymbol{I} - \Delta t \nabla \boldsymbol{u}_h, \tag{3.63b}$$

and a non linear mapping $\boldsymbol{N} : \mathbb{R}^{n_{\mathrm{Q}}} \longrightarrow \mathbb{R}^{n_{\mathrm{Q}}}$. The entries of the non linear mapping $\boldsymbol{N}$ are defined by

$$N_i(\boldsymbol{x}^{\mathrm{Q},n+1}) := \frac{\Delta t}{2\mathrm{Wi}} \left(\boldsymbol{F}_{\mathrm{FENE}}^{\mathrm{S}} \left(\sum_{k=1}^{n_{\mathrm{Q}}} x_k^{\mathrm{Q},n+1} \boldsymbol{\phi}_k^{Q_h} \right), \boldsymbol{\phi}_i^{Q_h} + \frac{h_K}{|\boldsymbol{u}_h|} \left(\boldsymbol{u}_h \cdot \nabla \boldsymbol{\phi}_i^{Q_h} \right) \right). \tag{3.64}$$

One ansatz to approximate the solution $\boldsymbol{x}^{\mathrm{Q},n+1}$ of (3.62) in an iterative way, is to apply Newtons method on the function $\boldsymbol{H} : \mathbb{R}^{n_{\mathrm{Q}}} \longrightarrow \mathbb{R}^{n_{\mathrm{Q}}}$ with

$$\boldsymbol{H}(\boldsymbol{x}) := \boldsymbol{S}\boldsymbol{x} + \boldsymbol{N}(\boldsymbol{x}) - \boldsymbol{g}(\boldsymbol{Q}_h^n, \boldsymbol{u}_h). \tag{3.65}$$

Note that the solution of (3.62) is a root of (3.65). The Jacobian $D\boldsymbol{H} : \mathbb{R}^{n_{\mathrm{Q}}} \longrightarrow \mathbb{R}^{n_{\mathrm{Q}} \times n_{\mathrm{Q}}}$ of (3.65) is given by

$$D\boldsymbol{H}(\boldsymbol{x}) := \boldsymbol{S} + D\boldsymbol{N}(\boldsymbol{x}) \tag{3.66}$$

with

$$D\boldsymbol{N}(\boldsymbol{x})_{ij} := \frac{\Delta t}{2\mathrm{Wi}} \left(\nabla \boldsymbol{F}_{\mathrm{FENE}}^{\mathrm{S}} \left(\sum_{k=1}^{n_{\mathrm{Q}}} x_k^{\mathrm{Q},n+1} \boldsymbol{\phi}_k^{Q_h} \right) \boldsymbol{\phi}_j^{Q_h}, \boldsymbol{\phi}_i^{Q_h} + \frac{h_K}{|\boldsymbol{u}_h|} \left(\boldsymbol{u}_h \cdot \nabla \boldsymbol{\phi}_i^{Q_h} \right) \right). \tag{3.67}$$

In (3.67), the gradient of the FENE spring force $\nabla \boldsymbol{F}_{\mathrm{FENE}}^{\mathrm{S}} : \mathbb{R}^d \longrightarrow \mathbb{R}^{d \times d}$ is given by

$$\nabla \boldsymbol{F}_{\mathrm{FENE}}^{\mathrm{S}}(\boldsymbol{Q}) = \frac{1}{1 - |\boldsymbol{Q}|^2/b} \boldsymbol{I} + \frac{2}{b\,(1 - |\boldsymbol{Q}|^2/b)^2} \boldsymbol{Q} \otimes \boldsymbol{Q}. \tag{3.68}$$

One can express (3.67) through (3.57) with the mapping

$$\boldsymbol{F}_3(\boldsymbol{x}) := \frac{\Delta t}{2\mathrm{Wi}} \nabla \boldsymbol{F}_{\mathrm{FENE}}^{\mathrm{S}} \left(\sum_{k=1}^{n_{\mathrm{Q}}} x_k \boldsymbol{\phi}_k^{Q_h} \right), \tag{3.69}$$

i.e., $DN(x) = M^{u_h}_{F_3(x)}$ for given $x \in \mathbb{R}^{n_Q}$.

The Newton iteration for approximating the root $x^{Q,n+1}$ of (3.65), is then given by

$$x^{i+1} := x^i - DH(x^i)^{-1} H(x^i). \tag{3.70}$$

A good initial guess for x^0 in (3.70) is the degree of freedom vector $x^{Q,n}$ that represents the previous solution Q_h^n at time t_n. In each iteration of (3.70), a linear system of equation with the non symmetric system matrix $DH(x^i)$ has to be solved.

Polymeric stress tensor To convert (3.55) into a linear system of equations, one represents an element $\tau_{\mathrm{p},h}^n \in \Sigma_h$ with a degree-of-freedom vector $x^{\tau,n} \in \mathbb{R}^{n_\Sigma}$, where $n_\Sigma \in \mathbb{N}$ is the dimension of the space Σ_h. The representation is then given by

$$\tau_{\mathrm{p},h}^n = \sum_{i=1}^{n_\Sigma} x_i^{\tau,n} \phi_i^{\Sigma_h}, \tag{3.71}$$

where $\phi_i^{\Sigma_h}$ are the basis functions of the space Σ_h, i.e., $\Sigma_h = \operatorname{span}\{\phi_i^{\Sigma_h}\}_{i=1}^{n_Q}$.

Converting weak formulation (3.55) into an equivalent linear system of equation yields

$$E x^{\tau,n} = y(Q_h^{n,1}, \ldots, Q_h^{n,N_f}), \tag{3.72}$$

where E is defined in (3.31) and the entries of the right hand side $y(Q_h^{n,1}, \ldots, Q_h^{n,N_f})$ are given by

$$y_i(Q_h^{n,1}, \ldots, Q_h^{n,N_f}) := \frac{\epsilon}{\mathrm{Wi}\,\alpha_{b,d} N_f} \sum_{j=1}^{N_f} \int_\Omega \left(Q_h^{n,j} \otimes F^{*\mathrm{S}}(Q_h^{n,j}) - I \right) \phi_i^{\Sigma_h}. \tag{3.73}$$

The mass matrix E is symmetric positive definite.

Typically, tensor valued basis functions ϕ_j^V of a finite dimensional space $V := W^{d \times d}$ are constructed from scalar valued basis functions ϕ_p^W of a finite dimensional space $W \subset L^2(\Omega)$. Let $n_W := \dim W$. Then it holds $n_V = d^2 n_W$. One approach is then to define ϕ_k^V, $k = 1, \ldots, n_V$, via

$$\phi_{k(p,i,j)}^V := \phi_p e_i \otimes e_j, \tag{3.74}$$

where $k(p,i,j) := p + [(i-1) + (j-1)d]\, n_W$ with $p = 1, \ldots, n_W$ and $i, j = 1, \ldots, d$. Such an approach leads to a special block diagonal structure of the mass matrix $(M_V)_{k,l} := (\phi_k^V, \phi_l^V)$. It then holds

$$M_V = \operatorname{diag}(M_W, \ldots, W_W) \in \mathbb{R}^{d^2 n_W \times d^2 n_W} \tag{3.75}$$

with d^2 blocks of the mass matrix $(M_W)_{p,q} := (\phi_p^W, \phi_q^W)$ on the diagonal.

Using such an approach for the basis functions $\phi_i^{\Sigma_h}$, leads to a decoupling of (3.72) into d^2 smaller linear system of equations of size n_Σ / d^2, which can be solved more efficiently with preconditioned iterative solvers. Additionally, the symmetry of $\boldsymbol{\tau}^n_{\mathrm{p},h}$ can be exploited, such that it is only necessary to solve $d(d+1)/2$ instead of d^2 smaller linear system of equations. Well-suited preconditioned iterative solvers for (3.59), (3.70), and (3.72) are presented in the next section.

3.3.2 Iterative solvers and preconditioning

The system matrices in (3.59) and (3.70) are non symmetric. Therefore, we apply the preconditioned GMRES solver for the iterative approximation of their solutions. GMRES is an iterative Krylov subspace method, similar to MINRES, which solves iteratively the non symmetric linear system of equations

$$\boldsymbol{F}\boldsymbol{x} = \boldsymbol{b}. \tag{3.76}$$

The kth GMRES iterate $\boldsymbol{x}^{(k)}$ minimizes the residual

$$\boldsymbol{r}^{(k)} := \boldsymbol{b} - \boldsymbol{F}\boldsymbol{x}^{(k)} \tag{3.77}$$

in the Euclidean norm $\|\boldsymbol{r}^{(k)}\|_2$ over the shifted Krylov space (3.45) with $\boldsymbol{F}$ instead of $\mathcal{B}$.

There are two ways to apply a general invertible preconditioning matrix $\boldsymbol{P}$ on (3.76). System (3.76) can be preconditioned from the left

$$\boldsymbol{P}^{-1}\boldsymbol{F}\boldsymbol{x} = \boldsymbol{P}^{-1}\boldsymbol{b} \tag{3.78}$$

or from the right

$$\boldsymbol{F}\boldsymbol{P}^{-1}\boldsymbol{y} = \boldsymbol{b} \tag{3.79}$$

with $\boldsymbol{y} = \boldsymbol{P}\boldsymbol{x}$. Right preconditioning has the advantage that the Euclidean norm of the original residual in (3.79), i.e., $\boldsymbol{b} - \boldsymbol{F}\boldsymbol{x}^{(k)}$ is independent of $\boldsymbol{P}$ due to

$$\|\boldsymbol{b} - \boldsymbol{F}\boldsymbol{P}^{-1}\boldsymbol{y}^{(k)}\|_2 = \|\boldsymbol{b} - \boldsymbol{F}\boldsymbol{P}^{-1}\boldsymbol{P}\boldsymbol{x}^{(k)}\|_2 = \|\boldsymbol{b} - \boldsymbol{F}\boldsymbol{x}^{(k)}\|_2. \tag{3.80}$$

Left preconditioning minimizes the original residual weighted with $\boldsymbol{P}^{-1}$, i.e.,

$$\|\boldsymbol{P}^{-1}\boldsymbol{b} - \boldsymbol{P}^{-1}\boldsymbol{F}\boldsymbol{x}^{(k)}\|_2 = \|\boldsymbol{P}^{-1}(\boldsymbol{b} - \boldsymbol{F}\boldsymbol{x}^{(k)})\|_2. \tag{3.81}$$

GMRES requires more memory compared to MINRES, as in each iteration an additional vector needs to be stored. This leads to the common practice to restart GMRES after a fixed number of iterations. After each restart, the initial iterate is set to the last iterate of the previous restart. See Chapter 7.1.1 in [23] for more details.

In this thesis, we chose a parallel version of ILU [43] as preconditioner. The idea of ILU (incomplete lower upper) preconditioning (cf. Chapter 10 in [71]) is based on the following incomplete factorization

$$\boldsymbol{F} = \boldsymbol{L}\boldsymbol{U} - \boldsymbol{R}, \tag{3.82}$$

Option	Value
HYPRE_EuclidSetLevel	1 [ILU(1)]
HYPRE_EuclidSetBJ	0
HYPRE_EuclidSetRowScale	0

Table 3.3. Options used for the setup of Hypres Euclid PC [27].

where $\boldsymbol{L}, \boldsymbol{U} \in \mathbb{R}^{n\times n}$ are lower/upper triangular matrices. Matrix $\boldsymbol{L}$ has only ones on the diagonal and $\boldsymbol{R} \in \mathbb{R}^{n\times n}$ is a remainder matrix. Matrices $\boldsymbol{L}$, $\boldsymbol{U}$, and $\boldsymbol{R}$ satisfy special properties on a given sparsity pattern $P \subset \{1,\dots,n\}^2$. The sparsity pattern P should satisfy

$$\left\{(i,j) \in \{1,\dots,n\}^2 \,|\, F_{i,j} \neq 0\right\} \subset P \tag{3.83}$$

and

$$\{(i,i) |\, i \in \{1,\dots,n\}\} \subset P. \tag{3.84}$$

The entries of $\boldsymbol{L}$, $\boldsymbol{U}$, and $\boldsymbol{R}$ should then satisfy $\boldsymbol{F}_{ij} = (\boldsymbol{L}\boldsymbol{U})_{ij}$, $\boldsymbol{R}_{ij} = 0$ for all $(i,j) \in P$ and $\boldsymbol{L}_{ij} = \boldsymbol{U}_{ij} = 0$ for all $(i,j) \notin P$. The special choice of P depends on the underlying algorithm. The matrix

$$\boldsymbol{P} := \boldsymbol{L}\boldsymbol{U} \tag{3.85}$$

can then be used as a preconditioner for matrix $\boldsymbol{F}$, where the actions $\boldsymbol{z} \mapsto \boldsymbol{L}^{-1}$ and $\boldsymbol{z} \mapsto \boldsymbol{U}^{-1}$ can be efficiently computed due to the (sparse) triangular shape.

In the simulations, we used the parallel ILU implementation of the library Hypre [27] with the options summarized in Table 3.3. Table 3.4 lists the required iterations it took the (left) preconditioned GMRES solver to solve (3.59) in a periodic shear flow scenario on the unit square during the first time step. In Table 3.4, we varied the number of uniform mesh refinements, time step sizes Δt, and Weissenberg numbers Wi. The solver stopped after the relative residual $\|\boldsymbol{P}^{-1}\boldsymbol{r}\|_2/\|\boldsymbol{P}^{-1}\boldsymbol{b}\|_2$ dropped below 10^{-10}. GMRES restarts after 50 iterations if not already converged. In the case of $\Delta t = 0.001$, the required number of iterations are more or less independent of the considered meshes and Weissenberg numbers. However, for $\Delta t = 0.1$, one can clearly observe a h^{-1}-dependency on the required number of iterations as with each uniform mesh refinement, the number of iteration approximately doubles. In the case of System (3.70), which arises during the Newton iterations, a behavior similar to Table 3.4 can be observed.

For the linear system of equations (3.72) with a symmetric positive definite matrix $\boldsymbol{E}$, which arises during the computation of the polymeric stress $\boldsymbol{\tau}_{\mathrm{p},h}$, we apply the preconditioned conjugate gradient (PCG) method with Jacobi preconditioning. The kth CG iterate $\boldsymbol{x}^k$ minimizes the error $\|\boldsymbol{x} - \boldsymbol{x}^k\|_{\boldsymbol{E}}$ in the affine Krylov subspace (3.45) with matrix $\boldsymbol{E}$ instead of $\mathcal{B}$, where $\boldsymbol{x}$ is the solution of

$$\boldsymbol{E}\boldsymbol{x} = \boldsymbol{b}. \tag{3.86}$$

	Wi = 0.1		Wi = 0.5		Wi = 0.9	
DOF	$\Delta t = 0.1$	$\Delta t = 0.001$	$\Delta t = 0.1$	$\Delta t = 0.001$	$\Delta t = 0.1$	$\Delta t = 0.001$
33024	35	14	47	14	48	14
131584	72	15	96	15	97	15
525312	141	14	187	14	189	14

Table 3.4. Required number of iterations for preconditioned GMRES with preconditioner (3.85) to solve (3.59) in the first time step for varying numbers of uniform mesh refinements, time step sizes Δt, and Weissenberg numbers Wi. The stopping criterion of the solver is set to $\|\boldsymbol{P}^{-1}\boldsymbol{r}\|_2/\|\boldsymbol{P}^{-1}\boldsymbol{b}\|_2 < 10^{-10}$.

Preconditioning is done in the same manner as in the MINRES case (cf. (3.47)) with a symmetric positive definite matrix $\boldsymbol{P} = \boldsymbol{H}\boldsymbol{H}^{\mathrm{T}}$. In contrast to preconditioned MINRES, where the residual is minimized w.r.t. the norm $\|\boldsymbol{r}^k\|_{\mathcal{P}^{-1}}$ (depends on $\mathcal{P}$), preconditioned CG minimizes the error $\|\boldsymbol{x} - \boldsymbol{x}^k\|_E$ in a norm, which is independent of the preconditioner [23, p. 81]. Consider the preconditioned system

$$\boldsymbol{H}^{-1}\boldsymbol{E}\boldsymbol{H}^{-\mathrm{T}}\boldsymbol{y} = \boldsymbol{H}^{-1}\boldsymbol{b}, \quad \boldsymbol{y} = \boldsymbol{H}^{\mathrm{T}}\boldsymbol{x}. \tag{3.87}$$

Let $\boldsymbol{y}^k$ denote the CG iterate after k CG iterations on (3.87). Then, it holds for the error

$$\begin{aligned}
\|\boldsymbol{y} - \boldsymbol{y}^k\|^2_{\boldsymbol{H}^{-1}\boldsymbol{E}\boldsymbol{H}^{-\mathrm{T}}} &= (\boldsymbol{y} - \boldsymbol{y}^k)^{\mathrm{T}}\boldsymbol{H}^{-1}\boldsymbol{E}\boldsymbol{H}^{-\mathrm{T}}(\boldsymbol{y} - \boldsymbol{y}^k) &(3.88)\\
&= \left[\boldsymbol{H}^{\mathrm{T}}(\boldsymbol{x} - \boldsymbol{x}^k)\right]^{\mathrm{T}} \boldsymbol{H}^{-1}\boldsymbol{E}\boldsymbol{H}^{-\mathrm{T}} \left[\boldsymbol{H}^{\mathrm{T}}(\boldsymbol{x} - \boldsymbol{x}^k)\right] &(3.89)\\
&= (\boldsymbol{x} - \boldsymbol{x}^k)^{\mathrm{T}}\boldsymbol{E}(\boldsymbol{x} - \boldsymbol{x}^k) = \|\boldsymbol{x} - \boldsymbol{x}^k\|^2_E, &(3.90)
\end{aligned}$$

i.e., applying CG on (3.87) minimizes the error $\|\boldsymbol{x} - \boldsymbol{x}^k\|^2_E$ over the space (3.45) with matrix $\boldsymbol{H}^{-1}\boldsymbol{E}\boldsymbol{H}^{-\mathrm{T}}$.

In the case of mass matrices $\boldsymbol{M}_p$, as used here, the combination of CG with Jacobi preconditioning is optimal in the sense that the Jacobi preconditioner

$$\boldsymbol{P} := \operatorname{diag}(\boldsymbol{M}_p) \tag{3.91}$$

is spectrally equivalent to the mass matrix $\boldsymbol{M}_p$, i.e., the required number of iterations it takes to reach a certain error tolerance are uniformly bounded from above in the mesh size h (cf. Lemma 4.3 in [23]). Note that without preconditioning, the required number of iterations is also uniformly bounded from above in h on quasi-uniform meshes (cf. Theorem 9.8 in [24]).

In the following, we solve

$$\boldsymbol{M}_p\boldsymbol{x} = \boldsymbol{b}, \tag{3.92}$$

where $\boldsymbol{M}_p$ is defined in (3.50) and

$$b_i = \int_\Omega f\phi_i^{P_h}, \quad f(x,y) := 100(x-0.5)^2(y-0.5)^2 - \frac{100}{144}, \tag{3.93}$$

iteratively with the above mentioned PCG method with Jacobi preconditioning. The solution of (3.92) can be interpreted as the L^2-projection of f into the space P_h (cf. (3.17c) for the definition of P_h). Here, domain Ω is the unit square, which is periodic on the left and right boundary. Figure 3.5 visualizes the required number of PCG iterations k it takes to reach $\|\boldsymbol{r}^k\|_{\boldsymbol{P}^{-1}}/\|\boldsymbol{r}^0\|_{\boldsymbol{P}^{-1}} < 10^{-7}$ for varying numbers of uniform mesh refinements. A reduction of the mesh width h does not increase the required number of iterations. This observation confirms the spectral equivalence of the mass matrix $\boldsymbol{M}_p$ to its diagonal in the case of $\mathbb{Q}_1$ elements.

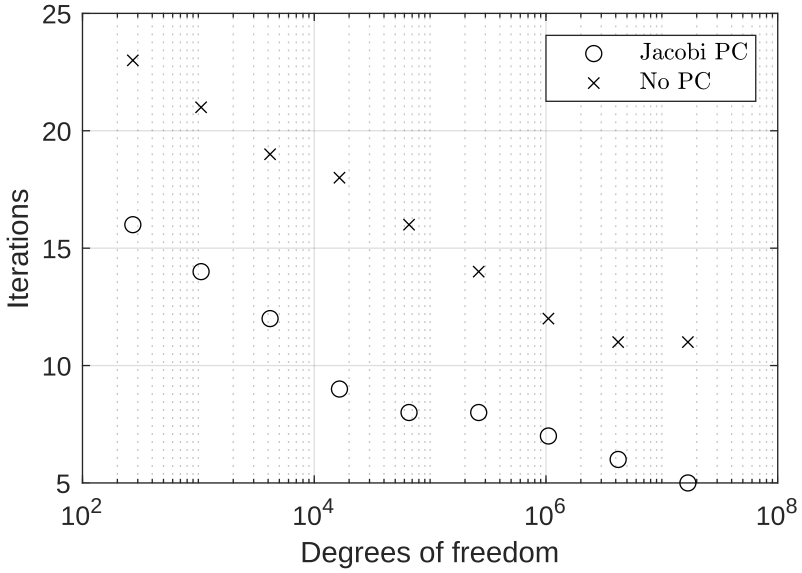

Figure 3.5. Number of CG iterations it takes to solve (3.92) with and without Jacobi PC. The solver stops when $\|\boldsymbol{r}^k\|_{\boldsymbol{P}^{-1}}/\|\boldsymbol{r}^0\|_{\boldsymbol{P}^{-1}} < 10^{-7}$ is reached.

3.3.3 Generating bead-spring dumbbells in equilibrium

In order to start the simulation with bead-spring dumbbells, initial configurations of the bead-spring connector vector $\boldsymbol{Q} \in \mathbb{D}_{\mathrm{BS}} \subset \mathbb{R}^d$ are required. In Section 2.1.2, equilibrium distribution functions ψ_{eq} for Hookean and FENE springs were derived. They are solutions of the Fokker–Planck equation (2.47) with $\boldsymbol{u} = \boldsymbol{0}$. In our case, the non-dimensionalized equilibrium distribution functions are

$$\psi_{\mathrm{eq}}^{\mathrm{Hookean}}(\boldsymbol{Q}) = (2\pi)^{-\frac{d}{2}} \exp\left(-\frac{\boldsymbol{Q}\cdot\boldsymbol{Q}}{2}\right), \tag{3.94a}$$

$$\psi_{\mathrm{eq}}^{\mathrm{FENE}}(\boldsymbol{Q}) = \begin{cases} C(d)^{-1}\left[1 - \frac{\boldsymbol{Q}\cdot\boldsymbol{Q}}{b}\right]^{\frac{b}{2}}, & |\boldsymbol{Q}| < \sqrt{b}, \\ 0, & |\boldsymbol{Q}| \geq \sqrt{b}, \end{cases} \tag{3.94b}$$

where the normalization constant $C(d)$ is given in (2.70) and b denotes the maximum squared extension of $\boldsymbol{Q}$ in the case of a FENE-spring.

Distribution (3.94a) is a d-dimensional normal distribution with zero mean vector and identity as covariance matrix. In this special case, connector vectors $\boldsymbol{Q}$ can be sampled by just sampling each component $Q_i \sim \mathcal{N}(0,1)$, $i = 1, \dots, d$, according to the one dimensional normal distribution with zero mean and variance 1.

In the case of distribution (3.94b), it is not straightforward to sample $\boldsymbol{Q} \sim \psi_{\text{eq}}^{\text{FENE}}$. In this thesis, we sample $\boldsymbol{Q} \sim \psi_{\text{eq}}^{\text{FENE}}$ via an acceptance rejection algorithm. The idea of this type of algorithm was presented the first time in [80]. The goal is to sample points $\boldsymbol{x} \in D \subset \mathbb{R}^d$, which are distributed according to an arbitrary probability density function $f : D \subset \mathbb{R}^d \to \mathbb{R}$. The idea is now to generate uniformly distributed points $\boldsymbol{x} \in D$ and accept them with probability $f(\boldsymbol{x})|D|/M$, where $M \in \mathbb{R}^+$ is chosen such that $f \leq M/|D|$ in D. The accepted points $\boldsymbol{x} \in D$ are then distributed according to pdf f. See Algorithm 1 for the pseudo code of the acceptance rejection method, which was outlined above.

Algorithm 1 Acceptance rejection algorithm to print N sample points $\boldsymbol{x} \in D \subset \mathbb{R}^d$ that are distributed with pdf $f : D \to \mathbb{R}$.

```
$i \leftarrow 0$
while $i < N$ do
    $\boldsymbol{x} \leftarrow$ Generate uniformly distributed point in $D$
    $y \leftarrow$ Generate uniformly distributed number in $[0,1]$
    if $yM/|D| \leq f(\boldsymbol{x})$ then
        Print $\boldsymbol{x}$
        $i \leftarrow i + 1$
    end if
end while
```

Figure 3.6a illustrates the steps of Algorithm 1 in the 1D case of $\psi_{\text{eq}}^{\text{FENE}}$ and $b = 1$. Then it holds $D = [-1, 1]$ with $|D| = 2$ and $M = 4/\pi$. At first, we sample a point x on the x-axis that is uniformly distributed in D and a $y \sim U(0, 1)$. Then we check if the pair $(x, yM/2)$ lies below the graph of f. If it is below the graph of f, x is accepted, otherwise x is rejected and a new pair (x, y) has to be sampled. Note that the pair $(x, yM/2)$ is uniformly distributed in $[-1, 1] \times [0, M/2]$. Figure 3.6b shows a histogram of the accepted values x, which was normalized such that it approximates the probability density function f. The histogram in Figure 3.6b is normalized such that the total area of the bins is 1, i.e., the bin value of the ith bin is $v_i = c_i/(Nw_i)$, where c_i is the number of elements in the bin, w_i the bin width, and N the total number of elements, which are used in the histogram.

3.4 Numerical scheme for bead-rod chains

In the following sections, we introduce and discuss the numerical schemes, which are required for the simulation of bead-rod chains in the Brownian configuration field (BCF) context. At first, Liu's algorithm [55] is introduced in Section 3.4.1. In order to compute the resulting polymeric stress (2.85) of the bead-rod chains, we state a noise filtering technique of [21] in Section 3.4.2. This enables the estimation of necessary relaxation times (2.97) (cf. Section 2.2.4). The estimation

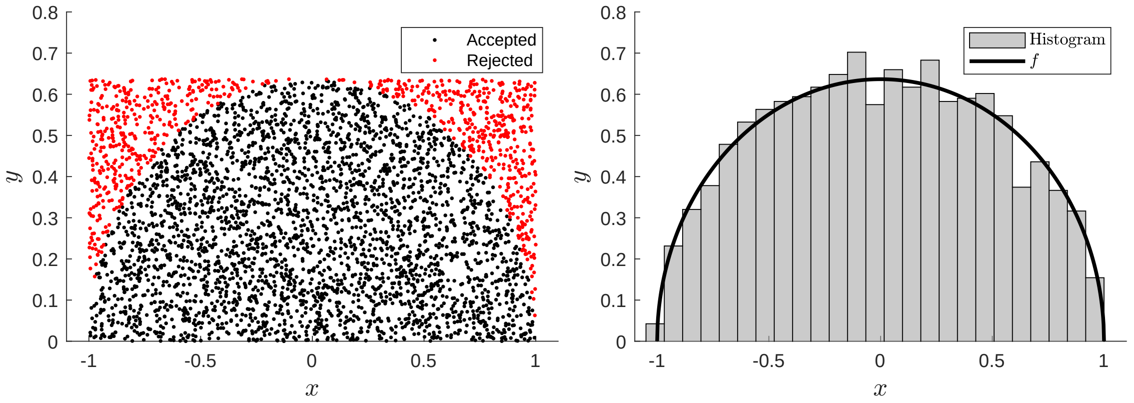

(a) Sample points.

(b) Normalized histogram of accepted points.

Figure 3.6. Left: Visualization of 4000 sample points, which are accepted or rejected. Right: Accepted points are used for a histogram to visualize the approximation of pdf f.

procedure is described in Section 3.4.3. Section 3.4.4 presents the numerical scheme for the simulation of bead-rod chains in the BCF context, where the schemes from Sections 3.4.1 and 3.4.2 are adapted to finite elements and into the Eulerian setting. Lastly, Section 3.4.6 discusses the choice of iterative solvers that are used to solve the arising (non) linear system of equations of the previous sections.

3.4.1 Liu's algorithm

In this section, we want to derive an algorithm for the temporal evolution of individual bead-rod chains, i.e., an algorithm for approximating trajectories of the SDE

$$\mathrm{d}\boldsymbol{r}_i = \left[\boldsymbol{u}_i + \frac{\boldsymbol{F}_i^{\mathrm{C}}}{\xi}\right]\mathrm{d}t + \sqrt{\frac{2k_{\mathrm{B}}\vartheta}{\xi}}\mathrm{d}\boldsymbol{W}_i, \quad i = 1, \dots, N, \tag{3.95a}$$

$$(\boldsymbol{r}_{i+1} - \boldsymbol{r}_i) \cdot (\boldsymbol{r}_{i+1} - \boldsymbol{r}_i) - a^2 = 0, \quad i = 1, \dots, N-1, \tag{3.95b}$$

where $\boldsymbol{r}_i$ denotes the position of bead i, $\boldsymbol{u}_i$ the fluid velocity at $\boldsymbol{r}_i$, ξ the friction coefficient in the drag force (2.1), k_{B} the Boltzmann constant, ϑ the fluid temperature, $\boldsymbol{W}_i$ a Wiener process, a the rod length, and $\boldsymbol{F}_i^{\mathrm{C}}$ the constraint force, which is given by

$$\boldsymbol{F}_i^{\mathrm{C}} := \begin{cases} T_1(\boldsymbol{r}_2 - \boldsymbol{r}_1)/a, & i = 1, \\ T_i(\boldsymbol{r}_{i+1} - \boldsymbol{r}_i)/a - T_{i-1}(\boldsymbol{r}_i - \boldsymbol{r}_{i-1})/a =, & i = 2, \dots, N-1, \\ -T_{N-1}(\boldsymbol{r}_N - \boldsymbol{r}_{N-1})/a, & i = N. \end{cases} \tag{3.96}$$

In (3.96), tensions T_i act as Lagrangian multiplier due to the $N-1$ rod length constraints (3.95b). See Section 2.2.1 for the derivation of (3.95) and (3.96).

In the following, we non-dimensionalize (3.95) by choosing $l_{\mathrm{c}} = a$, $t_{\mathrm{c}} = \xi a^2/(k_{\mathrm{B}}\vartheta)$, $U_{\mathrm{c}} = l_{\mathrm{c}}/t_{\mathrm{c}}$ and $F_{\mathrm{c}} = k_{\mathrm{B}}\vartheta/a$, which leads to

$$\mathrm{d}\boldsymbol{r}_i^* = \left[\boldsymbol{u}_i^* + \boldsymbol{F}_i^{*\mathrm{C}}\right]\mathrm{d}t^* + \sqrt{2}\mathrm{d}\boldsymbol{W}_i^*, \quad i = 1, \dots, N, \tag{3.97a}$$

$$\left(\boldsymbol{r}_{i+1}^* - \boldsymbol{r}_i^*\right) \cdot \left(\boldsymbol{r}_{i+1}^* - \boldsymbol{r}_i^*\right) - 1^2 = 0, \quad i = 1, \dots, N-1. \tag{3.97b}$$

The dimensionless constraint force is defined by

$$\frac{\boldsymbol{F}_i^{\mathrm{C}}}{F_{\mathrm{c}}} = \frac{T_i}{F_{\mathrm{c}}}(\boldsymbol{r}_{i+1}^* - \boldsymbol{r}_i^*) - \frac{T_{i-1}}{F_{\mathrm{c}}}(\boldsymbol{r}_i^* - \boldsymbol{r}_{i-1}^*) = \hat{T}_i \boldsymbol{Q}_i^* - \hat{T}_{i-1}\boldsymbol{Q}_{i-1}^* =: \boldsymbol{F}_i^{*\mathrm{C}}(\hat{T}, \boldsymbol{Q}^*), \tag{3.98}$$

where $\hat{T}_i = aT_i/(k_{\mathrm{B}}\vartheta)$ are the dimensionless tensions and $\boldsymbol{Q}_i^* := \boldsymbol{r}_{i+1}^* - \boldsymbol{r}_i^*$, $i = 1, \dots, N-1$, are the dimensionless connector vectors. Note that (3.98) is only valid for $2 \le i \le N-1$, for the corner cases $i = 1$ and $i = N$, see (3.96).

The idea of Liu's algorithm [55] is to use a predictor-corrector approach. For given bead position vectors $\boldsymbol{r}_i^*(t^*)$, $i = 1, \dots, N$, which satisfy the rod length constraints (3.97b) at time t^*, updated $\boldsymbol{r}_i^*(t^* + \Delta t)$ are computed in two substeps that satisfy (3.97b) at time $t^* + \Delta t$. In the first (predictor) substep, we compute

$$\hat{\boldsymbol{r}}_i^* := \boldsymbol{r}_i^*(t^*) + \boldsymbol{u}_i^*(t^*)\Delta t + \sqrt{2\Delta t}\Delta \boldsymbol{W}_i^*, \quad i = 1, \dots, N, \tag{3.99}$$

by neglecting the constraint force $\boldsymbol{F}_i^{*\mathrm{C}}$. In (3.99), $\Delta \boldsymbol{W}_i^* \sim \mathcal{N}(0,1)^d$ denotes the Wiener increment with normally distributed components with zero mean and variance 1. Note that the $\hat{\boldsymbol{r}}_i^*$, $i = 1, \dots, N$, do not satisfy the rod length constraints (3.97b) anymore as the constraint force $\boldsymbol{F}_i^{*\mathrm{C}}$ was neglected. In the corrector substep, this violation of (3.97b) is fixed with the ansatz

$$\boldsymbol{r}_i^*(t^* + \Delta t) := \hat{\boldsymbol{r}}_i^* + \Delta t \boldsymbol{F}_i^{*\mathrm{C}}(\hat{T}, \boldsymbol{Q}^*(t^*)), \tag{3.100}$$

The unknowns in (3.100) are the tensions $\hat{T}$, which need to be chosen such that $\boldsymbol{r}_i^*(t^* + \Delta t)$, $i = 1, \dots, N$, satisfies the rod length constraints (3.97b) again. Substituting the expression (3.100) for $\boldsymbol{r}_i^*(t^* + \Delta t)$ into (3.97b) yields the system of equations

$$\begin{aligned}
&(2\Delta t)\hat{\boldsymbol{Q}}_1^* \cdot \left(-2\hat{T}_1 \boldsymbol{Q}_1^*(t^*) + \hat{T}_2 \boldsymbol{Q}_2^*(t^*)\right) \\
&\qquad + \left(-2\hat{T}_1 \boldsymbol{Q}_1^*(t^*) + \hat{T}_2 \boldsymbol{Q}_2^*(t^*)\right)^2 (\Delta t)^2 = 1 - |\hat{\boldsymbol{Q}}_1^*|^2, \quad i = 1,
\end{aligned} \tag{3.101a}$$

$$\begin{aligned}
&(2\Delta t)\hat{\boldsymbol{Q}}_i^* \cdot \left(\hat{T}_{i-1} \boldsymbol{Q}_{i-1}^*(t^*) - 2\hat{T}_i \boldsymbol{Q}_i^*(t^*) + \hat{T}_{i+1} \boldsymbol{Q}_{i+1}^*(t)\right) \\
&\qquad + \left(\hat{T}_{i-1} \boldsymbol{Q}_{i-1}^*(t^*) - 2\hat{T}_i \boldsymbol{Q}_i^*(t^*) + \hat{T}_{i+1} \boldsymbol{Q}_{i+1}^*(t^*)\right)^2 (\Delta t)^2 \\
&\qquad\qquad = 1 - |\hat{\boldsymbol{Q}}_i^*|^2, \quad i = 2, \dots, N-2,
\end{aligned} \tag{3.101b}$$

$$\begin{aligned}
&(2\Delta t)\hat{\boldsymbol{Q}}_{N-1}^* \cdot \left(\hat{T}_{N-2} \boldsymbol{Q}_{N-2}^*(t^*) - 2\hat{T}_{N-1} \boldsymbol{Q}_{N-1}^*(t^*)\right) \\
&\qquad + \left(\hat{T}_{N-2} \boldsymbol{Q}_{N-2}^*(t^*) - 2\hat{T}_{N-1} \boldsymbol{Q}_{N-1}^*(t^*)\right)^2 (\Delta t)^2 \\
&\qquad\qquad = 1 - |\hat{\boldsymbol{Q}}_{N-1}|^2, \quad i = N-1,
\end{aligned} \tag{3.101c}$$

Note that in (3.101), the connector vectors stemming from (3.98) are taken at time t^*, i.e. $\boldsymbol{Q}_i^*(t^*) := \boldsymbol{r}_{i+1}^*(t^*) - \boldsymbol{r}_i^*(t^*)$, and the connector vectors resulting from $\hat{\boldsymbol{r}}_i^*$

are denoted by $\hat{\boldsymbol{Q}}_i^* := \hat{\boldsymbol{r}}_{i+1}^* - \hat{\boldsymbol{r}}_i^*$. System (3.101) consists of $N-1$ nonlinear equations with unknowns $\hat{T}_i$, $i = 1, \ldots, N-1$. Solving (3.101) for the $\hat{T}_i$ enables then the explicit computation of the updated position vectors (3.100), which satisfy the rod length constraints (3.97b) at time $t^* + \Delta t$ by construction.

In [75], two fixed-point iteration approaches for solving (3.101) are compared with each other. The first Picard's type approach was initially suggested in [55], where (3.101) is solved for $\hat{T}_i$, $i = 1, \ldots, N-1$, by treating the quadratic terms that contain $\hat{T}_i$ explicitly. This results in the following scheme: For given $\hat{T}_i^n$, $i = 1, \ldots, N-1$, solve

$$\begin{aligned}(2\Delta t)\hat{\boldsymbol{Q}}_1^* \cdot \Big(-2\hat{T}_1^{n+1}\boldsymbol{Q}_1^*(t^*) + \hat{T}_2^{n+1}\boldsymbol{Q}_2^*(t^*)\Big)& \\ + \Big(-2\hat{T}_1^{n}\boldsymbol{Q}_1^*(t^*) + \hat{T}_2^{n}\boldsymbol{Q}_2^*(t^*)\Big)^2 (\Delta t)^2 &= 1 - |\hat{\boldsymbol{Q}}_1^*|^2, \quad i = 1,\end{aligned} \tag{3.102a}$$

$$\begin{aligned}&(2\Delta t)\hat{\boldsymbol{Q}}_i^* \cdot \Big(\hat{T}_{i-1}^{n+1}\boldsymbol{Q}_{i-1}^*(t^*) - 2\hat{T}_i^{n+1}\boldsymbol{Q}_i^*(t^*) + \hat{T}_{i+1}^{n+1}\boldsymbol{Q}_{i+1}^*(t)\Big) \\ &+ \Big(\hat{T}_{i-1}^{n}\boldsymbol{Q}_{i-1}^*(t^*) - 2\hat{T}_i^{n}\boldsymbol{Q}_i^*(t^*) + \hat{T}_{i+1}^{n}\boldsymbol{Q}_{i+1}^*(t^*)\Big)^2 (\Delta t)^2 = 1 - |\hat{\boldsymbol{Q}}_i^*|^2, \quad 2 \le i \le N-2,\end{aligned} \tag{3.102b}$$

$$\begin{aligned}&(2\Delta t)\hat{\boldsymbol{Q}}_{N-1}^* \cdot \Big(\hat{T}_{N-2}^{n+1}\boldsymbol{Q}_{N-2}^*(t^*) - 2\hat{T}_{N-1}^{n+1}\boldsymbol{Q}_{N-1}^*(t)\Big) \\ &+ \Big(\hat{T}_{N-2}^{n}\boldsymbol{Q}_{N-2}^*(t^*) - 2\hat{T}_{N-1}^{n}\boldsymbol{Q}_{N-1}^*(t^*)\Big)^2 (\Delta t)^2 = 1 - |\hat{\boldsymbol{Q}}_{N-1}|^2, \quad i = N-1,\end{aligned} \tag{3.102c}$$

for $\hat{T}_i^{n+1}$, $i = 1, \ldots, N-1$. System (3.102) is now linear in the unknowns $\hat{T}_i^{n+1}$. The resulting linear system of equations is tridiagonal of size $N-1$. Note that for given $\boldsymbol{Q}_i^*(t^*)$ and $\hat{\boldsymbol{Q}}_i^*$, the system matrix of (3.102) stays constant, i.e., during the fixed-point iteration, the system matrix has to be assembled only once and only the right hand side changes in each iteration. The second approach is to apply Newton's method on (3.101), which results in a changing system matrix in each iteration. Both approaches need suitable initial guesses for the tensions $\hat{T}_i^0$. These are typically the computed $\hat{T}_i$ of the previous time step or zero otherwise. In Section 4.1 of [75], a comparison of the CPU time ratios between the Newton's method and Picard's method is done for varying number of beads ranging from $N = 2$ to $N = 300$ in an uniaxial extensional flow at various flow strengths. They observed that the Picard approach (3.102) is always at least 10 % faster than the Newton approach regardless of chains size and flow strength.

From Section 2.2.2, we know that the equilibrium distribution of bead-rod chains does not coincide with the random-walk distribution. With the help of Liu's algorithm from above, we are able to generate bead-rod chains in equilibrium. For this, we consider System (3.97) with $\boldsymbol{u}_i^* = \boldsymbol{0}$, i.e., no underlying flow field. First, initial chains are randomly generated w.r.t. the random-walk distribution, i.e., the rod angles are uniformly distributed as this is close to the actual bead-rod chain equilibrium distribution [12]. For each bead-rod chain, we perform 10^6 time steps with $\Delta t = 10^{-3}$ and evolve the chain in this way into an equilibrium state. For the bead-rod chains, which are used in Section 5, this corresponds to around 240 to 6100 relaxation times (depending on the number of beads N) and should be sufficient to evolve the chains into equilibrium.

Now, we are able to simulate first sample trajectories of bead-rod chains, which are described by the SDE (3.95). Figure 3.7 visualizes the evolution of a bead-rod chain trajectory with $N = 25$ beads under steady shear flow. The bead-rod chain is initially in equilibrium, which is generated as described above. In 2D, the steady shear flow velocity field is given by

$$\boldsymbol{u}(\boldsymbol{r}) := \begin{bmatrix} 0 & \dot{\gamma} \\ 0 & 0 \end{bmatrix} \boldsymbol{r}, \tag{3.103}$$

where $\dot{\gamma} \in \mathbb{R}$ denotes the shear rate. As in [75] described, the corresponding $\boldsymbol{u}_i^*$ in (3.97a) is then given by

$$\boldsymbol{u}_i^* := \mathrm{Pe} \begin{bmatrix} 0 & 1 \\ 0 & 0 \end{bmatrix} \boldsymbol{r}_i^*, \tag{3.104}$$

where the dimensionless number $\mathrm{Pe} = \dot{\gamma} t_\mathrm{c}$ denotes the bead Peclet number, which is the ratio of bead diffusion time to characteristic flow time. In Figure 3.7, the Peclet number is set to $\mathrm{Pe} = 2.25$.

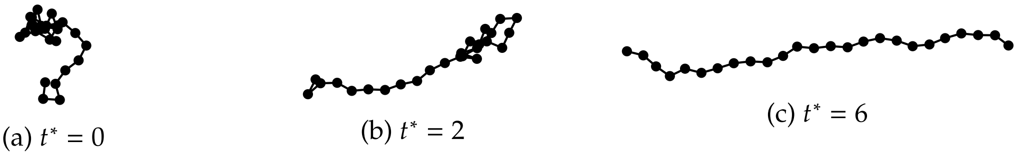
(a) $t^* = 0$ (b) $t^* = 2$ (c) $t^* = 6$

Figure 3.7. Bead-rod chain evolution in steady shear flow with $\mathrm{Pe} = 2.25$. Chain consists of $N = 25$ beads.

Performing certain averages with such sample trajectories, allows us to compute the polymeric stress tensor $\boldsymbol{\tau}_\mathrm{p}$, in which we are interested in. Details on how this is done are presented in the next section.

3.4.2 Noise filtering of the stress

For the computation of the polymeric stress tensor $\boldsymbol{\tau}_\mathrm{p}$, we start with the Kramers–Kirkwood expression

$$\boldsymbol{\tau}_\mathrm{p} := n \sum_{i=1}^{N} \langle \boldsymbol{R}_i \otimes \boldsymbol{F}_i^\mathrm{H} \rangle - n k_\mathrm{B} \vartheta \boldsymbol{I}, \tag{3.105}$$

where n is the polymeric number density, $\boldsymbol{R}_i$ the bead position vector relative to the chains center of mass $\boldsymbol{r}_\mathrm{c}$ (cf. Figure 2.5), $\boldsymbol{F}_i^\mathrm{H}$ the hydrodynamic drag force (2.1), k_B the Boltzmann constant, and ϑ the fluid temperature. See Section 2.2.3 for a discussion of other equivalent expressions for $\boldsymbol{\tau}_\mathrm{p}$. For the scope of this section, we non-dimensionalize (3.105) with $\tau_\mathrm{c}^\mathrm{p} = n k_\mathrm{B} \vartheta$, $l_\mathrm{c} = a$, and $F_\mathrm{c} = k_\mathrm{B} \vartheta / a$, which yields

$$\boldsymbol{\tau}_\mathrm{p}^* := \sum_{i=1}^{N} \langle \boldsymbol{R}_i^* \otimes \boldsymbol{F}_i^{*\mathrm{H}} \rangle - \boldsymbol{I}. \tag{3.106}$$

Utilizing (2.71), we transform (3.106) to

$$\boldsymbol{\tau}_{\mathrm{p}}^{*} := -\sum_{i=1}^{N} \langle \boldsymbol{R}_i^{*} \otimes \boldsymbol{F}_i^{*\mathrm{B}} + \boldsymbol{R}_i^{*} \otimes \boldsymbol{F}_i^{*\mathrm{C}} \rangle - \boldsymbol{I}, \tag{3.107}$$

where dimensionless Brownian force can be identified with

$$\boldsymbol{F}_i^{*\mathrm{B}} = \sqrt{\frac{2}{\Delta t}} \Delta \boldsymbol{W}_i^{*}, \quad \Delta \boldsymbol{W}_i^{*} \sim \mathcal{N}(0,1)^d, \tag{3.108}$$

from (3.99) and $\boldsymbol{F}_i^{*\mathrm{C}}$ from (3.98). As in [21] described, evaluating (3.107) is problematic from a numerically point of view due to stochastic noise of order $\Delta t^{-1/2}$. From (3.108), it is straightforward to see that $\boldsymbol{F}_i^{*\mathrm{B}} \in \mathcal{O}(\Delta t^{-1/2})$. The constraint force $\boldsymbol{F}_i^{*\mathrm{C}}$ also shows stochastic noise of order $\Delta t^{-1/2}$ as it has to compensate the Brownian force in some directions to enforce the constant rod length. Doyle, Shaqfeh and Gast developed in [21] a modified form of the Kramers–Kirkwood expression, which filters out the stochastic noise contributions of order $\Delta t^{-1/2}$. The expression is given by

$$\boldsymbol{\tau}_{\mathrm{p}}^{*}(t^{*} + \Delta t) := \boldsymbol{\tau}_{\mathrm{p}}^{*B}(t^{*} + \Delta t) + \boldsymbol{\tau}_{\mathrm{p}}^{*\mathrm{C}}(t^{*} + \Delta t). \tag{3.109}$$

The idea for the derivation of $\boldsymbol{\tau}_{\mathrm{p}}^{*B}(t^{*} + \Delta t)$ is to exploit the fact that $\boldsymbol{R}_i^{*}(t^{*})$ and $\boldsymbol{F}_i^{*\mathrm{B}}(t^{*})$ are uncorrelated together with $\langle \boldsymbol{F}_i^{*\mathrm{B}}(t^{*}) \rangle = \boldsymbol{0}$. Note that $\boldsymbol{F}_i^{*\mathrm{B}}$ changes discontinuously at the end of the time-step from $\boldsymbol{F}_i^{*\mathrm{B}}(t^{*})$ to $\boldsymbol{F}_i^{*\mathrm{B}}(t^{*} + \Delta t)$. As in [31] described, we thus take the mean of the two values for the evaluation at $t^{*} + \Delta t$. The evaluation of $\left\langle \boldsymbol{R}_i^{*} \otimes \boldsymbol{F}_i^{*\mathrm{B}} \right\rangle$ at $t^{*} + \Delta t$ is then given by

$$\left\langle \boldsymbol{R}_i^{*}(t^{*} + \Delta t) \otimes \frac{\boldsymbol{F}_i^{*\mathrm{B}}(t^{*}) + \boldsymbol{F}_i^{*\mathrm{B}}(t^{*} + \Delta t)}{2} \right\rangle. \tag{3.110}$$

Since $\boldsymbol{R}_i^{*}(t^{*} + \Delta t)$ and $\boldsymbol{F}_i^{*\mathrm{B}}(t^{*} + \Delta t)$ are uncorrelated, we can drop the term

$$\left\langle \frac{\boldsymbol{R}_i^{*}(t^{*} + \Delta t) \otimes \boldsymbol{F}_i^{*\mathrm{B}}(t^{*} + \Delta t)}{2} \right\rangle \tag{3.111}$$

in (3.110). With the same argumentation, one can subtract the term

$$\left\langle \frac{\boldsymbol{R}_i^{*}(t^{*}) \otimes \boldsymbol{F}_i^{*\mathrm{B}}(t^{*})}{2} \right\rangle \tag{3.112}$$

from (3.110), which yields

$$\boldsymbol{\tau}_{\mathrm{p}}^{*B}(t^{*} + \Delta t) := -\sum_{i=1}^{N} \left\langle \frac{\boldsymbol{R}_i^{*}(t^{*} + \Delta t) - \boldsymbol{R}_i^{*}(t^{*})}{2} \otimes \boldsymbol{F}_i^{*\mathrm{B}}(t^{*}) \right\rangle, \tag{3.113}$$

where $\boldsymbol{F}_i^{*\mathrm{B}}(t^*)$ is the Brownian force, which is used during the computation of (3.99), i.e., using the $\Delta \boldsymbol{W}_i^*$ from (3.99) for the computation of (3.108). Note that $\boldsymbol{R}_i^*(t^* + \Delta t) - \boldsymbol{R}_i^*(t^*)$ is $\mathcal{O}(\sqrt{\Delta t})$ and $\boldsymbol{F}_i^{*\mathrm{B}}(t^*)$ is $\mathcal{O}(1/\sqrt{\Delta t})$, which makes (3.113) an $\mathcal{O}(1)$ quantity.

For the derivation of the second term in (3.109), we note that the constraint force $\hat{\boldsymbol{F}}_i^{*\mathrm{C}} := \boldsymbol{F}_i^{*\mathrm{C}}(\hat{T}, \boldsymbol{Q}^*(t^*))$ in (3.100) consists of two contributions. A $\mathcal{O}(1)$-contribution due to the velocity $\boldsymbol{u}$ and a $\mathcal{O}(1/\sqrt{\Delta t})$-contribution due to the Brownian force $\boldsymbol{F}_i^{*\mathrm{B}}(t^*)$ as in [21] described. In the following, we capture this $\mathcal{O}(1/\sqrt{\Delta t})$-contribution, denoted by $\tilde{\boldsymbol{F}}_i^{*\mathrm{C}} := \boldsymbol{F}_i^{*\mathrm{C}}(\tilde{T}, \boldsymbol{Q}^*(t^*))$, with a separate computation such that $\hat{\boldsymbol{F}}_i^{*\mathrm{C}} - \tilde{\boldsymbol{F}}_i^{*\mathrm{C}} \in \mathcal{O}(1)$. For this, we set $\boldsymbol{u} = \boldsymbol{0}$ in (3.99), which yields

$$\hat{\boldsymbol{r}}_i^* := \boldsymbol{r}_i^*(t^*) + \sqrt{2\Delta t}\Delta \boldsymbol{W}_i^* \overset{(3.108)}{=} \boldsymbol{r}_i^*(t^*) + \Delta t \boldsymbol{F}_i^{*\mathrm{B}}(t^*), \quad i = 1, \ldots, N. \tag{3.114}$$

Substituting $\hat{\boldsymbol{r}}_i^*$ in (3.100) with (3.114) gives

$$\boldsymbol{r}_i^*(t^* + \Delta t) := \boldsymbol{r}_i^*(t^*) + \Delta t \left[\boldsymbol{F}_i^{*\mathrm{B}}(t^*) + \boldsymbol{F}_i^{*\mathrm{C}}(\tilde{T}, \boldsymbol{Q}^*(t^*))\right], \quad i = 1, \ldots, N. \tag{3.115}$$

where $\boldsymbol{F}_i^{*\mathrm{C}}(\tilde{T}, \boldsymbol{Q}^*(t^*))$ is defined in (3.98). In (3.115), the tensions $\tilde{T}_i$ are approximated by solving the linear system of equations

$$\underbrace{\left[\boldsymbol{F}_{i+1}^{*\mathrm{B}} - \boldsymbol{F}_i^{*\mathrm{B}} + \boldsymbol{F}_{i+1}^{*\mathrm{C}}(\tilde{T}, \boldsymbol{Q}^*(t^*)) - \boldsymbol{F}_i^{*\mathrm{C}}(\tilde{T}, \boldsymbol{Q}^*(t^*))\right]}_{=:\tilde{\boldsymbol{F}}_i^{*B+C}} \cdot \boldsymbol{Q}_i^*(t^*) = 0, \quad i = 1, \ldots, N-1, \tag{3.116}$$

which is obtained by using (3.115), (3.97b), and neglecting the nonlinear $(\Delta t)^2$-term in

$$\begin{aligned}
&\left|\boldsymbol{r}_{i+1}^*(t^* + \Delta t) - \boldsymbol{r}_i^*(t^* + \Delta t)\right|^2 \overset{(3.115)}{=} \left|\boldsymbol{r}_{i+1}^*(t^*) - \boldsymbol{r}_i^*(t^*) + \Delta t \tilde{\boldsymbol{F}}_i^{*B+C}\right|^2 && (3.117\text{a})\\
\Leftrightarrow \quad &\left|\boldsymbol{Q}_i^*(t^* + \Delta t)\right|^2 = \left|\boldsymbol{Q}_i^*(t^*) + \Delta t \tilde{\boldsymbol{F}}_i^{*B+C}\right|^2 && (3.117\text{b})\\
\Leftrightarrow \quad &\left|\boldsymbol{Q}_i^*(t^* + \Delta t)\right|^2 = \left|\boldsymbol{Q}_i^*(t^*)\right|^2 + 2\Delta t \tilde{\boldsymbol{F}}_i^{*B+C} \cdot \boldsymbol{Q}_i^*(t^*) + (\Delta t)^2 \left|\tilde{\boldsymbol{F}}_i^{*B+C}\right|^2 && (3.117\text{c})\\
\overset{(3.97\text{b})}{\Leftrightarrow} \quad &0 = 2\Delta t \tilde{\boldsymbol{F}}_i^{*B+C} \cdot \boldsymbol{Q}_i^*(t^*) + \cancel{(\Delta t)^2 \left|\tilde{\boldsymbol{F}}_i^{*B+C}\right|^2}. && (3.117\text{d})
\end{aligned}$$

System (3.116) is linear in the tensions $\tilde{T}_i$ and of tridiagonal structure.

With the help of the following lemma, we can derive the desired expression for $\boldsymbol{\tau}_\mathrm{p}^{*C}$.

Lemma 3.5. *Assume that* (3.116) *has a unique solution. Then it holds* $\left\langle \boldsymbol{R}_i^*(t^*) \otimes \tilde{\boldsymbol{F}}_i^{*\mathrm{C}} \right\rangle = \boldsymbol{0}$, $i = 1, \ldots, N$, *where* $\tilde{\boldsymbol{F}}_i^{*\mathrm{C}} := \boldsymbol{F}_i^{*\mathrm{C}}(\tilde{T}, \boldsymbol{Q}^*(t^*))$ *are the constraint forces computed in* (3.116).

Proof. For the proof, we use (3.116) and $\left\langle \boldsymbol{F}_i^{*\mathrm{B}}(t^*) \right\rangle = \boldsymbol{0}$, which follows form (3.108). Additionally, one has to assume that (3.116) has a unique solution. Since (3.116) is a linear system with unknowns $\tilde{T}_i$, $i = 1, \dots, N-1$, the tensions $\tilde{T}_i$ can be expressed via

$$\tilde{T}_i = -\sum_{j=1}^{N-1} C_{ij}^{-1} \left(\boldsymbol{F}_{i+1}^{*\mathrm{B}} - \boldsymbol{F}_i^{*\mathrm{B}} \right) \cdot \boldsymbol{Q}_j^*(t^*), \tag{3.118}$$

where C_{ij}^{-1} are the entries of the inverted system matrix associated to (3.116). Let $R_{q,n}^*(t^*)$ denote the nth entry of the vector $\boldsymbol{R}_q^*(t^*) \in \mathbb{R}^d$ with $q = 1, \dots, N$. The entries of the vectors $\boldsymbol{Q}_j^*(t^*), \boldsymbol{F}_i^{*\mathrm{B}} \in \mathbb{R}^d$ are denoted analogously. Multiplying both sides of (3.118) with $R_{q,n}^*(t^*) Q_{p,m}^*(t^*)$ gives

$$R_{q,n}^*(t^*) \tilde{T}_i Q_{p,m}^*(t^*) = -\sum_{j=1}^{N-1} \sum_{k=1}^{d} C_{ij}^{-1} \left(F_{i+1,k}^{*\mathrm{B}} - F_{i,k}^{*\mathrm{B}} \right) Q_{j,k}^*(t^*) Q_{p,m}^*(t^*) R_{q,n}^*(t^*). \tag{3.119}$$

By taking the expectation value of (3.119), one can exploit that the entries of the Brownian forces are uncorrelated to all remaining factors in (3.119). Together with $\langle F_{i,k}^{*\mathrm{B}}(t^*) \rangle = \langle F_{i+1,k}^{*\mathrm{B}}(t^*) \rangle = 0$, the expectation value of (3.119) reduces to

$$\begin{aligned}
\left\langle R_{q,n}^*(t^*) \tilde{T}_i Q_{p,m}^*(t^*) \right\rangle &= -\sum_{j=1}^{N-1} \sum_{k=1}^{d} \left\langle C_{ij}^{-1} \left(F_{i+1,k}^{*\mathrm{B}} - F_{i,k}^{*\mathrm{B}} \right) Q_{j,k}^*(t^*) Q_{p,m}^*(t^*) R_{q,n}^*(t^*) \right\rangle \\
&= \sum_{j=1}^{N-1} \sum_{k=1}^{d} \left\langle \left(F_{i+1,k}^{*\mathrm{B}} - F_{i,k}^{*\mathrm{B}} \right) \right\rangle \left\langle C_{ij}^{-1} Q_{j,k}^*(t^*) Q_{p,m}^*(t^*) R_{q,n}^*(t^*) \right\rangle \\
&= 0,
\end{aligned} \tag{3.120}$$

where $q \in \{1, \dots, N\}$, $p, i \in \{1, \dots, N-1\}$, and $m, n \in \{1, \dots, d\}$. Entry (n, m) of $\langle \boldsymbol{R}_i^*(t^*) \otimes \tilde{\boldsymbol{F}}_i^{*\mathrm{C}} \rangle$ can be expressed in terms of (3.120), which leads to

$$\left\langle R_{i,n}^*(t^*) \tilde{F}_{i,m}^{*\mathrm{C}} \right\rangle \overset{(3.98)}{=} \begin{cases} \langle R_{1,n}^*(t^*) \tilde{T}_1 Q_{1,m}^*(t^*) \rangle = 0, & i = 1, \\ \langle R_{i,n}^*(t^*) [\tilde{T}_i Q_{i,m}^*(t^*) - \tilde{T}_{i-1} Q_{i-1,m}^*(t^*)] \rangle = 0, & i = 2, \dots, N-1, \\ -\langle R_{N,n}^*(t^*) \tilde{T}_{N-1} Q_{N-1,m}^*(t^*) \rangle = 0, & i = N. \end{cases} \tag{3.121}$$

From (3.121), we deduce $\langle \boldsymbol{R}_i^*(t^*) \otimes \tilde{\boldsymbol{F}}_i^{*\mathrm{C}} \rangle = \boldsymbol{0}$. □

In the following, we start with the evaluation of $\left\langle \boldsymbol{R}_i^* \otimes \hat{\boldsymbol{F}}_i^{*\mathrm{C}} \right\rangle$ via

$$\left\langle \frac{\boldsymbol{R}_i^*(t^*) + \boldsymbol{R}_i^*(t^* + \Delta t)}{2} \otimes \hat{\boldsymbol{F}}_i^{*\mathrm{C}} \right\rangle, \tag{3.122}$$

which is still a $\mathcal{O}(1/\sqrt{\Delta t})$-quantity. Adding a zero to (3.122) yields

$$\left\langle \frac{\boldsymbol{R}_i^*(t^*) + \boldsymbol{R}_i^*(t^* + \Delta t)}{2} \otimes \left[\hat{\boldsymbol{F}}_i^{*\mathrm{C}} - \tilde{\boldsymbol{F}}_i^{*\mathrm{C}} \right] + \frac{\boldsymbol{R}_i^*(t^*) + \boldsymbol{R}_i^*(t^* + \Delta t)}{2} \otimes \tilde{\boldsymbol{F}}_i^{*\mathrm{C}} \right\rangle. \tag{3.123}$$

The second term of (3.109) is then obtained by subtracting $\left\langle \boldsymbol{R}_i^*(t^*) \otimes \tilde{\boldsymbol{F}}_i^{*\mathrm{C}} \right\rangle = \boldsymbol{0}$ (cf. Lemma 3.5) from (3.123), which gives

$$\begin{aligned} \boldsymbol{\tau}_\mathrm{p}^{*\mathrm{C}}(t^* + \Delta t) := -\sum_{i=1}^{N} & \left\langle \frac{\boldsymbol{R}_i^*(t^* + \Delta t) + \boldsymbol{R}_i^*(t^*)}{2} \otimes \left(\hat{\boldsymbol{F}}_i^{*\mathrm{C}} - \tilde{\boldsymbol{F}}_i^{*\mathrm{C}} \right) \right\rangle \\ & + \left\langle \frac{\boldsymbol{R}_i^*(t^* + \Delta t) - \boldsymbol{R}_i^*(t^*)}{2} \otimes \tilde{\boldsymbol{F}}_i^{*\mathrm{C}} \right\rangle , \end{aligned} \tag{3.124}$$

where $\hat{\boldsymbol{F}}_i^{*\mathrm{C}} := \boldsymbol{F}_i^{*\mathrm{C}}(\hat{T}, \boldsymbol{Q}^*(t^*))$ is the constraint force computed during (3.100) and $\tilde{\boldsymbol{F}}_i^{*\mathrm{C}} := \boldsymbol{F}_i^{*\mathrm{C}}(\tilde{T}, \boldsymbol{Q}^*(t^*))$ is obtained by solving the auxiliary problem (3.116) for the tensions $\tilde{T}_i$. Note that $\hat{\boldsymbol{F}}_i^{*\mathrm{C}}$ and $\tilde{\boldsymbol{F}}_i^{*\mathrm{C}}$ use the identical Brownian force $\boldsymbol{F}_i^{*\mathrm{B}}(t^*)$ during their computations. In (3.124), $\boldsymbol{R}_i^*(t^* + \Delta t) + \boldsymbol{R}_i^*(t^*)$ and $\hat{\boldsymbol{F}}_i^{*\mathrm{C}} - \tilde{\boldsymbol{F}}_i^{*\mathrm{C}}$ are in $\mathcal{O}(1)$ such that their product is also $\mathcal{O}(1)$. The difference $\boldsymbol{R}_i^*(t^* + \Delta t) - \boldsymbol{R}_i^*(t^*)$ is $\mathcal{O}(\sqrt{\Delta t})$ and $\tilde{\boldsymbol{F}}_i^{*\mathrm{C}} \in \mathcal{O}(1/\sqrt{\Delta t})$, i.e., the corresponding product in (3.124) is $\mathcal{O}(1)$, which makes $\boldsymbol{\tau}_\mathrm{p}^{*\mathrm{C}}(t^* + \Delta t)$ a $\mathcal{O}(1)$-quantity.

Figure 3.8 compares the shear stress component of the original Kramers–Kirkwood expression (3.107) with the modified version (3.109) over time in a steady shear flow scenario. For this, 2000 bead-rod chains with $N = 50$ beads in equilibrium and $\mathrm{Pe} = 0.56$ (cf. (3.104)) are evolved in time with $\Delta t = 2.5 \cdot 10^{-4}$. The unfiltered polymeric stress (3.107) and the corresponding filtered version (3.109) are then obtained by averaging. The actual shear stress is completely hidden behind the stochastic noise in Figure 3.8a. Applying the noise filtering technique of [21] from above, reveals the actual shear stress behavior in Figure 3.8b.

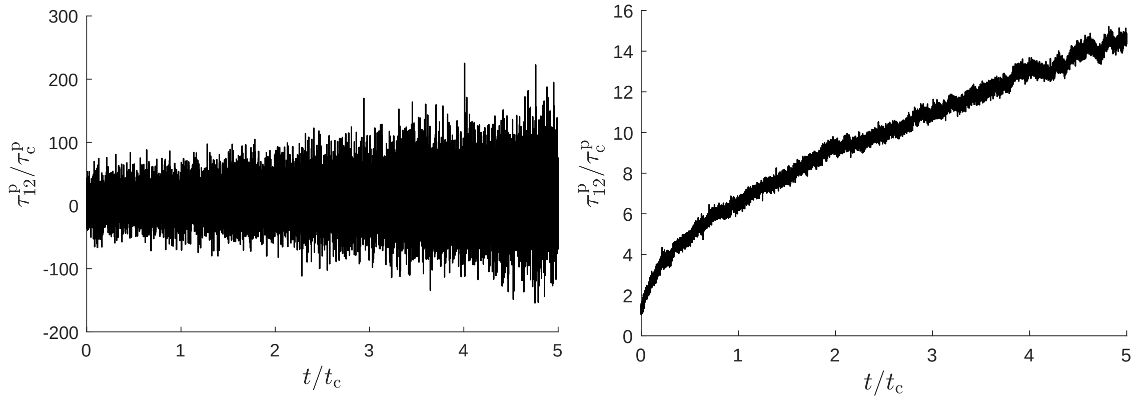

(a) Original expression (3.107)

(b) Filtered expression (3.109)

Figure 3.8. Comparison of shear stress computed with (3.107) and (3.109) in steady shear flow with $\mathrm{Pe} = 0.56$. Stresses are approximated with 2000 chains, $N = 50$ beads, and $\Delta t = 2.5 \cdot 10^{-4}$.

In Figure 3.9, we validated our own implementation in Matlab [44] of Liu's algorithm from Section 3.4.1 and the noise filtering from above. The validation is done by comparing the results to a reference solution from [51]. For this, we simulated the temporal evolution of the polymeric stress in steady uniaxial extensional flow in 3D. The corresponding velocities in (3.95a) and (3.97a) are given by

$$\boldsymbol{u}_i := \dot{\epsilon} \begin{bmatrix} 1 & 0 & 0 \\ 0 & -0.5 & 0 \\ 0 & 0 & -0.5 \end{bmatrix} \boldsymbol{r}_i, \qquad \boldsymbol{u}_i^* := \mathrm{Pe} \begin{bmatrix} 1 & 0 & 0 \\ 0 & -0.5 & 0 \\ 0 & 0 & -0.5 \end{bmatrix} \boldsymbol{r}_i^*, \tag{3.125}$$

where $\dot{\epsilon}$ denotes the strain rate and $\mathrm{Pe} = \dot{\epsilon} t_\mathrm{c}$ the dimensionless bead Peclet number, which is the ratio of bead diffusion time to characteristic flow time. The polymeric stress (3.109) is approximated by averaging 1000 bead-rod chains with $N = 50$ beads. Here, we choose $\mathrm{Pe} = 0.56$ as done in [51]. The time-step size is set to $\Delta t = 2.5 \cdot 10^{-4}$. From Figure 3.9, we deduce that the implementation works as intended. Small deviations from the reference solution cannot be prevented due to the stochastic nature of the problem and the use of a finite number of bead-rod chains for the approximation of the polymeric stress. Note that the stress curve in Figure 3.9 looks less noisy compared to the curve in Figure 3.8b, which is due to the nature of the logarithmic plot and the additional $1/(N-1)$ scaling of the stress in Figure 3.9.

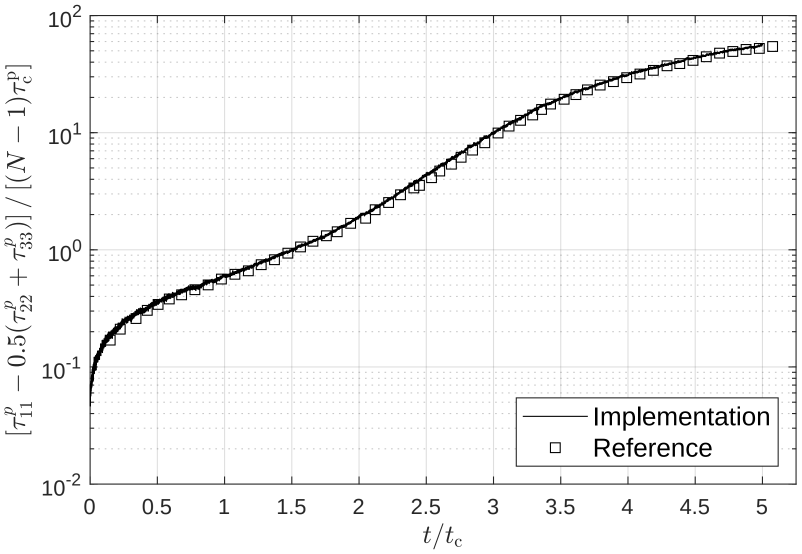

Figure 3.9. Comparison of computed polymeric stress evolution of bead-rod chains with $N = 50$ beads to reference data from Fig. 6 in [51]. Polymeric stress is approximated with 1000 bead-rod chains in uniaxial extensional flow with $\mathrm{Pe} = 0.56$ and $\Delta t = 2.5 \cdot 10^{-4}$.

3.4.3 Estimation of relaxation times

With the tools from Sections 3.4.1 and 3.4.2, we are able to estimate the dimensionless relaxation time

$$\lambda^*(N) = \lambda(N)/t_\mathrm{c} =: \alpha(N), \tag{3.126}$$

which appears in the non-dimensionalized system of SDEs (2.100) and the dimensionless polymeric stress tensor (2.105) from Section 2.2.4. The dimensionless relaxation time characterizes how fast the polymeric stress of perturbed chains decays. More precisely, the factor $1/\alpha$ is defined as the stress decay rate of initially perturbed chains that evolve towards their equilibrium states (cf. Figure 3.10).

In [21], the approximation

$$\alpha^{\text{formula}}(N) := 0.0142N^2, \tag{3.127}$$

is computed via a fit, which is only a good approximation for chains with many beads (cf. Table 3.5). In Section 5, chains are considered, where (3.127) is not suitable as it deviates too much from the actual value of $\alpha(N)$. Therefore, we estimate our own values for the dimensionless relaxation time $\alpha(N)$.

The dimensionless relaxation time $\alpha(N)$ is obtained by considering initially in x-direction fully stretched chains that are afterward driven to equilibrium. We consider the 3D version of System (3.97) with $\boldsymbol{u}_i^* = \boldsymbol{0}$ and are interested in the average transient stress

$$\bar{\tau}_{\mathrm{p},N} := \frac{(\boldsymbol{\tau}_{\mathrm{p}})_{11} - 0.5\big((\boldsymbol{\tau}_{\mathrm{p}})_{22} + (\boldsymbol{\tau}_{\mathrm{p}})_{33}\big)}{N-1} \tag{3.128}$$

over time. As in [21, 75] stated, the dimensionless relaxation time $\alpha(N)$ is then obtained by $-1/$slope of the linear part of the $\log(\bar{\tau}^*_{\mathrm{p},N})$ vs. t^* plot, i.e., we fit $\bar{\tau}^*_{\mathrm{p},N}$ with $A\exp(-t^*/\alpha(N))$. In Figure 3.10, this fitting procedure is visualized for the case $N = 5$ and $N = 10$. Table 3.5 lists the estimated dimensionless relaxation times for chains with $N = 2, \ldots, 10$ beads. We list our own computed relaxation times in column α^{est} and also the results $\alpha^{\text{birefringence}}$, α^{stress} from Table 2 in [21] for comparison. As the last column in Table 3.5 indicates, formula (3.127) is not precise for chains with beads $N \leq 10$ as the relative error ranges from 7% to 49%, which is not surprising since the formula is only intended for long chains. As expected, one can observe that the relative error decreases for increasing N. In this thesis, we consider only chains with $N \leq 20$ beads. We choose our own computed values $\alpha^{\text{est}}(N)$ for chains with $N \leq 10$ beads and formula (3.127) for chains with more than 10 beads.

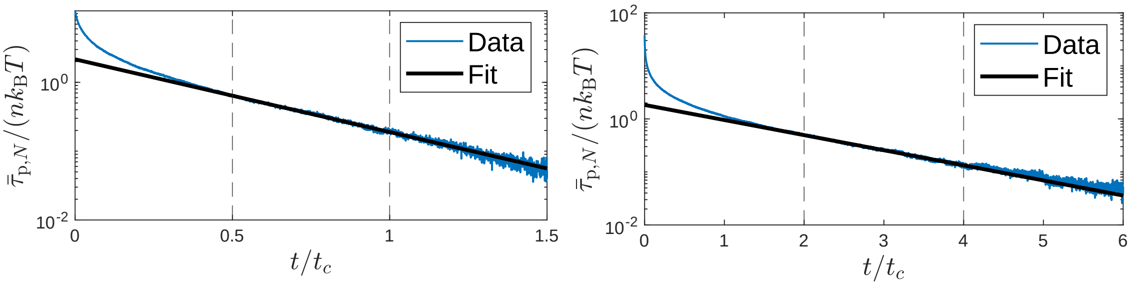

(a) $N = 5$, $\alpha^{\text{est}} = 0.4107$

(b) $N = 10$, $\alpha^{\text{est}} = 1.5250$

Figure 3.10. Estimation of the dimensionless relaxation times $\alpha(N)$ of bead-rod chains via linear fit with 10000 chains. Only the data enclosed by the vertical dashed lines is used for the fit.

N	$\alpha^{\text{birefrigence}}$	α^{stress}	α^{est}	α^{formula}	$\frac{\lvert\alpha^{\text{est}}-\alpha^{\text{formula}}\rvert}{\alpha^{\text{formula}}}$
2	0.0841	0.0836	0.0844	0.0568	0.4859
3	0.1420	0.1270	0.1634	0.1278	0.2785
4	–	–	0.2546	0.2272	0.1206
5	0.4110	0.3880	0.4107	0.3550	0.1569
6	–	–	0.5828	0.5112	0.1401
7	–	–	0.7739	0.6958	0.1122
8	–	–	0.9698	0.9088	0.0671
9	–	–	1.2372	1.1502	0.0756
10	1.4200	1.5200	1.5250	1.4200	0.0739

Table 3.5. Estimated relaxation times for bead-rod chains with $N = 2, \dots, 10$ beads. The first two columns ($\alpha^{\text{birefrigence}}$, α^{stress}) are results from Tab. 2 in [21]. Column α^{est} contains our own computed relaxation times. Column α^{formula} contains relaxation times evaluated with (3.127).

3.4.4 BCF Scheme

In Sections 3.4.1 and 3.4.2, we introduced the numerical schemes, which are required for the simulation of bead-rod chains in the Lagrangian setting and the computation of the polymeric stress tensor with special emphasis on noise filtering. To obtain the temporal discretization of the dimensionless connector-vector formulation in the Eulerian setting from Section 2.2.4, which is given by

$$\begin{aligned} \mathrm{d}\boldsymbol{Q}_i &= [-\boldsymbol{u} \cdot \nabla \boldsymbol{Q}_i + (\nabla \boldsymbol{u})\boldsymbol{Q}_i + \boldsymbol{F}_i]\,\mathrm{d}t \\ &\qquad + \sqrt{\frac{2\alpha(N)}{\mathrm{Wi}(N)}}(\mathrm{d}\boldsymbol{W}_{i+1} - \mathrm{d}\boldsymbol{W}_i), \quad i = 1, \dots, N-1, \end{aligned} \tag{3.129a}$$

$$\boldsymbol{Q}_i \cdot \boldsymbol{Q}_i - 1 = 0, \quad i = 1, \dots, N-1, \tag{3.129b}$$

we apply the idea of Liu's algorithm from Section 3.4.1. In (3.129), $\boldsymbol{Q}_i$ denotes the connector-vector from bead i to $i+1$, $\boldsymbol{u}$ the underlying velocity field, $\alpha(N)$ the dimensionless relaxation time, $\mathrm{Wi}(N)$ the Weissenberg number, $\boldsymbol{W}_i$ the Wiener processes, and $\boldsymbol{F}_i$ is the constraint force on $\boldsymbol{Q}_i$ given by

$$\boldsymbol{F}_i = \boldsymbol{F}_i(T, \boldsymbol{Q}) := \boldsymbol{F}^{\mathrm{C}}_{i+1}(T, \boldsymbol{Q}) - \boldsymbol{F}^{\mathrm{C}}_i(T, \boldsymbol{Q}), \quad i = 1, \dots, N-1, \tag{3.130}$$

where $\boldsymbol{F}^{\mathrm{C}}_i(T, \boldsymbol{Q})$ is defined in (3.98). This provides the basis for the Brownian configuration field (BCF) method from Section 3.1. Additionally, the computation of the polymeric stress (2.105) is adapted into the BCF setting. The required spatial discretizations are done with the finite element method. These are the last missing pieces, which are needed for simulating the fully coupled Navier–Stokes bead-rod chain System (3.164). In this section, we dropped the * again to simplify the notation. Here, all variables are treated dimensionless.

The following predictor-corrector algorithm for retrieving $\boldsymbol{Q}_i(t+\Delta t)$ for given $\boldsymbol{Q}_i(t)$ is based on the ideas from Section 3.4.1. For the spatial discretization, we approximate the vector fields $\boldsymbol{Q}_{i,h}$ in the space Q_h and the tensions $T_{i,h}$ in the space T_h, which are given by

$$Q_h := \left\{ \boldsymbol{Q} \in C(\bar{\Omega})^2 \mid \forall K \in \mathcal{T}_h, \boldsymbol{Q}_{|K} \in \mathbb{Q}_1^2(K) \right\}, \tag{3.131a}$$

$$T_h := \left\{ v \in C(\bar{\Omega}) \mid \forall K \in \mathcal{T}_h, v_{|K} \in \mathbb{Q}_1(K) \right\}. \tag{3.131b}$$

In the first substep, an unconstrained (predictor) step is done, where for given $\boldsymbol{u}_h \in U_h$ and $\boldsymbol{Q}_{i,h}^n \in Q_h$ a $\hat{\boldsymbol{Q}}_{i,h} \in Q_h$ is constructed by neglecting the constraint force $\boldsymbol{F}_i$ in (3.129a). After this, the rod length constraint (3.129b) does no longer hold for $\hat{\boldsymbol{Q}}_{i,h}$. The weak formulation of this substep is given by:

For given $\boldsymbol{u}_h \in U_h$ and $\boldsymbol{Q}_{i,h}^n \in Q_h$, find $\hat{\boldsymbol{Q}}_{i,h} \in Q_h$ such that

$$\begin{aligned}\left(\hat{\boldsymbol{Q}}_{i,h}, \boldsymbol{q}_h\right) + \Delta t \left(\boldsymbol{u}_h \cdot \nabla \hat{\boldsymbol{Q}}_{i,h}, \boldsymbol{q}_h\right) &= \left(\boldsymbol{Q}_{i,h}^n, \boldsymbol{q}_h\right) + \left((\nabla \boldsymbol{u}_h)\boldsymbol{Q}_{i,h}^n, \boldsymbol{q}_h\right)\Delta t \\ &+ \sqrt{\frac{2\alpha(N)\Delta t}{\mathrm{Wi}(N)}} \left(\Delta \bar{\boldsymbol{W}}_{i+1}^n - \Delta \bar{\boldsymbol{W}}_i^n, \boldsymbol{q}_h\right) \quad \forall \boldsymbol{q}_h \in Q_h,\end{aligned} \tag{3.132}$$

for $i = 1, \dots, N-1$. Note that $\Delta \bar{\boldsymbol{W}}_i^n \sim \mathcal{N}(0,1)^2$ for $i = 1, \dots, N$ is a spatially constant vector field. Additional stabilization is required, which is done with the SUPG method [45] by testing with

$$\boldsymbol{q}_h^{\mathrm{SUPG}} := \boldsymbol{q}_h + h_K \frac{\boldsymbol{u}_h}{|\boldsymbol{u}_h|} \nabla \boldsymbol{q}_h \tag{3.133}$$

instead of $\boldsymbol{q}_h$ in (3.132). In (3.133), h_K denotes the diameter of element $K \in \mathcal{T}_h$.

In the corrector step, tensions $\hat{T}_{i,h} \in T_h$, $i = 1, \dots, N-1$, are computed such that the rod length constraints are fulfilled again in the weak sense. The corresponding weak formulation to (3.101) in the connector-vector formulation is given by:

For given $\boldsymbol{Q}_{i,h}^n, \hat{\boldsymbol{Q}}_{i,h} \in \boldsymbol{Q}_h$ find $\hat{T}_{i,h} \in T_h$ such that

$$\begin{aligned}(2\Delta t) &\left(\hat{\boldsymbol{Q}}_{1,h} \cdot \left(-2\hat{T}_{1,h}\boldsymbol{Q}_{1,h}^n + \hat{T}_{2,h}\boldsymbol{Q}_{2,h}^n\right), v_h\right)_h \\ &+ \left(\left(-2\hat{T}_{1,h}\boldsymbol{Q}_{1,h}^n + \hat{T}_{2,h}\boldsymbol{Q}_{2,h}^n\right)^2, v_h\right)_h (\Delta t)^2 \\ &= \left(1 - |\hat{\boldsymbol{Q}}_{1,h}|^2, v_h\right)_h, \quad i = 1, \quad \forall v_h \in T_h,\end{aligned} \tag{3.134a}$$

$$\begin{aligned}(2\Delta t) &\left(\hat{\boldsymbol{Q}}_{i,h} \cdot \left(\hat{T}_{i-1,h}\boldsymbol{Q}_{i-1,h}^n - 2\hat{T}_{i,h}\boldsymbol{Q}_{i,h}^n + \hat{T}_{i+1,h}\boldsymbol{Q}_{i+1,h}^n\right), v_h\right)_h \\ &+ \left(\left(\hat{T}_{i-1,h}\boldsymbol{Q}_{i-1,h}^n - 2\hat{T}_{i,h}\boldsymbol{Q}_{i,h}^n + \hat{T}_{i+1,h}\boldsymbol{Q}_{i+1,h}^n\right)^2, v_h\right)_h (\Delta t)^2 \\ &= \left(1 - |\hat{\boldsymbol{Q}}_{i,h}|^2, v_h\right)_h, \quad i = 2, \dots, N-2, \quad \forall v_h \in T_h,\end{aligned} \tag{3.134b}$$

$\hat{K}$	n_q	$\hat{\boldsymbol{x}}_i$	$\hat{w}_i$
Square	4	$(0,0),(1,0),(1,1),(0,1)$	$1/4$
Triangle	3	$(0,0),(1,0),(0,1)$	$1/6$

Table 3.6. Quadrature rules, which are used for the lumped L^2-inner product (3.137).

$$\begin{aligned}(2\Delta t)&\left(\hat{\boldsymbol{Q}}_{N-1,h}\cdot\left(\hat{T}_{N-2,h}\boldsymbol{Q}^n_{N-2,h}-2\hat{T}_{N-1,h}\boldsymbol{Q}^n_{N-1,h}\right),v_h\right)_h\\&+\left(\left(\hat{T}_{N-2,h}\boldsymbol{Q}^n_{N-2,h}-2\hat{T}_{N-1,h}\boldsymbol{Q}^n_{N-1,h}\right)^2,v_h\right)_h(\Delta t)^2\\&=\left(1-|\hat{\boldsymbol{Q}}_{N-1,h}|^2,v_h\right)_h,\quad i=N-1,\quad \forall v_h\in T_h.\end{aligned}\tag{3.134c}$$

After the tension fields $\hat{T}_{i,h}$, $i=1,\dots,N-1$, are obtained, $\boldsymbol{Q}^{n+1}_{i,h}\in Q_h$ can be computed via the L^2-projection

$$\left(\boldsymbol{Q}^{n+1}_{i,h},\boldsymbol{q}_h\right)_h=\left(\hat{\boldsymbol{Q}}_{i,h},\boldsymbol{q}\right)_h+\Delta t\left(\boldsymbol{F}_i(\hat{T}_h,\boldsymbol{Q}^n_h),\boldsymbol{q}_h\right)_h\quad\forall\boldsymbol{q}_h\in Q_h,\tag{3.135}$$

where $\boldsymbol{F}_i(\hat{T}_h,\boldsymbol{Q}^n_h)$ is defined in (3.130). By construction, $\boldsymbol{Q}^{n+1}_{i,h}$ satisfies the rod length constraint (3.129b) in the weak sense

$$\left(\boldsymbol{Q}^{n+1}_{i,h}\cdot\boldsymbol{Q}^{n+1}_{i,h}-1,v_h\right)_h=0\quad\forall v_h\in T_h.\tag{3.136}$$

Above, we used a lumped L^2-inner product denoted by $(\cdot,\cdot)_h$ (mass-lumping), where a specific quadrature rule is applied during integration, see [78]. The quadrature rule is chosen such that the locations of the quadrature points $\hat{\boldsymbol{x}}_i$ coincide with the element nodes (degress of freedom). The expression of the lumped L^2-inner product w.r.t. scalar valued functions is given by

$$(v,w)_h:=\sum_{K\in\mathcal{T}_h}\sum_{i=1}^{n_q}\hat{w}_i v(T_K(\hat{\boldsymbol{x}}_i))w(T_K(\hat{\boldsymbol{x}}_i))|\det DT_K|,\tag{3.137}$$

where $T_K:\hat{K}\longrightarrow K$ is the transformation that maps the reference element $\hat{K}$ (triangle or square) to the corresponding mesh element K, $\hat{w}_i$ denotes the quadrature weight w.r.t. quadrature point $\hat{\boldsymbol{x}}_i$ on the reference element $\hat{K}$, and n_q the number of quadrature points. Table 3.6 lists the quadrature rules that are used in the case of triangles or quadrilaterals in (3.137). The lumped L^2-inner product w.r.t. vector valued functions is defined analogously. The mass-lumping approach leads then to the property that $\boldsymbol{Q}^{n+1}_{i,h}$ satisfies the rod length constraint (3.129b) in each element node.

In Figure 3.11, we demonstrate the effect of using mass-lumping in (3.134) and (3.135). For this, we considered a bead-rod chain with $N=4$ beads in a constant Poiseuille flow with

$$\boldsymbol{u}(x,y)=\begin{bmatrix}(1-y)y\\0\end{bmatrix}.\tag{3.138}$$

The flow domain Ω is a unit square $(0,1)^2$, which is periodic on the left and right. The Weissenberg number is set to $\mathrm{Wi} = 1$. Figure 3.11 visualizes the maximum rod length deviation in Ω over time. One can clearly observe that without mass-lumping, the rod lengths deviate over time from the intended length of 1 in each DOF. With mass-lumping, the rod lengths stay constant over time.

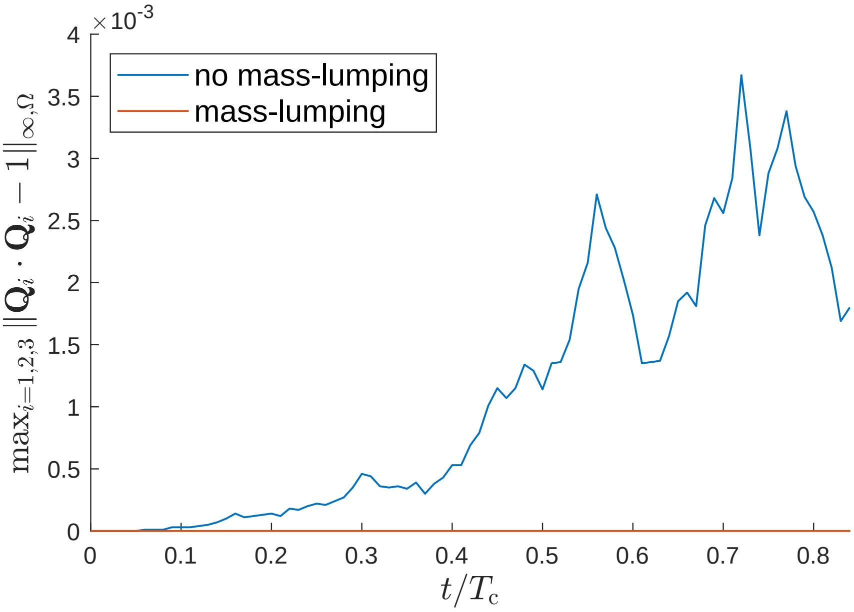

Figure 3.11. Maximum rod length deviation $\max_{i=1,2,3} \|\boldsymbol{Q}_i \cdot \boldsymbol{Q}_i - 1\|_{\infty,\Omega}$ over time with and without mass-lumping in (3.134) and (3.135) for fixed velocity (3.138).

For the computation of the polymeric stress tensor $\boldsymbol{\tau}_{\mathrm{p},h} \in \Sigma_h$ with

$$\Sigma_h := \left\{ \boldsymbol{d}_h \in C(\bar{\Omega})^{2\times 2} \mid \forall K \in \mathcal{T}_h, \boldsymbol{d}_{h|K} \in (\mathbb{Q}_1^m(K))^{2\times 2} \right\}, \tag{3.139}$$

we adapt the noise filtering technique from Section 3.4.2 to the dimensionless polymeric stress expression

$$\boldsymbol{\tau}_{\mathrm{p}} = \frac{\alpha(N)\epsilon}{\beta(N)\mathrm{Wi}} \left(\sum_{i=1}^{N} \langle \boldsymbol{R}_i \otimes \boldsymbol{F}_i^{\mathrm{H}} \rangle - \boldsymbol{I} \right), \tag{3.140}$$

where $\alpha(N)$ denotes the dimensionless relaxation time, ϵ polymeric viscosity ratio, $\beta(N) := \frac{1}{36}(N^2 - 1)$, Wi the Weissenberg number, $\boldsymbol{R}_i$ the bead position relative to the chains center of mass, and $\boldsymbol{F}_i^{\mathrm{H}}$ the hydrodynamic drag force. The polymeric stress tensor $\boldsymbol{\tau}_{\mathrm{p},h}^{n+1}$ is then obtained by the L^2-projection

$$\left(\boldsymbol{\tau}_{\mathrm{p},h}^{n+1}, \boldsymbol{f}_h \right) = \frac{\alpha(N)\epsilon}{\beta(N)\mathrm{Wi}} \left(\boldsymbol{\tau}_{\mathrm{p},h}^{B,n+1} + \boldsymbol{\tau}_{\mathrm{p},h}^{C,n+1}, \boldsymbol{f}_h \right) \quad \forall \boldsymbol{f}_h \in \Sigma_h. \tag{3.141}$$

In (3.141), the first linear form is given by

$$\left(\boldsymbol{\tau}_{\mathrm{p},h}^{B,n+1}, \boldsymbol{f}_h \right) := -\sum_{i=1}^{N} \left(\left\langle \frac{\boldsymbol{R}_{i,h}^{n+1} - \boldsymbol{R}_{i,h}^{n}}{2} \otimes \boldsymbol{F}_i^{\mathrm{B},n} \right\rangle, \boldsymbol{f}_h \right) \quad \forall \boldsymbol{f}_h \in \Sigma_h, \tag{3.142}$$

where the bead position vector fields $\boldsymbol{R}_{i,h}$ can be computed via the connector-vector fields $\boldsymbol{Q}_{i,h}$ (cf. (2.88)). The Brownian force vector field is given by

$$\boldsymbol{F}_i^{\mathrm{B},n} := \sqrt{\frac{2\alpha(N)}{\mathrm{Wi}\mathit{\Delta} t}}\mathit{\Delta}\bar{\boldsymbol{W}}_i^n, \quad i = 1, \dots, N, \tag{3.143}$$

where $\mathit{\Delta}\bar{\boldsymbol{W}}_i^n$ is the constant vector field, which is used in (3.132). The expectation value $\langle\cdot\rangle$ in (3.142) is approximated by considering N_f realization of the connector-vector field $\boldsymbol{Q}_{i,h}$ (Brownian configuration field) denoted by $\boldsymbol{Q}_{i,h}^j$, $i = 1, \dots, N-1$, $j = 1, \dots, N_f$, which transforms (3.142) to

$$\left(\boldsymbol{\tau}_{\mathrm{p},h}^{B,n+1}, \boldsymbol{f}_h\right) := -\sum_{i=1}^{N}\left(\frac{1}{N_f}\sum_{j=1}^{N_f}\left(\frac{\boldsymbol{R}_{i,h}^{j,n+1} - \boldsymbol{R}_{i,h}^{j,n}}{2} \otimes \boldsymbol{F}_i^{j,\mathrm{B},n}\right), \boldsymbol{f}_h\right). \tag{3.144}$$

In (3.141), the second linear form is given by

$$\begin{aligned}\left(\boldsymbol{\tau}_{\mathrm{p},h}^{\mathrm{C},n+1}, \boldsymbol{f}_h\right) := -\frac{1}{N_f}\sum_{i=1}^{N}\sum_{j=1}^{N_f}\Bigg[&\left(\frac{\boldsymbol{R}_{i,h}^{j,n+1} + \boldsymbol{R}_{i,h}^{j,n}}{2} \otimes \left(\hat{\boldsymbol{F}}_{i,h}^{j,\mathrm{C},n} - \tilde{\boldsymbol{F}}_{i,h}^{j,\mathrm{C},n}\right), \boldsymbol{f}_h\right)\\ &+\left(\frac{\boldsymbol{R}_{i,h}^{j,n+1} - \boldsymbol{R}_{i,h}^{j,n}}{2} \otimes \tilde{\boldsymbol{F}}_{i,h}^{j,\mathrm{C},n}, \boldsymbol{f}_h\right)\Bigg],\end{aligned} \tag{3.145}$$

where $\hat{\boldsymbol{F}}_{i,h}^{j,\mathrm{C},n} := \boldsymbol{F}_i^{\mathrm{C}}(\hat{T}_h^j, \boldsymbol{Q}_h^{j,n})$ is the constraint force, which uses the tensions $\hat{T}_{i,h}^j$ computed during (3.134) w.r.t. the jth realization $\boldsymbol{Q}_{i,h}^{j,n}$, and $\tilde{\boldsymbol{F}}_{i,h}^{j,\mathrm{C},n} := \boldsymbol{F}_i^{\mathrm{C}}(\tilde{T}_h^j, \boldsymbol{Q}_h^{j,n})$ is obtained by solving the auxiliary problem:

For given $\boldsymbol{F}_i^{j,\mathrm{B},n}$ and $\boldsymbol{Q}_{i,h}^{j,n} \in Q_h$, find $\tilde{T}_{i,h}^j \in T_h$ such that

$$\left(\left[\boldsymbol{F}_{i+1}^{j,\mathrm{B},n} - \boldsymbol{F}_i^{j,\mathrm{B},n} + \boldsymbol{F}_i(\tilde{T}_h^j, \boldsymbol{Q}_h^{j,n})\right] \cdot \boldsymbol{Q}_{i,h}^{j,n}, w_h\right)_h = 0 \quad \forall w_h \in T_h, \quad \forall i = 1, \dots, N-1. \tag{3.146}$$

In (3.146), the constraint force $\boldsymbol{F}_i(\tilde{T}_h^j, \boldsymbol{Q}_h^{j,n})$ is defined in (3.130).

3.4.5 (Non) linear system of equations

In this section, we transform the weak formulations of the previous section into (non) linear system of equations and discuss their properties. Analog to Sections 3.2.2 and 3.4.5, we represent connector-vectors $\boldsymbol{Q}_{i,h} \in Q_h$ with the degree-of-freedom (DOF) vector $\boldsymbol{x}^{Q_i} \in \mathbb{R}^{n_Q}$ via (3.56). In the case of tensions $T_{i,h} \in T_h$, we have DOF vector $\boldsymbol{x}^{T_i} \in \mathbb{R}^{n_T}$, where n_T denotes the dimension of the space T_h. The spaces Q_h and T_h are defined in (3.131). Tension $T_{i,h} \in T_h$ and DOF vector $\boldsymbol{x}^{T_i} \in \mathbb{R}^{n_T}$ are connected via

$$T_{i,h} = \sum_{j=1}^{n_T} x_j^{T_i}\phi_j^{T_h}, \tag{3.147}$$

where $\phi_j^{T_h}$ are the basis functions with the property $T_h = \operatorname{span}\{\phi_j^{T_h}\}_{j=1}^{n_T}$.

The linear system of equations associated to the weak formulation (3.132) is given by

$$\left(\boldsymbol{M}_{\boldsymbol{F}_4}^{\boldsymbol{u}_h} + \Delta t \boldsymbol{C}^{\boldsymbol{u}_h}\right) \boldsymbol{x}^{\hat{Q}_i} = \boldsymbol{g}(\boldsymbol{Q}_{i,h}^n, \boldsymbol{u}_h, \Delta \bar{\boldsymbol{W}}_i^n, \Delta \bar{\boldsymbol{W}}_{i+1}^n), \quad i = 1, \dots, N-1. \tag{3.148}$$

The matrices $\boldsymbol{M}_{\boldsymbol{F}_4}^{\boldsymbol{u}_h}$ and $\boldsymbol{C}^{\boldsymbol{u}_h}$ are defined in (3.57) and (3.58). The coefficient matrix $\boldsymbol{F}_4$ in $\boldsymbol{M}_{\boldsymbol{F}_4}^{\boldsymbol{u}_h}$ is given by

$$\boldsymbol{F}_4 := \boldsymbol{I}. \tag{3.149}$$

The entries of the right hand side $\boldsymbol{g}(\boldsymbol{Q}_{i,h}^n, \boldsymbol{u}_h, \Delta \bar{\boldsymbol{W}}_i^n, \Delta \bar{\boldsymbol{W}}_{i+1}^n) \in \mathbb{R}^{n_Q}$ in (3.148) are

$$\begin{aligned} g_j(\boldsymbol{Q}_{i,h}^n, \boldsymbol{u}_h, \Delta \bar{\boldsymbol{W}}_i^n, \Delta \bar{\boldsymbol{W}}_{i+1}^n) &:= \\ \sum_{K \in \mathcal{T}_h} \int_K & \left[\boldsymbol{Q}_{i,h}^n + \Delta t \nabla \boldsymbol{u}_h \boldsymbol{Q}_{i,h}^n + \sqrt{\frac{2\alpha(N)\Delta t}{\mathrm{Wi}}} \left(\Delta \bar{\boldsymbol{W}}_{i+1}^n - \Delta \bar{\boldsymbol{W}}_i^n \right) \right] \\ & \cdot \left[\boldsymbol{\phi}_j^{Q_h} + \frac{h_K}{|\boldsymbol{u}_h|} \left(\boldsymbol{u}_h \cdot \nabla \boldsymbol{\phi}_j^{Q_h} \right) \right], \quad j = 1, \dots, n_Q. \end{aligned} \tag{3.150}$$

The system matrix in (3.148) is in general non symmetric.

In order to solve (3.134) numerically, we apply Newtons method on the function $\boldsymbol{H} : \mathbb{R}^{(N-1)n_T} \longrightarrow \mathbb{R}^{(N-1)n_T}$ instead of the Picard iteration scheme from Section 3.4.1. In our simulations, it turned out that Newtons method is more robust compared to the Picard scheme. The function $\boldsymbol{H}$ consists of $N-1$ blocks denoted by $\boldsymbol{H}^{(i)} : \mathbb{R}^{(N-1)n_T} \longrightarrow \mathbb{R}^{n_T}$, $i = 1, \dots, N-1$. Let $\boldsymbol{x}^{\hat{\boldsymbol{T}}} \in \mathbb{R}^{(N-1)n_T}$ be the block vector, which contains $\boldsymbol{x}^{\hat{T}_i} \in \mathbb{R}^{n_T}$ in the ith block. Vector $\boldsymbol{x}^{\hat{T}_i}$ is the DOF vector associated to $\hat{T}_{i,h} \in T_h$ (cf. (3.147)). The entries of $\boldsymbol{H}^{(i)}(\boldsymbol{x}^{\hat{\boldsymbol{T}}})$ are given by

$$\begin{aligned} H_j^{(i)}(\boldsymbol{x}^{\hat{\boldsymbol{T}}}) &:= (2\Delta t) \left(\hat{\boldsymbol{Q}}_{i,h} \cdot \left(\hat{T}_{i-1,h} \boldsymbol{Q}_{i-1,h}^n - 2\hat{T}_{i,h} \boldsymbol{Q}_{i,h}^n + \hat{T}_{i+1,h} \boldsymbol{Q}_{i+1,h}^n \right), \phi_j^{T_h} \right)_h \\ &+ \left(\left(\hat{T}_{i-1,h} \boldsymbol{Q}_{i-1,h}^n - 2\hat{T}_{i,h} \boldsymbol{Q}_{i,h}^n + \hat{T}_{i+1,h} \boldsymbol{Q}_{i+1,h}^n \right)^2, \phi_j^{T_h} \right)_h (\Delta t)^2 - \left(1 - |\hat{\boldsymbol{Q}}_{i,h}|^2, \phi_j^{T_h} \right)_h . \end{aligned} \tag{3.151}$$

Note that in (3.151), we used (3.147) to compress the expressions. The Jacobian $D\boldsymbol{H} : \mathbb{R}^{(N-1)n_T} \longrightarrow \mathbb{R}^{(N-1)n_T \times (N-1)n_T}$ of $\boldsymbol{H}$ has block tridiagonal structure. The blocks $D\boldsymbol{H}^{(i,j)} : \mathbb{R}^{(N-1)n_T} \longrightarrow \mathbb{R}^{n_T \times n_T}$ are given by

$$\begin{aligned} D\boldsymbol{H}_{p,q}^{(i,i)}(\boldsymbol{x}^{\hat{\boldsymbol{T}}}) &:= -(4\Delta t) \left(\hat{\boldsymbol{Q}}_{i,h} \cdot \boldsymbol{Q}_{i,h}^n \phi_q^{T_h}, \phi_p^{T_h} \right)_h \\ &- 2(\Delta t)^2 \left(\left(\hat{T}_{i-1,h} \boldsymbol{Q}_{i-1,h}^n - 2\hat{T}_{i,h} \boldsymbol{Q}_{i,h}^n + \hat{T}_{i+1,h} \boldsymbol{Q}_{i+1,h}^n \right) \cdot \boldsymbol{Q}_{i,h}^n \phi_q^{T_h}, \phi_p^{T_h} \right)_h , \end{aligned} \tag{3.152a}$$

$$\begin{aligned} D\boldsymbol{H}_{p,q}^{(i,i+1)}(\boldsymbol{x}^{\hat{\boldsymbol{T}}}) &:= (2\Delta t) \left(\hat{\boldsymbol{Q}}_{i,h} \cdot \boldsymbol{Q}_{i+1,h}^n \phi_q^{T_h}, \phi_p^{T_h} \right)_h \\ &+ 2(\Delta t)^2 \left(\left(\hat{T}_{i-1,h} \boldsymbol{Q}_{i-1,h}^n - 2\hat{T}_{i,h} \boldsymbol{Q}_{i,h}^n + \hat{T}_{i+1,h} \boldsymbol{Q}_{i+1,h}^n \right) \cdot \boldsymbol{Q}_{i+1,h}^n \phi_q^{T_h}, \phi_p^{T_h} \right)_h , \end{aligned} \tag{3.152b}$$

$$\begin{aligned} D\boldsymbol{H}^{(i,i-1)}_{p,q}(\boldsymbol{x}^{\hat{\boldsymbol{T}}}) &:= (2\Delta t)\left(\hat{\boldsymbol{Q}}_{i,h}\cdot\boldsymbol{Q}^{n}_{i-1,h}\phi^{T_h}_q,\phi^{T_h}_p\right)_h \\ &+ 2(\Delta t)^2\left(\left(\hat{T}_{i-1,h}\boldsymbol{Q}^{n}_{i-1,h}-2\hat{T}_{i,h}\boldsymbol{Q}^{n}_{i,h}+\hat{T}_{i+1,h}\boldsymbol{Q}^{n}_{i+1,h}\right)\cdot\boldsymbol{Q}^{n}_{i-1,h}\phi^{T_h}_q,\phi^{T_h}_p\right)_h. \end{aligned} \tag{3.152c}$$

Note that (3.151) and (3.152) are only valid for $i = 2,\dots,N-2$. In the case of $i = 1$, there is no left off diagonal block and the terms in $H^{(1)}$, $D\boldsymbol{H}^{(1,1)}$, and $D\boldsymbol{H}^{(1,2)}$ have to be adapted to (3.134a). For $i = N-1$, there is no right off diagonal block and the terms in $H^{(N-1)}$, $D\boldsymbol{H}^{(N-1,N-1)}$, and $D\boldsymbol{H}^{(N-1,N-2)}$ have to be adapted to (3.134c). Newtons fixed-point iteration applied on $\boldsymbol{H}$ is then given by

$$\boldsymbol{x}^{\hat{\boldsymbol{T}},k+1} := \boldsymbol{x}^{\hat{\boldsymbol{T}},k} - D\boldsymbol{H}^{-1}(\boldsymbol{x}^{\hat{\boldsymbol{T}},k})\boldsymbol{H}(\boldsymbol{x}^{\hat{\boldsymbol{T}},k}). \tag{3.153}$$

In (3.153), vector $\boldsymbol{x}^{\hat{\boldsymbol{T}},k}$ denotes the kth Newton iterate. As described in Section 3.4.4, the lumped L^2-inner product $(\cdot,\cdot)_h$ is used in (3.151) and (3.152). This leads to the property that the individual block matrices in (3.152) are diagonal. The system matrix $D\boldsymbol{H}(\boldsymbol{x}^{\hat{\boldsymbol{T}},k})$ is in general non symmetric.

After a fixed-point of (3.153) is obtained, the resulting tensions $\hat{T}_{i,h} \in T_h$ are used to compute the updated connector-vector fields $\boldsymbol{Q}^{n+1}_{i,h} \in Q_h$ via (3.135). The corresponding linear systems of equations are

$$\boldsymbol{M}_l\boldsymbol{x}^{\mathrm{Q}_i,n+1} = \boldsymbol{h}^{(i)}, \quad i = 1,\dots,N-1, \tag{3.154}$$

where $\boldsymbol{M}_l \in \mathbb{R}^{n_\mathrm{Q}\times n_\mathrm{Q}}$ and $\boldsymbol{h}^{(i)} \in \mathbb{R}^{n_\mathrm{Q}}$ are given by

$$(\boldsymbol{M}_l)_{p,q} := \left(\boldsymbol{\phi}^{Q_h}_q,\boldsymbol{\phi}^{Q_h}_p\right)_h, \tag{3.155a}$$

$$(h^{(i)})_q := \left(\hat{\boldsymbol{Q}}_{i,h} + \Delta t\boldsymbol{F}_i(\hat{T}_h,\boldsymbol{Q}^n_h),\boldsymbol{\phi}^{Q_h}_q\right)_h. \tag{3.155b}$$

In (3.155), the constraint force $\boldsymbol{F}_i$ is defined in (3.130) and uses the tensions $\hat{T}_{i,h}$, which solve (3.153). System (3.154) is trivially to solve as $\boldsymbol{M}_l$ is diagonal.

The polymeric stress tensor $\boldsymbol{\tau}_{\mathrm{p},h} \in \Sigma_h$ consists of the two terms $\boldsymbol{\tau}^B_{\mathrm{p},h}, \boldsymbol{\tau}^C_{\mathrm{p},h} \in \Sigma_h$ (cf. (3.141)). They are obtained by solving (3.144) and (3.145), which is done at once with the linear system of equations

$$\boldsymbol{E}\boldsymbol{x}^{\tau_\mathrm{p}} = \frac{\alpha(N)\epsilon}{\beta(N)\mathrm{Wi}}\left(f_\mathrm{B} + f_\mathrm{C}\right). \tag{3.156}$$

In (3.156), mass matrix $\boldsymbol{E} \in \mathbb{R}^{n_\Sigma\times n_\Sigma}$ is defined in (3.31) and the entries of the rhs vectors are

$$f_{\mathrm{B},p} := -\sum_{i=1}^{N}\left(\frac{1}{N_f}\sum_{j=1}^{N_f}\left(\frac{\boldsymbol{R}^{j,n+1}_{i,h}-\boldsymbol{R}^{j,n}_{i,h}}{2}\otimes\boldsymbol{F}^{j,\mathrm{B},n}_i\right),\boldsymbol{\phi}^{\Sigma_h}_q\right), \tag{3.157a}$$

$$\begin{aligned} f_{\mathrm{C},p} := -\frac{1}{N_f}\sum_{i=1}^{N}\sum_{j=1}^{N_f}&\left[\left(\frac{\boldsymbol{R}^{j,n+1}_{i,h}+\boldsymbol{R}^{j,n}_{i,h}}{2}\otimes\left(\hat{\boldsymbol{F}}^{j,\mathrm{C},n}_{i,h}-\tilde{\boldsymbol{F}}^{j,\mathrm{C},n}_{i,h}\right),\boldsymbol{\phi}^{\Sigma_h}_q\right)\right. \\ &\left.+\left(\frac{\boldsymbol{R}^{j,n+1}_{i,h}-\boldsymbol{R}^{j,n}_{i,h}}{2}\otimes\tilde{\boldsymbol{F}}^{j,\mathrm{C},n}_{i,h},\boldsymbol{\phi}^{\Sigma_h}_q\right)\right]. \end{aligned} \tag{3.157b}$$

In (3.157a), the $\boldsymbol{R}_{i,h}^{j,n}$ are evaluated with $\boldsymbol{Q}_i^{j,n}$, $i = 1, \dots, N-1$, via relation (2.88). The spatially constant vector field $\boldsymbol{F}_i^{j,\mathrm{B},n}$ is the one, which is used during the computation of $\hat{\boldsymbol{Q}}_{i,h}^{j}$ (cf. (3.143) and (3.148)). Note that the mass matrix $\boldsymbol{E}$ is symmetric positive definite.

Prior to the evaluation of (3.157b), the constraint force $\tilde{\boldsymbol{F}}_{i,h}^{j,\mathrm{C},n}$ needs to be computed. This is done by solving (3.146). The corresponding linear system of equations is

$$\boldsymbol{W}\boldsymbol{x}^{\tilde{\boldsymbol{T}}} = \boldsymbol{j}, \tag{3.158}$$

where the system matrix $\boldsymbol{W} \in \mathbb{R}^{(N-1)n_T \times (N-1)n_T}$ has tridiagonal block structure and $\boldsymbol{x}^{\tilde{\boldsymbol{T}}}, \boldsymbol{j} \in \mathbb{R}^{(N-1)n_T}$. The diagonal blocks $\boldsymbol{W}^{(i,i)} \in \mathbb{R}^{n_T \times n_T}$, left and right off diagonal blocks $\boldsymbol{W}^{(i,i-1)}, \boldsymbol{W}^{(i,i+1)} \in \mathbb{R}^{n_T \times n_T}$ are defined by

$$\boldsymbol{W}_{p,q}^{(i,i)} := -2\left(\boldsymbol{Q}_{i,h}^{j,n} \cdot \boldsymbol{Q}_{i,h}^{j,n} \phi_q^{T_h}, \phi_p^{T_h}\right)_h, \tag{3.159a}$$

$$\boldsymbol{W}_{p,q}^{(i,i-1)} := \left(\boldsymbol{Q}_{i,h}^{j,n} \cdot \boldsymbol{Q}_{i-1,h}^{j,n} \phi_q^{T_h}, \phi_p^{T_h}\right)_h, \tag{3.159b}$$

$$\boldsymbol{W}_{p,q}^{(i,i+1)} := \left(\boldsymbol{Q}_{i,h}^{j,n} \cdot \boldsymbol{Q}_{i+1,h}^{j,n} \phi_q^{T_h}, \phi_p^{T_h}\right)_h. \tag{3.159c}$$

Note that (3.159) is only valid for $i = 2, \dots, N-2$. In the case of $i = 1$ or $i = N-1$, there is no left or right off diagonal block. The entries of the ith block of the rhs block vector $\boldsymbol{j} \in \mathbb{R}^{(N-1)n_T}$ are

$$j_q^{(i)} := \left(\left[\boldsymbol{F}_i^{j,\mathrm{B},n} - \boldsymbol{F}_{i+1}^{j,\mathrm{B},n}\right] \cdot \boldsymbol{Q}_{i,h}^{j,n}, \phi_q^{T_h}\right)_h, \quad i = 1, \dots, N-1, \tag{3.160}$$

where $\boldsymbol{F}_i^{j,\mathrm{B},n}$ is defined in (3.143). From (3.159), we deduce that $\boldsymbol{W}$ is symmetric and due to the lumped L^2-inner product $(\cdot,\cdot)_h$, the individual blocks are diagonal.

3.4.6 Iterative solvers and preconditioning

In this section, we discuss the solvers and preconditioner, which are used for solving the linear system of equations of the previous section.

The system matrix in (3.148) has the same structure as System (3.59). Thus, we use the same type of solver and preconditioner (GMRES/ILU(1)), which is used for solving (3.59). For further details see Section 3.3.2, where this type of combination is tested in Table 3.4.

System (3.156) can be solved very efficiently. Since the system matrix (mass matrix) is symmetric positive definite, we apply the combination CG/Jacobi. This problem and solver choice was already discussed in Section 3.3.1. In Figure 3.5, the outstanding performance is visualized.

In order to solve the linear system in the Newton fixed-point iteration (3.153) and (3.158), we apply the GMRES solver with Jacobi preconditioner. The system matrices in (3.153) and (3.159) are extremely sparse due to the block tridiagonal structure together with the fact that each block is diagonal. The density ρ_{nnz} (ratio of non zero entries to the total number of entries) is given by

$$\rho_{nnz}(N, n_T) := \frac{[(N-1) + 2(N-2)]\, n_T}{[(N-1)n_T]^2}. \tag{3.161}$$

In Table 3.7, the considered N and n_T lead to densities $\rho_{nnz}(N, n_T)$ that range from $1.5 \cdot 10^{-4}$ to $3.1 \cdot 10^{-6}$. Note that it is possible to decouple the block tridiagonal systems of size $(N-1)n_T$ into n_T tridiagonal systems of size $N-1$, which could further increase the overall performance.

Table 3.7 lists the iterations it took to solve (3.153) and (3.158) in the first time step, respectively, with varying parameters. The flow scenario is a constant shear flow on the periodic unit square $(0, 1)^2$, which is periodic on the left and right, as domain. The corresponding velocity $\boldsymbol{u}$ is given by

$$\boldsymbol{u}(x, y) := \begin{bmatrix} y \\ 0 \end{bmatrix}. \tag{3.162}$$

In each cell of Table 3.7, the triple n_1 (n_2) n_3 lists the number of Newton iterations n_1, the rounded average number of GMRES iterations n_2 it took to solve the linear system of equations in (3.153), and the number of GMRES iterations n_3 it took to solve (3.158). The Newton fixed point iteration stops after residual $\|(\boldsymbol{x}^{\hat{T},k})\|_2$ drops below $10^{-9.5}$. The GMRES solver in (3.153) and (3.158) stops after the relative residual drops below 10^{-10} or the absolute residual drops below 10^{-11}. We varied the step size Δt, number of beads N, Weissenberg number Wi, and mesh width h to observe their influence on the required number of iterations. The corresponding values are $\Delta t \in \{0.1, 0.001\}$, $N \in \{5, 10, 15\}$, $\mathrm{Wi} \in \{1, 5, 10\}$, and $h \in \{2^{-6}, 2^{-7}, 2^{-8}\}$. One can see that the number of GMRES iterations are almost independent on Δt, h, Wi, and only a $\mathcal{O}(N^{-1})$-dependency on the number of beads N can be observed for the considered parameters. However, there is a Δt dependency on the number of Newton iterations, which is not surprising, as it is commonly the case to get faster convergence in the Newton fixed point iteration for decreasing Δt. In the case of $\mathrm{Wi} = 1$ and $\Delta t = 0.1$, the Newton iteration did not converge (dnc) for $N = 10$ and $N = 15$ (cf. Tables 3.7b and 3.7c). For the considered parameters in Table 3.7, it almost holds $n_2 = n_3$, which is probability due to the similar and extremely sparse structure of the linear systems in (3.153) and (3.158).

3.5 Combining the numerical schemes

In this section, we describe how the discretization of the bead-spring dumbbell model from Section 3.3 and the discretization of the bead-rod chain model from Section 3.4 are coupled with the Navier–Stokes discretization from Section 3.2.

In this thesis, the following approach is pursued: At first, we update the velocity with the current polymeric stress tensor $\boldsymbol{\tau}_{\mathrm{p},h}^{n}$ and then use the newly obtained velocity $\boldsymbol{u}_h^{n+1}$ to update the bead-spring dumbbells or bead-rod chains,

	Wi = 1		Wi = 5		Wi = 10	
DOF	$\Delta t = 0.1$	$\Delta t = 0.001$	$\Delta t = 0.1$	$\Delta t = 0.001$	$\Delta t = 0.1$	$\Delta t = 0.001$
16640	5 (4) 4	3 (4) 4	4 (4) 4	3 (4) 4	4 (4) 4	2 (4) 4
66048	4 (4) 4	3 (4) 4	4 (4) 4	3 (4) 4	3 (4) 4	2 (4) 4
263168	5 (4) 4	3 (4) 4	3 (4) 4	3 (4) 4	3 (4) 4	3 (4) 4

(a) $N = 5$

	Wi = 1		Wi = 5		Wi = 10	
DOF	$\Delta t = 0.1$	$\Delta t = 0.001$	$\Delta t = 0.1$	$\Delta t = 0.001$	$\Delta t = 0.1$	$\Delta t = 0.001$
37440	dnc	4 (9) 9	5 (9) 9	3 (9) 9	5 (9) 9	3 (9) 9
148608	dnc	3 (9) 9	5 (9) 9	3 (9) 9	5 (9) 9	3 (9) 9
592128	dnc	3 (9) 9	6 (9) 9	3 (9) 9	4 (9) 9	3 (9) 9

(b) $N = 10$

	Wi = 1		Wi = 5		Wi = 10	
DOF	$\Delta t = 0.1$	$\Delta t = 0.001$	$\Delta t = 0.1$	$\Delta t = 0.001$	$\Delta t = 0.1$	$\Delta t = 0.001$
58240	dnc	4 (14) 14	6 (14) 14	3 (14) 14	5 (14) 14	3 (14) 14
231168	dnc	4 (14) 14	5 (14) 14	3 (14) 14	5 (14) 14	3 (14) 14
921088	dnc	3 (14) 14	7 (15) 14	3 (14) 14	5 (14) 14	3 (14) 14

(c) $N = 15$

Table 3.7. The triple n_1 (n_2) n_3 lists the number of Newton iterations n_1 to solve (3.153), the rounded average number of GMRES iterations n_2 to solve the linear system of equations during the Newton iteration, and the number of GMRES iterations n_3 to solve (3.158).

which are then used to get the polymeric stress tensor $\boldsymbol{\tau}_{\mathrm{p},h}^{n+1}$ for the next time step. Figure 3.12 visualizes this general procedure.

Bead-spring dumbbell coupling Applying the BCF approach from Section 3.1 to the Navier–Stokes equations coupled with the bead-spring dumbbell model from Section 2.1 yields the system

$$\partial_t \boldsymbol{u} + \boldsymbol{u} \cdot \nabla \boldsymbol{u} - 2\frac{1-\epsilon}{\mathrm{Re}} \nabla \cdot \boldsymbol{D}(\boldsymbol{u}) - \frac{1}{\mathrm{Re}} \nabla \cdot \boldsymbol{\tau}_{\mathrm{p}} + \nabla p = 0, \tag{3.163a}$$

$$-\nabla \cdot \boldsymbol{u} = 0, \tag{3.163b}$$

$$\boldsymbol{\tau}_{\mathrm{p}} = \frac{\epsilon}{\alpha_{b,d} \mathrm{Wi}} \left[\frac{1}{N_f} \sum_{j=1}^{N_f} \left(\boldsymbol{Q}^j \otimes \boldsymbol{F}^{\mathrm{S}}(\boldsymbol{Q}^j) \right) - \boldsymbol{I} \right], \tag{3.163c}$$

$$\mathrm{d}\boldsymbol{Q}^j = \left[-\boldsymbol{u} \cdot \nabla \boldsymbol{Q}^j + (\nabla \boldsymbol{u}) \boldsymbol{Q}^j - \frac{1}{2\mathrm{Wi}} \boldsymbol{F}^{\mathrm{S}}(\boldsymbol{Q}^j) \right] \mathrm{d}t + \sqrt{\frac{1}{\mathrm{Wi}}} \mathrm{d}\boldsymbol{W}_{\boldsymbol{Q}^j}. \tag{3.163d}$$

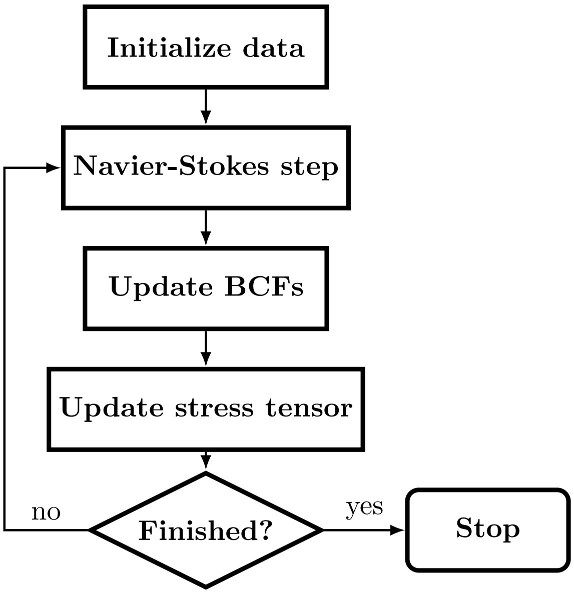

Figure 3.12. Flowchart to illustrate general computation procedure in the simulation of a time step.

See Sections 3.2 and 3.3 for a description of the unknowns and parameters of (3.163) with suitable initial and boundary conditions. The computation of the next time step of the fully discretized version of System (3.163) is then given by:

Let $\boldsymbol{u}_h^n \in U_h$, $\boldsymbol{\tau}_{\mathrm{p},h}^n \in \Sigma_h$, and $\boldsymbol{Q}_h^{j,n} \in Q_h$, $j = 1, \ldots, N_f$, be given, where N_f is the number of Brownian configuration fields (BCF). The spaces U_h, Σ_h, P_h, and Q_h are defined in (3.17a), (3.17b), (3.17c), and (3.51), respectively. At first, we solve (3.30) to obtain the new velocity $\boldsymbol{u}_h^{n+1} \in U_h$ and pressure $p_h^{n+1} \in P_h$. The new velocity $\boldsymbol{u}_h^{n+1}$ is then used in (3.59) or (3.62) to compute the new $\boldsymbol{Q}_h^{j,n+1} \in Q_h$ for each $j = 1, \ldots, N_f$. Afterwards, the new polymeric stress tensor $\boldsymbol{\tau}_{\mathrm{p},h}^{n+1} \in \Sigma_h$ is obtained by solving (3.72). In the case of Hookean dumbbells, i.e., using (3.59) for the computation of $\boldsymbol{Q}_h^{j,n+1}$, there are in total $2 + N_f$ linear systems of equations to be solved in each time step. In the case of FENE dumbbells, where (3.62) is used, 2 linear and N_f nonlinear systems of equations need to be solved in each time step. Table 3.8 summarizes the numbers of linear and nonlinear system of equations, which need to be solved. As the number of BCF N_f is typically $\mathcal{O}(10^3)$, this leads to an extreme computational effort, which requires special treatment concerning the implementation of the discretization.

Concerning the existence of solutions of (3.163), there are various papers by Barrett and Süli [5–8, 81], where the existence of weak solutions is analyzed w.r.t. different spring forces and regularized versions of (3.163) in the equivalent Fokker–Planck formulation. In [46], local in time existence and uniqueness of solutions for System (3.163) is proven in the case of FENE dumbbells in a shear flow scenario. In [22], convergence analysis is done for a temporal discretization of (3.163) with Hookean dumbbells in a 1D shear flow. There, they prove optimal rate of convergence for the error $\|\boldsymbol{u}^n - \boldsymbol{u}(t_n)\|_{L^2} \in \mathcal{O}(\Delta t + 1/\sqrt{N_f})$. In [54], System (3.163) with Hookean dumbbells is fully discretized with finite differences and backward Euler on a periodic d-dimensional unit cube. For $d = 2, 3$, their convergence result of the error is given by $\max_n \|\boldsymbol{u}_h^n - \boldsymbol{u}(t_n)\|_{L^2}^2 \leq C(\Delta t^2 + h^4 + 1/N_f^{1-\epsilon})$ with arbitrary but fixed $0 < \epsilon < 1$.

	Number of systems of equations	
Model	linear	nonlinear
Bead-spring dumbbell (Hookean)	$2 + N_f$	–
Bead-spring dumbbell (FENE)	2	N_f
Bead-rod chain	$2 + N_f\,[2(N-1)+1]$	N_f

Table 3.8. Overview of the number of linear and nonlinear systems of equations, which need to be solved during one time step. The number of beads and BCF are denoted by N and N_f, respectively.

Bead-rod chain coupling Applying the BCF approach from Section 3.1 to the Navier–Stokes equations coupled with the bead-rod chain model from Section 3.4 gives

$$\partial_t \boldsymbol{u} + \boldsymbol{u} \cdot \nabla \boldsymbol{u} - 2\frac{1-\epsilon}{\mathrm{Re}} \nabla \cdot \boldsymbol{D}(\boldsymbol{u}) - \frac{1}{\mathrm{Re}} \nabla \cdot \boldsymbol{\tau}_{\mathrm{p}} + \nabla p = 0, \tag{3.164a}$$

$$-\nabla \cdot \boldsymbol{u} = 0, \tag{3.164b}$$

$$\boldsymbol{\tau}_{\mathrm{p}} = \frac{\alpha\epsilon}{\beta \mathrm{Wi} N_f} \left(\sum_{i=1}^{N} \sum_{j=1}^{N_f} \left(\boldsymbol{R}_i^j \otimes \boldsymbol{F}_i^{\mathrm{H},j} \right) - \boldsymbol{I} \right), \tag{3.164c}$$

$$\begin{aligned} \mathrm{d}\boldsymbol{Q}_i^j = {} & \left[-\boldsymbol{u} \cdot \nabla \boldsymbol{Q}_i^j + (\nabla \boldsymbol{u}) \boldsymbol{Q}_i^j + \boldsymbol{F}_i^j \right] \mathrm{d}t \\ & + \sqrt{\frac{2\alpha(N)}{\mathrm{Wi}(N)}} (\mathrm{d}\boldsymbol{W}_{i+1}^j - \mathrm{d}\boldsymbol{W}_i^j), \quad i = 1, \dots, N-1, \end{aligned} \tag{3.164d}$$

$$\boldsymbol{Q}_i^j \cdot \boldsymbol{Q}_i^j - 1 = 0, \quad i = 1, \dots, N-1. \tag{3.164e}$$

See Section 3.2 and Section 3.4 for a description of the individual unknowns and parameters of (3.164). Let $\boldsymbol{u}_h^n \in U_h$, $\boldsymbol{\tau}_{\mathrm{p},h}^n \in \Sigma_h$, and $\boldsymbol{Q}_{i,h}^{j,n} \in Q_h$, $i = 1, \dots, N-1$, $j = 1, \dots, N_f$, be given, where N is the number of beads and N_f is the number of Brownian configuration fields (BCF). As above, we obtain the updated velocity $\boldsymbol{u}_h^{n+1} \in U_h$ and pressure $p_h^{n+1} \in P_h$ by solving (3.30). For each j, the bead-rod chains $\boldsymbol{Q}_{i,h}^{j,n}$ are updated via solving (3.132), (3.134), and (3.135) with the new velocity $\boldsymbol{u}_h^{n+1}$. This yields the updated $\boldsymbol{Q}_{i,h}^{j,n+1} \in U_h$. Before the polymeric stress $\boldsymbol{\tau}_{\mathrm{p},h}^{n+1} \in \Sigma_h$ is obtained, System (3.158) has to be solved for each BCF.

Afterwards, (3.156) has to be solved to get the new $\boldsymbol{\tau}_{\mathrm{p},h}^{n+1}$. Overall, this leads to $2 + N_f\,[2(N-1)+1]$ linear and N_f nonlinear system of equations in each time step. In Table 3.8, these numbers are summarized and one can directly compare the bead-spring dumbbell model with the bead-rod chain model w.r.t. to the computational effort. The largest simulation in Section 5 uses $N_f = 2233$ Brownian configuration fields and bead-rod chains with $N = 17$ beads, which leads to 73691 linear and 2233 nonlinear systems of equations in each time step. Solving such amounts of problems in a realistic time frame requires a custom implementation of the discretization that particularly addresses this problem and immense computational power.

In the next section, we present the details concerning the implementation of the various discretizations from Section 3 that enable the simulation of (3.164) and (3.163).

4 Implementation

The goal of this section is to emphasize the crucial role of parallel computing for this dissertation. For this, a brief introduction into parallel computing, based on [15], and its various parallelization concepts is given in Section 4.1. Section 4.2 discusses the algorithm schemes in detail, which are crucial to gain an outstanding speed-up in the computation time of our simulations. In Section 4.3, measures for quantifying parallel scalability are introduced and used to examine the performance of our code on practical problems of this thesis. Afterwards, the full implementation is tested w.r.t. parallel scalability. Lastly, Section 4.4 gives insight and remarks into the libraries that are used in the implementation.

4.1 Parallel computing

This introduction is based on [15]. Parallelization is essential for large scale simulations to drastically reduce their computation times. Large scale simulations require typically a huge amount of memory, which immediately eliminates the use of a single personal computer due to memory/hardware limitations. Parallelization lifts these limitation through the use of multiple computers (nodes) connected via network, which is known as distributed memory parallelization. This unlocks the possibility to study more advanced models through simulations. It is widely used across many fields in research and industry such as the simulation of detonations [20] and computing air flow around cars [79]. Figure 4.1 visualizes different simulations from above mentioned research fields.

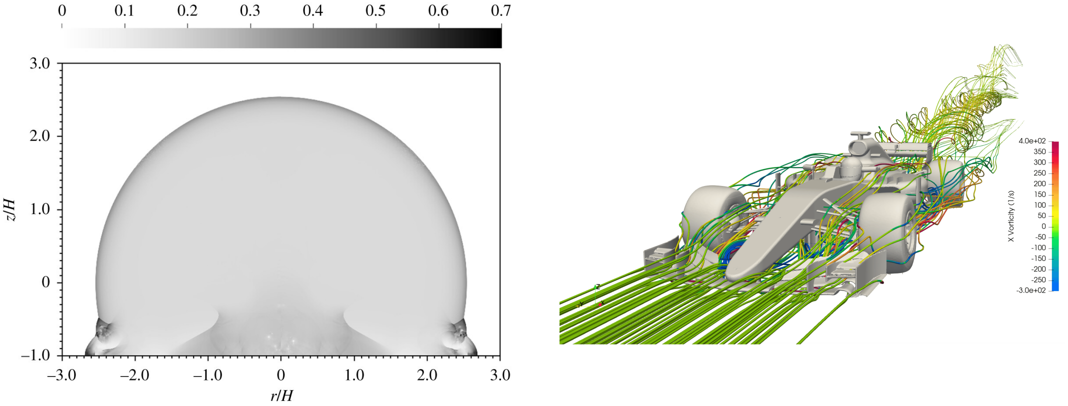

(a) Pressure of near surface detonation. Graphic from [20] by Cook, Bauer, and Spriggs. Licensed under CC BY 4.0. No changes were made.

(b) Streamlines of the axial vorticity around F1 car. Graphic from [34] by Guerrero and Castilla. Licensed under CC BY 4.0. No changes were made.

Figure 4.1. Visualization of large scale simulations, which use extensive parallelization.

4.1.1 Memory architecture

The hybrid distributed-shared memory architecture is the most common type of architecture, which is used in large computation clusters today. It consists of several nodes connected with each other over a network as visualized in Figure 4.2. Each node consists of several CPUs or GPUs with their own locally shared memory and can be viewed as an own independent computer. The nodes can perform tasks independently from each other on their own local memory. Accessing data across nodes requires communication between the corresponding nodes over a network. In order to use multiple nodes to solve one large problem, the problem has to be split into tasks that can be solved concurrently on each node. Additionally, the problem data associated to the tasks has to be distributed to the corresponding nodes. This is not always possible without introducing additional overhead in form of communication between the nodes. Depending on the level of parallelization, this overhead can lead to parallel slowdown causing a reduction of efficiency. The advantage of this type of memory architecture is the simple memory scalability with the number of processors, i.e., adding more nodes to the network. However, it comes with the price of an increased code complexity, as communication across nodes needs to be additionally addressed. Typically, this leads to more complex data structures such as for vectors or matrices and their corresponding operations.

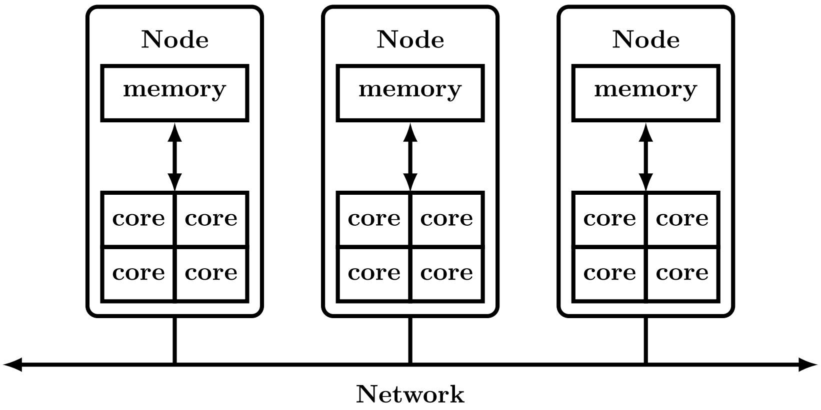

Figure 4.2. Visualization of hybrid distributed-shared memory architecture. Computing nodes are connected with each other over a network.

4.1.2 Mesh partitioning

The most common approach to split large problems into smaller tasks in the context of finite element simulations with fine discretization meshes $\mathcal{T}_h$, is the use of domain/mesh partitioning. Here, the discretization mesh $\mathcal{T}_h$ is partitioned into N_p smaller submeshes $\mathcal{T}_{h,p}$, $p = 1, \dots, N_p$, of roughly equal size and minimal boundary to neighboring submeshes. Figure 4.3 visualizes an admissible mesh partition into 4 submeshes. Each submesh $\mathcal{T}_{h,p}$ is then assigned to a computing node/processor. A typical task in finite element simulations is the assembling

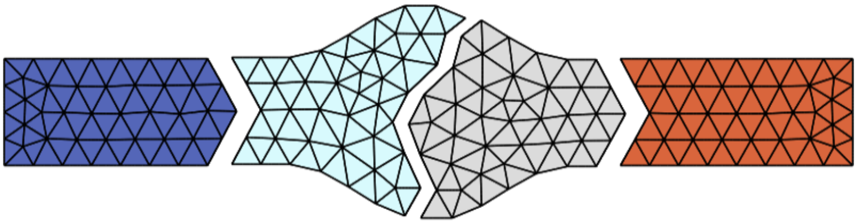

Figure 4.3. Visualization of mesh partitioning into four submeshes.

of matrices and vectors, which correspond to bilinear- and linearforms (cf. Sections 3.3.1 and 3.4.5). In the inner regions of each submesh (excluding boundaries that touch neighboring submeshes), this assembling procedures can be done concurrently on each node without further communication. At the boundary regions, additional communication between the nodes of neighboring submeshes is required to exchange information/data. This leads to parallel overhead. To minimize this overhead, the intersecting boundaries of submeshes should be therefore kept minimal. Additionally, the tasks on each submesh should take the same amount of computing time (load balancing) to prevent unnecessary delays in form of already finished nodes waiting.

This type of parallelization can only be done to some extend. If the submesh size gets too small and the resulting communication dominates, no additional speedup can be achieved. Using too much parallelization can actually lead to an increasing computation time. Section 4.3 introduces measures that help to quantify the parallel efficiency.

4.1.3 Master/Helper grouping

In the simulations of this thesis, most of the computation time is spent in updating the Brownian configuration fields (cf. Figure 3.12). This can be speed up only to some extend with mesh partitioning due to the mesh size and the resulting communication overhead. Updating the BCFs can be done concurrently, as they do not depend on each other. This aspect is not exploited by mesh partitioning at all and gives rise to the following approach.

Instead of further partitioning the mesh, we partition the set of processes P into workers W_k as visualized in Figure 4.4. Each worker W_k has a copy of the mesh $\mathcal{T}_h$, which is additionally partitioned and distributed across the workers' processes. The BCFs are then evenly distributed across the workers. This enables

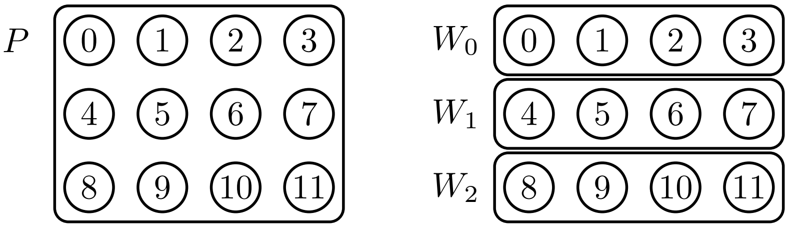

Figure 4.4. Admissible partition of P (left) with size $N_p = 12$ into $N_w = 3$ workers (right).

the parallelization of updating the BCFs and leads to an enormous speedup as demonstrated in Section 4.3. This idea is also used in [37].

In the implementation, there are two types of workers. A master worker W_0, which is responsible for the Navier–Stokes and polymeric stress tensor step (cf. Figure 3.12), and a helper worker W_i, $i > 0$, for updating the BCFs. Ideally, each helper worker should be responsible for updating $N_f/(N_w - 1)$ BCFs to achieve a good load balancing. Figure 4.5 visualizes the workflow for various tasks, which are processed by workers W_k. The type of worker is determined by its index k. The distribution of the BCFs among the helper workers W_k, $k > 0$, leads to an enormous speed up of the Monte–Carlo part of the simulation, i.e., solving the SDEs multiple times. In the Navier–Stokes part, W_0 computes the updated velocity $\boldsymbol{u}_h^{n+1}$ as described in Section 3.5. Then, $\boldsymbol{u}_h^{n+1}$ is sent to the workers W_k, $k > 0$, where the BCFs are updated. After that, each worker W_k, $k > 0$ computes its portion of the updated polymeric stress tensor $\boldsymbol{\tau}_{\mathrm{p},h}^{n+1}$ and sends it back to W_0.

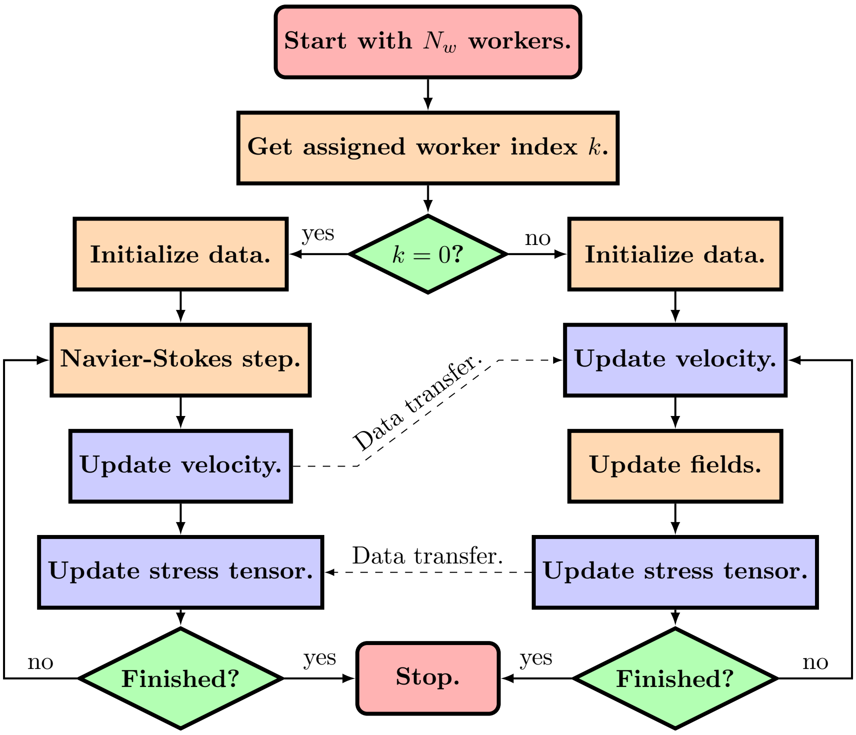

Figure 4.5. Flowchart of the implementation to illustrate the interplay between workers. Blue boxes can only continue if the indicated data transfer is completed.

For a given number of processes N_p, there is now a free parameter to control the level of parallelization. The number of workers N_w determines their corresponding worker size via

$$w_s(N_w, N_p) := \frac{N_p}{N_w}. \tag{4.1}$$

Note that all workers have the same size and the number of processes N_p has to be divisible by N_w. Choosing N_w large, leads to a small worker size $w_s(N_w, N_p)$ and a coarse mesh partitioning into $w_s(N_w, N_p)$ submeshes on each worker. Contrary, a small number of workers yields a fine grained mesh partitioning on each worker. For a given number of processes N_p, the optimal number of workers N_w depends on the discretization mesh $\mathcal{T}_h$ and the number of BCFs N_f.

This type of parallelization comes with the price of additional memory consumption, as the discretization mesh and the resulting data has to be stored for each worker on the local memory space to avoid unnecessary data transfers across the workers. An example of such data are the assembled system matrices of Sections 3.3.1 and 3.4.5. The above introduced parallelization scheme is discussed in detail in the next section.

4.2 Master/Helper algorithm

In this section, we discuss the master/helper algorithms, which are motivated in the previous section. Algorithms 2 to 4 realize the flowchart of Figure 4.5.

Note that Algorithm 2 is called N_p times, where N_p is the number of processes that are available for parallelization. Thus, there are N_p instances of Algorithm 2 running at the same time. In the first line of Algorithm 2, the parallelization environment is initialized among the N_p instances. Each instance gets assigned a unique global rank $r_G \in \{0, N_p - 1\}$. The ranks are then later on used to communicate between specific instances, e.g., send data from instance $r_G = 1$ to instance $r_G = 2$. In line 2, the workers W_k are created. This is done by assigning each rank r_G a worker index k via

Algorithm 2 Entry point of simulation.

```
1: Initialize parallelization environment
2: Assign worker $W_k$
3: if $k == 0$ then
4:     Enter Master routine (Algorithm 3)
5: else
6:     Enter Helper routine (Algorithm 4)
7: end if
```

$$k(r_G) := \left\lfloor \frac{r_G}{w_s(N_w, N_p)} \right\rfloor, \tag{4.2}$$

where the worker size $w_s(N_w, N_p)$ is defined in (4.1). Assigning each rank r_G its worker index via (4.2), yields a grouping as visualized in Figure 4.4. Additionally, we define the local rank r_L of an instance with global rank r_G w.r.t. its worker W_k via

$$r_L(r_G) := r_G - k(r_G) w_s(N_w, N_p). \tag{4.3}$$

In Figure 4.4, the local ranks r_L of the workers W_k are then $\{0, 1, 2, 3\}$ for each k. One can easily convert (r_L, k) back to the corresponding r_G via (4.3). After each r_G is assigned a worker index k, the individual r_G enter the master or helper routine depending on their worker index k.

In the first line of Algorithms 3 and 4, the global (coarse) mesh is loaded by each rank r_G and partitioned into w_s submeshes. Depending on their local rank r_L, r_G keeps their corresponding submesh and applies additional mesh refinements. After this, each rank r_G has their to r_L corresponding submesh, which forms the basis for further computations. In the second line of the master/helper algorithm, necessary data is initialized and assembled, which is later on reused during the simulations. In the case of the master routine, the linear system matrices from Section 3.2.2 are assembled w.r.t. their corresponding submesh. This already introduces communication between the local ranks r_L in worker W_0. In the helper routine, ranks r_G assemble the system matrices from Section 3.3.1 or Section 3.4.5 and load/initialize $N_f/(N_w - 1)$ BCFs w.r.t. their corresponding submesh.

Algorithm 3 Master algorithm.

```
1: Load mesh, apply partitioning, and refine
2: Initialize/assemble data
3: for {$n = 0$; $n < N_{\text{steps}}$; $n$++} do
4:     Compute $\boldsymbol{u}_h^{n+1}$ for given $\boldsymbol{u}_h^n$, $\boldsymbol{\tau}_{\mathrm{p},h}^n$
5:     Send $\boldsymbol{u}_h^{n+1}$ to $W_k$, $k > 0$
6:     Receive polymeric stress contributions from $W_k$, $k > 0$
7:     Compute $\boldsymbol{\tau}_{\mathrm{p},h}^{n+1}$
8:     Save solution
9: end for
```

Algorithm 4 Helper algorithm.

```
1: Load mesh, apply partitioning, and refine
2: Initialize/assemble data
3: for {$n = 0$; $n < N_{\text{steps}}$; $n$++} do
4:     Receive $\boldsymbol{u}_h^{n+1}$ from $W_0$
5:     Update $N_f/(N_w - 1)$ BCFs
6:     Compute polymeric stress contribution
7:     Send polymeric stress contribution to $W_0$
8: end for
```

Now, both routines enter the for loop over the time steps. The master worker ranks r_L compute the new velocity $\boldsymbol{u}_h^{n+1}$ for given velocity $\boldsymbol{u}_h^n$ and polymeric stress tensor $\boldsymbol{\tau}_{\mathrm{p},h}^n$. Note that internally, the velocity $\boldsymbol{u}_h$ is distributed across the local ranks of worker W_0 and analog for other variables that are related to the corresponding submesh. During the computation of $\boldsymbol{u}_h^{n+1}$, the to the helper workers W_k, $k > 0$, associated ranks r_G have to idle.

After $\boldsymbol{u}_h^{n+1}$ is computed, the local ranks r_L of W_0 in the master routine send their parts of $\boldsymbol{u}_h^{n+1}$ to the corresponding local ranks r_L of W_k, $k > 0$ in the helper routine. The helper workers W_k are now able to start updating the BCFs and compute their contributions $\boldsymbol{\tau}_{\mathrm{p},h}^{n+1,(r_L,k)}$ to the polymeric stress tensor $\boldsymbol{\tau}_{\mathrm{p},h}^{n+1}$, which are send to $(r_L, 0)$, i.e., the local ranks of W_0. During the update of the BCFs, the master worker ranks r_G have to wait. In the master routine, the polymeric stress contributions $\boldsymbol{\tau}_{\mathrm{p},h}^{n+1,(r_L,k)}$, $k > 0$ are received and the final polymeric stress tensor $\boldsymbol{\tau}_{\mathrm{p},h}^{n+1}$ can be computed by W_0. Above steps in the master/helper routine are repeated until the end of the for loop is reached.

Note that during the computation of $\boldsymbol{u}_h^{n+1}$ and the updating of the BCFs, only communication withing the local ranks r_L of the corresponding workers W_k is present (cf. Figures 4.6a and 4.6c). The sending/receiving of the velocity/polymeric stress contributions, leads to communication between the local ranks $(r_L, 0)$ of worker W_0 and (r_L, k), $k > 0$ as visualized in Figure 4.6b.

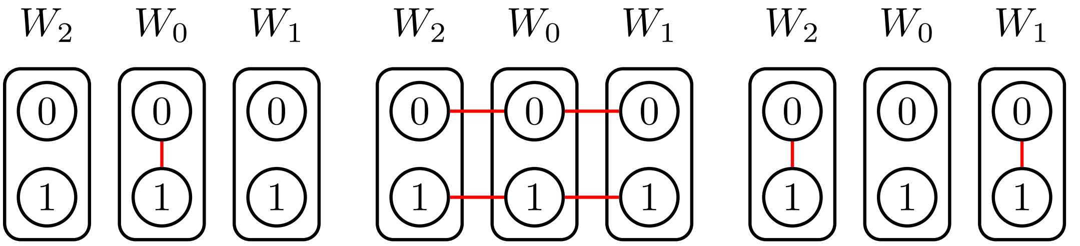

(a) Computation of $\boldsymbol{u}_h^{n+1}$.

(b) Communication during send/receive of $\boldsymbol{u}_h^{n+1}/\boldsymbol{\tau}_{\mathrm{p},h}^{n+1}$-contributions.

(c) Communication during BCF update.

Figure 4.6. Visualization of communication (red lines) between local ranks r_L within worker W_k and communication between local ranks r_L across workers during different stages.

4.3 Parallel scaling

The measures for quantifying parallel performance of code are introduced in Section 4.3.1, where they are discussed on the example of the scaling of the parallelized assembling of a mass matrix. Section 4.3.2 examines the scaling effects of mesh-partitioning and master/helper grouping combined in an idealized setting. In Section 4.3.1, the parallel scaling of the full implementation is evaluated.

4.3.1 Strong scaling

In this section, we introduce the measures for quantifying the scalability of code w.r.t. the parallelization of a problem with constant size (strong scaling). Afterwards, these measures are discussed on the parallelized assembling of a mass matrix. The introduction of the measures is based on Chapter 15 of [82].

At first, we define the speedup $S(N_p)$ and the parallel efficiency $E(N_p)$ via

$$S(N_p) := \frac{t(1)}{t(N_p)}, \tag{4.4}$$

$$E(N_p) := \frac{S(N_p)}{N_p}, \tag{4.5}$$

where $t(N_p)$ is the runtime of the code, which is parallelized on N_p processes. The speedup is a measure on how fast the code with N_p processes is compared to using only one process. The parallel efficiency puts the speedup in relation to the number of processes used. Ideally, we want a speedup of $S(N_p) = N_p$, e.g., $S(2) = 2$ can be interpreted as halving the computation time by doubling the computing resources. From the optimal value $S(N_p) = N_p$ follows $E(N_p) = 1$.

Note that the speedup $S(N_p)$ is bounded in practice as parts of the code do not scale with the number of processes N_p and due to an increasing communication overhead for larger N_p. By neglecting the communication overhead, this effect is known as Amdahl's law, which states that the runtime $t(N_p)$ of a code can be expressed via

$$t(N_p) = f t(1) + (1 - f)\frac{t(1)}{N_p}, \tag{4.6}$$

where $f \in (0, 1]$ is the fraction of the code that cannot be parallelized (cf. Def. 15.5 in [82]). From (4.6) follows

$$S(N_p) = \frac{1}{f + (1 - f)/p} \leq \frac{1}{f}, \tag{4.7}$$

i.e., the speedup is strictly monotonically increasing and bounded by the inverse fraction of the code that cannot be parallelized.

Figure 4.7 visualizes a realistic speedup scaling behavior, where the parallelized assembling of a velocity mass matrix is timed for a different number of processes N_p. One can clearly observe that the maximal attainable speedup $S(N_p)$ is around 16 with $N_p = 56$. The associated parallel efficiency is $E(56) = 0.28$, which indicates a very inefficient use of the computing resources. One can deduce via (4.7) a theoretical sequential fraction of the code of $f = 1/16$ (for the assembling of the velocity mass matrix with $\mathbb{Q}_4^2$-elements on a mesh with 131328 elements). At $N_p = 4$, we have $S(4) = 3.56$ and $E(4) = 0.89$, which is as close as we can get to the optimal values. Therefore, $N_p = 4$ would be the most economic/efficient choice. For very large N_f, the additional communication overhead can get so high that the speedup $S(N_p)$ can actually drop again (parallel slowdown).

Alternatively, one could observe the scaling of the computation time of a problem, where the task size for each process is kept constant. This is done by also increasing the total problem size when the number of processes is increased. Such a test of scaling is called weak scaling.

4.3.2 Amdahl's law applied on mesh partitioning and master/helper grouping

In the previous section, we observed the strong scaling on the example of assembling a mass matrix, where the parallelization is done with mesh partitioning only. Now, we can apply the idea of Amdahl's law to the problem of computing a single time step of the problem in Figure 4.5, where we have the freedom to additionally

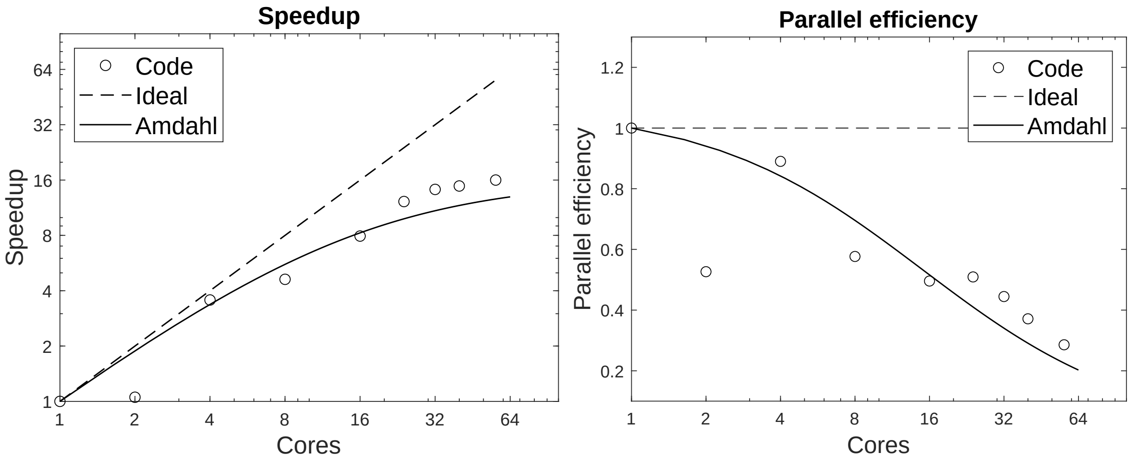

Figure 4.7. Speedup and parallel efficiency of the assembling process of a velocity mass matrix with $\mathbb{Q}_4^2$-elements on a mesh with 131328 elements. The Amdahl curves use (4.6) with $f = 1/16$.

adjust the number of workers N_w for a given number of processes N_p and BCF N_f, i.e., we combine the parallelization approaches from Sections 4.1.2 and 4.1.3.

For simplicity, we neglect communication effects, i.e., instant transfer times. The computation time of a single time step t_{Step} with N_w workers of size w_s and N_f BCFs can then be decomposed into

$$t_{\text{Step}} = t_{\text{M}} + t_{\text{H}}, \tag{4.8}$$

where t_{M} and t_{H} are the computation times of the master worker W_0 (Navier–Stokes part) and the helper worker W_k, $k > 0$ (BCF part). It is assumed that t_{H} is identical for each W_k, $k > 0$, as visualized in Figure 4.8. Using Amdahl's law (4.6) to

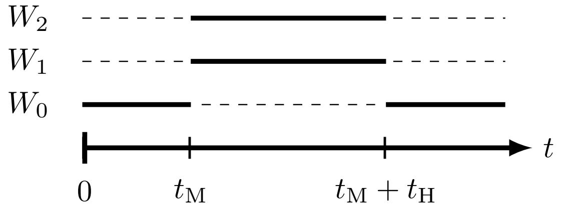

Figure 4.8. Visualization of worker activity during the computation of a single time step. The dashed line marks the time interval, where worker W_k is idle.

express $t_{\text{M}}(w_s)$ gives

$$t_{\text{M}}(w_s) := f_{\text{M}} t_{\text{M}}(1) + (1 - f_{\text{M}}) \frac{t_{\text{M}}(1)}{w_s}, \tag{4.9}$$

where $f_{\text{M}} \in (0, 1]$ is the sequential fraction of the master part of the code, which cannot be parallelized. Note that (4.9) only depends on the worker size w_s. We further decompose the helper worker runtime t_{H} into

$$t_{\text{H}}(w_s) := t_{\text{I}}(w_s) + \frac{N_f}{N_w - 1} t_{\text{BCF}}(w_s), \tag{4.10}$$

where t_I is the time it takes for each helper worker for initializing/assembling data, which is required before the update of the BCFs can start, and t_BCF is the time it takes to update one BCF. Thus, t_BCF has to be multiplied by the number of BCFs that each helper worker has to update, which is done in (4.10). Analog to (4.9), the expressions for $t_\mathrm{I}(w_s)$ and $t_\mathrm{BCF}(w_s)$ are given by

$$t_\mathrm{I}(w_s) \coloneqq f_\mathrm{I} t_\mathrm{I}(1) + (1 - f_\mathrm{I})\frac{t_\mathrm{I}(1)}{w_s}, \tag{4.11a}$$

$$t_\mathrm{BCF}(w_s) \coloneqq f_\mathrm{BCF} t_\mathrm{BCF}(1) + (1 - f_\mathrm{BCF})\frac{t_\mathrm{BCF}(1)}{w_s}. \tag{4.11b}$$

Substituting the expressions for the various runtimes into (4.8) yields

$$\begin{aligned} t_\mathrm{Step}(w_s, N_w) =& f_\mathrm{M} t_\mathrm{M}(1) + f_\mathrm{I} t_\mathrm{I}(1) + \frac{(1 - f_\mathrm{M})t_\mathrm{M}(1) + (1 - f_\mathrm{I})t_\mathrm{I}(1)}{w_s} \\ &+ \frac{N_f}{N_w - 1}\left[f_\mathrm{BCF} t_\mathrm{BCF}(1) + (1 - f_\mathrm{BCF})\frac{t_\mathrm{BCF}(1)}{w_s}\right]. \end{aligned} \tag{4.12}$$

For a given number of processes N_p, there are in general multiple possibilities of w_s and N_w that satisfy $w_s N_w = N_p$. The optimal pair (w_s, N_w) should then minimize $t_\mathrm{Step}(w_s, N_w)$ under the condition $w_s N_w = N_p$.

Expression (4.12) is of the shape

$$t_\mathrm{Step}(w_s, N_w) = C_1 + \frac{C_2}{w_s} + \frac{N_f}{N_w - 1}\left[C_3 + \frac{C_4}{w_s}\right] \tag{4.13}$$

with constants $C_i > 0$. It clearly reveals that constant C_3 can only be scaled down by increasing N_w. From (4.13), one can deduce the following lower bounds for t_Step. In the case of just applying mesh partitioning and no master/helper grouping, i.e., $N_w = 2$ is fixed, we have

$$t_\mathrm{Step}(w_s, 2) \geq C_1 + N_f C_3. \tag{4.14}$$

Applying both parallelization approaches, yields

$$t_\mathrm{Step}(w_s, N_w) \geq t_\mathrm{Step}(w_s, N_f + 1) \geq C_1 + C_3. \tag{4.15}$$

Note that the number of workers N_w is bounded by N_f, i.e., each helper worker W_k, $k > 0$, has to update at least one BCF. A comparison of (4.14) and (4.15) reveals that the theoretical lower bound (4.14), which is obtained by using only mesh partitioning, can be greatly reduced to (4.15) by applying additional master/helper grouping.

Note that N_f is typically $\mathcal{O}(10^3)$, i.e, the last term in (4.12) or (4.13) dominates compared to first terms. A good guideline is therefore to favor a higher number of workers with a smaller size compared to less workers with larger sizes. However, one has to keep in mind that (4.12) completely neglects the communication overhead. Additionally, the memory usage increases drastically with the number of workers, as individual copies of the same data are stored for each worker (cf. Table 4.1).

In the next section, we test the strong scaling of our implementation of the above presented parallelization approaches.

4.3.3 Strong scaling of the implementation

In the following section, we test the strong scalability of our implementation. For this, we computed 25 time steps of a startup shear flow scenario on a periodic unit square with $N_f = 3000$ bead-rod chains. Each chain consists of $N = 7$ beads. The domain is discretized with 4096 square shaped elements. The worker size is kept fixed at $w_s = 4$ and the number of worker N_w is varied from 5 to 320, where in each test, the previous number of workers is doubled.

The computations of the following scaling test and the simulations from Section 5 are run on the Meggie compute cluster at RRZE [58]. It consists of 728 compute nodes. Each node has two Intel Xeon E5-2630v4 "Broadwell" (10 x 2.2GHz), 25 MB shared cache per chip, and 64 GB of RAM. The nodes communicate via Intel OmniPath interconnect with up to 100 GBit/s bandwidth per link and direction. The measured LINPACK performance is about 481 TFlop/s.

In Figure 4.9, the parallel scaling of the implementation is demonstrated by running the same simulation from above on varying numbers of computing nodes. One can directly observe the excellent parallel scaling due to the master/helper grouping parallelization approach from Section 4.1.3 on up to $N_p = 1280$ processes. The mesh partitioning approach alone is not sufficient to achieve such a strong scaling as demonstrated in Section 4.3.1 for the assembling of a mass matrix, which already suffers a loss of parallel efficiency for $N_p < 64$. Table 4.1 lists a more detailed summary of the scaling test results. There one can observe the increasing memory consumption of this parallelization approach, which rises from 4.1 GiB to 93.0 GiB. The last column lists the average number of BCF per helper worker, i.e. the factor $N_f/(N_w - 1)$ in (4.12) is reduced from 750 to 9.4.

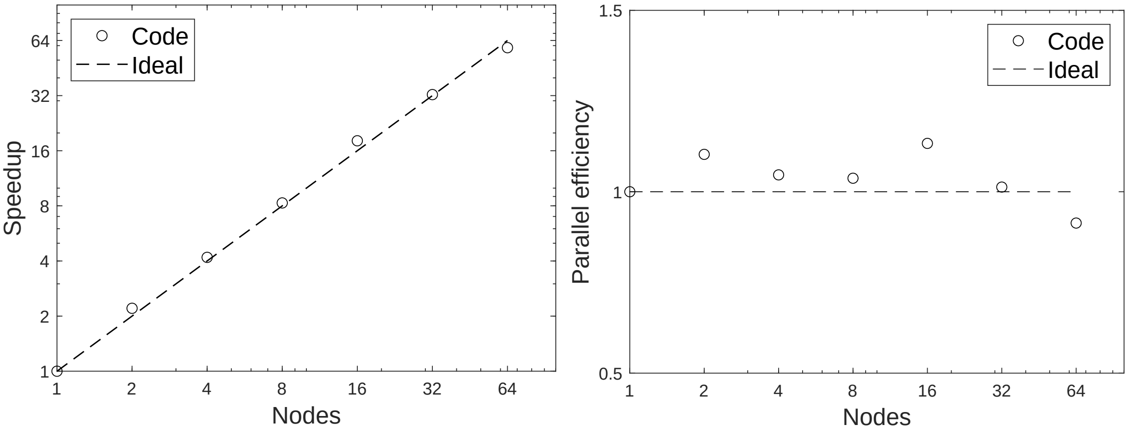

Figure 4.9. Parallel (strong) scaling of the implementation on the Meggie compute cluster of the RRZE [58]. The total computation time of the same simulation with $N_f = 3000$ configuration fields was timed on $1, 2, 4, 8, 16, 32, 64$ computing nodes. Each node consists of 20 processes. Worker size is fixed to 4 processes.

Table 4.2 considers the same simulation as in Figure 4.9 with $N_f = 1500$. It lists the runtimes for varying worker sizes w_s. The shortest runtime w.r.t. a fixed number of processes N_p is marked in bold. For fixed N_p, it is always better to

nodes	N_p	N_w	Runtime [s]	Memory [GiB]	$N_f/(N_w-1)$
1	20	5	23151.50	4.1	750.00
2	40	10	10494.60	5.6	333.33
4	80	20	5530.91	8.6	157.89
8	160	40	2789.97	14.6	76.92
16	320	80	1276.83	25.8	37.97
32	640	160	714.30	47.2	18.87
64	1280	320	395.90	93.0	9.40

Table 4.1. Summary of more detailed results from scaling test in Figure 4.9.

	Number of processes N_p						
w_s	20	40	80	160	320	640	1280
1	**11958.90**	6127.69	3148.98	1651.46	1000.03	666.09	529.14
2	12773.30	**6035.31**	3392.56	1738.73	**880.84**	520.24	367.91
4	15957.20	6424.95	**3119.99**	1710.69	888.05	481.26	267.42
5	16727.30	6721.50	3156.32	**1573.00**	896.58	477.39	258.26
8	–	8017.71	4040.52	1627.57	891.06	485.84	251.91
10	25364.40	8522.47	3704.86	1898.11	942.31	504.23	283.06
16	–	–	3943.97	1886.06	885.20	**461.91**	**250.19**
20	–	17148.40	5497.60	2166.19	1028.94	548.62	297.17
32	–	–	–	2117.33	1014.24	491.91	251.31
40	–	–	8073.60	2667.62	1187.56	577.77	302.73
64	–	–	–	–	1227.56	544.07	268.17

Table 4.2. Runtime [s] of the implementation on the Meggie compute cluster of the RRZE [58]. The total computation time of the same simulation with $N_f = 1500$ configuration fields was timed on $1, 2, 4, 8, 16, 32, 64$ computing nodes with varying worker sizes w_s. Each node consists of 20 processes.

choose a smaller worker size w_s. Choosing a too large w_s results in longer runtimes. This effects is especially significant in the first three columns of Table 4.2.

Having obtained such an optimal strong scaling on up to $N_p = 1280$ processes with our implementation, we are able to run efficiently simulations of the models discussed in Section 2.

4.4 Remarks on the code

The code is written in C++ in an object oriented fashion and has a length of around 10000 lines. It uses a distributed memory parallelization via the MPI (message-passing interface) standard. MPI offers suitable routines that help to establish communication between the processes. For the assembling and solving process of the linear system of equations from Sections 3.3.1 and 3.4.5, the open-source finite-element library MFEM [3, 59] (ver. 4.3) is used. It provides parallelized versions of iterative solvers such as the Krylov subspace methods MINRES, CG, and GMRES. The preconditioners are provided by Hypre [27] (ver. 2.18.2). The meshes are generated with GMSH [29] (ver. 4.9.3) and the partitioning is done with METIS [48] (ver. 5.1.0).

Running simulations on the HPC cluster at the RRZE [58], which take longer than 24 hours, required the additional implementation of a custom checkpoint/restart feature, as the maximum allowed code runtime is 24 hours. This can be circumvented by creating checkpoints during the simulation. After 24 hours of runtime are reached and the simulation has to be stopped, it can be restarted from the last checkpoint and no data is lost. This feature unlocks to run simulations that take longer than 24 hours. Since most of the data (system matrices) can be assembled again on the fly without knowledge of the current state of the simulation, only the unknowns (velocity, pressure, BCFs, etc.) have to be saved during a checkpoint. This reduces the required disk space of a checkpoint tremendously.

The Brownian dynamic simulations for the computation of relaxation times in Section 3.4.3 and generation of initial equilibrium configurations for the chains, as described in Section 3.4.1, were done in Matlab [44] (ver. 2020a Update 4) on a personal computer with two Intel Xeon E5-2680v4 (14 x 2.4GHz) and 128 GB of RAM.

5 Simulations

In the following sections, we present and discuss the simulation results of the Navier–Stokes equations coupled to the bead-spring dumbbell or bead-rod chain model from Sections 2.1 and 2.2. This is done in various 2D flow scenarios across Sections 5.1 to 5.3. The model that is obtained by coupling the Navier–Stokes equations (1.43) with the Hookean dumbbell model (cf. Section 2.1) is abbreviated with (NS-Hookean), (NS-FENE) for FENE dumbbells, and (NS-BR) for the bead-rod chain model (cf. Section 2.2).

The flow around a cylinder and 4:1 planar contraction flow are typical benchmark scenarios to test the stability and accuracy of discretizations of a viscoelastic fluid model (cf. overview paper [1]). In this thesis, it its the first time that a discretization of (NS-BR) and resulting simulations are presented. Thus, there are no other meaningful simulation results in the literature at this point for quantitative comparisons. However, we can do qualitative comparisons between (NS-BR) and (NS-Hookean)/(NS-FENE) and observe their different behaviors in various scenarios.

Section 5.1 considers a start-up shear flow scenario, where we compare (NS-Hookean) solutions to the macroscopic Oldroyd-B (NS-OB) model solutions to verify our implementation as these two models are formally equivalent. Further (NS-Hookean) and (NS-FENE) simulations are done to demonstrate characteristic viscoelastic fluid properties (velocity overshoot). Additionally, different bead-rod chain parameters studies are done to observe the effect on the solutions. In Section 5.2, we consider the more challenging flow around a cylinder benchmark scenario. There, parameter studies for the (NS-BR) model are done to observe the influence on the stresses/velocity near the cylinder and the drag coefficient. Additional (NS-Hookean) simulations demonstrate qualitative similarities to the (NS-BR) model. Section 5.3 considers a realistic flow scenario through a planar 4:1 contraction and compares (NS-BR) solutions with varying numbers of beads to observations from experiments in the literature.

5.1 Start up shear flow

In this section, we consider the (NS-Hookean), (NS-FENE), and (NS-BR)-models in a start-up shear flow scenario. This scenario is characterized by considering a 2D channel $\Omega = (0, L^*) \times (0, 1) \subset \mathbb{R}^2$ of height 1 and length $L^* > 0$ with homogeneous Dirichlet boundary conditions (1.36) on the bottom $[0, L^*] \times \{0\} \subset \partial\Omega$, i.e., no fluid flow, and inhomogeneous Dirichlet BC on the top $[0, L^*] \times \{1\} \subset \partial\Omega$, where the velocity is prescribed by

$$g_{\mathrm{D}}(x^*, y^*, t^*) = \begin{cases} (1, 0)^{\mathrm{T}}, & y^* = 1, t^* > 0, \\ (0, 0)^{\mathrm{T}}, & \text{else}. \end{cases} \tag{5.1}$$

At the start of the simulation ($t^* = 0$), we assume the fluid to be at rest and set the initial velocity to $\boldsymbol{u}_0 = \boldsymbol{0}$. In Section 5.1.1, the left and right side of the channel Ω are assigned homogeneous Neumann BC (1.37). In the non-periodic setting, one has to prescribe an additional inflow boundary condition for the bead-spring dumbbells, which is set to be $\boldsymbol{Q}(t) = \boldsymbol{Q}(0)$ on $\partial\Omega^-$, where $\partial\Omega^- = \{\boldsymbol{x} \in \partial\Omega \,|\, \boldsymbol{u} \cdot \boldsymbol{n} < 0\}$ denotes the inflow boundary of $\partial\Omega$. The $\boldsymbol{Q}(0)$ are distributed according to (2.69a) or (2.69b). The corresponding inflow boundary condition for the polymeric stress in the Oldroyd-B model is $\boldsymbol{\tau}_\mathrm{p} = \mathbf{0}$ on $\partial\Omega^-$. Sections 5.1.2 and 5.1.3 apply periodic BC (1.39) on the left and right part of $\partial\Omega$, such that no additional inflow boundary conditions for the bead-spring dumbbells and bead-rod chains are necessary. For the choice of finite dimensional ansatz spaces of the unknowns, see Sections 3.2 and 3.3. Note that the initial bead-spring dumbbells or bead-rod chains in equilibrium are generated as described in Sections 3.3.3 and 3.4.1.

In Section 5.1.1, model (NS-Hookean) is compared to the Oldroyd-B model (NS-OB) from Section 1.4.3. As already mentioned in Section 2, the Hookean dumbbell model is formally equivalent to the Oldroyd-B model. Thus, we can validate our own implementation by comparing our (NS-Hookean) model simulation results with the (NS-OB) simulations, which are done with a different software (COMSOl [19]).

5.1.1 Comparison the Hookean dumbbell model to the Oldroyd-B model

The macroscopic equivalent of the Hookean dumbbell model is the Oldroyd-B model as mentioned in Section 2. This fact can be exploited to validate our own implementation of Brownian configuration field method. Solving the same scenario with the microscopic Hookean dumbbell model and macroscopic Oldroyd-B model should yield similar solutions. The solutions do not coincide perfectly due to the finite number of realizations for the approximation of the polymeric stress tensor $\boldsymbol{\tau}_\mathrm{p}$. The simulation software COMSOL [19] is used for solving the scenario with respect to the macroscopic Oldroyd-B model.

Model parameter	
T^*	5
ϵ	8/9
Re	1
Wi	1

(a)

Discretization parameter	
Δt	$5 \cdot 10^{-3}$
N_f	10000
N_p	1000
N_w	250

(b)

Mesh parameter	
Ω	$(0,6) \times (0,1)$
h	1/32
n_x	192
n_y	32

(c)

Table 5.1. Model, discretization, and mesh parameters.

Table 5.1 summarizes the model, discretization, and mesh parameters, which are used for the simulations in Figures 5.1 and 5.2. The mesh consists of $n_x = 192$ square shaped elements in x-direction and $n_y = 32$ in y-direction, which yields a total of 6144 elements. The resulting mesh size is $h = 1/32$. The boundary conditions are mentioned at the beginning of Section 5.1. The length of the channel Ω is set to $L^* = 6$. In each time step of the (NS-Hookean) simulations, 10002 linear systems of equations have to be solved. Both implementations use the identical discretization mesh $\mathcal{T}_h$.

Figure 5.1. Velocity magnitude at $t^* = 5$ of the Hookean dumbbell solution.

Figure 5.1 visualizes the velocity magnitude of the (NS-Hookean) solution at $t^* = 5$. Figure 5.2 compares three realizations of the (NS-Hookean) model with the corresponding solutions of the (NS-OB) model over time at the center of the domain. One can directly observe the stochastic nature of the (NS-Hookean) solutions in form of small stochastic noise in the polymeric stress graphs. Note that the polymeric stress $(\tau_{\mathrm{p},h})_{yy}$ for the (NS-Hookean) model shows almost pure noise as the deterministic (NS-OB) solution that is approximated, is close to 0. The deterministic (NS-OB) stress entry $(\tau_{\mathrm{p},h})_{yy}$ is not exactly 0 due to the unnatural BC choice of homogeneous Neumann BC, homogeneous inflow condition for the polymeric stress, and inhomogeneous Dirichlet BC for the velocity at the top of $\partial\Omega$. Unfortunately, the more natural choice of periodic boundary conditions was not realisable in COMSOL. The velocity graphs match almost perfectly over time. The (NS-Hookean) graphs of $(\tau_{\mathrm{p},h})_{xx}$ and $(\tau_{\mathrm{p},h})_{xy}$ closely follow the deterministic (NS-OB) solution at the beginning. Over time the graphs drift a bit apart from the Oldroyd-B solution due to the stochastic nature of the BCF ansatz, which cannot be avoided as the polymeric stress tensor is approximated with a finite number of BCFs. From Figure 5.2, we deduce that our implementation of the BCF ansatz is correct.

This simulation already demonstrates fluid characteristics (cf. velocity overshoot in Figure 5.2), where the velocity behaves completely different compared to Newtonian fluids. A Newtonian fluid would approach its stationary velocity from below without an overshoot, which is visualized in the next section (cf. Figure 5.3).

5.1.2 Bead-spring dumbbell

In the following, we compare the Hookean dumbbell model and the FENE dumbbell model from Section 2.1 with each other in a periodic start up shear flow scenario. Here, we consider the same setup as in Section 5.1.1 with periodic boundary conditions on the left and right side of the channel instead of homogeneous Neumann BC. The model and discretization parameters are the same as summarized in Table 5.1. In the case of FENE dumbbells, we have the additional parameter b, which controls the squared maximum extension of the FENE-spring. Here, we considered the values $b = 5, 10, 50$. The Hookean dumbbell model is obtained in the limiting case $b = \infty$.

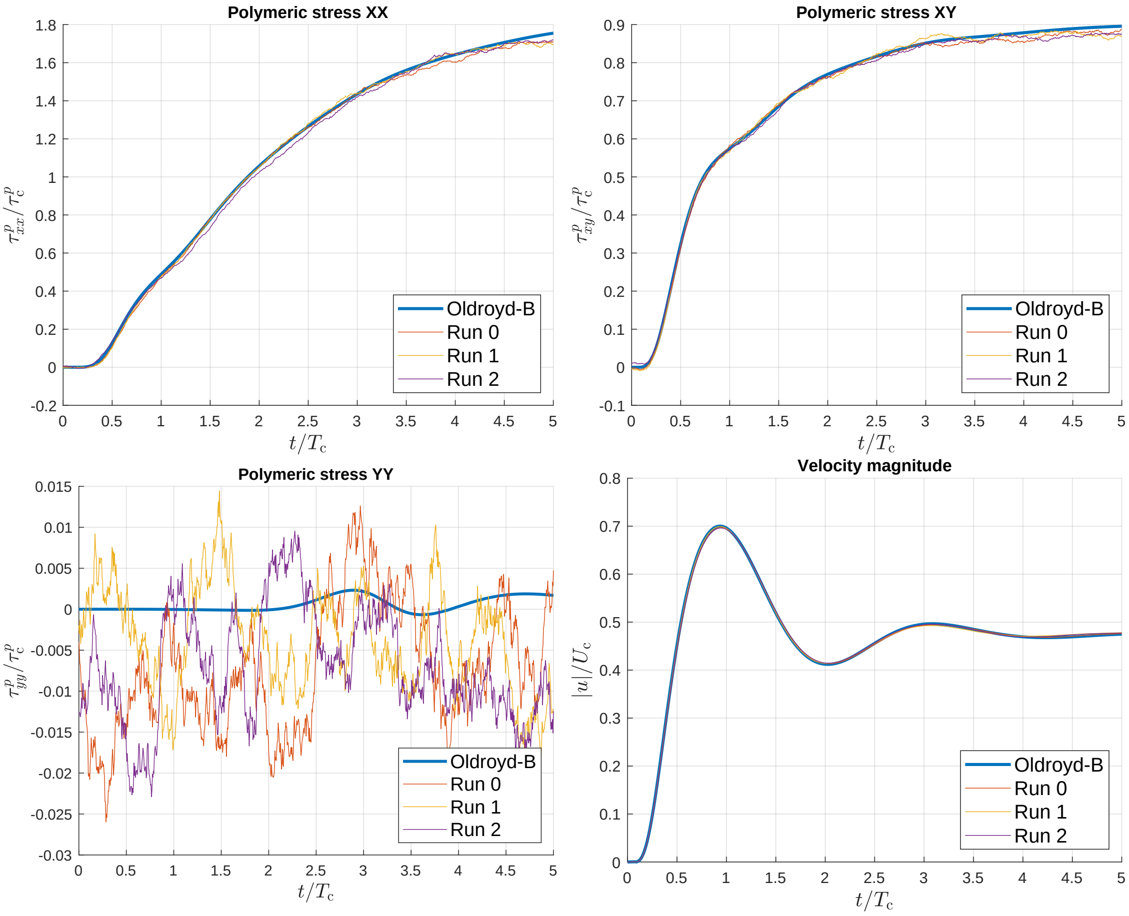

Figure 5.2. Visualization of the polymeric stress entries and velocity w.r.t. the macroscopic Oldroyd-B solution and three realizations of the microscopic Hookean dumbbell model at $(3, 0.5)$ over time.

In Figure 5.3, we visualized the Hookean and FENE solutions at the center of the domain over time. In the velocity plot, a plain Navier–Stokes solution ($\epsilon = 0$) is additionally visualized. There, one can clearly observe the characteristic difference between a viscoelastic and Newtonian fluid. As expected, the FENE graphs approach the Hookean dumbbell graphs for increasing b. The graphs of the polymeric stress gets noisier for decreasing b. The polymeric stress entries $(\boldsymbol{\tau}_{p,h})_{xx}$ and $(\boldsymbol{\tau}_{p,h})_{xy}$ get stationary in a shorter time for smaller values of b. Additionally, one can observe that the stationary value of $(\boldsymbol{\tau}_{p,h})_{xx}$ highly depends on b. Contrary, the stationary value of $(\boldsymbol{\tau}_{p,h})_{xy}$ seems to be almost independent of b.

In the next section, the (NS-BR) model is considered. Figure 5.3 can be used for qualitative comparisons.

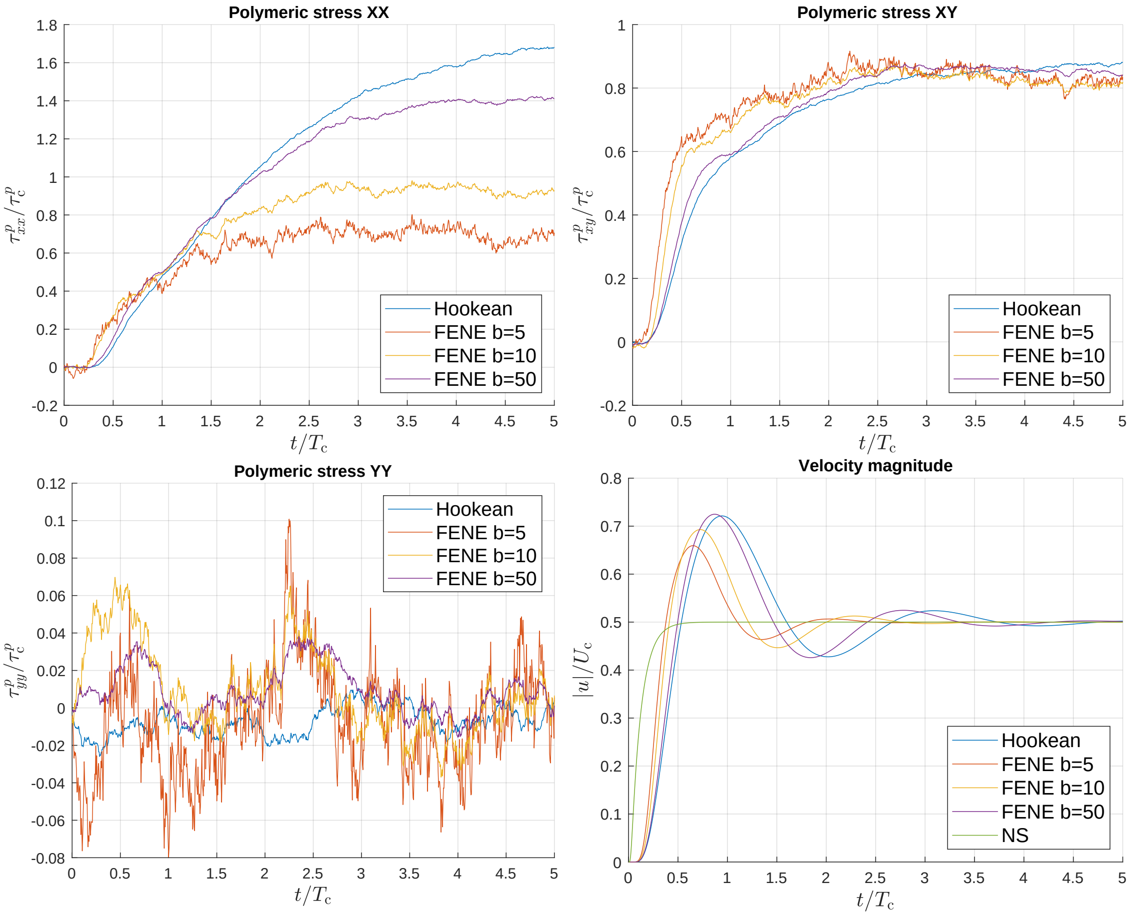

Figure 5.3. Visualization of Hookean and FENE dumbbell solutions at $(3, 0.5)$ over time with $N_f = 10000$. The velocity magnitude plot additionally shows the Navier–Stokes solution ($\epsilon = 0$).

5.1.3 Bead-rod chains

In the following, a periodic square-shaped domain Ω is considered, i.e., we set the length of the channel to $L^* = 1$. Figure 5.4 visualizes the boundary conditions and the discretization mesh $\mathcal{T}_h$. The mesh consists of $64 \times 64 = 4096$ square-shaped elements with mesh width $h = 1/64$. The simulations consider two studies to examine the influence of bead-rod chains on the polymeric stress and velocity.

Study 1: Increasing the number of beads In this study, we compare fluids with varying bead-rod chain lengths, i.e., varying number of beads N and fixed rod-length a. We additionally assume the friction coefficient ξ, number density n, temperature ϑ, and solvent viscosity η_s to be independent of the number of beads N. With these assumptions, we can prescribe Wi, ϵ, and Re for a fixed number of beads and then compute Wi(N), $\epsilon(N)$, and Re(N) for varying N accordingly via

$$\mathrm{Re} = (1 - \epsilon)\frac{\rho_c U_c L_c}{\eta_s}, \tag{5.2}$$

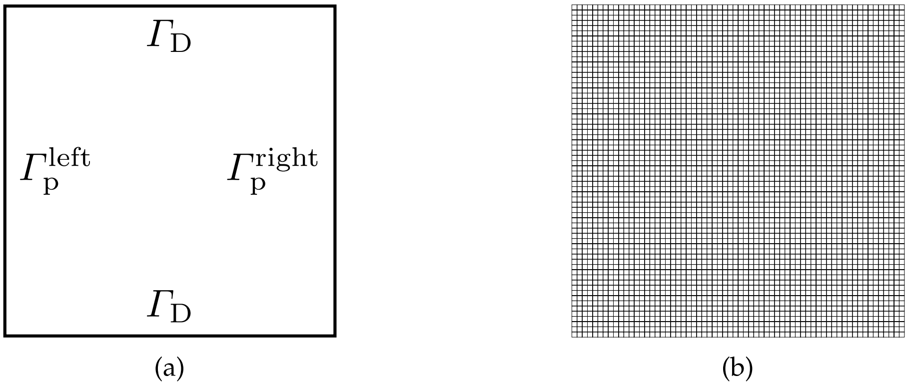

(a) (b)

Figure 5.4. Shear flow domain with boundary info (left) and visualization of the mesh (right) with 4096 elements.

(1.42), (2.103), and (2.96). To obtain (5.2), combine (1.42) and (1.41). See Table 5.2 for the computed parameter values and the required computation times t_{comp}. Figure 5.5 visualizes the approach of increasing the chain length by adding beads.

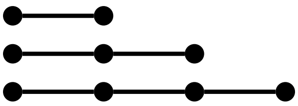

Figure 5.5. Visualization of study 1.

Study 1 model parameter				
N	Wi	ϵ	Re	t_{comp} [h:min]
5	5.7845	0.3249	1.0127	09:49
10	21.4789	0.6650	0.5026	24:39
15	45.0000	0.8179	0.2732	49:11

Table 5.2. Parameters for shear flow study 1 and required computation time t_{comp}.

Study 2: Successive chain dissection In this study, we start by considering chains with a fixed rod length a and an odd number of beads N. After that, we cut the chains in half. Doing this doubles the previous number density n and the number of beads reduces accordingly, as we have now doubled the amount of physical chains with only half of the previous length. This procedure is repeated multiple times until single rods are left. Again, we additionally assume the friction coefficient ξ, temperature ϑ, and solvent viscosity η_{s} to be independent of the number of beads N. With these assumptions, we are able to compute for prescribed Wi, ϵ, Re, and given number of beads, the corresponding Wi(N), $\epsilon(N)$, and Re(N) for varying N. See Table 5.3 for the computed parameter values and the required computation times t_{comp}. Figure 5.7 visualizes the chain dissection procedure.

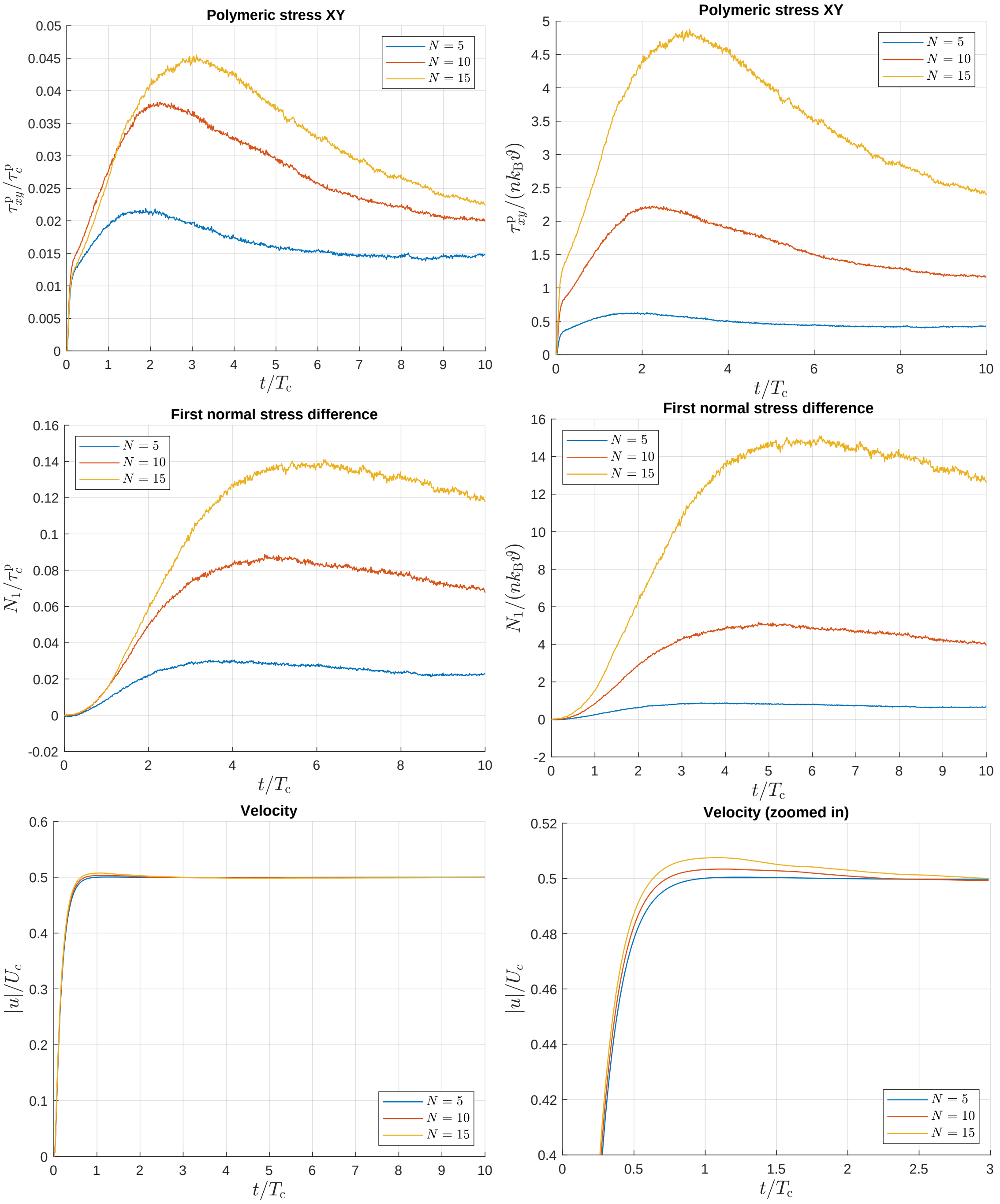

Figure 5.6. Start-up shear flow simulation results of study 1. Data over time at point (0.5, 0.5).

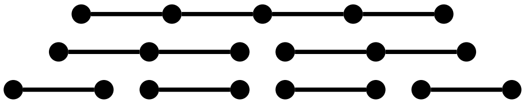

Figure 5.7. Visualization of the dissection steps in study 2 for $N = 5$ to $N = 2$.

Study 2 model parameter				
N	Wi	ϵ	Re	t_{comp} [h:min]
17	57.8000	0.8727	0.1909	59:29
9	17.4254	0.7921	0.3119	23:23
5	5.7845	0.6957	0.4565	10:07
3	2.3014	0.6038	0.5943	04:39
2	1.1737	0.5334	0.7000	02:16

Table 5.3. Parameters for shear flow study 2 and required computation time t_{comp}.

In Figure 5.6 and Figure 5.8, we visualized the simulation results of study 1 and study 2 by plotting the data at the center point $(0.5, 0.5)$ of Ω over time. For the evaluation of the polymeric stress tensor $\boldsymbol{\tau}_{\text{p}}$, $N_f = 2233$ configuration fields were used. This way, each worker W_k, $k > 0$, has 7 configuration fields. The simulations are run until $T^* = 10$ with $N_s = 4000$ time steps. Table 5.4 summarizes the associated discretization and mesh parameters.

Discretization parameter	
Δt	$2.5 \cdot 10^{-3}$
N_f	2233
N_p	1280
N_w	320

(a)

Mesh parameter	
Ω	$(0, 1)^2$
h	$1/64$
n_x	64
n_y	64

(b)

Table 5.4. Mesh and discretization parameters of the simulations in Figures 5.6 and 5.8.

In Figure 5.6, one can observe that the maximum of the polymeric shear stress rises and delays further in time if the number of beads is increased. The first normal stress difference $N_1 := (\boldsymbol{\tau}_{p,h})_{xx} - (\boldsymbol{\tau}_{p,h})_{yy}$ behaves similarly, i.e., the maximum rises and delays in time for bead-rod chains with more beads. The first normal stress difference is one of the three *material functions* or *viscometric functions* that is used for the characterization of the stress tensor in shear flow [63, p. 10]. In the case of Newtonian fluids, the first normal stress difference is always zero in shear flow. Concerning the velocity, the characteristic overshoot over 0.5 is for $N = 5$ almost not present, which indicates a low impact of short bead-rod chains on the fluid. For $N = 10$ and $N = 15$, the viscoelastic bead-rod chain impact on the fluid increases, and a velocity overshoot over the 0.5-barrier can be clearly seen.

In Figure 5.8, dissecting the chains and thus increasing the number density n leads to a reduction of the maximum polymeric shear stress, and the maximum is attained faster in time. From $N = 17$ to $N = 9$, the maximum is almost the same and only shifts back in time. The velocity overshoot over the 0.5-barrier reduces if the chains are dissected into smaller segments and the number density is adjusted accordingly.

In Figure 5.9, a discretization parameter study is performed to observe the sensitivity of mesh resolution and time step size on the solutions at the point $(0.5, 0.5)$. The simulations use the parameters from study 2 w.r.t. $N = 3$ (cf. Table 5.3). The mesh size h varies now from 2^{-3} to 2^{-5} and the number of time steps is 100, 500, 1000, 2000, and 4000. Note that simulations with the same step size Δt use the same random number generator seed. This ensures that the Brownian forces are identical across all considered meshes, enabling a better comparison.

Increasing the mesh resolution, i.e., reducing h, has only a negligible effect on the solutions for a fixed time step size Δt, which indicates a fast mesh convergence. Note that the velocity is approximated with quadratic Lagrangian elements. For time step sizes $\Delta t \leq 0.01$, convergence w.r.t. Δt can be observed. It can be inferred from this that the mesh size and time step size used in study 1 and study 2 were adequately small.

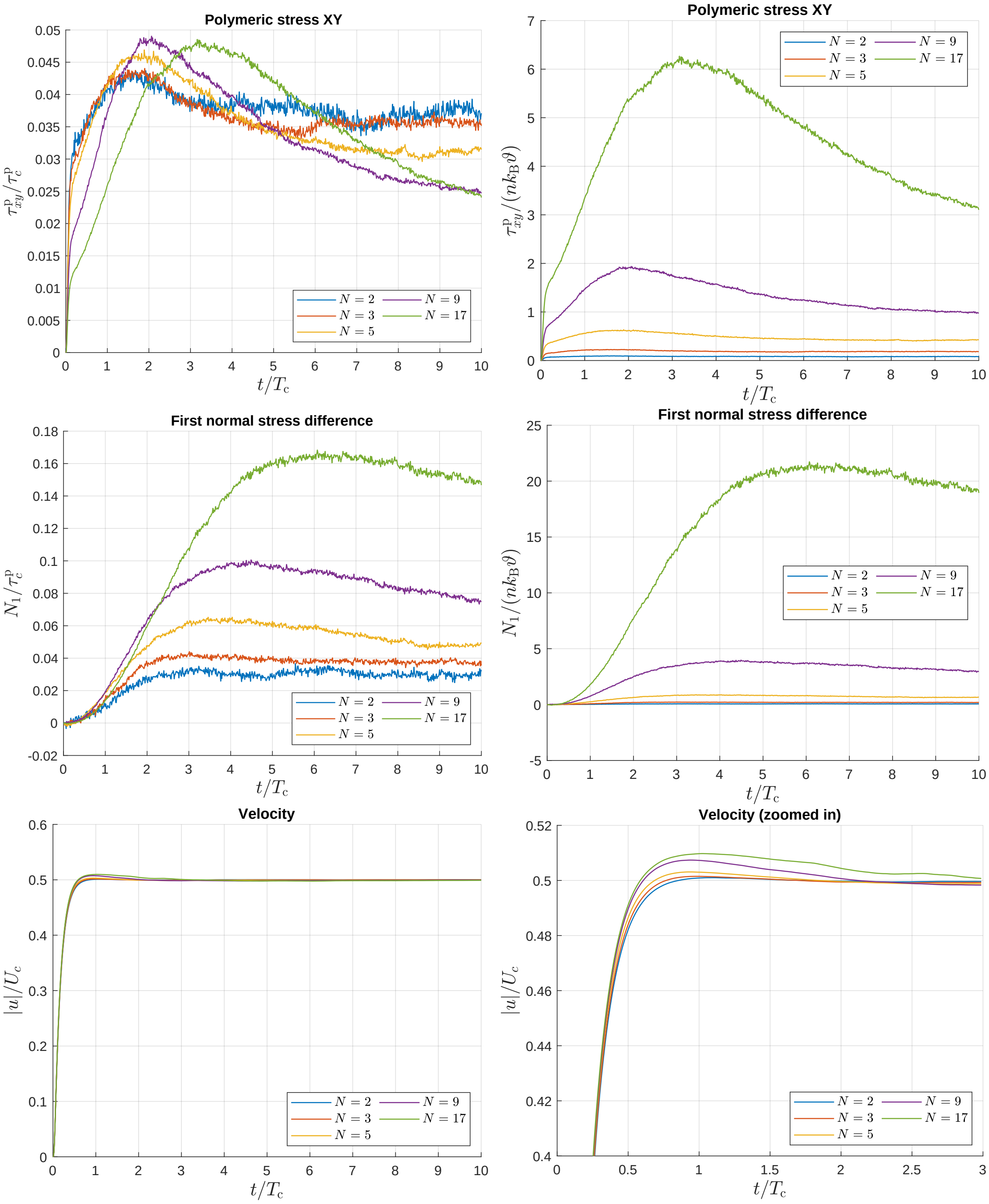

Figure 5.8. Start-up shear flow simulation results of study 2. Data over time at point $(0.5, 0.5)$.

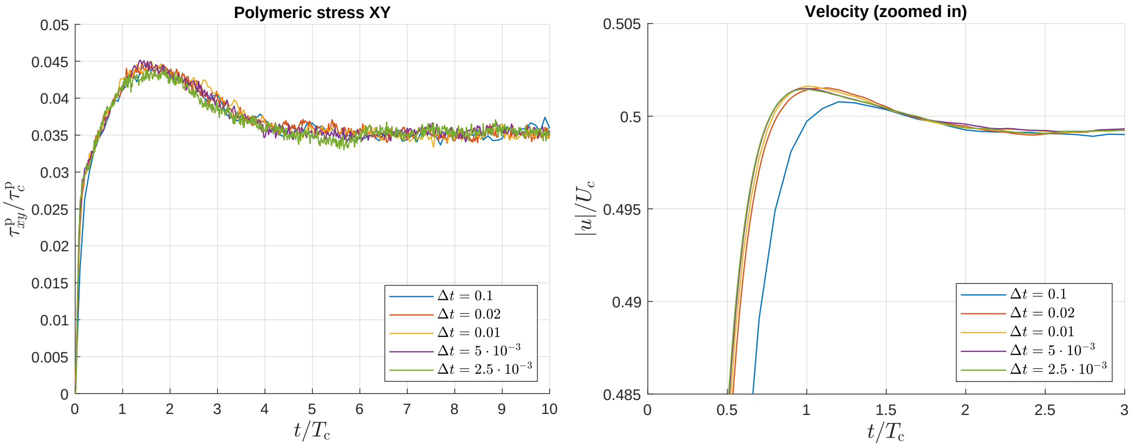

(a) $h = 1/8$.

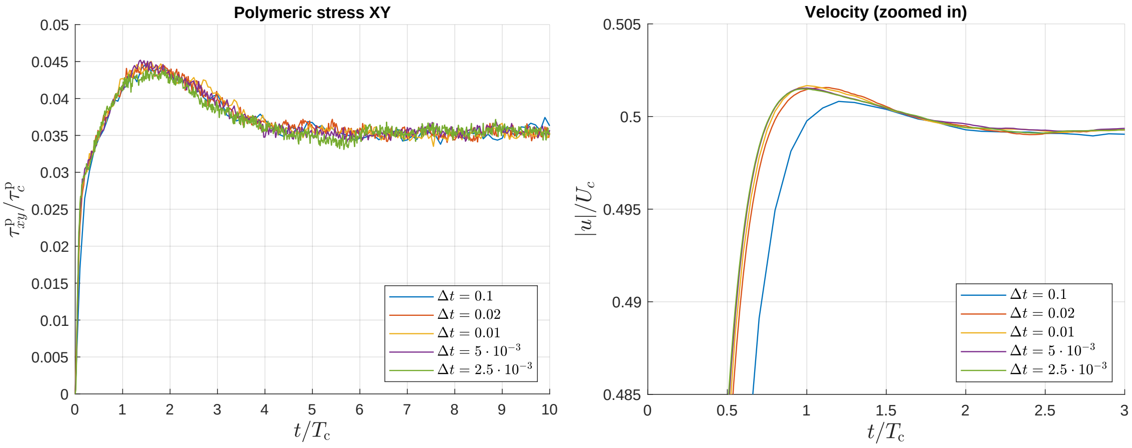

(b) $h = 1/16$.

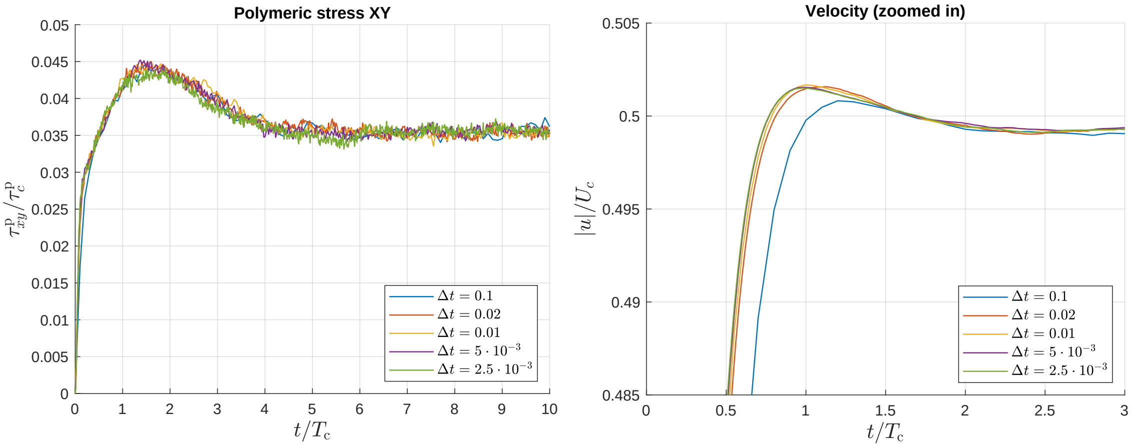

(c) $h = 1/32$.

Figure 5.9. Start-up shear flow simulation results of the $(h, \Delta t)$-study for $N = 3$, $\mathrm{Re} = 0.5943$, $\mathrm{Wi} = 2.3014$, $\epsilon = 0.6038$, $h \in \{2^{-3}, 2^{-4}, 2^{-5}\}$, and $\Delta t \in \{0.1, 0.02, 0.01, 5 \cdot 10^{-3}, 2.5 \cdot 10^{-3}\}$. Data over time at point $(0.5, 0.5)$.

5.2 Flow around a cylinder scenario

To model the flow around a cylinder, we consider as domain $\Omega \subset \mathbb{R}^2$ the top half of a channel, where at the center a disk is cut out with radius r, cf. Figure 5.10. The channel has a length of $15r$ and a height of $2r$. The characteristic length scale is $L_\mathrm{c} = 0.5r$ such that the channel length is 30 after non-dimensionalization. The boundary on the top and on the disk belongs to Γ_D, where we have a homogeneous Dirichlet boundary condition (1.36) with $\boldsymbol{u}_\mathrm{D} = \boldsymbol{0}$. On the symmetry line Γ_S of the channel, we prescribe symmetric boundary conditions (1.38). On the right and left endings of the channel, we have periodic boundary conditions (1.39). To generate a flow in x-direction, we use an additional constant flow rate condition (1.40) with flow rate $Q > 0$ over $\Gamma_\mathrm{P}^\mathrm{right}$. The characteristic velocity is $U_\mathrm{c} = Q/(2H)$, which leads to a dimensionless flow rate of $Q^* = Q/(U_\mathrm{c} L_\mathrm{c}) = 4$. The drag coefficient c_d is a well-suited dimensionless quantity for comparison of the different bead-rod models as the drag reduction phenomenon of viscoelastic fluids can be observed with it. We compute the drag coefficient via

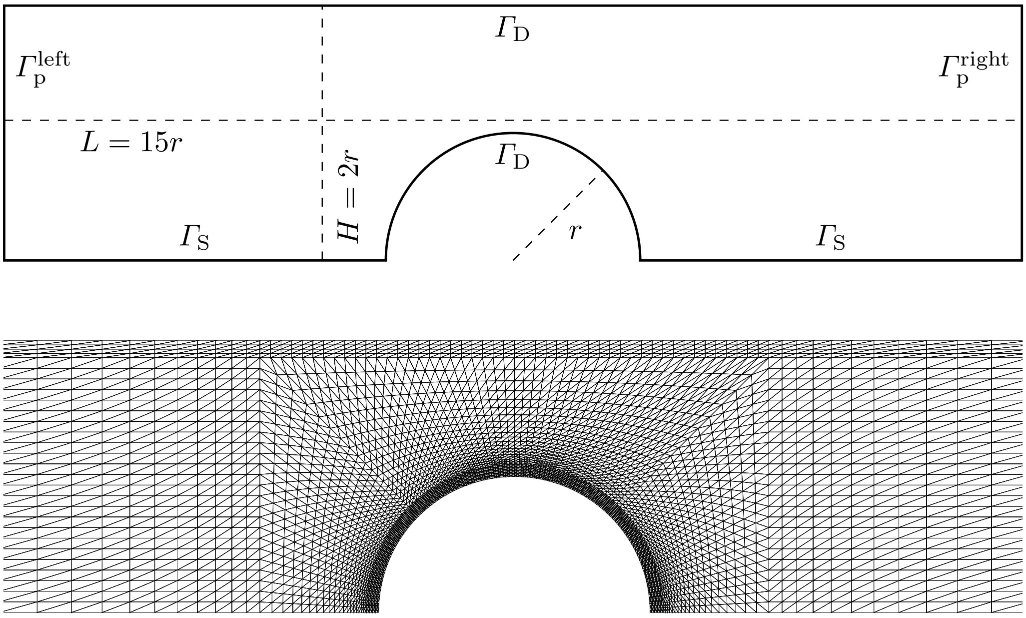

Figure 5.10. Flow around a cylinder domain with boundary condition information and visualization of the middle part of the mesh. The whole mesh consists of 7888 triangles. The minimum mesh width is $h = 0.0156$.

$$c_\mathrm{d} := \frac{-2F_\mathrm{x}}{\rho U_\mathrm{c}^2 A} = -\int_{\text{cylinder}} \boldsymbol{e}_1^\mathrm{T} \left[\frac{1}{\mathrm{Re}} \left(\boldsymbol{\tau}_\mathrm{p}^* + \boldsymbol{\tau}_\mathrm{s}^* \right) - p^* \boldsymbol{I} \right] \cdot \boldsymbol{n}, \tag{5.3}$$

where F_x denotes the x-component of the drag force over the cylinder wall, A the cross-sectional area of the cylinder, ρ the fluid density, and U_c the characteristic velocity. In (5.3), $\int_{\text{cylinder}}$ denotes the surface integral over the top half cylinder arc as visualized in Figure 5.10. The simulations use the same finite elements as in the shear flow scenario on triangles instead of squares.

5.2.1 Bead-spring dumbbells

In the following simulations, we considered the (NS-Hookean) model. Table 5.5 summarizes the model and discretization parameters. Here, the polymeric stress entries along the symmetric boundary and over the cylinder wall are compared with each other for varying Weissenberg numbers Wi. Figure 5.11 visualizes the polymeric stresses for Wi = 0.6, 0.8, 1.0, 1.1, and 1.3. Note the very steep peaks on left side of the cylinder for the polymeric stress entry $(\boldsymbol{\tau}_{p,h})_{yy}$, which grow for higher Wi. Fully resolving these peaks requires a very fine mesh resolution near the cylinder as visualized in Figure 5.10. Figure 5.11 is used in the next section for quantitative comparisons with the (NS-BR) model.

Model parameter	
T^*	15
ϵ	8/9
Re	1
Wi	varied

(a)

Discretization parameter	
Δt	0.015
N_f	10000
N_p	1000
N_w	250

(b)

Table 5.5. Model and discretization parameters of the Hookean dumbbell simulations in Figure 5.11.

5.2.2 Bead-rod chains

We consider the two studies from the shear flow scenario Section 5.1.3, i.e., increasing the chain length by adding beads with constant number density n and dissecting chains into smaller chains to increase the number density n. The parameters for studies 1 and 2 in the case of the flow around a cylinder scenario are listed in Table 5.7 and Table 5.8. Table 5.6 summarizes the parameters, which are used for the simulation of study 1 and 2 w.r.t. the flow around a cylinder scenario. The time step size is set to $\Delta t = 2.5 \cdot 10^{-3}$. The number of BCFs is set to $N_f = 2233$, which are distributed across 319 helper workers. Figure 5.12 and Figure 5.13 show several plots: the polymeric stress entries and velocity magnitude along the symmetry line at $y^* = 0$ and over the top cylinder arc between $x^* = 13$ and $x^* = 17$, the vertical velocity magnitude profile at $x^* = 15$ (center of the domain)

Discretization parameter	
Δt	$2.5 \cdot 10^{-3}$
N_f	2233
N_p	1280
N_w	320

Table 5.6. Discretization parameters for the simulations in Figures 5.12 to 5.15.

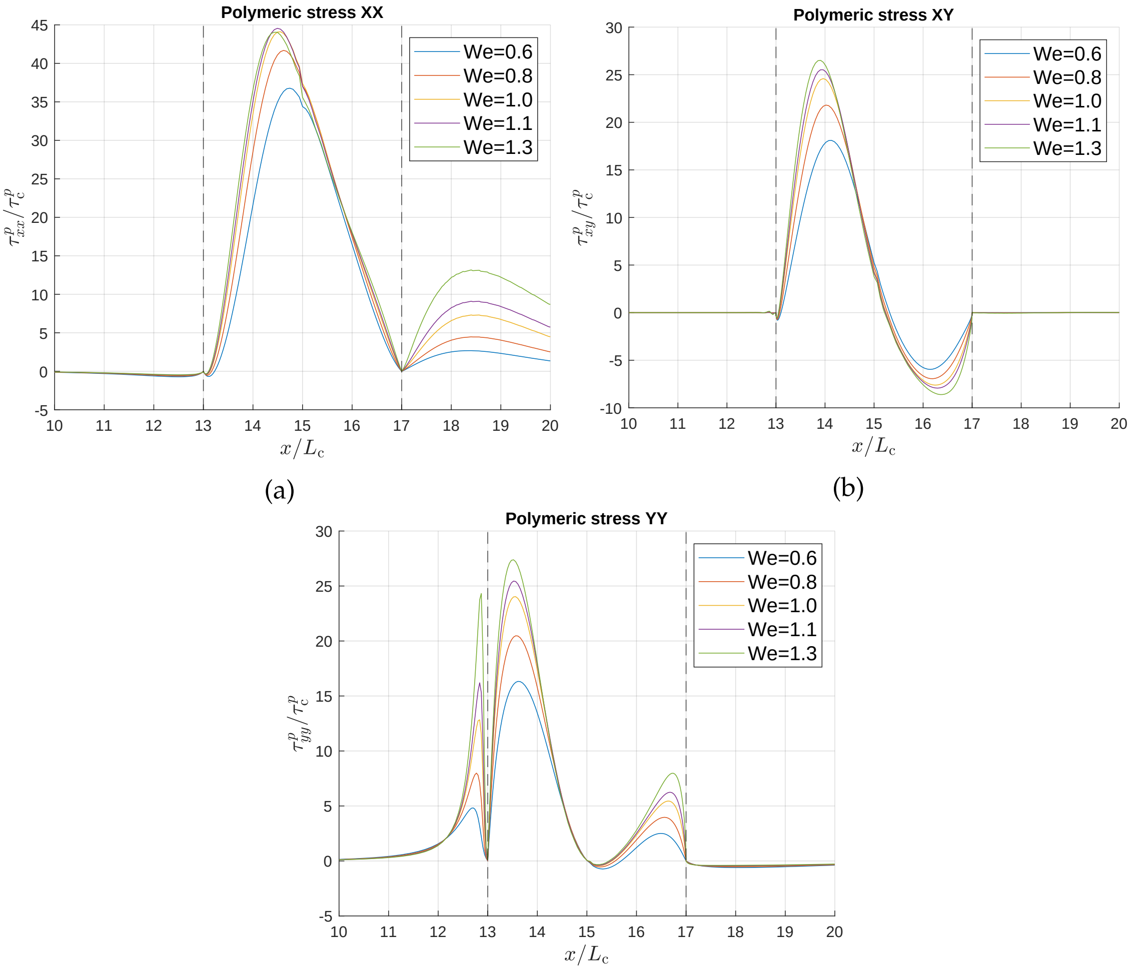

(a) (b)

(c)

Figure 5.11. Visualization of Hookean dumbbell polymeric stresses along the symmetric boundary and over the cylinder wall at $t^* = 13.5$. The vertical dashed lines denote the start and end of the cylinder wall at $x^* = 13$ and $x^* = 17$.

between the cylinder ($y^* = 2$) and top wall ($y^* = 4$), and the drag coefficient over time. The dashed lines indicate the start and end of the cylinder. For comparison in the velocity and drag coefficient plots, a plain Navier–Stokes solution ($\epsilon = 0$) with the same Re as in the $N = 15$ case is plotted.

One can clearly see a reduction of the drag coefficient c_d between the plain Navier–Stokes solution and the viscoelastic bead-rod chain solutions. Among the bead-rod chain solutions, the stationary drag coefficient $c_\mathrm{d}(N)$ of N beads can be ordered to $c_\mathrm{d}(5) < c_\mathrm{d}(10) < c_\mathrm{d}(15)$ and it holds $c_\mathrm{d}(15)/c_\mathrm{d}(5) = 1.11$ for study 1. In the case of study 2, a similar behavior of the drag coefficients $c_\mathrm{d}(N)$ can be observed with $c_\mathrm{d}(9)/c_\mathrm{d}(2) = 1.06$. Both studies showed that increasing the length of bead-rod chains by adding beads and keeping the number density n fixed (study 1) or not fixed (study 2), leads to an increase in the drag coefficient.

The vertical velocity profile coincides for all considered N with the Navier–Stokes solution almost perfectly in both studies. The velocities for $N = 5, 10, 15$

Study 1 model parameter				
N	Wi	ϵ	Re	t_{comp} [h:min]
5	5.7845	0.3249	1.0127	07:14
10	21.4789	0.6650	0.5026	21:15
15	45.0000	0.8179	0.2732	36:50
–	–	0	0.2732	00:15

Table 5.7. Parameters for flow around a cylinder study 1 simulations (cf. Figure 5.12) and required computation time t_{comp}.

Study 2 model parameter				
N	Wi	ϵ	Re	t_{comp} [h:min]
9	17.4254	0.7921	0.3119	18:47
5	5.7845	0.6957	0.4565	07:20
3	2.3014	0.6038	0.5943	03:12
2	1.1737	0.5334	0.7000	01:23
–	–	0	0.3119	00:15

Table 5.8. Parameters for flow around a cylinder study 2 simulations (cf. Figure 5.13) and required computation time t_{comp}.

(study 1) on the symmetry line behind the cylinder clearly differ from the plain Navier–Stokes solution. The velocity of the plain Navier–Stokes solution increases faster in the wake of the cylinder compared to the bead-rod chain solutions. In the case of study 2, the velocities on the symmetry line for $N = 2, 3, 5$ in the wake of the cylinder are almost identical. For $N = 9$, the velocity increases slower compared to $N = 2, 3, 5$.

N	Wi	ϵ	Re	t_{comp} [h:min]
4	5	0.8889	1	8:16
–	–	0	1	0:16

Table 5.9. Parameters for flow around a cylinder simulation (cf. Figures 5.14 and 5.15) and required computation time t_{comp}.

Additionally, we considered a chain with $N = 4$, cf. Table 5.9 for the parameters, and compared it with a plain Navier–Stokes solution ($\epsilon = 0$) with the same Re. In Figure 5.14, the vertical velocity profile at $x^* = 15$ and the velocity along the symmetry line differs clearly compared to the Navier–Stokes solution. See also Figure 5.15, which visualizes the velocity streamlines for the plain Navier–Stokes solution (a) and the bead-rod chain solution (b). In contrast to the plain Navier–Stokes solution, the bead-rod chain solution has a vortex in the wake of the cylinder. In Figure 5.15, the dimensionless polymeric shear stress $(\boldsymbol{\tau}_{\text{p}})_{xy}$ is visualized for $t^* = 0.25$ (c), $t^* = 1.25$ (d), and $t^* = 15$ (e).

A qualitative comparison between the bead-rod chain polymeric stress graphs of Figure 5.12 with the bead-spring graphs from Figure 5.11 yields the following observations: In the bead-rod chain case for increasing N, there is a growing steep peak in the $(\boldsymbol{\tau}_{p,h})_{yy}$-plot near the left front of the cylinder wall. A similar peak arises for bead-spring dumbbells. However, the second peak in bead-rod chain case is significantly smaller compared to its first peak height. In the bead-spring dumbbell case, the height of the second peak tends to be larger compared to the height of the first peak. The behavior of the $(\boldsymbol{\tau}_{p,h})_{xy}$-graphs are similar for both models in the corresponding figures. Taking a look at the $(\boldsymbol{\tau}_{p,h})_{xx}$-plots in both figures reveals two peaks for each graph. In the bead-rod chain case, the taller peak is always in the back of the cylinder. Contrarily, for bead-spring dumbbells, the peak is higher on the cylinder.

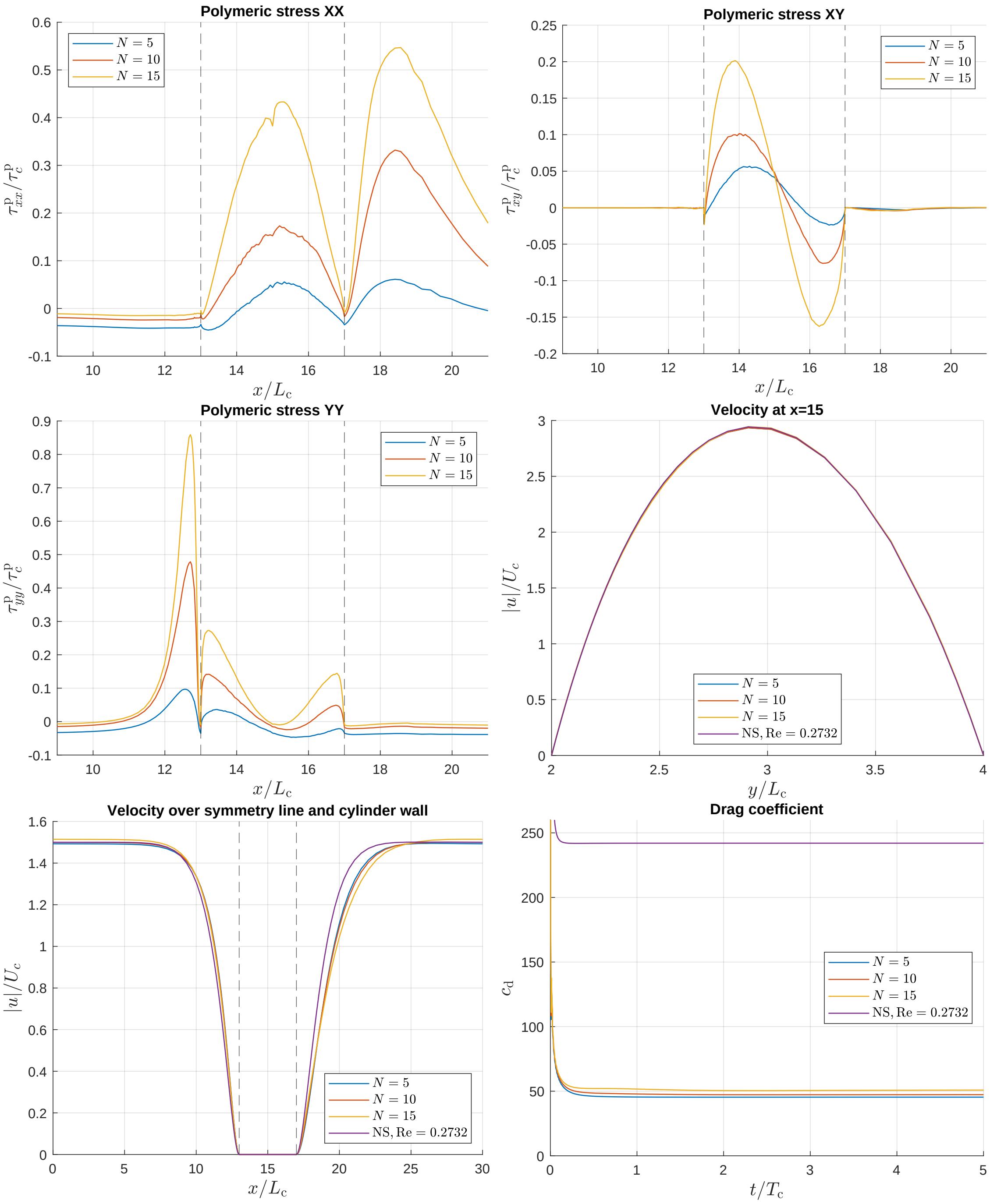

Figure 5.12. Flow around a cylinder simulation results of study 1. Data at $t/T_{\mathrm{c}} = 5$. The dashed lines indicate the start and end of the cylinder.

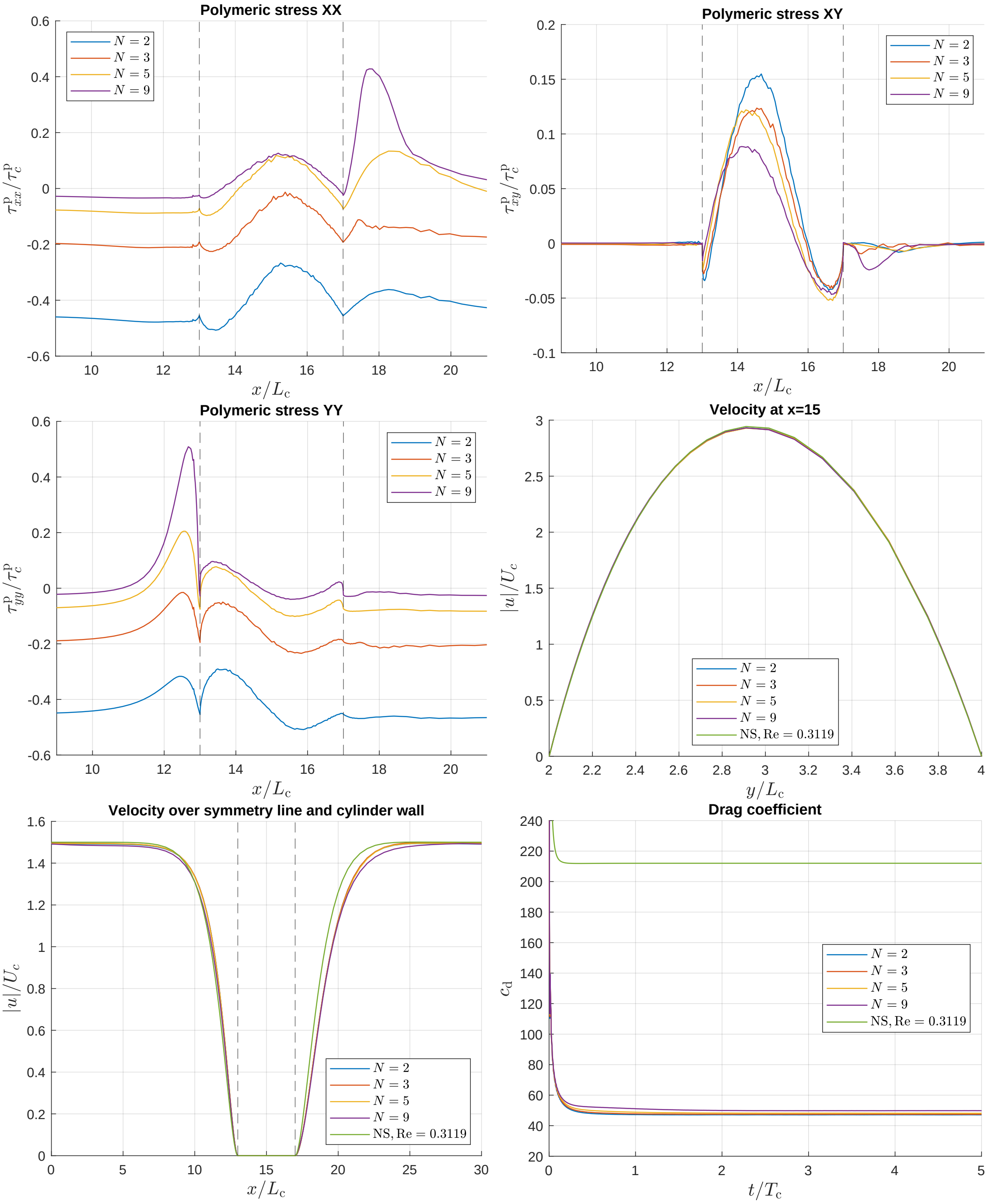

Figure 5.13. Flow around a cylinder simulation results of study 2. Data at $t/T_{\mathrm{c}} = 5$. The dashed lines indicate the start and end of the cylinder.

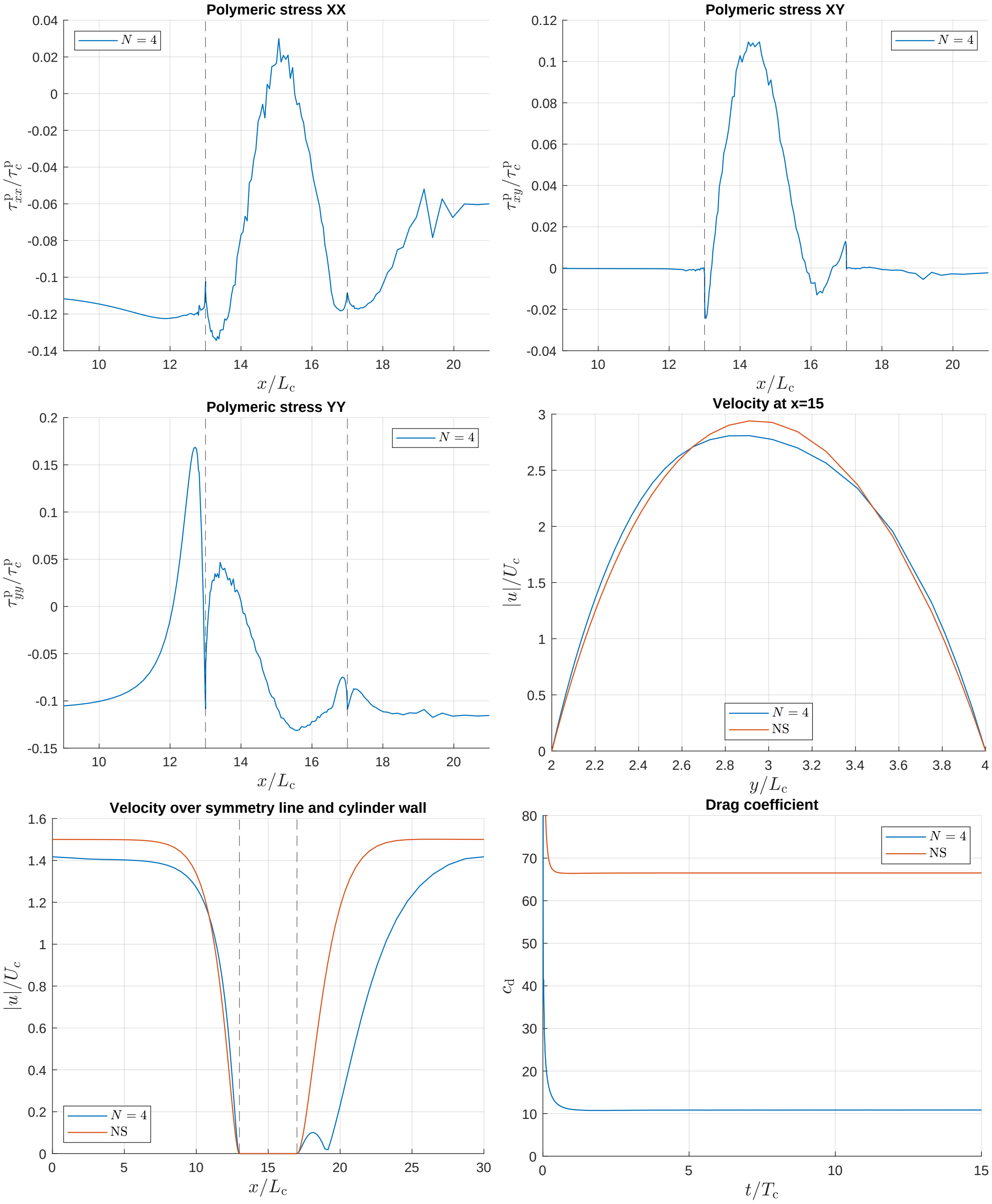

Figure 5.14. Flow around a cylinder simulation results for bead-rod chain with $N = 4$ beads. See Table 5.9 for the parameters. Plots show data at $t/T_{\mathrm{c}} = 15$. The dashed lines indicate the start and end of the cylinder.

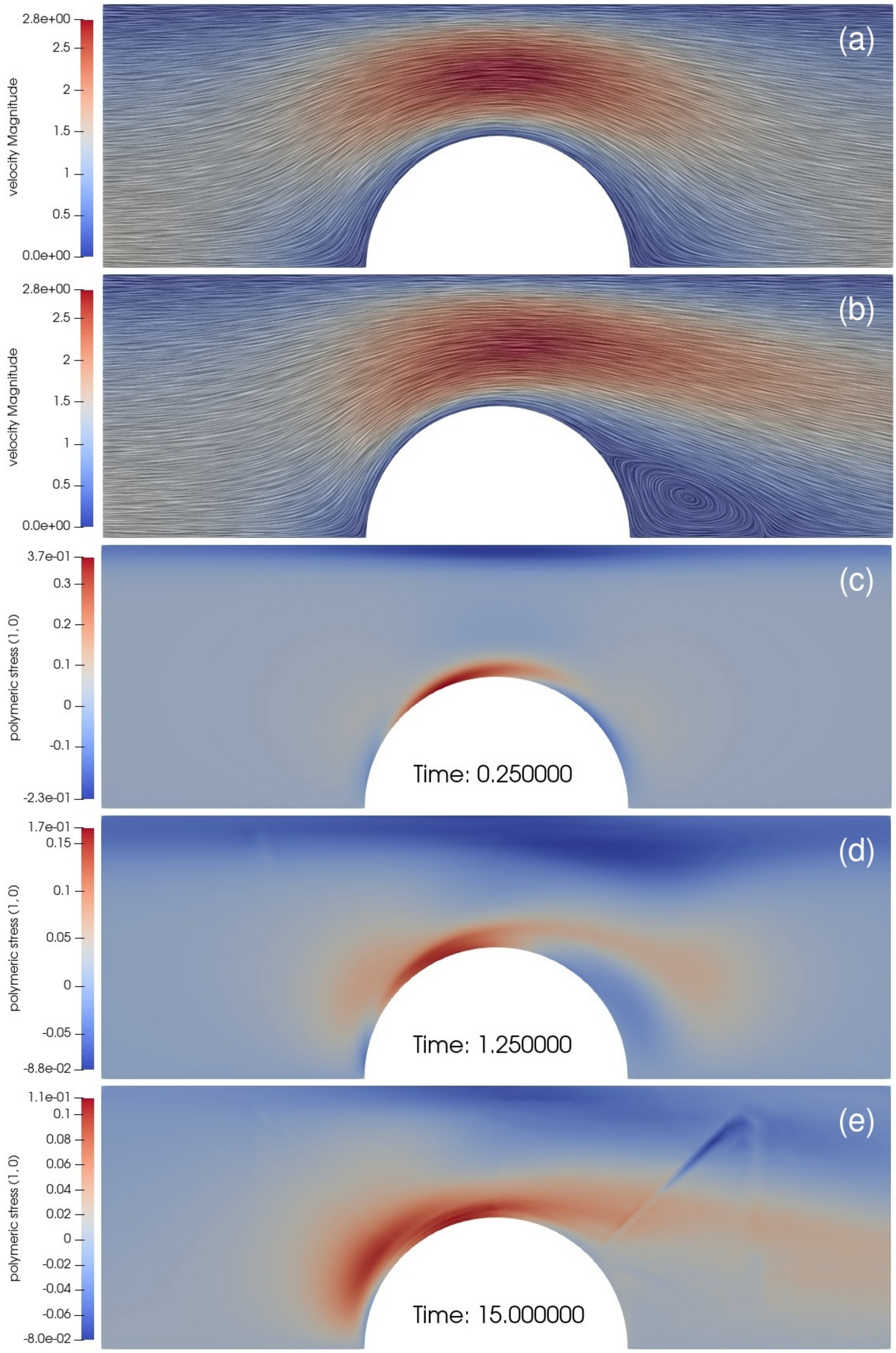

Figure 5.15. Velocity streamlines near the cylinder at $t/T_c = 15$ for plain Navier–Stokes (a) and $N = 4$ bead-rod chain (b). Plots (c)-(e) visualize the polymeric shear stress at various time points. See Table 5.9 for the parameters.

5.3 Flow through planar contraction

In the following section, we simulate the fluid flow through a 4:1 planar contraction as visualized in Figure 5.16. Such flow scenarios are present in lab on a chip systems, where understanding flow conditions and parameters is crucial to support the optimal functionality of such systems. In [36], measurements of DNA solutions through a planar contraction are made to quantify the kinematics of such flows. In [25, 26], flow characteristics of aqueous solutions of polyacrylamide through abrupt changing geometries are examined. In their experiments, they considered different contraction ratios and corner geometries and observed vortex enhancements in the corner of the contraction similar to Figure 5.16, where the corner vortices completely stretch to the reentrant corners of the contraction. In [64], attempts are made to reproduce observations from [25, 26] with the FENE-P model [14], which is a macroscopic closure approximation of the FENE bead-spring dumbbell model from Section 2.1.

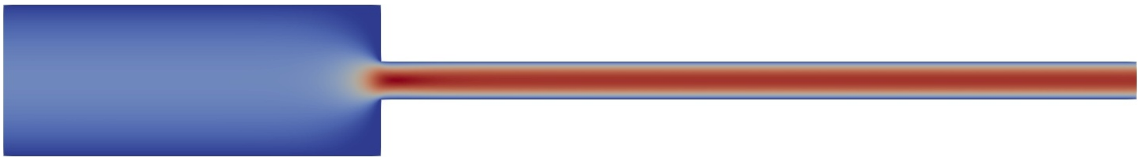

(a) Full domain.

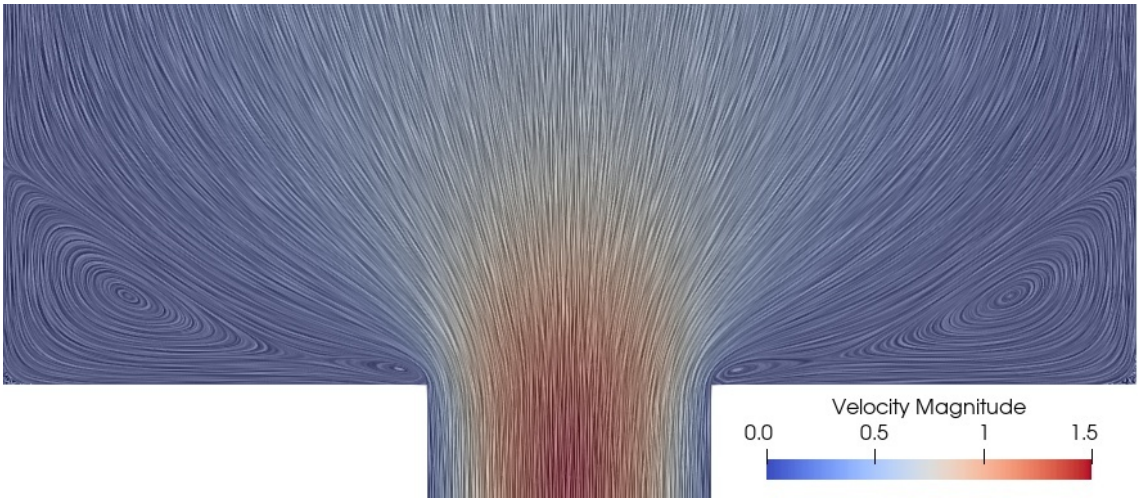

(b) Corner vortices that are stretched to the reentrant corner.

Figure 5.16. Visualization of a 4:1 planar contraction flow of the stationary viscoelastic FENE-P model in COMSOL [19].

Analog to [64], we reproduce a scenario from [26] with the bead-rod chain model. The simulations consider bead-rod chains with $N = 5, 10, 15$ beads. In the experiment, they considered an aqueous solution of polyacrylamide. We use the same realistic fluid parameters of a 0.25% polyacrylamide solutions as done in [26, 64], see Table 5.10b for the corresponding dimensionless numbers. Note that the dimensionless numbers in Table 5.10b correspond to Figure 11B in [64] with a planar flowrate of $149.8\,\mathrm{mm}^2\,\mathrm{s}^{-1}$.

At first, we describe the periodic 4:1 planar contraction geometry, which is used as domain in the simulations. Figure 5.17 visualizes the lower symmetric half of the 4:1 planar contraction with the corresponding boundaries. On the top, we have a symmetric boundary condition (1.38). The left and right side are periodic with BC (1.39) and constant flowrate condition (1.40) with planar flowrate $Q > 0$. At the remaining boundaries, a Homogeneous Dirichlet BC (1.36) is applied. Half of the height of the contraction (downstream channel) is denoted by H_d, which fully determines the domain (cf. Figure 5.17). The characteristic length and velocity are given by $L_c := H_d$ and $U_c = Q/H_d$, which leads to a dimensionless flow rate of $Q^* = Q/(U_c L_c) = 1$. The discretization mesh consists of 11904 triangles with a minimum mesh size of $h = 0.0768$. The mesh has a finer resolution near the contraction (cf. Figure 5.18).

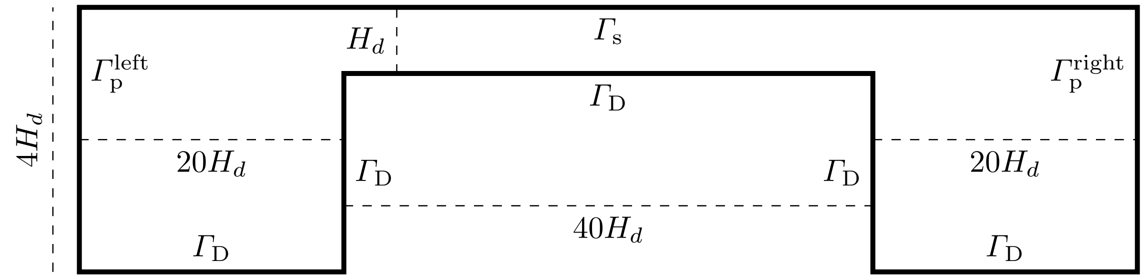

Figure 5.17. Visualization of the lower half of the periodic 4:1 planar contraction geometry, which is used for the simulations in Figure 5.19.

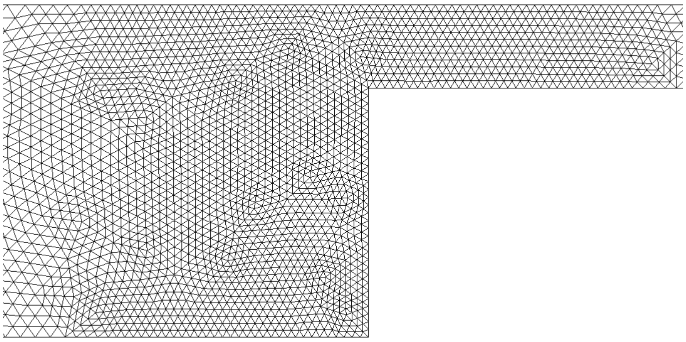

Figure 5.18. Visualization of the mesh near the reentrant corner of the contraction. The whole mesh consists of 11904 elements and the minimum mesh size is $h = 0.0768$.

Figure 5.19 visualizes the stationary velocity magnitude and streamlines near the contraction of the fluid domain for $N = 5, 10, 15$. One can clearly see that the vortex size increases for increasing N. However, the vortices in the experiment are more stretched towards the reentrant corner (similar to Figure 5.16). From the observed behavior in Figure 5.19, it might be the case that the number of beads is not high enough to fully capture the viscoelastic fluid characteristics. The computation time t_{comp} for the simulation with $N = 15$ beads is already almost 26 days (cf. Table 5.10b). Note that in each time step for $N = 15$, already a total of

64759 linear and 2233 nonlinear system of equations have to be solved (cf. Table 3.8). Simulations with a significant higher number of beads N cannot be realized with the current available computational resources at the moment. In Figure 5.19, the simulations are run until the velocity is stationary and the corner vortex does not change its size anymore.

Discretization parameter	
$\varDelta t$	$5 \cdot 10^{-4}$
N_f	2233
N_p	1280
N_w	320

(a)

N	Wi	ϵ	Re	t_{comp} [d:h:min]
5	4.6	0.9286	1.073	05:02:07
10	4.6	0.9286	1.073	13:12:56
15	4.6	0.9286	1.073	25:17:18
–	–	0	1.073	00:00:18

(b)

Table 5.10. Discretization and model parameters of the simulations in Figure 5.19.

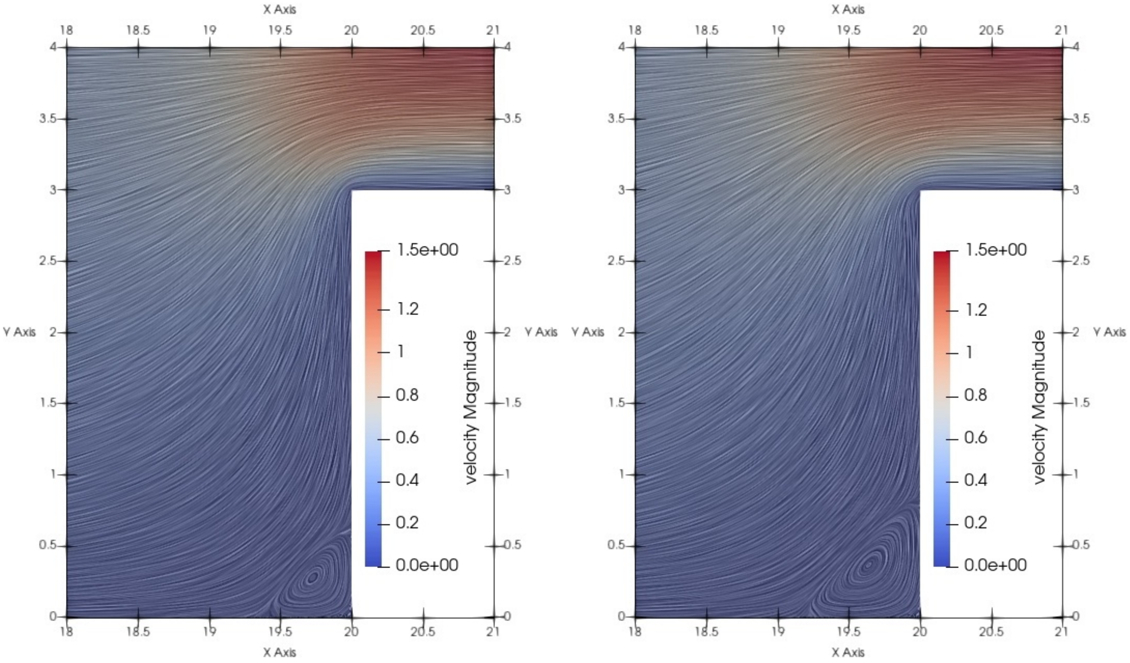

(a) $N = 5$.

(b) $N = 10$.

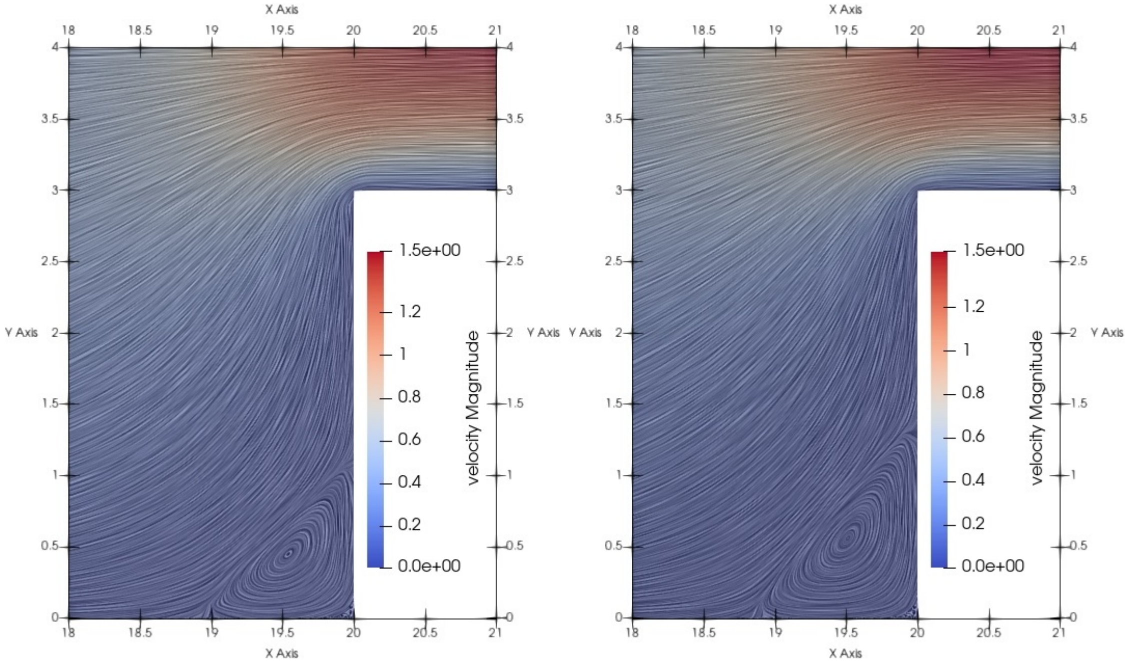

(c) $N = 15$.

(d) Navier–Stokes solution (Re = 1.073).

Figure 5.19. Visualization of stationary velocity magnitude and velocity streamlines near the contraction. See Table 5.10 for the model parameters.

6 Conclusion

In this thesis, we considered two microscopic approaches from the kinetic theory to model non-Newtonian dilute polymeric fluids: the coarse grained approximation of polymer molecules with bead-spring (BS) dumbbells and the more complex finer grained approximation with bead-rod (BR) chains (Kramers chain). The additional coupling of these microscopic models to the macroscopic Navier–Stokes equations over an additional stress tensor yields the micro-macro models, which are in the following denoted by (NS-BS) and (NS-BR). The coupled models enabled the consideration of flow scenarios on complex structured domains. This thesis considered challenging benchmark scenarios, such as the start-up shear flow, the flow around a cylinder, and 4:1 contraction flow. In the latter, resulting corner vortices were quantitatively compared to observations from experiments in the literature with physical meaningful parameters. Model (NS-BS) was already simulated multiple times in the literature and is used in this thesis for verification purposes and for qualitative comparison to the (NS-BR) model. Up to this point, the (NS-BR) model was never considered in the literature. With this thesis, we closed this research gap by presenting novel simulation results of the (NS-BR) model.

In order to perform such challenging simulations of the (NS-BR) model, the consideration of multiple aspects w.r.t. modeling, discretization, and implementation were necessary. Starting at the non-dimensionalization of the (NS-BR) model, additional work had to be done to get correct values for the number beads dependent longest relaxation times, which were computed and verified by additional simulations in Matlab with own parallelized and fully vectorized code.

The discretization of (NS-BS) and (NS-BR) uses finite elements combined with the computational challenging Brownian configuration field (BCF) method, which is the only feasible choice for the bead-rod chain model due to the high number of internal degrees of freedom (DOF). Additionally, Liu's algorithm for the temporal discretization of the bead-rod chains had to be adapted into the finite element and BCF setting with extra work on the preservation of the rod length constraints in each DOF over time. In the case of the (NS-BR) model, the computation of the extra stress tensor required an extra noise filtering technique, which also had to be adapted into the finite element and BCF setting.

The use of efficient C++ code with distributed memory parallelization was mandatory for the large scale simulations of the (NS-BS) and (NS-BR) model. An additional custom master/helper parallelization for the distribution of the BCFs among the processes was crucial. Through this, a speedup of up to 64 on 1280 processes was achieved. The longest simulation in this thesis took 25 days. Without master/helper parallelization, the same simulation would have taken over 4 years, which emphasizes the significance of this parallelization approach. To run simulations that are longer than 24 hours on the computation cluster, a checkpoint/restart functionality had to be included into the code. The use of iterative solvers instead of direct ones, required extra work as special care had to be taken on preconditioning. The use of special boundary conditions (BC), e.g, periodic BC with constant flowrate condition, required extra work, as it is not well documented in the literature on how these BC need to be treated from a numerical point of view. Additionally, well-posedness of the stationary Stokes problem w.r.t. to these BC was proven. The implementation of the numerical scheme was verified by comparing (NS-BS) results to an equivalent macroscopic model, which was already implemented in COMSOL.

After the above mentioned aspects were solved, we were able to run simulations of the (NS-BR) model with up to 17 beads. Note that in each time step of the simulation with 17 beads, over 73000 linear and 2200 nonlinear system of equations had to be solved, which again underlines the significance of the master/helper parallelization to handle such numbers.

As a next step, a more elaborate discretization for the Navier–Stokes equations could be utilized with adaptive mesh refinement, to consider scenarios with higher Reynolds numbers. Additionally, it could be examined if the computation of the tensions can be improved by considering a different approach to solve the corresponding nonlinear system of equations.

List of symbols

General

$\delta(x)$	Dirac delta
δ_{ij}	Kronecker delta
d	Spatial dimension
$\boldsymbol{e}_1$	Unit vector in x-direction
$\boldsymbol{I}$	Identity matrix
L	Length of domain in flow direction
$\boldsymbol{n}$	Normal vector
Ω	Flow domain
$\partial\Omega$	Boundary of Ω
$\boldsymbol{t}$	Tangential vector
$\boldsymbol{x}$	Coordinate in Ω

Differential operators

∂_t	Partial time derivative
∂_i	Partial derivative in x_i-direction $i = 1, \dots, d$
∇u	Gradient $\nabla u := (\partial_1 u, \dots, \partial_d u)^{\mathrm{T}}$ for $u : \Omega \to \mathbb{R}$
$\nabla_{\boldsymbol{r}_i}$	Gradient w.r.t. variable $\boldsymbol{r}_i$
$\nabla \boldsymbol{u}$	Gradient $(\nabla \boldsymbol{u})_{ij} := \partial_j u_i$, $i, j = 1, \dots, d$ for $\boldsymbol{u} : \Omega \to \mathbb{R}^d$
$\boldsymbol{D}(\boldsymbol{u})$	$\boldsymbol{D}(\boldsymbol{u}) := \frac{1}{2}(\nabla \boldsymbol{u} + (\nabla \boldsymbol{u})^{\mathrm{T}})$, symmetrized gradient for $\boldsymbol{u} : \Omega \to \mathbb{R}^d$
$\nabla \cdot \boldsymbol{u}$	Divergence of $\boldsymbol{u}$: $\nabla \cdot \boldsymbol{u} := \sum_{i=1}^{d} \partial_i u_i$ for $\boldsymbol{u} : \Omega \to \mathbb{R}^d$
$\boldsymbol{u} \cdot \nabla \boldsymbol{u}$	$(\boldsymbol{u} \cdot \nabla \boldsymbol{u})_i := \sum_{j=1}^{d} u_j \partial_j u_i$, $i = 1, \dots, d$, for $\boldsymbol{u} : \Omega \to \mathbb{R}^d$
Δu	$\Delta u := \nabla \cdot (\nabla u)$, Laplacian of u for $u : \Omega \to \mathbb{R}$
$\Delta \boldsymbol{u}$	$(\Delta \boldsymbol{u})_i = \Delta u_i$, $i = 1, \dots, d$, for $\boldsymbol{u} : \Omega \to \mathbb{R}^d$
$\Delta_{\boldsymbol{Q}}$	Laplacian w.r.t. variable $\boldsymbol{Q}$
$\overset{\triangledown}{\boldsymbol{\tau}}$	$:= \partial_t \boldsymbol{\tau} + \boldsymbol{u} \cdot \nabla \boldsymbol{\tau} - (\nabla \boldsymbol{u})^{\mathrm{T}} \boldsymbol{\tau} - \boldsymbol{\tau} \nabla \boldsymbol{u}$, upper convected time derivative of $\boldsymbol{\tau} : \Omega \to \mathbb{R}^{d \times d}$ and velocity $\boldsymbol{u}$

Boundary conditions

Γ_{D}	Dirichlet boundary
Γ_{N}	Neumann boundary
Γ_{S}	Symmetric boundary
$\Gamma_{\mathrm{P}}^{\mathrm{left}}, \Gamma_{\mathrm{P}}^{\mathrm{right}}$	Left and right periodic boundary
g_{D}	Dirichlet boundary condition data
g_{N}	Neumann boundary condition data
$\bar{p}$	Lagrangian multiplier for constant flowrate BC
Q	Constant flowrate across periodic boundary

Modeling

ρ	Fluid density
$\boldsymbol{u}$	Fluid velocity
p, p_p	Fluid pressure
$\boldsymbol{\sigma}$	Stress tensor
$\boldsymbol{\tau}$	Deviatoric stress tensor
$\boldsymbol{\tau}_\mathrm{s}$	Solvent stress tensor ($\boldsymbol{\tau} = \boldsymbol{\tau}_\mathrm{s} + \boldsymbol{\tau}_\mathrm{p}$)
$\boldsymbol{\tau}_\mathrm{p}$	Polymeric stress tensor ($\boldsymbol{\tau} = \boldsymbol{\tau}_\mathrm{s} + \boldsymbol{\tau}_\mathrm{p}$)
μ, η, η_0	Viscosity
η_s	Solvent viscosity
η_p	Polymeric viscosity
t	Time
$\mathbb{T}$	Time interval $(0, T)$
$\dot{\gamma}$	Shear rate
$\dot{\epsilon}$	Strain rate
λ	Relaxation time
λ_1, λ_2	Time constants
k_B	Boltzmann constant
ϑ	Fluid temperature
ξ	Friction coefficient
n	Polymer number density
G	Deformation modulus
$\epsilon_\mathrm{s}, \epsilon_\mathrm{d}$	Deformations
$F_\mathrm{s}, F_\mathrm{d}$	Spring and dashpod forces
N	Number of beads
$\boldsymbol{r}_i$	Position vector of ith bead
$\boldsymbol{r}_\mathrm{c}$	$:= N^{-1} \sum_{i=1}^{N} \boldsymbol{r}_i$, center of mass
$\boldsymbol{R}_i$	$:= \boldsymbol{r}_i - \boldsymbol{r}_\mathrm{c}$, position vector of ith bead relative to center of mass
$\boldsymbol{u}_\mathrm{c}$	Fluid velocity at $\boldsymbol{r}_\mathrm{c}$
$\boldsymbol{Q}$	$:= \boldsymbol{r}_2 - \boldsymbol{r}_1$, dumbbell connector vector
$\boldsymbol{Q}_i$	$:= \boldsymbol{r}_{i+1} - \boldsymbol{r}_i$, connector vector of ith rod
$\boldsymbol{F}_i^\mathrm{H}$	Hydrodynamic drag force at $\boldsymbol{r}_i$
$\boldsymbol{F}_i^\mathrm{B}$	Brownian force at $\boldsymbol{r}_i$
$\boldsymbol{F}_i^\mathrm{S}$	Spring force at $\boldsymbol{r}_i$
$\boldsymbol{F}_i^\mathrm{C}$	Constraint force at $\boldsymbol{r}_i$
$\boldsymbol{W}$	Wiener process
U	Spring potential
H	Hookean spring constant
Q_0	Maximum spring extension
a	Rod length
$\mathcal{H}$	Bead-spring dumbbell Hamiltonian
$\boldsymbol{\mathcal{L}}$	Bead-spring dumbbell Lagrangian
$\boldsymbol{p}_\mathrm{c}$	Conjugate generalized momentum w.r.t. $\boldsymbol{r}_\mathrm{c}$

$\boldsymbol{P}$	Conjugate generalized momentum w.r.t. $\boldsymbol{Q}$
T_i	Tension w.r.t. ith bead

Distributions

f_{eq}	Single-molecule-phase-space distribution function
Ψ_{eq}	Configurational distribution function
ψ_{eq}	Probability density function
$\psi_{\mathrm{eq}}^{\mathrm{Hookean}}$	Hookean dumbbell probability density function
$\psi_{\mathrm{eq}}^{\mathrm{FENE}}$	FENE dumbbell probability density function
$\mathcal{N}(0, \Delta t)$	Normal distribution with mean 0 and variance Δt

Characteristic units

L_{c}	Macroscopic characteristic length
l_{c}	Microscopic characteristic length
T_{c}	Macroscopic characteristic time
t_{c}	Microscopic characteristic time
U_{c}	Characteristic velocity
p_{c}	Characteristic pressure
$\tau_{\mathrm{c}}^{\mathrm{p}}$	Characteristic polymeric stress
F_{c}	Characteristic force

Dimensionless numbers

Re	Reynolds number
Wi	Weissenberg number
Pe	Peclet number
ϵ	Polymeric viscosity ratio
b	Squared maximum spring extension Q_0^2/l_{c}^2
$\alpha(N)$	Dimensionless longest relaxation time of N bead-rod chain

Spaces

$\mathbb{R}$	Real numbers
$\mathbb{N}$	Natural numbers
U	Velocity space
P	Pressure space
Σ	Stress space
$C^0(\bar{\Omega})$	Continuous functions from $\bar{\Omega}$ to $\mathbb{R}$
$L^2(\Omega)$	Lebesgue space

$L^2_0(\Omega)$	Lebesgue space $\{v \in L^2(\Omega) \mid \int_\Omega v = 0\}$
$H^1(\Omega)$	Sobolev space
$\mathcal{L}(X, Y)$	Vector space of bounded linear operators from X to Y
$\ker A$	Kernel of linear operator A
$\mathbb{Q}_k$	Vector space of polynomials in the variables $x_1, \dots, x_d$ of partial degree at most k
$\mathbb{P}_k$	Vector space of polynomials in the variables $x_1, \dots, x_d$ of global degree at most k
Π_k	Vector space of polynomials in the variable $x \in \mathbb{R}$ of global degree at most k
$\mathbb{D}_{\mathrm{BS}}$	Bead spring dumbbell configuration space
$\mathbb{D}^{\mathrm{H}}_{\mathrm{BS}}$	Hookean dumbbell configuration space $\mathbb{R}^d$
$\mathbb{D}^{\mathrm{F}}_{\mathrm{BS}}$	FENE dumbbell configuration space $\{\boldsymbol{Q} \in \mathbb{R}^d \mid \lvert\boldsymbol{Q}\rvert < Q_0\}$
$\mathbb{D}_{\mathrm{BR}}$	Bead rod configuration space $\{\boldsymbol{Q} \in \mathbb{R}^d \mid \lvert\boldsymbol{Q}\rvert = a\}$

Discretization

Δt	Time step size
h	Characteristic mesh size
N_f	Number of Brownian configuration fields
U_h	Finite dimensional velocity ansatz space
P_h	Finite dimensional pressure ansatz space
Σ_h	Finite dimensional stress ansatz space
Q_h	Finite dimensional connector-vector Q ansatz space
T_h	Finite dimensional tension ansatz space
$\mathcal{T}_h$	Regular family of non-overlapping partitions of Ω in quadrilaterals/triangles
K	Quadrilaterals or triangles $K \in \mathcal{T}_h$

Implementation

N_w	Number of workers
w_w	Worker size
N_p	Number of processes
r_L	Local rank
r_G	Global rank
$S(N_p)$	Speedup with N_p processes
$E(N_p)$	Parallel efficiency with N_p processes
$t(N_p)$	Code runtime with N_p processes

References

[1] M. Alves, P. Oliveira, and F. Pinho. "Numerical Methods for Viscoelastic Fluid Flows." *Annual Review of Fluid Mechanics* 53.1 (Jan. 2021), pp. 509–541. ISSN: 1545-4479. DOI: `10.1146/annurev-fluid-010719-060107`.

[2] M. R. Ambler, D. McIntyre, and L. J. Fetters. "Solution Properties of Poly(n-butyl isocyanate). 1. Characterization and Intrinsic Viscosity Behavior Over an Extended Molecular Weight Range." *Macromolecules* 11.2 (Mar. 1978), pp. 300–306. DOI: `10.1021/ma60062a004`.

[3] R. Anderson, J. Andrej, A. Barker, J. Bramwell, J.-S. Camier, J. C. V. Dobrev, Y. Dudouit, A. Fisher, T. Kolev, W. Pazner, M. Stowell, V. Tomov, I. Akkerman, J. Dahm, D. Medina, and S. Zampini. "MFEM: A Modular Finite Element Methods Library." *Computers & Mathematics with Applications* 81 (Jan. 2021), pp. 42–74. DOI: `10.1016/j.camwa.2020.06.009`.

[4] F. P. Baaijens. "Mixed finite element methods for viscoelastic flow analysis: a review." *Journal of Non-Newtonian Fluid Mechanics* 79.2-3 (Nov. 1998), pp. 361–385. DOI: `10.1016/s0377-0257(98)00122-0`.

[5] J. W. BARRETT, C. SCHWAB, and E. SÜLI. "EXISTENCE OF GLOBAL WEAK SOLUTIONS FOR SOME POLYMERIC FLOW MODELS." *Mathematical Models and Methods in Applied Sciences* 15.06 (June 2005), pp. 939–983. ISSN: 1793-6314. DOI: `10.1142/s0218202505000625`.

[6] J. W. BARRETT and E. SÜLI. "EXISTENCE AND EQUILIBRATION OF GLOBAL WEAK SOLUTIONS TO KINETIC MODELS FOR DILUTE POLYMERS I: FINITELY EXTENSIBLE NONLINEAR BEAD-SPRING CHAINS." *Mathematical Models and Methods in Applied Sciences* 21.06 (June 2011), pp. 1211–1289. DOI: `10.1142/s0218202511005313`.

[7] J. W. BARRETT and E. SÜLI. "EXISTENCE AND EQUILIBRATION OF GLOBAL WEAK SOLUTIONS TO KINETIC MODELS FOR DILUTE POLYMERS II: HOOKEAN-TYPE MODELS." *Mathematical Models and Methods in Applied Sciences* 22.05 (Apr. 2012), p. 1150024. ISSN: 1793-6314. DOI: `10.1142/s0218202511500242`.

[8] J. W. Barrett and E. Süli. "Existence of Global Weak Solutions to Some Regularized Kinetic Models for Dilute Polymers." *Multiscale Modeling & Simulation* 6.2 (Jan. 2007), pp. 506–546. ISSN: 1540-3467. DOI: `10.1137/060666810`.

[9] J. W. Barrett and E. Süli. "Existence of global weak solutions to the kinetic Hookean dumbbell model for incompressible dilute polymeric fluids." *Nonlinear Analysis: Real World Applications* 39 (Feb. 2018), pp. 362–395. DOI: `10.1016/j.nonrwa.2017.07.012`.

[10] G. K. Batchelor. *An Introduction to Fluid Dynamics*. Cambridge University Press, Feb. 2000. ISBN: 9780511800955. DOI: `10.1017/cbo9780511800955`.

[11] R. B. Bird, R. C. Armstrong, and O. Hassager. *Dynamics of polymeric liquids Volume 1 Fluid mechanics*. John Wiley & Sons, Apr. 1977. ISBN: 0-471-07375-X.

[12] R. B. Bird, R. C. Armstrong, O. Hassager, and C. F. Curtiss. *Dynamics of polymeric liquids Volume 2 Kinetic Theory*. 2nd ed. John Wiley & Sons, Apr. 1987. ISBN: 0-471-80244-1.

[13] R. B. Bird. "The Kramers chain model for polymers." *Chemical Engineering Communications* 9.1–6 (Jan. 1981), pp. 321–329. DOI: `d9ng38`.

[14] R. Bird, P. Dotson, and N. Johnson. "Polymer solution rheology based on a finitely extensible bead—spring chain model." *Journal of Non-Newtonian Fluid Mechanics* 7.2–3 (Jan. 1980), pp. 213–235. ISSN: 0377-0257. DOI: `10.1016/0377-0257(80)85007-5`.

[15] B. Blaise and D. Frederick. *Introduction to Parallel Computing Tutorial*. URL: `https://hpc.llnl.gov/documentation/tutorials/introduction-parallel-computing-tutorial` (visited on 01/30/2024).

[16] D. Boger. "A highly elastic constant-viscosity fluid." *Journal of Non-Newtonian Fluid Mechanics* 3.1 (Sept. 1977), pp. 87–91. ISSN: 0377-0257. DOI: `10.1016/0377-0257(77)80014-1`.

[17] C. L. Bris and T. Lelièvre. "Micro-macro models for viscoelastic fluids: modelling, mathematics and numerics." *Science China Mathematics* 55.2 (Feb. 2012), pp. 353–384. DOI: `10.1007/s11425-011-4354-y`.

[18] D. Cao, C. Li, H. Li, and F. Yang. "Effect of dispersing time on the prediction equation of drag reduction rate and its application in the short distance oil pipeline." *Petroleum Science and Technology* 36.16 (May 2018), pp. 1312–1318. ISSN: 1532-2459. DOI: `10.1080/10916466.2018.1471501`.

[19] *COMSOL Multiphysics® v. 6.0*. `www.comsol.com`. 2021.

[20] A. W. Cook, J. D. Bauer, and G. D. Spriggs. "The reflection of a blast wave by a very intense explosion." *Proceedings of the Royal Society A: Mathematical, Physical and Engineering Sciences* 477.2250 (June 2021). ISSN: 1471-2946. DOI: `10.1098/rspa.2021.0154`.

[21] P. S. Doyle, E. S. G. Shaqfeh, and A. P. Gast. "Dynamic simulation of freely draining flexible polymers in steady linear flows." *Journal of Fluid Mechanics* 334 (Mar. 1997), pp. 251–291. DOI: `10.1017/s0022112096004302`.

[22] W. E, T.-j. Li, and P.-w. Zhang. "Convergence of a Stochastic Method for the Modeling of Polymeric Fluids." *Acta Mathematicae Applicatae Sinica, English Series* 18.4 (Nov. 2002), pp. 529–536. DOI: `10.1007/s102550200055`.

[23] H. Elman, D. Silvester, and A. Wathen. *Finite Elements and Fast Iterative Solvers: with Applications in Incompressible Fluid Dynamics*. Oxford University Press, June 2014. ISBN: 9780191780745. DOI: `10.1093/acprof:oso/9780199678792.001.0001`.

[24] A. Ern and J.-L. Guermond. *Theory and Practice of Finite Elements*. Springer New York, 2004. ISBN: 0-387-20574-8. DOI: `10.1007/978-1-4757-4355-5`.

[25] R. Evans and K. Walters. "Flow characteristics associated with abrupt changes in geometry in the case of highly elastic liquids." *Journal of Non-Newtonian Fluid Mechanics* 20 (Jan. 1986), pp. 11–29. DOI: `10.1016/0377-0257(86)80013-1`.

[26] R. Evans and K. Walters. "Further remarks on the lip-vortex mechanism of vortex enhancement in planar-contraction flows." *Journal of Non-Newtonian Fluid Mechanics* 32.1 (Jan. 1989), pp. 95–105. DOI: `10.1016/0377-0257(89)85043-8`.

[27] R. D. Falgout, J. E. Jones, and U. M. Yang. "The Design and Implementation of hypre, a Library of Parallel High Performance Preconditioners." *Lecture Notes in Computational Science and Engineering*. Springer-Verlag, pp. 267–294. DOI: `10.1007/3-540-31619-1_8`.

[28] M. Fortin, R. Guénette, and R. Pierre. "Numerical analysis of the modified EVSS method." *Computer Methods in Applied Mechanics and Engineering* 143.1-2 (Apr. 1997), pp. 79–95. DOI: `10.1016/s0045-7825(96)01145-0`.

[29] C. Geuzaine and J.-F. Remacle. "Gmsh: A 3-D finite element mesh generator with built-in pre- and post-processing facilities." *International Journal for Numerical Methods in Engineering* 79.11 (May 2009), pp. 1309–1331. DOI: `10.1002/nme.2579`.

[30] I. Ghosh, Y. L. Joo, G. H. McKinley, R. A. Brown, and R. C. Armstrong. "A new model for dilute polymer solutions in flows with strong extensional components." *Journal of Rheology* 46.5 (Sept. 2002), pp. 1057–1089. DOI: `10.1122/1.1501963`.

[31] P. Grassia and E. J. Hinch. "Computer simulations of polymer chain relaxation via Brownian motion." *Journal of Fluid Mechanics* 308 (Feb. 1996), pp. 255–288. DOI: `10.1017/s0022112096001474`.

[32] G. Grün and S. Metzger. "On micro–macro-models for two-phase flow with dilute polymeric solutions — modeling and analysis." *Mathematical Models and Methods in Applied Sciences* 26.05 (Feb. 2016), pp. 823–866. DOI: `10.1142/s0218202516500196`.

[33] R. Guénette and M. Fortin. "A new mixed finite element method for computing viscoelastic flows." en. *Journal of Non-Newtonian Fluid Mechanics* 60.1 (Oct. 1995), pp. 27–52. ISSN: 0377-0257. DOI: `10.1016/0377-0257(95)01372-3`.

[34] A. Guerrero and R. Castilla. "Aerodynamic Study of the Wake Effects on a Formula 1 Car." *Energies* 13.19 (Oct. 2020), p. 5183. ISSN: 1996-1073. DOI: `10.3390/en13195183`.

[35] C. Guillopé and J. Saut. "Existence results for the flow of viscoelastic fluids with a differential constitutive law." *Nonlinear Analysis: Theory, Methods & Applications* 15.9 (Jan. 1990), pp. 849–869. ISSN: 0362-546X. DOI: `10.1016/0362-546x(90)90097-z`.

[36] S. Gulati, S. J. Muller, and D. Liepmann. "Direct measurements of viscoelastic flows of DNA in a 2:1 abrupt planar micro-contraction." *Journal of Non-Newtonian Fluid Mechanics* 155.1-2 (Nov. 2008), pp. 51–66. DOI: `10.1016/j.jnnfm.2008.05.005`.

[37] X.-W. Guo, X.-H. Xu, Q. Wang, H. Li, X.-G. Ren, L. Xu, and X.-J. Yang. "A Hybrid Decomposition Parallel Algorithm for Multi-scale Simulation of Viscoelastic Fluids" (May 2016). DOI: `10.1109/ipdps.2016.21`.

[38] V. K. Gupta. "A new ALS model for dilute polymer solutions in flows with strong shear components." *Rheologica Acta* 51.1 (Aug. 2011), pp. 51–70. DOI: `10.1007/s00397-011-0579-5`.

[39] X. Hu and F. Lin. "Global Solutions of Two-Dimensional Incompressible Viscoelastic Flows with Discontinuous Initial Data." *Communications on Pure*

and Applied Mathematics 69.2 (Jan. 2015), pp. 372–404. ISSN: 1097-0312. DOI: `10.1002/cpa.21561`.

[40] M. A. Hulsen, A. P. G. van Heel, and B. H. A. A. van den Brule. "Simulation of viscoelastic flows using Brownian configuration fields." *Journal of Non-Newtonian Fluid Mechanics* 70.1 (May 1997), pp. 79–101. ISSN: 0377-0257. DOI: `10.1016/S0377-0257(96)01503-0`.

[41] J. S. Hur, E. S. G. Shaqfeh, and R. G. Larson. "Brownian dynamics simulations of single DNA molecules in shear flow." *Journal of Rheology* 44.4 (July 2000), pp. 713–742. DOI: `10.1122/1.551115`.

[42] W. R. Hwang, M. A. Walkley, and O. G. Harlen. "A fast and efficient iterative scheme for viscoelastic flow simulations with the DEVSS finite element method." *Journal of Non-Newtonian Fluid Mechanics* 166.7-8 (Apr. 2011), pp. 354–362. DOI: `10.1016/j.jnnfm.2011.01.003`.

[43] D. Hysom and A. Pothen. "A Scalable Parallel Algorithm for Incomplete Factor Preconditioning." *SIAM Journal on Scientific Computing* 22.6 (Jan. 2001), pp. 2194–2215. ISSN: 1095-7197. DOI: `10.1137/s1064827500376193`.

[44] T. M. Inc. *MATLAB version: 9.8.0 (R2020a)*. Natick, Massachusetts, United States, 2020.

[45] V. John and E. Schmeyer. "Finite element methods for time-dependent convection–diffusion–reaction equations with small diffusion." *Computer Methods in Applied Mechanics and Engineering* 198.3-4 (Dec. 2008), pp. 475–494. DOI: `10.1016/j.cma.2008.08.016`.

[46] B. Jourdain, T. Lelièvre, and C. L. Bris. "Existence of solution for a micro–macro model of polymeric fluid: the FENE model." *Journal of Functional Analysis* 209.1 (Apr. 2004), pp. 162–193. DOI: `10.1016/s0022-1236(03)00183-6`.

[47] N. G. Kampen. "Statistical mechanics of trimers." *Applied Scientific Research* 37.1-2 (1981), pp. 67–75. DOI: `10.1007/bf00382618`.

[48] G. Karypis and V. Kumar. "A Fast and High Quality Multilevel Scheme for Partitioning Irregular Graphs." *SIAM Journal on Scientific Computing* 20.1 (Jan. 1998), pp. 359–392. DOI: `10.1137/s1064827595287997`.

[49] P. Knabner and W. Barth. "Lineare Algebra: Grundlagen und Anwendungen." *Springer-Lehrbuch* (2013). ISSN: 0937-7433. DOI: `10.1007/978-3-642-32186-3`.

[50] P. Kumar and I. Saha Dalal. "Effects of chain resolution on the configurational and rheological predictions from Brownian dynamics simulations of an isolated polymer chain in flow." *Journal of Non-Newtonian Fluid Mechanics* 315 (May 2023), p. 105017. ISSN: 0377-0257. DOI: `10.1016/j.jnnfm.2023.105017`.

[51] T. C. B. Kwan, N. J. Woo, and E. S. G. Shaqfeh. "An experimental and simulation study of dilute polymer solutions in exponential shear flow: Comparison to uniaxial and planar extensional flows." *Journal of Rheology* 45.2 (Mar. 2001), pp. 321–349. DOI: `10.1122/1.1346599`.

[52] M. Laso and H. Öttinger. "Calculation of viscoelastic flow using molecular models: the connffessit approach." *Journal of Non-Newtonian Fluid Mechanics* 47 (June 1993), pp. 1–20. ISSN: 0377-0257. DOI: `10.1016/0377-0257(93)80042-a`.

[53] Y. N. Lee and R. L. Johnston. "Chapter 5 - Polymeric drag reduction in pipelines." *Surface Process, Transportation, and Storage*. Ed. by Q. Wang. Vol. 4. Oil and Gas Chemistry Management Series. Gulf Professional Publishing, 2023, pp. 227–259. ISBN: 978-0-12-823891-2. DOI: `https://doi.org/10.1016/B978-0-12-823891-2.00005-3`.

[54] T. Li and P. Zhang. "Convergence Analysis of BCF Method for Hookean Dumbbell Model with Finite Difference Scheme." *Multiscale Modeling & Simulation* 5.1 (Jan. 2006), pp. 205–234. DOI: `10.1137/05063430x`.

[55] T. W. Liu. "Flexible polymer chain dynamics and rheological properties in steady flows." *The Journal of Chemical Physics* 90.10 (May 1989), pp. 5826–5842. DOI: `10.1063/1.456389`.

[56] A. Lozinski, R. G. Owens, and T. N. Phillips. "The Langevin and Fokker–Planck Equations in Polymer Rheology." *Numerical Methods for Non-Newtonian Fluids*. Ed. by R. Glowinski and J. Xu. Vol. 16. Handbook of Numerical Analysis. Elsevier, 2011, pp. 211–303. DOI: `https://doi.org/10.1016/B978-0-444-53047-9.00002-2`.

[57] J. Marchal and M. Crochet. "A new mixed finite element for calculating viscoelastic flow." *Journal of Non-Newtonian Fluid Mechanics* 26.1 (Jan. 1987), pp. 77–114. DOI: `10.1016/0377-0257(87)85048-6`.

[58] *Meggie Compute-Cluster, RRZE, Friedrich-Alexander-Universität Erlangen Nürnberg*. URL: `https://hpc.fau.de/systems-services/systems-documentation-instructions/clusters/meggie-cluster/` (visited on 01/30/2024).

[59] *MFEM: Modular Finite Element Methods [Software]*. `mfem.org`. DOI: `10.11578/dc.20171025.1248`.

[60] W. Nolting. *Grundkurs Theoretische Physik 2: Analytische Mechanik*. Springer Berlin Heidelberg, 2014. ISBN: 978-3-642-41979-9. DOI: `10.1007/978-3-642-41980-5`.

[61] W. Nolting. *Grundkurs Theoretische Physik 6: Statistische Physik*. Springer Berlin Heidelberg, 2014. ISBN: 9783642253935. DOI: `10.1007/978-3-642-25393-5`.

[62] J. G. Oldroyd. "On the formulation of rheological equations of state." *Proceedings of the Royal Society of London. Series A. Mathematical and Physical Sciences* 200.1063 (Feb. 1950), pp. 523–541. DOI: `10.1098/rspa.1950.0035`.

[63] H. C. Öttinger. *Stochastic Processes in Polymeric Fluids*. Springer Berlin Heidelberg, 1996. DOI: `10.1007/978-3-642-58290-5`.

[64] B. Purnode and M. Crochet. "Flows of polymer solutions through contractions Part 1: flows of polyacrylamide solutions through planar contractions." *Journal of Non-Newtonian Fluid Mechanics* 65.2-3 (Aug. 1996), pp. 269–289. DOI: `10.1016/0377-0257(96)01446-2`.

[65] M. Renardy and B. Thomases. "A mathematician's perspective on the Oldroyd B model: Progress and future challenges." *Journal of Non-Newtonian Fluid Mechanics* 293 (July 2021), p. 104573. ISSN: 0377-0257. DOI: `10.1016/j.jnnfm.2021.104573`.

[66] A. M. Robertson. "Review of Relevant Continuum Mechanics." *Hemodynamical Flows*. Birkhäuser Basel, 2008, pp. 1–62. ISBN: 9783764378066. DOI: `10.1007/978-3-7643-7806-6_1`.

[67] D. Roylance. *Engineering Viscoelasticity*. `https://ocw.mit.edu/courses/3-11-mechanics-of-materials-fall-1999/d173f95347f59d59dd9b7387ab4303e7_MIT3_11F99_visco.pdf`. Accessed: 28-11-2023. Oct. 2001.

[68] H. Rubin. "Drag Reduction Application in Fire Fighting Systems." *Journal of the Sanitary Engineering Division* 98.1 (Feb. 1972), pp. 01–09. ISSN: 2690-3350. DOI: `10.1061/jsedai.0001364`.

[69] J. W. Ruge and K. Stüben. "4. Algebraic Multigrid" (Jan. 1987), pp. 73–130. DOI: `10.1137/1.9781611971057.ch4`.

[70] A. Rüttgers and M. Griebel. "Multiscale simulation of polymeric fluids using the sparse grid combination technique." *Applied Mathematics and Computation* 319 (Feb. 2018), pp. 425–443. DOI: `10.1016/j.amc.2017.04.025`.

[71] Y. Saad. "Iterative Methods for Sparse Linear Systems" (Jan. 2003). DOI: `10.1137/1.9780898718003`.

[72] J. D. Schieber and H. C. Öttinger. "The effects of bead inertia on the Rouse model." *The Journal of Chemical Physics* 89.11 (Dec. 1988), pp. 6972–6981. DOI: `10.1063/1.455323`.

[73] J. D. Schieber. "Generalized Brownian configuration fields for Fokker–Planck equations including center-of-mass diffusion." *Journal of Non-Newtonian Fluid Mechanics* 135.2-3 (May 2006), pp. 179–181. DOI: `10.1016/j.jnnfm.2006.02.007`.

[74] D. Silvester, H. Elman, D. Kay, and A. Wathen. "Efficient preconditioning of the linearized Navier–Stokes equations for incompressible flow." *Journal of Computational and Applied Mathematics* 128.1-2 (Mar. 2001), pp. 261–279. DOI: `10.1016/s0377-0427(00)00515-x`.

[75] M. Somasi, B. Khomami, N. J. Woo, J. S. Hur, and E. S. Shaqfeh. "Brownian dynamics simulations of bead-rod and bead-spring chains: numerical algorithms and coarse-graining issues." *Journal of Non-Newtonian Fluid Mechanics* 108.1-3 (Dec. 2002), pp. 227–255. DOI: `10.1016/s0377-0257(02)00132-5`.

[76] J. Su, C. Hou, Y. Ma, and Y. Wang. "Multilevel Monte Carlo method for the Brownian configuration field of polymer fluids." *AIP Advances* 10.9 (Sept. 2020), p. 095013. DOI: `10.1063/5.0023398`.

[77] R. Temam. *Navier-stokes equations*. 3rd ed. Studies in Mathematics & its Applications Vol. 2. Elsevier Science, 1984. ISBN: 044487559X.

[78] V. Thomée. *Galerkin finite element methods for parabolic problems*. Springer-Verlag, Berlin, 1997. ISBN: 3-540-12911-1.

[79] M. Tsubokura, K. Kitoh, N. Oshima, T. Nakashima, H. Zhang, K. Onishi, and T. Kobayashi. "Large Eddy Simulation of Unsteady Flow Around a Formula Car on Earth Simulator." ANNUAL (Apr. 2007). ISSN: 0148-7191. DOI: `10.4271/2007-01-0106`.

[80] J. von Neumann. "Various techniques used in connection with random digits." *John von Neumann, Collected Works* 5 (1963), pp. 768–770.

[81] J. W. Barrett and E. Süli. "Existence of global weak solutions to Fokker-Planck and Navier-Stokes-Fokker-Planck equations in kinetic models of dilute polymers." *Discrete & Continuous Dynamical Systems - Series S* 3.3 (2010), pp. 371–408. ISSN: 1937-1179. DOI: `10.3934/dcdss.2010.3.371`.

[82] T. Weinzierl. *Principles of Parallel Scientific Computing. A First Guide to Numerical Concepts and Programming Methods*. Cham, Switzerland: Springer International Publishing AG, Feb. 2021. ISBN: 9783030761936. DOI: `10.1007/978-3-030-76194-3`.

[83] X. Xu and P. Yu. "A multiscale SPH method for simulating transient viscoelastic flows using bead-spring chain model." *Journal of Non-Newtonian Fluid Mechanics* 229 (Mar. 2016), pp. 27–42. DOI: `10.1016/j.jnnfm.2016.01.005`.